University of Strathclyde

Department of Mechanical & Aerospace Engineering

Micro Gas Flows: Modelling the Dynamics of Knudsen Layers

Nishanth Dongari

A thesis presented in fulfilment of the requirements

for the degree of Doctor of Philosophy

2012

Declaration of author's rights

This thesis is the result of the author's original research. It has been composed by the author and has not been previously submitted for examination which has led to the award of a degree.

Nishanth Dongari

December 2012

Abstract

The behaviour of gas flows in microscale systems cannot be accurately described by the Navier-Stokes-Fourier (N-S-F) equations of macroscale fluid dynamics. Micro and nano-scale gas flows often display non-standard fluid behaviour, and near a solid bounding surface they are dominated by the effect of gas molecule-surface interactions. This leads to the formation of a Knudsen layer (KL): a local thermodynamically non-equilibrium region of thickness of a few mean free paths (MFP) from the surface. Linear constitutive relations for shear stress and heat flux are no longer necessarily valid in the KL.

To account for this, we investigate a power-law (PL) form of the probability distribution function for free paths of rarefied gas molecules in arbitrary wall confinements. PL based geometry dependent MFP models are derived for planar and non-planar geometry systems by taking into account the boundary limiting effects on the molecular free paths. Molecular dynamics (MD) numerical experiments are carried out to rigorously validate the PL model, under a wide range of rarefaction conditions. MD is the most appropriate simulation tool as it is deterministic, allowing for realistic molecular behaviour, i.e. molecular attractions, repulsions, movements and scatterings. The free path measurements of individual molecules convey that conventional form of exponential distribution function is not valid under rarefied conditions and follow Lévy type of flights, irrespective of the presence of the wall. MFP profiles of MD measurements and PL model for confined surfaces in the transition flow regime show sharp gradients close to the wall, while exponential model predicts shallower gradients.

As gas transport properties can be related to the MFP through kinetic theory, the

N-S-F constitutive relations, and the velocity slip and the temperature jump boundary conditions are then modified in order to better capture the flow behaviour in the Knudsen layers close to surfaces. The new modelling technique is tested for isothermal and non-isothermal gas flows in both planar and non-planar confinements. The results show that our approach greatly improves the near-wall accuracy of the N-S-F equations, well beyond the slip-flow regime. In general, the current method exhibits good agreement for velocity and temperature profiles up to $Kn \sim 1$, and for integral flow parameters up to $Kn \sim 5$, without tuning any slip and jump coefficients. The PL scaling can be readily extended to complex geometries, and straightforwardly incorporated into existing computational fluid dynamics (CFD) codes. The current work is significant from the numerical simulation point of view because simulation tools are better developed for N-S-F equations, when compared to other higher order equations such as Burnett, R26 etc.

Acknowledgements

It is a pleasure to thank all those who helped make this thesis possible. I would first of all like to extend my gratitude and deepest appreciation to my supervisors Dr. Yonghao Zhang and Prof. Jason M. Reese. Their expertise, understanding, patience and continuous support have set an example which I hope to emulate.

I am also thankful to my colleagues, Dr. Matthew K. Borg, and Craig White for helping me in MD and DSMC simulation methods, respectively. They have supported me in a number of ways including technical advice and answers to many queries.

The research leading to results in this thesis has received funding from the European Community's Seventh Framework Programme (ITN - FP7/2007-2013) under grant agreement n^o 215504.

Finally, this dissertation is dedicated to my family who have provided unconditional love, support, words of encouragement and sacrifice throughout the course of my doctorate. I owe all my success and achievements to you.

Contents

List of Figures

List of Tables

Nomenclature

Symbols

A	cross-sectional area
$\mathbf{a}$	molecule acceleration
C_1	first-order slip coefficient
C_2	second-order slip coefficient
C_f	friction factor
C_v	specific heat capacity at constant volume
C_p	specific heat capacity at constant pressure
$\overline{c}$	mean speed of molecules
d	molecular diameter
e	total energy
$\mathbf{f}$	molecule force vector
f	molecular velocity distribution
f^{eq}	Maxwell-Boltzmann equilibrium velocity distribution
G	normalised mass flow rate
H	height
i, j	arbitrary pair of molecules
k_b	Boltzmann constant
Kn	Knudsen number
K_P	controller proportional constant
L	length
Ma	Mach number
m	molecule mass
$\dot{m}$	mass flux
n	power-law exponent

N	number of molecules
N_{av}	Avogadro's constant
$\hat{\mathbf{n}}$	normal unit-vector
$\mathbf{P}$	stress tensor
$p(r)$	probability distribution function
P	normal pressure
q	heat flux
$\mathbf{r}$	position vector
r_{cut}	potential cut-off radius
Re	Reynolds number
T	temperature
t	time
Δt	time interval
$\mathbf{U}$	macroscopic velocity vector
U	macroscopic velocity in axial direction
$\mathbf{v}$	molecule velocity
V	volume
w	width
ΔX	cell size
x, y, z	spatial Cartesian co-ordinates

Greek

α	thermal accommodation coefficient
β	normalised mean free path
δ	inverse Knudsen number
ϵ	characteristic energy scale
ζ	relative error
θ	angle
$\dot{\theta}_v$	inter-molecular collision rate
κ	thermal conductivity
λ	mean free path
λ_{HS}	hard-sphere based mean free path
λ_k	kinetic mean free path
λ_M	Maxwell based mean free path
μ	dynamic viscosity
ω	angular velocity
Ω	solid angle
ρ	mass density
$\Re$	specific gas constant
$\Re_u$	Universal gas constant
σ	tangential momentum accommodation coefficient
τ	time constant
τ_w	wall shear stress
Γ	torque
ϕ	field property

Superscripts

*	reduced unit
eq	equilibrium
neq	non-equilibrium
H	higher-order

Subscripts

av	average
c	continuum
$conc$	concave
$conv$	convex
eff	effective
i	inside
i, j	pair of molecule indices
m	mean
o	outside
PL	power-law
ϕ	tangential coordinate
r	radial coordinate
ST	Stops
w	wall value
x, y, z	spatial Cartesian co-ordinates

Acronyms

CE	Chapman-Enskog
CFD	Computational Fluid Dynamics
DSMC	Direct Simulation Monte Carlo
LJ	Lennard-Jones
MD	Molecular Dynamics
MFP	Mean Free Path
N-S-F	Navier-Stokes-Fourier
NP	Non-planar
P	Planar
PL	Power-law
TAC	Thermal Accommodation Coefficient
TMAC	Tangential Momentum Accommodation Coefficient

Chapter 1

Introduction

Not everything that can be counted counts,
and not everything that counts can be counted
- Albert Einstein

Gas flows in microscale systems display behaviour that cannot be replicated with the governing equations of classical fluid dynamics, the Navier-Stokes-Fourier equations (N-S-F). This thesis details how the N-S-F equation set can be modified to model microscale gas flows successfully, and demonstrates, for the first time, such approach is rigorously validated using the molecular dynamics simulation technique by measuring microscopic properties. It describes a power-law based modification for the constitutive relations and boundary conditions that is a generalised and extended alternative to previously available models.

1.1 Background to rarefied gas flows

Until recently, non-continuum (rarefied) gas flows have primarily been encountered in low-density applications such as high-altitude aircraft or high-vacuum equipment (Karniadakis et al., 2005; Saha and Srivastava, 1958). However, rapid advancements in micro and nano fabrication technologies over the past few years have triggered the introduction of intricate small-scale devices in several emerging technological applications (Karniadakis et al., 2005; Gad-el-Hak, 1999). The tiny length scales

usually encountered in microfluidic devices imply that non-equilibrium effects may turn out to be important even at much higher pressures. For example, the mean free path of air molecules at the standard temperature and pressure is approximately 70 nm. Consequently, the ratio of the mean free path of gas molecules to the characteristic dimensions of a MEMS device can be appreciable. This ratio is referred to as the Knudsen number (Kn).

The primary distinction between fluid flows in the micro-scale and the conventional devices originates from the pertinent surface area to volume ratios. For traditional devices, this may be of the order of 1 m^{-1}, as compared to as low as 10^6 m^{-1} for typical microdevices with characteristic length scales of the order of 10^{-6}m (Gad-el-Hak 1999). Due to the involvement of tiny length scales, the continuum flow assumption implemented in conventional fluid dynamics may break down for the accurate prediction of fluid transport in micro devices. Hence, many researchers had emphatically ruled out the possibilities of using N-S-F based models for microscale gas flows with significant effects of rarefaction. Central to these considerations, the applicability of the classical continuum hypothesis has often been seriously debated in the presence of prominent micro-scale effects. As such, the continuum hypothesis is based on the postulate that there are sufficiently large numbers of molecules in chosen elemental volumes so that statistical uncertainties with regard to their respective positions and velocities do not perceptibly influence the averaged fluid/ flow property predictions, as well as the predictions in the local gradients of properties through well-known rules of differential calculus.

It has been traditionally well recognised that the attainment of local thermodynamic equilibrium, so as to render continuum considerations appropriate, necessitates theoretically infinite numbers of collisions involving the gas molecules. When gas molecules collide with a solid boundary, those are temporarily adsorbed on the wall and are subsequently ejected. This allows a partial transfer of momentum and energy of the walls to the gas molecules. If the frequency of collisions is very large, the momentum and energy exchange is virtually complete and the no-slip/ no-jump boundary conditions may prevail for all practical considerations. However, in a less-dense system, deviations from such idealization are significantly more ominous.

The extent of this deviation is not merely dictated by the mean free path (λ) in an absolute sense, but also its comparability with the characteristic system length scale (L) that describes the relative importance of rarefaction in the system. The ratio of these two, known as the Knudsen number ($Kn = \lambda/L$), appears to the single important decisive parameter that determines the applicability of a particular flow modeling strategy as against the extent of rarefaction of the flow medium.

Thus, both the size and non-continuum effects profoundly affects the mass, momentum and energy transport; and leads to additional effects like slip flow, rarefaction, compressibility, etc. The later effects are particularly more perceptible and prominent in gases than in liquids, primarily attributable to the significant characteristic alterations in the density of gases with changes in pressure as compared to liquids. In addition to exhibiting rarefied behavior, gas flows in micro-conduits also tend to exhibit significant compressibility effects even for cases with low Mach numbers (Beskok and Karniadakis, 1993; Pong et al., 1994; Colin, 2005; Dongari et al., 2007, 2009, 2010a; Turner et al., 2004; Jang and Wereley, 2004; Yohung and Chan, 2004), which is a significant deviation from the corresponding macro-scale counterpart. This contradicts the criteria for isothermal normal scale flows which at the most has density variations of 5% below a Mach number of 0.3, but above this value the density variations become significant. It is shown by Yuhong and Chan that for a pressure-driven flow in-between a two planar-wall geometry the modelled rarefaction effects counteract the modelled compressibility effects causing the non-linear axial pressure profile tend to a more linear shape (Yohung and Chan, 2004).

For micro gas flows the surface-effects also become important and must be taken into account as a result of the scale difference between the relatively large ratio of the confining boundary surface area to the volume of the confined gas. The surface-effects considerably influence a flow in the near-wall region, referred to as the Knudsen layer, which, because of the small scale of the system, represents a substantial portion of the gas volume. These effects are transmitted by the gas molecules interactions with surfaces. The structure of the Knudsen layer in the gas and the conditions on fundamental modelling techniques have been investigated by

Trilling (1975).

1.2 Technological applications

Rapid advancements in micro and nano fabrication technologies over the past few years have triggered the introduction of intricate small-scale devices in several emerging applications, including lab-on-a-chip based sensors for performing complex biochemical assays (Burns et al., 1998), micro-heat-exchangers for cooling of electronic circuits (Weisberg et al., 1992), micro-pumps used for inkjet printing (Bassous et al., 1977), and hand-held gas chromatography systems for the detection of trace concentrations in air-borne pollutants (Squires and Quake, 2005), to name a few. Micro-scale fluid mechanics (or equivalently, microfluidics) has been found to hold the key towards efficient design, synthesis and performance of almost every device of this kind, encompassing the flows of liquids and gases through fluidic channels of micron and sub-micron dimensions. Other important micro-nanofluidic devices comprise Winchester-type hard disk drives, with air gaps of less than 50 nm, handling air flows at very high speeds. A variety of Micro Electro Mechanical Systems (MEMS) devices also contain micro-channel flows, such as electro static comb micro drives (Tai et al., 1989), and electro statically side-driven micromotor (Mehregany et al., 1990; Trimmer, 1997).

Some other small devices that have been produced so far are valves, gears, cantilevers, diaphragms and tweezers of a dimension of less than 100 μm which can function by electrostatic, magnetic, electromagnetic, pneumatic and thermal actuators. Many of these devices can be used in sensors of micro-flow measurements for pressure, temperature, mass-flow, velocity, sound, chemical composition and as actuators for linear and angular motion (Gad-el-Hak, 1999) for example. An interesting and common micro environment where an alternative gas modelling technique is of particular concern is for hard disk drives where the reading head is situated about 65 nm above the disk, for which the load capacity would be erroneously predicted by using conventional macroscopic methods (Karniadakis et al., 2005). Other engineering based modelling areas are:- micro-motors where the gap between rotor

and the stator is about 3μm (Karniadakis et al., 2005), micro-channel cooling of IC chips (Mahulikar et al., 2007) and micro-reactors for chemical synthesis (Mahulikar et al., 2007).

With a better understanding of the surface effects experienced by gas flows in a micro scale environment, here referred to as micro gas flows, we are not only likely to improve our micro-scale manufacturing techniques but we might also be able to understand mysteries in nature such as the way mosquitoes manage to hear sounds using brush-like micro-scale antennae (Jackson and Robert, 2006). In the medical field, a better understanding of micro gas flows can bring forward techniques to provide more efficient delivery of inhaled medications and to understand the effects of inhaled pollutants better (Gemci et al., 2008). There are similar effects present for both micro gas flows and aerospace-flows. For the latter flows these effects occur because of the dilute gas situation even though the length-scale of aerospace flows often are of normal dimensions. Therefore, perhaps a better understanding of the nature of micro gas flows will help to improve modelling capabilities in micro gas flows as well as gas flows related to aerospace research. It is, for instance, argued in the article by Flieseler (1998) that orbital travel in the lower atmosphere could be made possible using solar sails, for which a correct understanding of the molecular surface interactions would be of major concern. Other similarities between micro-scale flows and macro-scale flows could be the description of granular flows, which avalanches could be characterised as according to Reese et al. (2003).

Karniadakis et al. (2005) has listed the supporting funding for this field in the years 1997, 2002 and 2004 amounting to $ 432 million, $ 2.2 billion and $ 3.5 billion respectively, showing a marked increase. This vast and increasing investment reflects the interest and desire for better understanding of these flows which will hopefully lead to cheaper production of more efficient micro-devices becoming more common in our everyday life in the future.

1.3 Research objectives

Investigations of gas flows at microscales raise questions regarding the non-standard behaviour of the fluid, as noticed in numerous experiments. There are great difficulties in investigating microscale/rarefied gas flows experimentally. Conventionally bulk properties can be measured reliably, such as average mass flow rate through a channel. Interpretation of these integral flow parameters, however, is problematic because there can be multiple causes of deviation of these quantities from those expected from conventional macroscopic theory, assigning their relative contributions is difficult. In addition, fitting of macroscopic theories to experimental data with the aid of tuning parameters, may not be physically realistic. This is due to the fact that fluid dynamic effects occurring over disparate physical scales are intensely coupled with a number of significant thermodynamic criticalities.

In this situation, methods for simulating microflows have come to the forefront. Many of the unusual effects observed in rarefied gas flow systems arise from the gas not being in thermodynamic equilibrium. To test this, fundamental properties of the gas - the inter-molecular collision rate, the molecular velocity distribution and the distribution of free paths between inter-molecular collisions need to be measured over a range of rarefied conditions. These properties can be measured in molecular dynamics (MD) simulations of a moving gas in unconfined and confined spaces. MD is an appropriate method, compared to other simulation methods such as direct simulation Monte Carlo (DSMC), to estimate these fundamental properties as it is the only deterministic approach (Rappaport, 2004), allowing for realistic molecular behaviour, i.e. molecular attractions, repulsions, movements and scatterings.

The spatial and temporal variation of these averaged collision properties can give an indication of the non-equilibrium processes occurring in rarefied gases over disparate length and time scales. This information is very difficult to obtain experimentally, so MD can be used to explore unresolved issues in anomalous transport in rarefied gases. As macroscopic gas transport properties can be related to microscopic details through kinetic theory, the MD data may help to modify existing constitutive relationships (Dongari et al., 2011a), which may then be fed into N-S-F

equations and these results prove useful for the effective modeling of micro gas flows in the transition flow regime (Lockerby et al., 2004; Lockerby and Reese, 2008; Dongari et al., 2011b). Thus the primary contribution of this research is the production of a design oriented simple tool for fluid flow and heat transfer in gas microflows. The work makes use of specialised boundary conditions alongside modifications to the N-S-F equations that can replicate Knudsen layer behaviour.

Modeling the non-equilibrium flow regions such as Knudsen layer (KL) should ideally be performed using detailed kinetic theory (Sone, 2002). It is important to stress that we do not attempt to assess the accuracy of the proposed new modelling technique underpinning the Boltzmann equation. However an appropriate extension to the N-S-F equations would be less time-consuming and less demanding of computational capacity and our motivation is to compare the predictive capabilities of competing continuum equation sets relative to a more computationally expensive molecular and kinetic theory based techniques. It provides engineers with the capability to rationally design gas microsystems using the same type of numerical studies that are common in macroscale fluid dynamics. With microscale engineering often at the forefront of developing technology, this is a valuable new capability for the field.

1.4 Thesis structure

Chapter 2 Characterising parameters for microscale flows are introduced. Critical evaluation of the most commonly applied techniques for modelling rarefied flows is provided for approaches ranging from discrete molecular simulations through to classical macroscale fluid dynamics.

Chapter 3 A new probability distribution function to describe gas free paths has been hypothesised, and a geometry dependent effective mean free path (MFP) expression derived. The theoretically derived effective MFP is based on a gas molecules probability of colliding with other gas molecules in addition to solid walls. The effective MFP model is investigated in the close vicinity of geometries with one planar wall, two planar walls, cylindrical obstacle, hallow cylinder and a spherical obstacle.

Chapter 4 A molecular dynamics simulation tool has been developed and used to assess the fundamental gas properties: inter-molecular collision rates, molecular free path probability distribution, and mean free path values in unconfined and confined planar spaces. We simulated neon and argon gas molecules using the simple Lennard-Jones interaction potential function, over a wide rage of Kn.

Chapter 5 Using the theoretical and simulation results obtained in Chapters 3 and 4, respectively, a simple constitutive scaling approach to model the Knudsen layer flow within a conventional continuum fluid dynamics framework has been described, in accordance with the kinetic theory of gases. The new approach is validated whenever possible against rigorous MD and DSMC simulation data for field properties, and experimental data and kinetic theory for integral flow parameters.

Chapter 6 Conclusions are drawn about the effectiveness of the power-law (PL) wall MFP model applied, and about the potential of the constitutive scaling method as an engineering design tool. Related work ongoing in the James Weir Fluids Laboratory is briefly discussed, and suggestions are made for further research.

Appendices We re-visit the Navier-Stokes-Fourier model in the framework of Boltzmann statistics, and propose a new and more appropriate way of assessing non-equilibrium in the local flowfield, and the corresponding appropriateness of the Navier-Stokes-Fourier model for both low and high speed gas flows. Our theoretical analysis and numerical simulations ($0.01 < Kn < 1$ and $0.2 < Ma < 10$) confirm our proposed method.

1.4.1 Highlights of scientific achievements

- Lévy statistics based power-law (PL) distribution function hypothesised and derived a geometry dependent effective mean free path (MFP) model for planar and non-planar geometric configurations. The new method is devised as a means of circumventing many of the short comings associated with the use of classical exponential distribution function for simulating real-world flows.
- New measurements tools are added to the existing mdFoam solver in OpenFOAM software. Numerical experiments are carried out and the PL model is rigor-

ously validated under wide range of rarefaction conditions.

- Consequently constitutive relations of Navier-Stokes-Fourier (N-S-F) equations and boundary conditions are modified. Modified governing equations successfully implemented to predict engineering test cases comprising of isothermal and thermal flows in planar and non-planar surfaces. The new modelling technique vastly improves the near-wall accuracy of the N-S-F equations, well beyond the slip-flow regime. The PL scaling can be readily extended to complex geometries, and straightforwardly incorporated into existing computational fluid dynamics (CFD) codes.
- Addressed how to accurately assess the departure of flow fields from equilibrium, and to identify when the N-S-F model is applicable. Two new kinetic parameters based on the molecular distribution function are proposed and they show a complicated dependency on both Kn and Ma. Our proposed parameters are not only of theoretical interest, but could be used for model switching criteria in kinetic-continuum hybrid numerical schemes.
- The current thesis work is significant from the numerical simulation point of view because simulation tools are better developed for N-S-F equations, when compared to other higher order equations such as Burnett, R26 etc.

1.4.2 Publications

The research results in this thesis are reported in the following peer reviewed publications:

International Journals

- Dongari, N., Zhang, Y.H., and Reese, J. M., Molecular free path distribution in rarefied gases, Journal of Physics D: Applied Physics 44 125502, 2011.
- Dongari, N., Zhang, Y.H., and Reese, J. M., Modeling of Knudsen layer effect in micro/nano scale gas flows, Journal of Fluids Engineering 133 071101, 2011.
- Dongari, N., Barber, R.W., Emerson, D.R., Stefanov, S.K., Zhang, Y.H., and Reese, J. M., The effect of Knudsen layers on rarefied Couette gas flows, Microfluidics and Nanofluidics (2012), DOI:10.1007/s10404-012-1019-2.

International Conferences - Peer Reviewed Proceedings

- Dongari, N., White, C., Scanlon, T. J., Zhang, Y. H., and Reese, J. M., Rarefaction effects in gas flows over curved surfaces, 28th International Symposium on Rarefied Gas Dynamics (RGD28), Zaragoza, Spain, 2012.
- Dongari, N., Zhang, Y. H., and Reese, J. M., Molecular dynamics simulations of high speed rarefied gas flows, 28th International Symposium on Rarefied Gas Dynamics (RGD28), Zaragoza, Spain, 2012.
- Dongari, N., Barber, R. W., Emerson, D. R., Zhang, Y. H., and Reese, J. M., Velocity inversion in cylindrical Couette gas flows, in Journal of Physics: Conference Series - Proceedings of 1st European Conference on Gas MicroFlows (GASMEMS2012), vol. 362, pp. 012009, 2012.
- Meng, J. P., Dongari, N., Reese, J. M., and Zhang, Y. H., A kinetic switching criterion for hybrid modelling of multiscale gas flows, in Journal of Physics: Conference Series - Proceedings of 1st European Conference on Gas MicroFlows (GASMEMS2012), vol. 362, pp. 012006, 2012.
- Dongari, N., Zhang, Y.H., and Reese, J. M., Behaviour of microscale gas flows based on a power-law free path distribution function In: Rarefied Gas Dynamics. AIP Conference Proceedings, 1333 (1st). Springer, pp. 724-729. ISBN 978-0-7354-0889-0, 2011.
- Dongari, N., Zhang, Y.H., and Reese, J. M., The importance of mean free path in determining gas micro flow behaviour, ASME 2010 8th International Conference on Nanochannels, Microchannels, and Minichannels: Parts A and B, FEDSM-ICNMM2010-30743, pp. 481-490, 2010.
- Dongari, N., Zhang, Y., and Reese, J. M., Molecular dynamics studies of anomalous transport in rarefied gases, in Proceedings on CDROM of 2nd European Conference on Microfluidics (μFlu'10), Toulouse, France, S. Colin and G. L. Morini (Eds.). SHF (Publisher), ISBN 978-2-906831-85-8, pp. μFLU2010-185:1-10, 2010.
- Dongari, N., Zhang, Y., and Reese, J. M., Power-law free path distribution for thermal transpiration, in Proceedings on CDROM of 2nd International GASMEMS Workshop (GASMEMS10), Les Embiez, France, pp. GASMEMS2010-DY06:1-10,

2010.

- Dongari, N., Zhang, Y., and Reese, J. M., The 'Knudsen layer' effect on thermal transpiration of rarefied gases, in Proceedings on CDROM of 1st International GASMEMS Workshop (GASMEMS09), Eindhoven, The Netherlands, pp. GASMEMS09-14:1-7, 2009.

Chapter 2

State of the art: modelling rarefied gas flows

The mind is the root from which all things grow
if you can understand the mind, everything else is included
- Bodhidharma

2.1 Classification of rarefied gas flows

The Knudsen number has been introduced in Chapter 1 as the extent of deviation from the equilibrium. The mean free path of the gas is the average distance that a molecule will travel before a collision with another molecule. It is typically defined for a gas in equilibrium, and depends on the velocity distribution of the molecules in the gas. For the equilibrium state, molecular velocities conform to the Maxwellian statistical distribution function, commonly referred to as the equilibrium distribution (Maxwell, 1867). An example of a typical Maxwellian distribution (in one spatial dimension) is shown in Fig. 2.1. The premise of the equilibrium distribution is that the most probable velocity of a molecule will be the average velocity, and that it is statistically unlikely that a large number of molecules will have either a much greater or much lower velocity than the average value. The shape of a gas equilibrium distribution will be influenced by its molecular mass, its temperature,

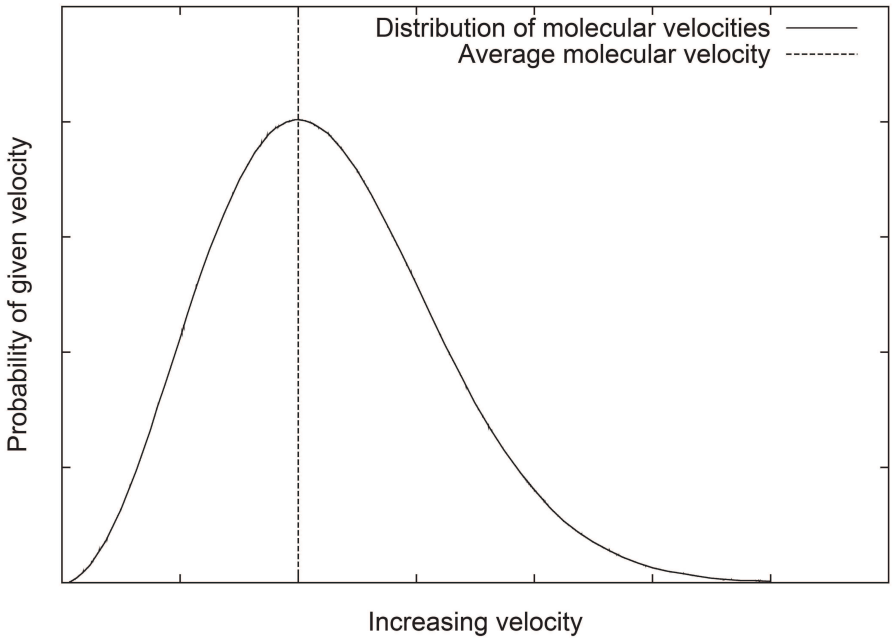

Figure 2.1: Example of a Maxwellian distribution of molecular velocities in a 1D case. The most probable molecular velocity is the average value, with probability decreasing towards the maximum and minimum velocities.

and its velocity in three-dimensional space. In turn, the expression that describes the mean free path of gas in a system will be determined by both its equilibrium distribution function and the choice of force-interaction model used to represent the gas molecules.

The simplest molecular interaction law is the hard-sphere model, which treats each molecule as an elastic sphere whose diameter is finite, but small in comparison to the mean molecular separation. Beyond the sphere diameter, there is no interaction potential between molecules, but when the spheres collide the repulsion is taken to be infinite (Kogan, 1969). The hard-sphere model is used throughout this thesis, as it can offer a reasonable approximation to the behaviour of monoatomic gases. For the hard-sphere model in a single-species gas, the mean free path is defined as:

$$\lambda = \frac{1}{\sqrt{2}\pi\eta d^2}, \tag{2.1}$$

where η is the molecular density per unit volume (the number density), and d is the diameter of the elastic spheres (Kennard, 1938). A more common expression of this

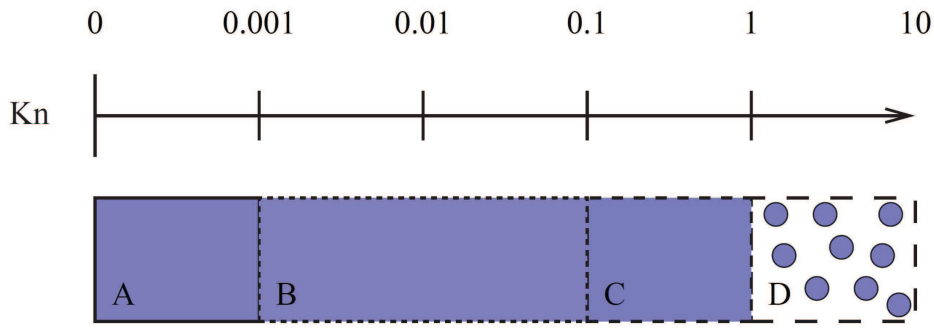

Figure 2.2: Gas flow regimes classified by Knudsen number; A represents fully continuous flow, B slip/jump flow, C transitional behaviour and D free molecular flow.

form, given in terms of macroscopic quantities, is

$$\lambda = \frac{\mu}{\rho}\sqrt{\frac{\pi}{2\Re T}}, \tag{2.2}$$

where μ is the dynamic viscosity of the gas, $\Re$ the specific gas constant and T the temperature (Cercignani, 1990).

The Knudsen number is also dependent on L, a characteristic system dimension. This will depend on the system geometry, but in simple configurations it is most common to use the smallest dimension of the system, normally channel height or pipe diameter. In other cases the choice is less obvious, for example, in flow over an unconfined microsphere the sphere radius is used to define the Knudsen number (Barber et al., 2004). In each case study examined in this thesis, the characteristic dimension used to define Knudsen number will be stated. As outlined in Chapter 1, the Knudsen number characterises the degree of rarefaction of gas flows. The behaviour of rarefied gases is classified into four main categories, as shown in Fig. 2.2, which are described below (Karniadakis et al., 2005).

In the limit of $Kn \to 0$, regime A, the gas behaves as an entirely continuous fluid at, or very near to, the equilibrium state. In this flow regime, which extends to $Kn \sim 0.001$, the N-S-F equations remain valid (Gad-el-hak, 1999). The Knudsen layer, a region of non-equilibrium flow found within one to two mean free paths of a surface, has no appreciable impact on the flow. The gas is equilibrated with its bounding surfaces, and the no-slip and no-jump boundary conditions of macroscale

fluid dynamics hold.

As Kn increases into regime B, in the range $0.001 < Kn < 0.1$, the flow moves further from local thermodynamic equilibrium. In this flow regime the Knudsen layer is traditionally considered to have a negligible impact on the flow, although research conducted in the production of this thesis has demonstrated that this is unlikely to be true in some microsystem cases, particularly in the upper range of the regime (Dongari et al., 2011b). The main evidence of rarefaction in the gas presents at the system boundaries, where discontinuities of energy and momentum occur. These discontinuities must be modelled using slip or jump boundary conditions, hence, this regime is often referred to in the literature as the slip flow regime.

In the range of $0.1 < Kn < 1$ gas flows are said to be transitional, whereby increasingly fewer intermolecular collisions take place in a given time period as Kn becomes larger. In regime C, the nonlinear structure of the Knudsen layer can represent a large proportion of the flow. In microflows, which are most commonly internal flows, the extent of the Knudsen layer increases until at approximately $Kn = 1$, the Knudsen layers extending from bounding surfaces would represent the entire flow field. Accordingly, it is imperative that any numerical model intended for use in the transition regime has the ability to model the Knudsen layer structure reliably. As Knudsen number increases beyond $Kn = 1$ into regime D, the gas flow is partially free molecular in nature, and becomes completely so beyond $Kn \sim 10$ (Gad el Hak, 1999). In free molecular flows, the gas molecules act individually and collisions between them are negligible. In this regime simple solutions to many flow configurations exist, as only collisions between gas molecules and bounding surfaces need be considered.

In this thesis the flows analysed are typically in regimes B and C, where gas rarefaction has a significant impact on the behaviour of the flow. In these regimes, the increased importance of individual molecular interactions at system boundaries and the structure of the non-equilibrium Knudsen layer are the dominant effects of rarefaction. They are the most important flow features to capture in numerical analyses (Karniadakis et al., 2005).

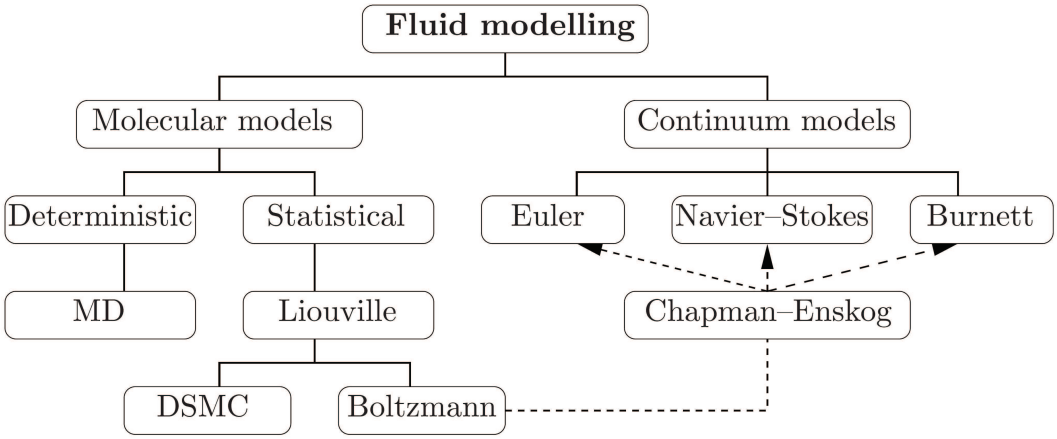

Figure 2.3: Molecular and continuum gas flow models (Gad-el-Hak, 1999).

2.1.1 Methods to describe gas flows

The modelling techniques available for rarefied flows are illustrated in Fig. 2.3, and their interconnections. Fluid flows can either be modelled as they really are, i.e. a collection of molecules, or as a continuum, being indefinitely divisible. Molecular models can either be deterministic, consisting of the technique of molecular dynamics (MD), or statistical, originating from the Liouville equation. The Liouville equation can be used for deriving the Boltzmann equation, being a fundamental description of kinetic theory for gases. The Liouville equation is also a fundamental building block for the conventional continuum methods and for the popular modelling method of direct simulation Monte Carlo (DSMC).

The loss of local thermodynamic equilibrium assumption in rarefied gas flows lead to the breakdown of the classical governing equations of fluid dynamics. As Kn increases beyond 0.001 the N-S-F equations are no longer able to accurately predict the behaviour of gas flows. In order to simulate the macroscopic behaviour of rarefied gases properly it is necessary to consider the influence of their molecular nature. A large number analytical and numerical approaches exist to model rarefied gases, through extensions of the traditional hydrodynamic equations. The following brief review considers the most commonly applied techniques, assessing their suitability for integration into mainstream engineering design tools.

2.2 The Boltzmann equation

The Boltzmann equation is derived from the Liouville equation, which is a fundamental statistical mechanics equation for gases. The Liouville equation is based on the phase-space function which consists of the combination of three coordinates describing location in physical-space and three coordinates describing velocity-space, resulting in a six-dimensional space. From the phase-space function the probability of finding a molecule with a particular position and velocity at any given time can be defined based on the conservation of the $6N$ phase-space distribution function over the N molecules in the system. The Liouville equation does not consider the changes of the phase-space distribution due to molecular collisions as opposed to the Boltzmann equation (Bird, 1994).

Although it would be ideal to achieve the exact dynamics of N particles, this is not possible since in practical calculations this requires a number of variables in the order of 6^N (Cercignani, 2000). This is why Boltzmann and Maxwell derived the Boltzmann equation which is only dependent on the one particle distribution function, obtained by integrating the Liouville equation and using the assumption of the studied gas being dilute and considered to be in a state of molecular chaos (Bird, 1994). With molecular chaos it is assumed that the phase-space of two colliding molecules is the same as the product of the corresponding phase-spaces for both molecules. In contrast to the Liouville equation the Boltzmann equation is dependent on a non-linear collision integral that describes the net effect of populating and depopulating collisions on the distribution function (Gad-el-Hak, 1999).

The Boltzmann equation is the master equation of the kinetic theory of gases, which describes the variation of the molecular velocity distribution function in space and time. It uses classical mechanics to describe the velocity, position, and state of a gas molecule in a flow at any given time. If the Boltzmann equation can be solved for a particular molecular model and boundary conditions, then the velocity distribution function is known everywhere and all thermodynamic and flow properties (pressure, temperature, bulk velocity, shear stress, heat flux, etc.) can be calculated without making any further assumptions about the nature of the flow. Transport

properties such as the viscosity and thermal conductivity appear naturally as part of the solution and it is not required to introduce them via empirical equations. It is based on several simplifications of the molecular behaviour of gases; it is assumed that the molecular diameters remain small in comparison to the molecular separation, that the molecules are in constant random motion, and that they undergo frequent collisions. As mentioned above, it is also assumed that molecular chaos prevails, and that bulk motion may be superimposed on the random molecular motion. Further simplifications, assuming that the gas flow is dilute and composed of a single, monoatomic species, lead to the Boltzmann equation (Sone, 2002):

$$\frac{\partial f}{\partial t} + \mathbf{v}.\frac{\partial f}{\partial r} + \mathbf{F}.\frac{\partial f}{\partial \mathbf{v}} = C(f), \tag{2.3}$$

where $f(\mathbf{r}, \mathbf{v}, t)$ describes the number of gas molecules in a volume of gas that possess velocity $\mathbf{v}$ at the time t. The spatial position of a molecule is given by $\mathbf{r}$, and the flow is acted upon by a body force, $\mathbf{F}$. The first term on the left hand side of the equation describes the transient changes of the molecular distribution, f, while the second term on the left hand side is the convective change in the distribution. The Boltzmann equation describes how the bulk motion of the gas, on the left hand side, relates to the molecular collisions taking place in the gas, given by the collision integral $C(f)$ on the right hand side. The collision integral is highly complex, involving velocity-space coordinates as independent variables, with the result that it is computationally intractable to solve the equation for most flows (Reese et al., 2003).

In order to apply the Boltzmann equation practically, the collision integral can be replaced by a simplified kinetic model of the collision processes in the flow. The kinetic models linearise the Boltzmann equation, replacing the complex function $C(f)$ with expressions that can be solved to determine the distribution function f of macroscopic quantities. One of the most widely used kinetic models is the Bhatnagar-Gross-Krook (BGK) model (Bhatnagar et al., 1954). In this model, the collision integral is replaced with the product of the collision frequency between molecules and the difference between a Maxwellian distribution function and the

actual distribution function sought (Frangi et al., 2007). For analysis of near-wall regions, the collision integral may be replaced with specialised synthetic scattering kernels, such as the Cercignani-Lampis model, which include the effects of interactions between the gas and the wall (Cercignani and Lampis, 1971).

Linearising the Boltzmann equation using kinetic models, it is possible to produce very accurate solutions for some fundamental cases. Unfortunately, simplified kinetic models are rarely appropriate for complex geometry. The assumptions implicit in the linearisation process greatly limit applicability of the results for practical rarefied flows (Cercignani, 2000), such as non-linear pressure distribution cannot be captured. Sharipov (1999) also stated that the Boltzmann equation is particularly recommended for modelling low Mach flows and flows with simple geometrical configurations. In this thesis, we compare various kinetic models with our theoretical and simulation results.

2.3 Conventional continuum models

The continuum models consisting of the Euler, Navier-Stokes-Fourier (N-S-F) and Burnett equations are non-linear partial differential equations describing the conservation of the macroscopic flow parameters mass, momentum and energy in every small sub-volume of a flow. These equations can be obtained through a Chapman-Enskog expansion of the Boltzmann equation using Kn as a smallness parameter. This expansion yields a zeroth-, first-, and second-order of accuracy with respect to Kn for the Euler, N-S-F and Burnett equations respectively. Alternatively the Euler and N-S-F equations can be derived directly, although for the N-S-F equations some empiricism is necessary to close the resulting indeterminate set of equations (Gad-el-Hak, 1999). The Euler equation is a form of the N-S-F momentum equation, which is obtained in case the viscous forces terms are excluded. The Euler equations do not have viscous stress terms and comprises therefore a simple and appropriate solution method for equilibrium flows at $Kn \sim 0$, as noted by Xue et al. (2001). When solving non-equilibrium flows viscous stresses are common which makes the Euler equations inappropriate for these flows. Another approach has

been the employment of Burnett equations (Burnett, 1935; Reese, 1993), which are higher order accurate than the N-S-F equations. However, the Burnett equations are found to be somewhat unstable in response to small wavelength disturbances. Also, the higher order terms require higher-order boundary conditions, which are not necessarily known a priori. This is particularly problematic at solid boundaries, where the physical interactions between gas molecules and wall molecules are not well understood.

Given the difficulties inherent in physically modelling non-equilibrium gas flows, the primary advantage of an extended N-S-F model would be that it would remain relatively computationally less intensive compared to alternatives such as kinetic theory and particle methods. Also, modifying the N-S-F equations, which are already in widespread use, is likely to make for a more practical analysis tool than other higher order equations such as Burnett (1935). If we consider solving the Boltzmann equation directly as a bottom-up approach to the problem, in that it directly incorporates all aspects of the physical behaviour of the gas, then using extended N-S-F equations constitutes a top-down approach.

2.3.1 Navier-Stokes-Fourier equations

The N-S-F equation set in 3D comprises five conservation equations; one equation for mass, three for momentum and one for energy. The equations are linked by linear constitutive relationships for shear stress and heat flux. Using a Cartesian coordinate system where spatial coordinates x, y, z have velocity components U, V, W, respectively, and $\mathbf{U}$ is a velocity vector, the N-S-F equations are given in unsteady 3D form as follows:

$$\frac{\partial \rho}{\partial t} + \nabla.(\rho \mathbf{U}) = 0, \tag{2.4}$$

$$\frac{\partial (\rho \mathbf{U})}{\partial t} + \nabla.U(\rho \mathbf{U}) = -\nabla P + \nabla.\tau + S_M, \tag{2.5}$$

where τ is the stress tensor and S_M represents momentum sources. The energy

equation is

$$\frac{\partial(\rho h_0)}{\partial t} + \nabla.(\rho h_0 \mathbf{U}) = -\nabla.(\kappa \nabla T) + \frac{\partial P}{\partial t} + \Phi + S_h, \tag{2.6}$$

where h_0 is enthalpy, S_h represents source/sink terms, κ is the thermal conductivity and Φ is the dissipation function given by

$$\begin{aligned}\Phi =& 2\mu \left[\left(\frac{dU}{dx}\right)^2 + \left(\frac{dV}{dy}\right)^2 + \left(\frac{dW}{dz}\right)^2 \right] + \mu \left(\frac{dU}{dy} + \frac{dV}{dx}\right)^2 \\ & \mu \left(\frac{dU}{dz} + \frac{dW}{dx}\right)^2 + \mu \left(\frac{dV}{dz} + \frac{dW}{dy}\right)^2 - \frac{2}{3}\mu \left(\nabla \mathbf{U}\right)^2 .\end{aligned} \tag{2.7}$$

These equations are widely used at the macroscale for computation of a range of fluid flow and heat transfer problems. At the microscale, where Kn increases and the molecular nature of gas flows becomes important, the N-S-F equations alone do not predict the effects of gas rarefaction (Gad-el-hak, 1999). In the slip- and transitional-Kn regimes, the most apparent effects of gas rarefaction are velocity slip/temperature jump and the Knudsen layer. Using slip and jump boundary conditions, it is possible to extend the applicability of the N-S-F equations into the slip flow regime: $0.001 < Kn < 0.1$ (Maxwell, 1879; Smoluchowski, 1898). This is the most commonly applied numerical technique for weakly rarefied flows.

2.3.2 Discontinuous boundary conditions

Boundary discontinuities arise when the energy and momentum of a gas flow in contact with a surface are not fully transferred to the surface. When full accommodation takes place, it leads to the no-slip condition of macroscale flow, where the velocity and temperature of the gas at a solid boundary are equivalent to the velocity and temperature of the boundary. In rarefied flows, a smaller number of intermolecular collisions take place within a given timescale. If the timescale of convective transport in the system is much shorter than the diffusive relaxation time, in which gas molecules would reach an equilibrium with the wall, then on average

molecules will flow through the system without their energy and momentum ever relaxing to that of the system boundaries.

It has commonly been proposed that the no-slip boundary condition may cease to remain applicable when the Kn becomes greater than of the order of 10^{-3}, although bulk continuum considerations still appear to hold appropriate within that limit. Experimental investigations (Pfahler et al., 1991; Arkilic et al., 1994, 1997; Harley et al., 1995; Maurer et al., 2003; Ewart et al., 2007) have confirmed that the conventional forms of the N-S-F equations together with the no-slip boundary condition may under-predict the experimentally observed mass flow rates, and the concerned discrepancies tend to become more severe for higher values of the Kn (Maurer et al., 2003; Ewart et al., 2007).

Several authors have theoretically addressed the phenomenon of enhanced mass flow rates as a consequence of this deviation, by employing the continuum equations in conjunction with the application of the Maxwell slip boundary condition (Maxwell, 1879). Maxwell (1879) originally introduced a first-order slip model, which assumes that the slip velocity is equal to the velocity at a mean free path away from the wall. The extent of slip was modeled to be proportional to the local mean free path, for partially specular and partially diffuse walls. When appropriately normalized, the Maxwell slip velocity condition shows that the slip velocity is proportional to the local Knudsen number.

The description derived by Maxwell considers molecular reflections from solid surfaces, which are either specular reflections, diffusive reflections or a mixture of the two (Fig. 2.4). If the reflections of the molecules are diffusive the molecules are adsorbed by the surface (due to surface roughness of the wall, or due to a condensationevaporation process) (Kandlikar et al., 2005) and their tangential momentum is, on average, lost relative to the wall as they are re-emitted. For specular reflections, however, the molecular tangential momentum is retained and the momentum in the normal direction is mirrored in the normal direction of the wall. These different types of wall reflections are modelled using the tangential momentum accommodation coefficient (TMAC), σ, which is set to $\sigma = 1$ for purely diffusive reflections and $\sigma = 0$ for purely specular reflections.

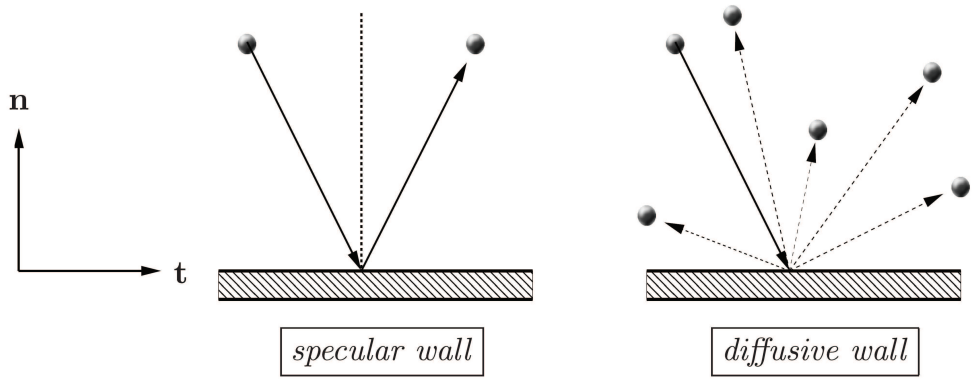

Figure 2.4: Left, specular reflections experienced by the fraction $(1-\sigma)$ of all the molecules. Right, one incoming molecule has many alternative trajectories due to diffusive reflections with the wall, which is experienced by the fraction σ of all reflected molecules. The axes indicate the wall normal direction, n, and the wall tangential direction, t.

The contribution of the stream-wise temperature gradients associated with the thermal creep phenomenon was subsequently added to the Maxwell-slip conditions, with a consideration that the slip velocity is simultaneously caused by the velocity gradient normal to the wall and a temperature gradient tangential to the wall. Identical considerations were also invoked by Smoluchowski (1898) for modeling the temperature jump boundary conditions at the walls (Karniadakis et al., 2005).

As reported by Steckelmacher (1986), it was recognised by Knudsen that the mode of scattering of gas molecules from surfaces was fundamental to his analysis. Knudsen postulated and found empirically that, under free molecular conditions, diffuse reflections was the most reasonable model to describe the gas-surface interactions. For engineering purposes, therefore, σ is usually set to unity. In an experimental investigation by Arkilic et al. (2001) it was found that argon, carbon dioxide and nitrogen all have σ values around 0.8 under standard temperature and pressure conditions in a silicon channel, which corresponds well to the expected MEMS conditions. It is found by Ewert et al. (2007), from experimental studies of pressurised gas flows for Kn ranging from 0.03 to 0.3, that $\sigma = 0.84$.

Results of σ are obtained using molecular dynamics by Sun and Li (2009) for planar wall configurations at $Kn = 0.12$, showing that σ decreases from about 0.6 to 0.35 with temperatures rising from 100K to 350K. These results vary significantly from the normally used values of σ, but Sun and Li also show results where an

approximate wall roughness increasing from about 0.5nm to about 1.4nm (relevant to micro and nano devices) yields σ values starting at about 0.80 and increasing to about 0.84. The thermal accommodation coefficient was also measured by Sun and Li: σ has a value of about 0.35 for gases at 300K, when confined by walls with an approximate roughness of 0.7nm. This value is found by other investigators to be between 0.31 and 0.97 for various gases and surfaces, as listed by Karniadakis et al. (2005).

As an alternative to Maxwells model, it has been suggested that Langmuirs theory of the adsorption of gases could be used (Langmuir, 1933). Adsorption is a process where gas molecules become temporarily attached to a solid bounding surface upon collision with it, and are released again into the bulk flow after some finite time lag. The Langmuir model is based on surface chemistry, but may be shown to make equivalent predictions of slip to Maxwells model in some key cases (Myong et al., 2005). Although the Langmuir model is obviously more complex than Maxwells model, its key advantage is that it is possible to determine the slip velocity from knowledge of the chemical interactions between particular gases and surfaces. The properties of surface interactions are both more physical and less open to interpretation than the accommodation coefficient used in Maxwells model.

Another alternative to Maxwells slip model is Sharipovs model, in which the Cercignani-Lampis scattering kernel is used to describe molecular interactions at the wall, rather than Maxwells specular/diffuse scattering model (Cercignani and Lampis, 1971; Sharipov, 2003). The Cercignani-Lampis model for the behaviour of molecules receding from the wall is chosen as it contains not one but two accommodation coefficients in the slip velocity: a tangential momentum accommodation coefficient (TMAC), and a thermal accommodation coefficient (TAC). There is also a separate energy accommodation coefficient used in the expression for temperature jump. This type of model gives a more accurate representation of both the physical interactions near the wall, and the interdependence between velocity slip and thermal transpiration effects (creep). Sharipov (2003) uses a more realistic description of the collision physics in the near wall region to inform general slip/jump equations and then, using kinetic theory to determine unknown constants, develops accurate

expressions for velocity slip and temperature jump.

Ultimately, while both Langmuir and Sharipovs models and several other alternatives (Cercignani, 1990; Yuhong et al., 2002; Schaaf and Chambre, 1961) are more accurate than Maxwell and Smoluchowskis expressions, in application they must be considered less robust. These alternative models are relatively complex and require available kinetic theory data, which, for practical flows and most engineering design applications renders them largely unsuitable. Also, it is difficult to justify the complexity of implementing models that are dependent on individual gas-surface interaction properties, but derived only for simple flow configurations (typically planar surfaces, and often isothermal cases). Large accuracy losses can occur when converting kinetic-theory dependent models to 3D, non-isothermal, compressible and transitional-Kn flows, which can negate the benefits of using kinetic-theory based slip models altogether in practical flows. As yet, no alternative to Maxwell or Smoluchowskis models has been widely accepted as suitable, particularly for application to complex flows.

Hence, following the conceptual paradigm of Maxwell slip, Arkilic et al. (1997) employed a perturbation analysis of the full compressible two-dimensional N-S-F equations in Cartesian coordinates, involving a first-order velocity slip boundary condition for flow between parallel plates. They also obtained analytical expressions for the velocity components and the mass flow rate, which were further verified with their experimental measurements. However, these solutions were constrained to be applicable for infinitesimally small values of the Mach number and Reynolds number, with the Knudsen number being of the order of unity.

Although early efforts in mathematical modeling of microscale gas flows were made following the classifications of the flow behavior according to the distinctive Knudsen number regimes, it needs to be appreciated at this point that precise demarcating boundaries between the continuum flow, slip flow, transitional flow and free molecular regimes have been found to be rather difficult to prescribe. It has been found that first-order slip/jump boundary conditions are not sufficient to model mass-flow rates in pressure-driven flows beyond about $Kn \sim 1$. They fail to predict the mass flow minimum phenomenon (see Chapter 5). To avoid the concerned

anomalies, researchers subsequently postulated unified high-order slip-based models that are designed to be applicable for a wide range of Knudsen numbers, within the framework of the classical N-S-F equations. In order to achieve better correspondence to mass-flow rates, a second-order velocity-slip boundary condition has been derived through an expansion series of the first-order velocity-slip, using λ as a smallness parameter. With this method better agreements can be acquired for mass-flow rates, at about $Kn = 1$, recovering the mass flow minimum (as is shown in Section 5.1).

Weng et al. (1999), for example, used a higher order slip model for flow in micro-capillaries, in conjunction with the N-S-F equation. They further claimed the applicability of their model for the entire range of Knudsen numbers, provided that the bulk velocity is negligible in comparison with the sonic velocity of the medium. However, the presence of several unknown coefficients appears to be a major drawback of their proposed slip model. Beskok and Karniadakis (1999) subsequently proposed a unified quasi-continuum model for providing results for transition ($0.1 < Kn < 10$) and free-molecular ($Kn > 10$) flow regimes. However, several parameters in their slip model need to be determined by tuning with experimental observations or molecular simulation data. Dongari et al. (2007) employed a generalized form of the second-order slip model earlier proposed by Sreekanth (1969) and accordingly solved the integral form of the Navier-Stokes equations by retaining the inertial terms. Their solution for long micro-channels yielded satisfactory results up to a Knudsen number value of 5, through the employment of tunable slip-flow parameters as tagged with the boundary conditions.

2.3.3 Scaling of constitutive relations

One important inference from the reported studies on microscale gas flows through classical slip model considerations, mentioned as above, is the fact that in an effort to stretch the applicability of these models over a large range of Knudsen numbers. These models have typically been closed with several heuristically-adjustable fitting parameters. Such empiricism has been primarily attributable to an apparent

abstraction from the seemingly non-trivial dependences of the fluid flow characteristics on the pertinent molecular level interaction mechanisms with characteristic sharp gradients adjacent to the confining boundaries. On system length scales, these details have often been abstracted with the notion of pre-defined sets of adjustable parameters in the slip/ jump based velocity/ temperature boundary conditions, with an intention of mimicking the underlying molecular level interactions in an up-scaled continuum limit. Such ad-hoc considerations, however, may not be physically complete in nature, since the fluid dynamic interactions occurring over disparate physical scales are intensely coupled with a number of significant thermodynamic criticalities and constraints in a rather complicated and dynamically-evolving manner, many of which might appear to be somewhat intuitive in nature but are by no means obvious.

If we consider the molecular behaviour of a gas flow near a solid bounding surface, it is dominated by the effect of gas molecule-surface interactions. This leads to the formation of a Knudsen layer (KL): a local thermodynamically non-equilibrium region extending $\sim O(\lambda)$ from the surface. Microscopic interactions in the Knudsen layer do not generate equilibrium distributions of the macroscopic variables. To illustrate, a schematic of the Knudsen layer structure is given in Fig. 2.5. The figure shows Knudsen layer velocity profiles for an isothermal, pressure-driven gas flow, moving parallel to a planar wall. The velocity of the wall is denoted by u_{wall}, and the actual speed of the gas at the wall by u_{slip}. The solid line indicates the true velocity of the gas, which is commonly referred to as the microslip, as would be found in experimental results or predicted in accurate molecular dynamics simulations. Although the Navier-Stokes-Fourier (N-S-F) equations with velocity-slip and temperature-jump boundary conditions (Maxwell, 1879) can often adequately predict the flow field outside the KL, they fail to capture the non-equilibrium flow behavior of the KL (Lockerby et al., 2004).

In the KL, gas molecule-surface collisions are more frequent than gas molecule-molecule collisions, i.e. the gas MFP will effectively be reduced in the KL. It is well-known from the kinetic theory of gases that viscosity and thermal conductivity can be interpreted in terms of the collisions of gas molecules, and of the free paths of the molecules between collisions. Linear constitutive relations for shear stress and

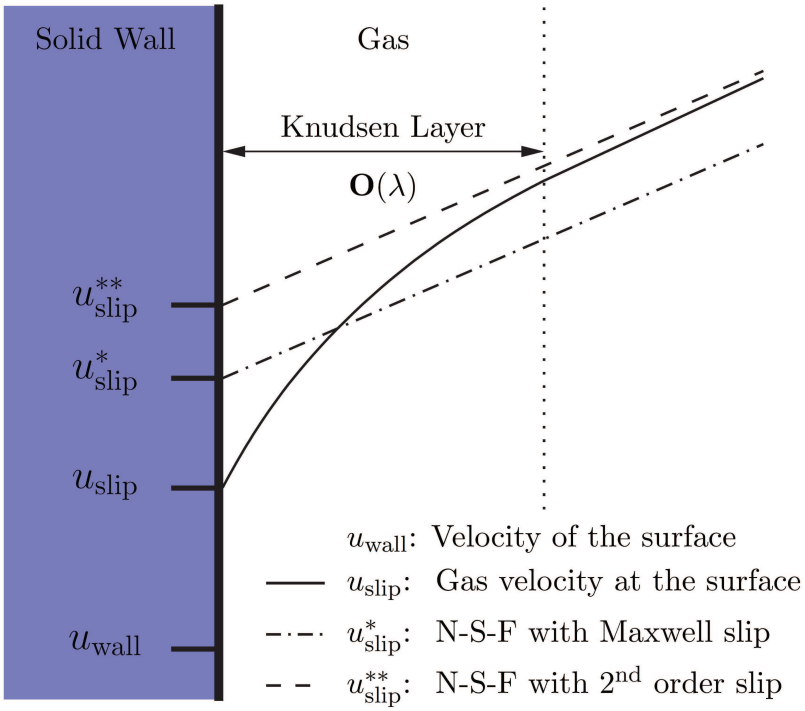

Figure 2.5: Schematic of the velocity structure of the Knudsen layer near a wall in a pressure-driven flow, comparing different types of slip boundary condition.

heat flux, with constant thermophysical transport coefficients such as viscosity and thermal conductivity, are no longer valid necessarily in the KL. As gas flows reach transitional-Kn values, moving from regime B to C as outlined in section 2.1, the structure of the Knudsen layer becomes more important. For example, in cases of pressure-driven gas flow in a microchannel with the relatively modest rarefaction of Kn = 0.05, velocity slip may be shown to increase the observed mass flowrate by 15%. The nonlinear structure of the Knudsen layer accounts for 30% of this difference between the true microscopic velocity profile and that predicted by the N-S-F equations (Lockerby et al., 2005b).

Hence, at transitional-Kn and in the upper slip flow regime, the effects of the non-equilibrium Knudsen layer must be incorporated into numerical simulations to obtain accurate results for the macroscopic properties of the flow. Constitutive scaling, where the relationship between viscous stress and strain-rate (and/or heat flux and temperature gradient) in the near wall region is modified to represent Knudsen layer behaviour, is one numerically economical approach to incorporating the Knudsen layer in continuum analyses.

Lockerby et al. (2005a) and O'Hare et al. (2008) developed wall-distance scaling models for the constitutive relationship for shear stress in planar flows. They used linearized kinetic theory results to determine phenomenological functions with which to scale the thermophysical properties to obtain nonlinear stress-strain relationships in the KL. The applicability of these models is limited to relatively low-Kn isothermal flows. Using previous work on Maxwells boundary conditions, Lockerby et al. (2005a) then extended the method to include curved surface geometries, analysing viscous drag over an unconfined microsphere. The method has also been applied to a quiescent thermal flow in planar half-space geometry, giving a successful prediction of the temperature profile normal to the wall (O'Hare et al., 2008).

In an attempt to improve the accuracy and generality of the constitutive scaling method, Reese et al. (2007) and Zheng et al. (2006) proposed new scaling functions for Knudsen layers of both momentum and energy. Kinetic theory data from a wide literature survey were used to determine separate scaling functions for effective dynamic viscosity, μ, and effective thermal conductivity, κ. Crucially, the use of different scaling for viscosity and thermal conductivity in these models implies a non-constant effective Prandtl number (which relates energy and momentum diffusivities) when they are used together (O'Hare et al., 2008). It is possible that this therefore highlights some physical inconsistency in the models, which needs further investigation if they are to be considered as a means of extending the applicability of constitutive scaling to more complex flows.

Several other scaling functions for rarefied gas flows have been proposed recently: Kn-dependent functions (Cercignani et al., 2007), and power-law scaling of constitutive relations (Lilley and Sader, 2007; Lockerby and Reese, 2008). Both of these latter predict an infinite shear-rate at the wall, and therefore a zero effective viscosity, which makes numerical results dependent on grid spatial resolution. Guo et al. (2007) implemented the effective MFP expression derived by Stops (1970) in conjunction with a second-order slip boundary condition and obtained good results for isothermal and non-isothermal pressure-driven rarefied gas flows when compared to conventional higher-order slip and jump models.

Stops (1970) appears to have been the first researcher to propose transport parameters that are dependent on an effective MFP, $\lambda_{\text{eff(ST)}}$, which is geometry-dependent. Stops investigated the classical probability distribution function, $\psi(r) = \lambda^{-1} \exp\ (-r/\lambda)$ (Kennard, 1938), for which the probability that a given gas molecule will travel a distance in the range r to $r + dr$ between two successive collisions is $\psi(r)dr$. If the gas is not bounded, the MFP of the gas molecule ensemble is simply $\int_0^\infty Nr\psi(r)dr/N = \lambda$, where N is the total number of molecules. If a solid bounding surface is included in the system, however, some molecules will hit the surface and their free flight paths will be terminated. The MFP of all the gas molecules in the system will therefore be smaller than λ, due to this boundary limiting effect. Recently, Arlemark et al. (2010) developed a probability function-based effective MFP expression, also using the classical exponential form of the distribution function. However, comparison of both of these effective MFP profiles with molecular dynamics (MD) simulation data (Dongari et al., 2011a) shows that both models are accurate only up to Knudsen numbers of about 0.2.

In summary, the constitutive-relation scaling approach is a simple but effective method for incorporating Knudsen layer simulation into N-S-F models. The approach was proposed originally by Lockerby et al. (2004), who have worked with their group and collaborators to further it (Reese et al., 2007; Lockerby et al., 2005b; Zheng et al., 2006, Arlemark et al., 2010). Other research groups have also attempted to move the approach forward and have proposed similar strategies (Fitchman and Hesroni, 2005; Lilley and Sader, 2007; Cercignani et al., 2007). To date, however, none of these models are implemented in mainstream CFD codes and most are for incompressible and/or isothermal flows in planar geometry. This thesis exploits the potential of the constitutive scaling method by developing it for application to compressible flows within a flexible CFD framework, to produce a design-focused tool for analysing fluid flow and heat transfer in gas microsystems of both planar and non-planar geometries. Momentum Knudsen layers, which are fundamental to almost all physical cases, are the primary focus of this research, although thermal Knudsen layers are included in later models where gas heat transfer is considered.

2.4 The direct simulation Monte Carlo (DSMC) method

Alternatively, for modelling rarefied gas flows, one may resort to molecular simulation techniques for resolving the pertinent physical features up to the molecular scales, such as the direct simulation Monte Carlo (DSMC) approach. The method was originally proposed by Bird, and is a particle-based approach to simulating the Boltzmann equation, rather than solving it directly (Bird, 1994). DSMC does not operate on individual molecules, but on a large number of computational particles, each of which is assumed to be representative of a much larger number of individual molecules. At each time step the particles are moved around the system, and can undergo binary collisions that will alter their velocity and internal energy, but not their physical position. In consequent time steps, particles have their physical positions adjusted around the system in a deterministic manner, i.e. according to their previous collision and the laws of classical mechanics. The simulation continues until ensemble averages of the individual observed states give a statistical simulation of the physical behaviour of the gas flow to sufficient accuracy.

Macroscopic properties of the gas are inferred from the averages of the particle behaviour. Although it can be shown that DSMC provides results that are directly equivalent to solving the Boltzmann equation, its computational intensity restricts its applicability for use as an engineering design tool (Reese et al., 2003; Wagner, 1992). There are two key factors that make DSMC a particularly computationally expensive process. Firstly, DSMC particles are tracked within a computational mesh, which is used to identify upcoming collisions at each time step and to produce the information used in the statistical averaging processes. In order to ensure that only physical results (i.e. system states) are produced, both the time step and the mesh-cell size must remain smaller than the mean collision time and mean free path, respectively (Bird, 1994). Thus, the memory requirements of DSMC processes can be extremely demanding, given the large number of time steps required for accurate ensemble-averaging of non-equilibrium systems.

The second factor that limits the use of DSMC as a design tool, particularly for gas-based microsystems, is susceptibility to statistical noise. In the low-speed cases commonly found in microscale flows, a much larger number of sample system states is required to produce accurate averages of the macroscopic quantities. The computational time necessary to obtain low-scatter results for low speed rarefied gas flows then becomes prohibitive even on massively parallel computing facilities (Reese et al., 2003). In recent work, Baker and Hadjiconstantinou have proposed a means of significantly reducing the computational effort involved in DSMC for microsystems by considering the relatively small departures from equilibrium observed in some low-speed flows (Baker and Hadjiconstantinou, 2005). Although this modified method may yet become the de facto standard for low-speed DSMC, it does not currently offer sufficient improvements in computational requirements for complex cases to provide the particle-based approach with an advantage over continuum models for microsystem design applications.

In spite of above limitations, DSMC is still predominantly used in academic research for the study of aerodynamics and hypersonics, but it is now also accepted as an analytical tool for other non-equilibrium flows. The method produces reliable data in many cases where equivalent experimental results are not available, and can also be applied to complex flows in realistic configurations, given sufficient time and computing resources are available (Moss et al., 1995; Moss et al., 2006). These features of DSMC are particularly attractive for analysis of gas microflows, where complex geometry is common, and where practical constraints often preclude detailed experimental work. In practice, however, the computational effort involved in most DSMC makes it prohibitively expensive, in terms of both time and required computational facilities, for consideration as an industrially applicable design tool.

In this thesis, the DSMC method is used to validate the modified N-S-F equations in Chapter 5 for few test cases, where experimental data is not available.

2.5 Molecular dynamics

Unlike DSMC, in molecular dynamics (MD) every single molecules position and velocity is modelled and is initialised from the start of a simulation. The molecular movements are determined by using Newtons law relating the present intermolecular forces to the molecular masses and accelerations. MD is therefore a deterministic model having only one possible simulation outcome (Rapaport, 2004). To obtain macroscopic flow quantities such as density, velocity, pressure and temperature from molecular dynamics an averaging over the molecular parameters is required. This vast amount of averaging can be understood considering that all changes in a flow spread out in the gas domain through molecular collisions, which for a neon gas molecule in a gas at the standard temperature and pressure occurs on average about of time scale $\sim 10^{-10}$s (as is shown in Section 4.2). So, if a certain resolution of a desired macroscopic parameter is to be evaluated an averaging is needed that covers a sufficient number of molecules sampled over a sufficient amount of time.

An example of the vast amount of sampling can be made by analysing the molecular dynamics method when used to sample the mean free path in Chapter 4. Here the mean free path is recorded for three different noble gases, for various cases, using between 50000 and 100000 molecules. The sampling of the molecular mean free paths is typically made over a time range of about 3ns. Since every molecule has its collision-free travelling distance recorded every time step of about 2×10^{-15}s this adds up to about 100 billion samples for the case of about 60000 molecules. If the sampling time is short compared to the averaged collision frequency time the result will be dominated by highly fluctuating values. If however the averaging is done over a time-scale which is too long compared to the time it takes for molecules to travel the average distance of the mean-free-path then the time-transient changes of the flow will be missed: Kandlikar et al. (2005). To give an idea of the appropriate sampling domain size it is reported by Karniadakis et al. (2005) that a sampling volume of 10000 molecules results in 1% statistical fluctuations of the macroscopic quantities, but this depends on whether there are transient changes in the gas domain. If the flow is at a steady state it is possible to sample fewer molecules but

over a longer time period.

Molecular dynamics is commonly used to simulate liquids at the nano-scale. This is due to the amount of simulated molecules being few enough at this scale, taking into consideration that the typical simulation time is proportional to the square of the number of simulated molecules. Molecular dynamics is also appropriate for simulating liquids since liquids require a correct description of a continuous intermolecular interaction potential as opposed to gas flows which mostly experience collision-less travelling paths. However, in this thesis the method of molecular dynamics is used to simulate gas flows since a deterministic validation method is desired. This method is also used because it is difficult to use discontinuous potential forces, such as the fixed diameter hard-sphere model, in direct numerical simulations where molecules are moved in discrete time-steps. This would yield infinite forces of repulsion when collisions occur at which point the molecular-diameters to cross over each other. The method of molecular dynamics is therefore of great value to this research and is used in Chapter 4 to validate the theoretical effective mean free path expression derived earlier in Chapter 3.

2.6 Summary

In summary, it is clear that modelling non-equilibrium flows is both particularly challenging and traditionally computationally intensive. In order to effectively design microsystems in the short-to-medium term, one promising approach is to identify the key features of gas rarefaction, and incorporate them into simpler numerical models. In order to do so, it is necessary to understand the physics that characterise the effects of rarefaction in the transition regime, primarily interface discontinuities and the Knudsen layer, and to discuss how such flow features are traditionally accommodated in analytical and numerical models.

Chapter 3

Mean free path scaling

"Begin at the beginning,", the King said, very gravely,
"and go on till you come to the end: then stop"
- Lewis Carroll

The path of the centre of mass of a molecule in a gas will be an irregular zigzag having at each corner a collision with another molecule and consisting of straight free paths between these. The individual free path-lengths of gas molecules between intermolecular collisions in a dilute gas vary widely. However, if we follow a molecule until it has traversed a great many "free paths", the average of these path-lengths will have a definite value, which is called the mean free path (MFP) and denoted by λ. The term free path is can hold for certain class of molecules, which are entirely free from mutual interaction, except when they are very close together. We shall call these $small - field$ molecules. In a gas composed of small-field molecules, the mean free path varies only with the density and is inversely proportional to the pressure at constant temperature (Kennard, 1938).

The mean free path concept is central to most models of the transport phenomena in gases. Although the term "free paths" lacks a precise quantitative theoretical assessment, it has qualitative connotations that are useful for predicting the way in which the associated transport coefficient of a fluid will depend upon certain properties and thermodynamic parameters. For example, classical kinetic theory gives the thermal conductivity of a gas in the form

$$\kappa = \frac{1}{3}\rho\bar{c}\lambda C_v, \tag{3.1}$$

where ρ is the density, $\bar{c}$ is the mean speed of the molecules and C_v is the specific heat. When the mean free path λ becomes comparable with a linear dimension L of a finite system, the boundaries may limit the effective free path values, according to the nature of the boundary collisions in respect of the transport considered. This was suggested long ago by Thomson (1901) for electrons in metals, and later extensively investigated by many researchers for confined gas flows (Stops, 1970; Sone, 2002).

Due to the boundary limiting effects, gas molecule-surface collisions will also occur along with gas molecule-molecule collisions. Hence, the gas MFP will effectively be reduced in the near-wall regions, leading to a non-linear variation of MFP with the wall normal distance. This leads to the formation of a Knudsen layer (KL): a local thermodynamically non-equilibrium region extending $\sim O(\lambda)$ from the surface (Sone, 2002). The state of non-equilibrium caused by a wall should be spatially extended in proportion to the probability of a collision-less trace of molecule traveling a certain distance from a wall. Therefore, by investigating the variation of the effective MFP profile a more accurate indication of the KL extent can be obtained.

Although the Navier-Stokes-Fourier (N-S-F) equations with the classical velocity-slip and temperature-jump boundary conditions can often adequately predict the flow field outside the KL, they fail to capture the non-equilibrium flow behavior of the KL. It is well-known from the kinetic theory of gases that viscosity and thermal conductivity can be interpreted in terms of the collisions of gas molecules, and of the free paths of the molecules between collisions, see Eq. (3.1). Linear constitutive relations for shear stress and heat flux, with constant thermophysical transport coefficients are no longer valid necessarily in the KL (Burnett, 1935; Grad, 1949; Chapman and Cowling, 1970).

Stops (1970) investigated the classical probability distribution function, $\psi(r) = \lambda^{-1} \exp\ (-r/\lambda)$, for which the probability that a given gas molecule will travel a distance in the range r to $r + dr$ between two successive collisions is $\psi(r)dr$. Recently, Arlemark et al. (2010) developed a probability function-based effective MFP expres-

sion, also using the classical exponential form of the distribution function. However, comparison of both of these effective MFP profiles with molecular dynamics (MD) simulation data (Dongari et al., 2011a) shows that both models are accurate only up to Knudsen numbers of about 0.2.

This chapter investigates the hypothesis that the anomalous transport behaviour of non-equilibrium gases is better understood by using power-law (PL) type of distribution functions for gas free paths. An effective MFP based on a PL probability distribution of free paths in a gas close to both planar and non-planar confinements are derived. In Chapter 4 the theoretical models for the PL based effective MFP are compared to simulation results using numerical experiments based on molecular dynamics (MD).

3.1 Distribution of molecular free paths

3.1.1 Equilibrium mean free path

In a time t that is long compared to the time of molecular collisions we can write the gas mean free path:

$$\lambda = \frac{\overline{v}}{\dot{\theta}_v}, \tag{3.2}$$

where $\dot{\theta}_v$ denotes the collision rate for a molecule of a group moving at speed $\overline{v}$ among molecules composing the gas. The collision rate is the chance per second that a particular molecule collides; it might also appropriately be called the collision probability per unit time.

To investigate the distribution of the lengths of the individual molecular paths, let us consider a group of similar molecules that are moving with velocity $\overline{v}$ through a region in which there is gas. The number originally in the group at time $t = 0$ is N_0, and by time t let N of them still be travelling without having had a collision. During the following interval dt, $N\dot{\theta}_v dt$ molecules will collide and drop out of the collision-less molecules group; N is thereby changed by the amount:

$$dN = -N\dot{\theta}_v dt. \tag{3.3}$$

We can easily integrate this equation under thermodynamic equilibrium conditions. By *thermodynamic equilibrium* we mean that the probability of a certain microscopic state averaged over the details of the interactions, does not change in time or space (Cercignani, 1990). So, with $\dot{\theta}_v$ constant, $dN/N = -\dot{\theta}_v dt$, thus $\ln N = -\dot{\theta}_v t + const.$ Choosing the constant of integration so as to make $N = N_0$ at $t = 0$, we find

$$N = N_0 \exp\ (-\dot{\theta}_v t) = N_0 \exp\ (-\frac{\dot{\theta}_v |r|}{\overline{v}}), \tag{3.4}$$

where $|r|$ is the length $\overline{v}t$ of free path that has been travelled at time t by each molecule. Let $\varphi(r)$ be the fraction of the original N_0 molecules that have travelled a distance r without collision, and $\psi(r)dr$ be the fraction of all the free paths that have a length between r and $r+dr$. Then $\varphi(r) = N/N_0$ and $\psi(r)dr = dN/N_0$, hence from Eq. (3.2)

$$\psi(r) = \frac{1}{\lambda} \exp\ (-\frac{|r|}{\lambda}), \tag{3.5}$$

so $\psi(r)$, the probability distribution of free paths, is only exponential in form under thermodynamic equilibrium conditions and when the gas is unbounded (Kennard, 1938). If the MFP, calculated for a molecule in an extensive material, is comparable with a linear dimension of the finite system confining the gas, the boundaries of the system may limit the effective free-path values. Stops (1970) and Arlemark et al. (2010) used the exponential form of the distribution function, Eq. (3.5), to derive effective MFP models as a function of distance from a bounding surface.

However, as mentioned earlier, the exponential form of the distribution is only valid if our system of molecules is in thermodynamic equilibrium. It has been traditionally well recognized that the attainment of local thermodynamic equilibrium necessitates theoretically infinite numbers of collisions involving the gas molecules. When gas molecules collide with a solid boundary, those are temporarily adsorbed on the wall and are subsequently ejected. This allows a partial transfer of momentum and energy of the walls to the gas molecules. If the frequency of collisions is very large, the momentum and energy exchange is virtually complete and the thermal equilibrium or exponential form of probability distribution may prevail for all

practical considerations. In a rarefied gas system, in which gas molecules may not experience sufficiently frequent collisions with other gas molecules to attain equilibrium conditions, deviations from thermodynamic equilibrium may have substantial effects.

Numerical experiments (Dongari et al., 2011a) illuminate the limitations of the conventional exponential form of probability distribution function for gases in the transition regime ($Kn > 0.1$). Stops (1970) also pointed out that the exponential form of distribution function only provides an accurate description of a gas under thermodynamic equilibrium. In the coarse-graining paradigm introduced by Einstein (1956), for times much larger than a characteristic time t_c that, in turn, is much larger than times characterising molecular collisions, the probability distribution of the free paths of ideal gas molecules takes an exponential form (Kennard, 1938). Exponential probability distribution functions are therefore fundamental models in many transport processes, however they miss some features of transport in non-equilibrium systems. This is evident in, e.g., the transport of tracer particles released in pressure-gradient-driven turbulence (del-Castillo et al., 2005), transient photoconductivity experiments (Scharfe, 1970) and the dynamics of electrons due to Langmuir waves (Benisti and Escande, 1998). This has triggered a series of studies in which the Brownian paradigm was abandoned, and anomalous diffusive transport was described using Lévy and power-law (PL) probability distributions (Shlesinger et al., 1999).

Although it is certainly difficult to evaluate the probability distribution function $\psi(r)$, introducing non-equilibrium into Eqs. (3.3) and (3.4) by means of physical arguments could allow us to propose a distribution function that may be more appropriate for non-equilibrium conditions than the exponential one (Cercignani, 1990).

3.1.2 A model for non-equilibrium mean free path

Montroll and Scher (1973) pointed out that a finite moment of the probability distribution function implies an exponential character of the randomness. The central

limit theorem means that the long-term transport behavior is determined by the average value of the model parameters. So results obtained using exponential forms of the distribution functions are essentially the same as those for homogeneous media at equilibrium. A distribution function with diverging higher-order moments, such as the standard deviation, is essential to anomalous transport. In transient photoconductivity experiments, and the adsorption of ions in semiconductors, concentration distributions may have a long tail such that the standard deviation is diverging (Scharfe, 1970). The experimental data show a long tail in the probability density distribution profile, while classical models generally only yield an exponential distribution. This long-tail problem is common to various flows in non-uniform media, in many fields such as chemical engineering and environmental sciences (Grolimund et al., 1995).

Montroll and Scher (1973) and Schlesinger (1974) theoretically showed that anomalous transport is characteristic of a distribution function with diverging higher-order moments, in particular a power-law (PL) form of the distribution functions, e.g.

$$\psi(t) = t^{-n}, \tag{3.6}$$

$$\psi(t) = \frac{1}{\sqrt{\pi\vartheta t}} - \frac{1}{\vartheta}\exp\ (\frac{t}{\vartheta})(\sqrt{\vartheta t}). \tag{3.7}$$

The second moment (i.e. standard deviation), $\int t^2\psi(t)dt$, of the distribution function of Eq. (3.6) indeed diverges for $n < 3$. Eq. (3.7) also has a PL form and the exponent $n < 3/2$ also results in diverging standard deviation.

Based on these theoretical considerations, we hypothesise a PL form for the probability distribution function for non-equilibrium MFP, with diverging higher-order moments, instead of the classical exponential form of distribution function.

Exponential distribution functions have randomness with finite standard deviation (Montroll and Scher, 1973). In the distribution functions given by Eqs. (3.6) and (3.7), the zero moments $\left[\int_0^\infty t^0\psi(t)dt\right]$ and first moments $\left[\int_0^\infty t^1\psi(t)dt\right]$ also diverge, whereas both moments should be finite in order to achieve finite probability and MFP values. So here we propose the following form of molecular free path

distribution function:

$$\psi_{\mathrm{PL}}(r) = B(a+r)^{-n}, \tag{3.8}$$

where a and B are constants with positive values that are determined through the zero and first moments. The range of values for the exponent n can be obtained by making one of the higher-order moments divergent. The zero and first moments are given as follows:

$$1 = \int_0^\infty B(a+r)^{-n} dr, \tag{3.9}$$

$$\lambda = \int_0^\infty Br(a+r)^{-n} dr. \tag{3.10}$$

Eq. (3.9) requires the probability to range only from zero to one. Eq. (3.10) defines the unconfined, conventional MFP value, λ. It then follows that

$$B = (n-1)a^{n-1}, \tag{3.11}$$

$$a = \lambda(n-2). \tag{3.12}$$

Collision relaxation times (and hence MFP) are different for transport of momentum and energy – called velocity persistence (Kennard, 1938). MFP for thermal case is defined as $\lambda_{\mathrm{T}} = 1.922\lambda$ (Sone, 2002), and modified constants for thermal case are defined as:

$$B_{\mathrm{T}} = (n-1)a_{\mathrm{T}}^{n-1}, \tag{3.13}$$

$$a_{\mathrm{T}} = \lambda(n-2). \tag{3.14}$$

If $n > 2$, $a > 0$, otherwise the distribution function is negative. The standard deviation (the second moment) of the distribution function given by Eq. (3.8) diverges only for $n \leq 3$; so $2 < n \leq 3$. If one wishes to make the i^{th} moment diverging, then

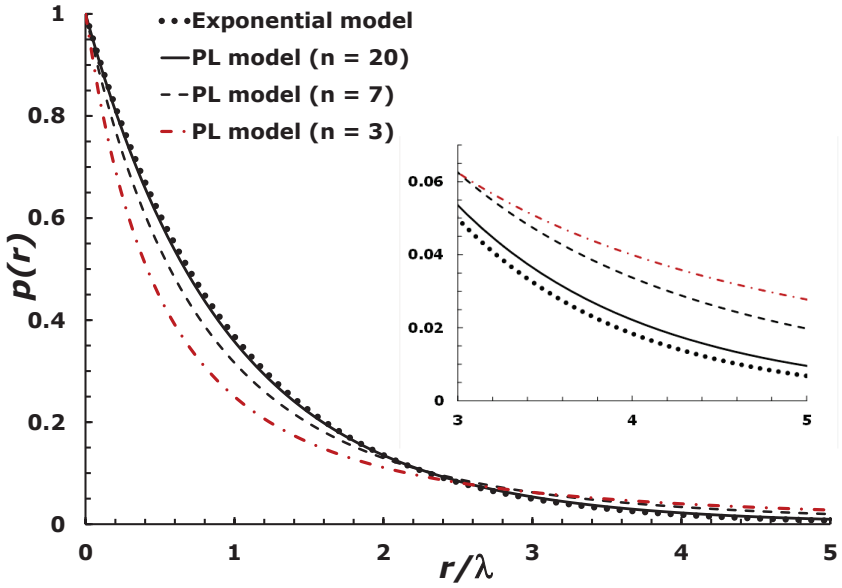

Figure 3.1: Probability of molecules experiencing a collisionless traveling distance r/λ. Power-law (PL) distributions with n = 3, 7 and 20 are compared with the classical exponential one. Inset figure shows tails of these distribution functions.

$n_{max} = i + 1$. As $n \to \infty$, the distribution function will have finite moments, which is the condition required of an equilibrium distribution function, i.e. for larger values of n the PL model simply reduces to the classical exponential one. For a finite n, the distribution function describes a system deviating from equilibrium. Thus, n acts as a decisive parameter to define the extent of deviation from equilibrium.

Fig. 3.1 shows the probability of gas molecules experiencing a collisionless traveling distance as a function of normalized distance r/λ. The power-law (PL) distribution model with different n values (3, 7 and 20) is compared to the classical exponential distribution function. The PL model with $n = 20$ has good agreement with the exponential model, which conveys that the PL model reduces to the classical one as $n \to \infty$. With a decrease in the n value, the deviations between the two distribution functions increase. Tails of these distribution functions are presented in the inset Fig. (3.1) and the length of the tail increases with a decrease in the n value. The long tail predicted by the PL model describes a Lévy type of gas motion under non-equilibrium situations.

3.2 Exponential effective mean free path models

The idea of using transport parameters that are influenced by an effective mean free path can be traced back to Stops (1970). Stops theory is based on the probability density function given in Eq. (3.5). The conventional (unconfined) mean free path, when no solid boundaries are present, can then be obtained by integrating $\psi(r)$ with respect to the travelling distance, r, from zero to infinity. The effective mean free path expression developed by Stops is achieved by using solid-angle analysis and by shortening the upper integrational limit of r from infinity to the distance of the confining wall. The integration of $\psi(r)$ then yields $\lambda_{\mathrm{eff(ST)}} = \lambda\beta_{\mathrm{ST}}$ for gas molecules confined between planar walls, where H is the wall spacing and

$$\begin{aligned}\beta_{\mathrm{ST}} =& \frac{1}{2}\left[2 + \left(\frac{y}{\lambda} - 1\right)\exp\left(\frac{y}{\lambda}\right) - \left(\frac{y}{\lambda}\right)^2 Ei\left(\frac{y}{\lambda}\right)\right. \\ &\left. + \left(\frac{H-y}{\lambda} - 1\right)\exp\left(\frac{H-y}{\lambda}\right) - \left(\frac{H-y}{\lambda}\right)^2 Ei\left(\frac{H-y}{\lambda}\right)\right], \end{aligned} \tag{3.15}$$

where the function Ei is the exponential integral function defined as:

$$Ei(z) = \int_1^\infty t^{-1}\exp(-zt)dt. \tag{3.16}$$

Eq. (3.15) has been used by Guo et al. (2007) for solving some micro-gas-flow cases with good results.

3.3 Power-law effective mean free path model

The effective MFP expression developed by Stops (1970), $\lambda_{\mathrm{eff(S)}}$, is derived using solid-angle-analysis. Here we use instead the approach given by Arlemark et al. (2010), based on an integrated form of the probability distribution function, i.e.

$$p(r) = \int_0^r \psi_{\mathrm{PL}}(r)dr = \left[1 - \left(1 + \frac{r}{a}\right)^{1-n}\right], \tag{3.17}$$

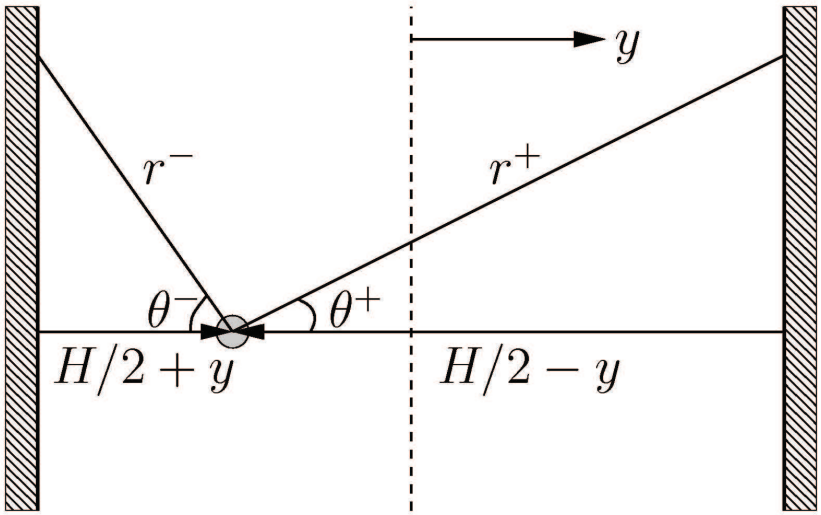

Figure 3.2: A molecule confined between two planar walls with spacing H. The molecule has an equal probability to travel in any zenith angle θ^- or θ^+ or to travel in either the positive or negative y-direction. The molecule under consideration is assumed to have just experienced an intermolecular collision at its current position $H/2 + y$.

which describes the probability a molecule travels a distance r without experiencing a collision.

3.3.1 Planar surface case

Our model is derived for the two-planar-wall configuration shown in Fig. 3.2. We use the notation r^- if a test molecule is travelling in the negative y-direction, and r^+ if the molecule is travelling in the positive y-direction. We also use the notations θ^- and θ^+ for the equally probable zenith angle travelling direction of the molecule. These quantities are related through $r^- = (H/2 + y)/\cos\theta^-$ and $r^+ = (H/2 - y)/\cos\theta^+$, where H is the distance between the two parallel plates.

The MFP based on the PL form of distribution function, $\lambda_{\text{eff(PL)}}$, is expressed by weighting the unconfined MFP, λ, with $p(r)$ as follows:

$$\lambda_{\text{eff(PL)}} = \frac{\lambda}{2}\left[p(r^-) + p(r^+)\right] = \lambda\left\{1 - \frac{1}{2}\left[\left(1 + \frac{r^-}{a}\right)^{1-n} + \left(1 + \frac{r^+}{a}\right)^{1-n}\right]\right\}. \tag{3.18}$$

A 3-dimensional MFP depending on the gas molecule's distance to a surface is

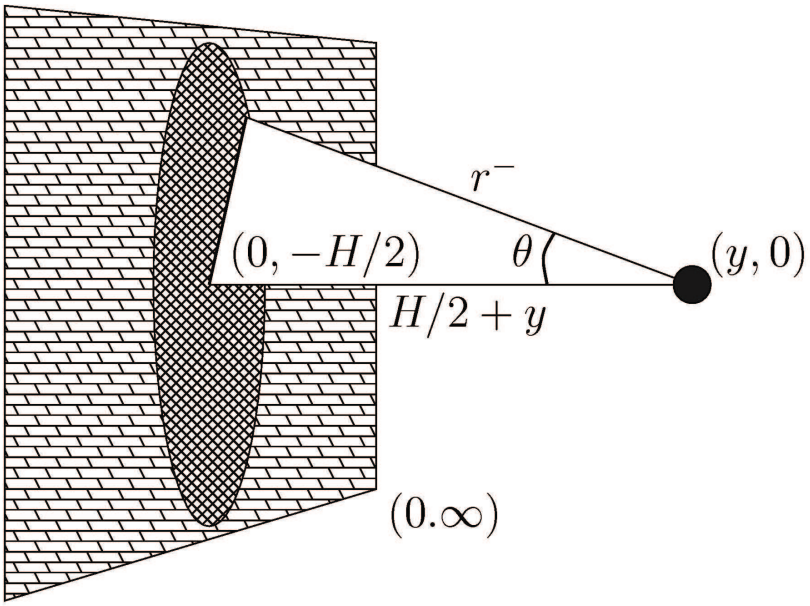

Figure 3.3: A molecule at a distance $H/2 + y$ from a planar wall; possible trajectories for travelling in the negative y-direction in cylindrical coordinates $[H/2 + y, (H/2 + y)\tan\theta]$.

then obtained by averaging the free path with respect to θ^- and θ^+ in the range $[0, \pi/2]$ using the mean integral theorem,

$$< \lambda_{\text{eff(PL)}}(\theta) > \; = \frac{2}{\pi}\int_0^{\pi/2} \lambda_{\text{eff(PL)}}(\theta) d\theta, \tag{3.19}$$

where the integration domain is illustrated in Fig. 3.3 for a gas molecule travelling in the negative y-direction. Averaging over the free path in Eq. (3.19), using Simpson's numerical integration involving 16 subintervals, results in $\lambda_{\text{eff(PL)}} = \lambda\beta_{\text{PL}}$, where

$$\begin{aligned}\beta_{\text{PL}} =& 1 - \frac{1}{96}\left[\left(1 + \frac{H/2 - y}{a}\right)^{1-n} + \left(1 + \frac{H/2 + y}{a}\right)^{1-n}\right. \\ &+ 4\sum_{i=1}^{8}\left(1 + \frac{H/2 - y}{a\cos[(2i-1)\pi/32]}\right)^{1-n} + 4\sum_{i=1}^{8}\left(1 + \frac{H/2 + y}{a\cos[(2i-1)\pi/32]}\right)^{1-n} \\ &\left. +2\sum_{i=1}^{7}\left(1 + \frac{H/2 - y}{a\cos[i\pi/16]}\right)^{1-n} + 2\sum_{i=1}^{7}\left(1 + \frac{H/2 + y}{a\cos[i\pi/16]}\right)^{1-n}\right],\end{aligned} \tag{3.20}$$

which is the normalized effective MFP based on the power-law distribution function, and is evaluated using the rarefaction parameter Kn as a is dependent on mean free

path. $\beta_{\mathrm{PL(T)}}$, effective MFP for thermal case can be evaluated using modified constant a_{T}, see Eq. (3.14). From Eq. (3.20) it is easy to see that our PL model satisfies the physically intuitive requirements for $Kn \to 0$, i.e.

$$\beta_{\mathrm{PL}}\,|_{wall} \;\approx\; 1/2, \text{ and } \beta_{\mathrm{PL}}\,|_{bulk} \;\approx\; 1. \tag{3.21}$$

The latter requirement, for molecules far away from a wall, means that the effective mean free path should approach its conventional unconfined value. The former requirement for molecules at the wall can be realised by considering the equal probabilities of a molecule traveling in the direction towards the confining wall (not yielding any traveling length contribution) and traveling into the bulk of the flow (yielding contribution length λ). It is interesting to note that the phenomenological viscosity model derived by Fichman and Hetsroni (2005), which also considered KL effects, gives an effective transport coefficient value at the wall that is half its bulk value.

The r-dependence of β_{PL} can be obtained, as λ and H are determined through the rarefaction parameter Kn. The β functions from Stops model, Eq. (3.15), and from the PL MFP model, Eq. (3.20), are compared in Fig. (3.4) for $Kn = 0.01$, 0.2, 1, 10; $n = 3$ is used to obtain the PL model results and this specific value is chosen as it gave good agreement with the MD results (Dongari et al., 2011a) (see Chapter 4).

The exponential and PL models show good agreement with each other for $Kn = 0.01$, i.e. in the early slip flow regime. This case also shows the limiting conditions ($Kn \to 0$) in the near-wall and bulk regions, as in Eq. (3.21). The exponential model shows significant deviations for $Kn = 0.2$ and 1, where the PL model exhibits sharper gradients in the near wall region. For $Kn = 0.2$, the channel is five unconfined mean free paths wide and since the β_{PL} profile approximately becomes flat at $y/H \sim 0.3$, the Knudsen layer can be estimated to be one and a half unconfined mean free paths wide. This estimation is in reasonable agreement with the estimation of Bird (1994), noting that the Knudsen layer is of the order of one mean free path wide, and also in agreement with the estimation of one and a half

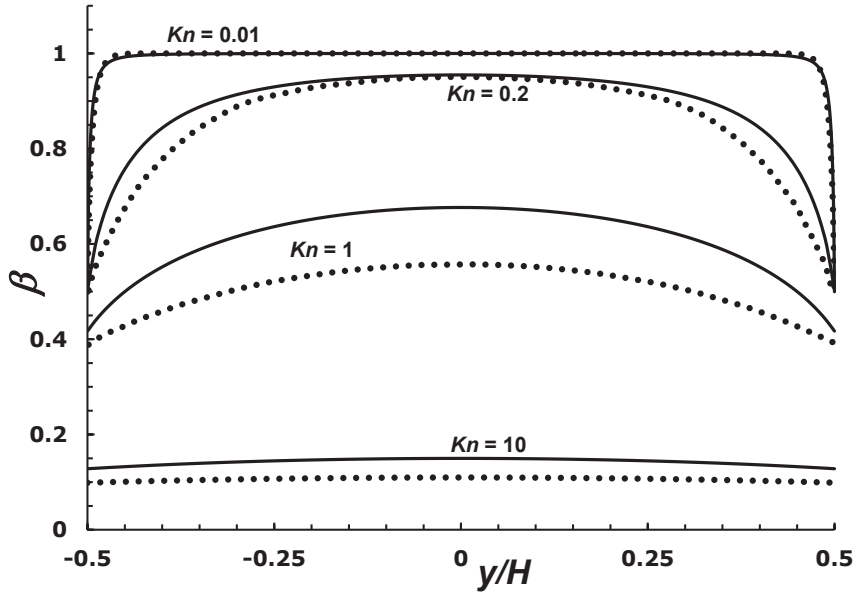

Figure 3.4: Variation of normalized mean free path, β, with normalized distance from a surface, for the planar parallel-surfaces case. Comparison of power-law (PL) model (thick line) with the classical exponential model (Stops, 1970) (dotted line) for Knudsen numbers ranging from the slip to the transition regimes.

as noted by Hadjiconstantinou (2003). The Stops exponential effective MFP profile overpredicts this value ($\sim 2\lambda$) due to shallower gradients in the near-wall region.

For higher Kn, both entire β profiles predict lower values due to the overlapping of the Knudsen layers of the left- and right-hand walls ($Kn = 1$). This stems from the fact that a molecule has a considerable likelihood of colliding with either wall at any position in the spacing between parallel walls. The basic physical requirement of decreasing β with increasing Kn can be seen by inspection of the very flat profile in the $Kn = 10$ case compared to other cases.

In the case with only one planar wall, Eq. (3.18) should be modified so that the $p(r^-)$ or $p(r^+)$ is replaced with unity to deduce the effective MFP variation. Using Eq. (3.20), we can also obtain the β variation as a function of y/λ for a single planar wall case, by keeping $Kn \to 0$. β profiles for a single planar surface are presented in Fig. 3.5. The power-law (PL) based models with different n values (3, 5 and 20) are compared to Stops effective MFP solution. As mentioned earlier, the PL model with larger n value reduces to the exponential one. The PL model predicts sharper

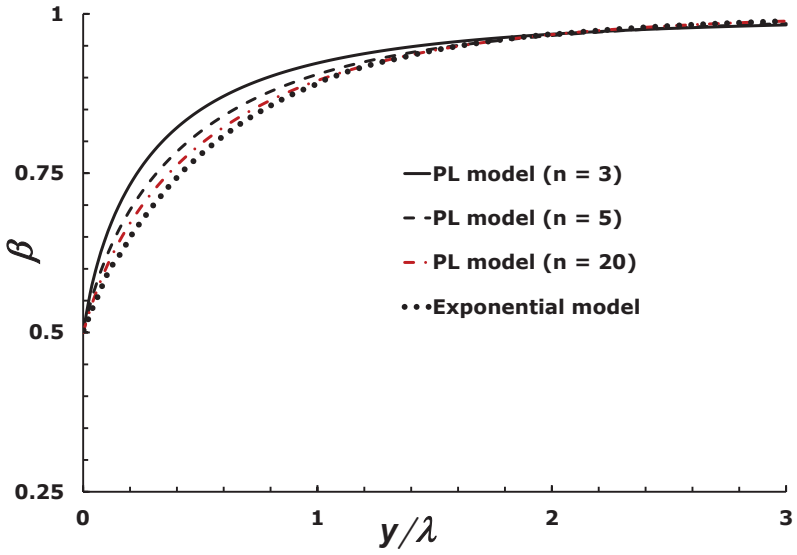

Figure 3.5: Variation of normalized mean free path, β, with normalized distance from a surface, for the single planar surface case. Comparison of power-law (PL) model (for various n values) to the classical exponential model (Stops, 1970).

gradients in the Knudsen layer and approaches the unconfined MFP value quicker than the exponential model.

3.3.2 Gas outside a cylinder

Following a similar approach to that adopted for planar surfaces, here we derive a geometry-dependent effective mean free path model for non-planar surfaces based on the PL form of free path distribution. Our model is derived for two generalized non-planar cases: (i) gas outside a cylinder of radius R_1, i.e. a surface with convex curvature, see Fig. 3.6a, and (ii) gas inside a hollow cylinder of radius R_2, i.e a surface with concave curvature, see Fig. 3.6b. Both convex and concave curvature models are used to deduce an effective MFP model for gas confined between concentric cylinders. We use the notation R^- if a test molecule is placed over a cylinder/surface with convex curvature and R^+ if the molecule is placed inside the cylinder/surface with concave curvature. We also use the notations θ^- and θ^+ for the equally probable zenith angle traveling direction of the molecule, towards convex and concave surfaces, respectively.

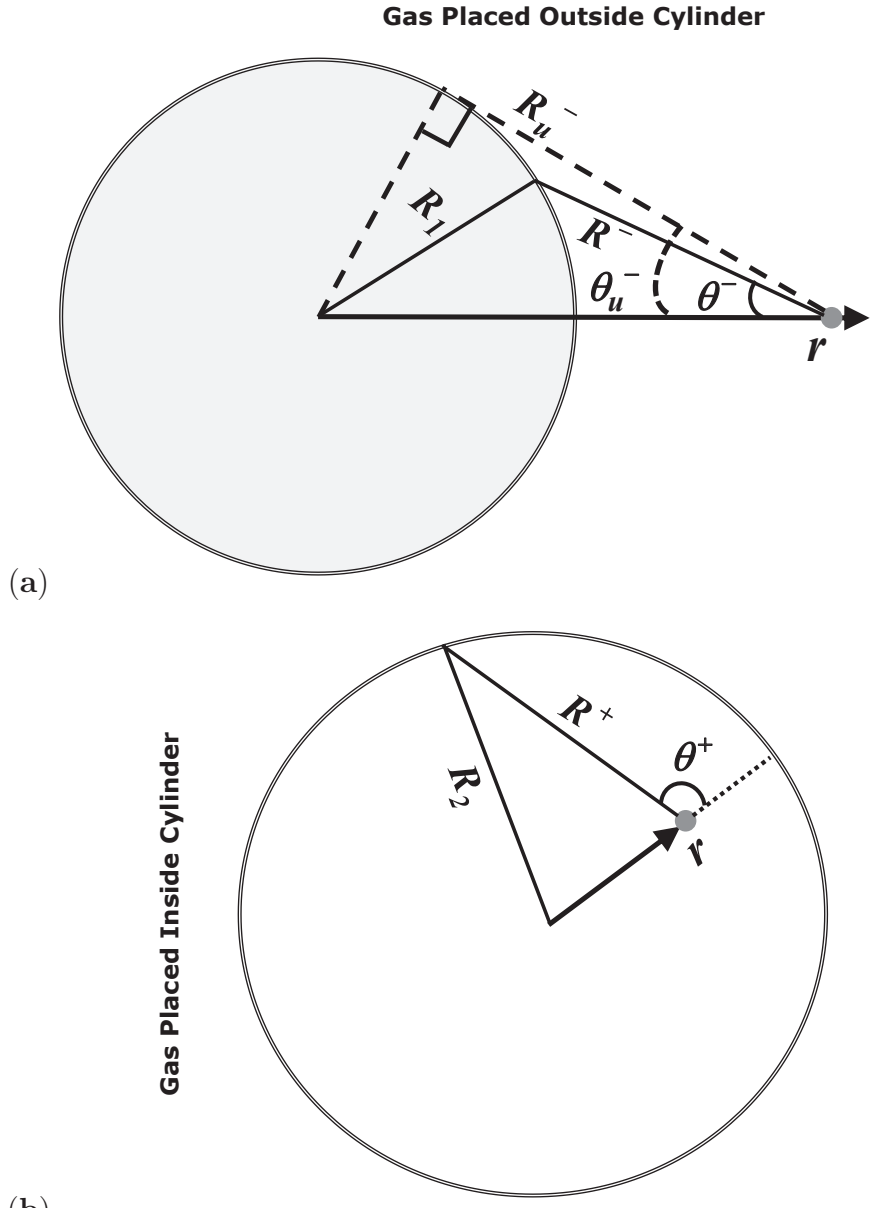

Figure 3.6: **(a)** A gas test molecule outside a solid cylinder and situated at a radial distance r from the centre of the cylinder of radius R_1. R^- is the travelling distance limit for a molecule moving towards the cylinder surface, for a given zenith angle θ^-. The largest travelling distance R_u^- is achieved for the zenith angle direction θ_u^-, above which the molecule by-passes the cylinder surface and travels into the bulk. **(b)** A gas molecule inside a cylindrical cavity of radius R_2, at a wall normal distance of $R_2 - r$, where r is the radial distance of the molecule from the centre of the cylinder. The molecule has a traveling distance of R^+ to the wall for a traveling direction of θ^+, where θ^+ is varied from 0 to π.

Fig. 3.6a presents the situation of a gas molecule outside a solid cylinder of radius R_1, at a distance r from the center of the cylinder. The traveling distance limit for a molecule traveling towards the cylinder is denoted R_u^-, and this is associated with a critical limit for θ^- defined as θ_u^-, above which the molecule passes the cylinder and travels back into the bulk. This angle can be calculated by using the geometry of a formed right-angled triangle, with its right angle at the point connecting the radius of the cylinder and R_u^- is tangential to the cylinder. The following relation can then be found:

$$r^2 = R_1^2 + \left(R_u^-\right)^2 . \tag{3.22}$$

By using the relation $R_1 = r\,\sin(\theta_u^-)$, the value of θ_u^- is obtained as:

$$\theta_u^- = \arcsin\left(\frac{R_1}{r}\right). \tag{3.23}$$

The distance of the molecule away from the cylinder surface, R^-, as a function of θ^-, can be determined in terms of r and R_1 by using the cosine law:

$$R_1^2 = r^2 + (R^-)^2 - 2rR^-\cos(\theta^-). \tag{3.24}$$

Eq. (3.24) is a simple quadratic in R^-, whose root is given by

$$R^-(r,\theta^-) = r\cos(\theta^-) - \sqrt{\left(r\cos(\theta^-)\right)^2 + R_1^2 - r^2}. \tag{3.25}$$

The average distance a molecule travels to the cylinder's surface, with respect to the angle θ^-, is achieved by the following integral mean value theorem:

$$\langle R^-\rangle = \frac{1}{\Omega}\int_0^{\Omega} R^-(r,\theta^-)d\theta^-, \tag{3.26}$$

where Ω is the solid angle subtended by the cylinder at a point in the base plane, at a distance r ($> R_1$) from the axis of the cylinder of length L, and which can be expressed as (Guest, 1960):

$$\Omega = \theta_u^- - \frac{1}{2}\left[\left(\left(\frac{r}{R_1}\right)^2 - 1\right)^{\frac{1}{2}} + \theta_u^- - \frac{\pi}{2}\right] L^{-2} + O\left(L^{-4}\right). \tag{3.27}$$

If we consider the length of the cylinder L tending to infinity, then Ω can be simplified to

$$\Omega = \theta_u^-. \tag{3.28}$$

Using Eq. (3.17), the mean free path of the molecules traveling in the direction of the cylinder (a surface with convex curvature) is then,

$$\lambda_{\text{eff(conv)}} = \lambda\left[1 - \frac{1}{\theta_u^-}\int_0^{\theta_u^-}\left(1 + \frac{R^-(r,\theta^-)}{a}\right)^{(1-n)} d\theta^-\right]. \tag{3.29}$$

The general mean free path expression is obtained by considering all possible molecular traveling directions. This is achieved in a similar manner to the analysis for a gas confined between planar parallel walls. In the case of planar parallel walls, it is equally probable that a molecule travels towards one surface or the other. In the present case, solid angle theory is used to determine the likelihood of a molecule traveling in the direction of the cylinder, as opposed to traveling towards the bulk; the probabilities are θ_u^-/π and $[1 - (\theta_u^-/\pi)]$, respectively. From this weighting, the general expression for the effective mean free path of a gas outside a cylinder is:

$$\lambda_{\text{eff(o)}} = \lambda_{\text{eff(conv)}}\left(\frac{\theta_u^-}{\pi}\right) + \lambda\left[1 - \left(\frac{\theta_u^-}{\pi}\right)\right], \tag{3.30}$$

where λ is the unconfined mean free path. This equation can also be written as $\lambda_{\text{eff(o)}} = \lambda\ \beta_{\text{(o)}}(r, R_1/\lambda)$, where

$$\beta_{\text{(o)}} = \left(\frac{\theta_u^-}{\pi}\right)\left[1 - \frac{1}{\theta_u^-}\int_0^{\theta_u^-}\left(1 + \frac{R^-(r,\theta^-)}{a}\right)^{(1-n)} d\theta^-\right] + \left[1 - \left(\frac{\theta_u^-}{\pi}\right)\right], \tag{3.31}$$

which is the normalized effective MFP based on a power-law distribution function,

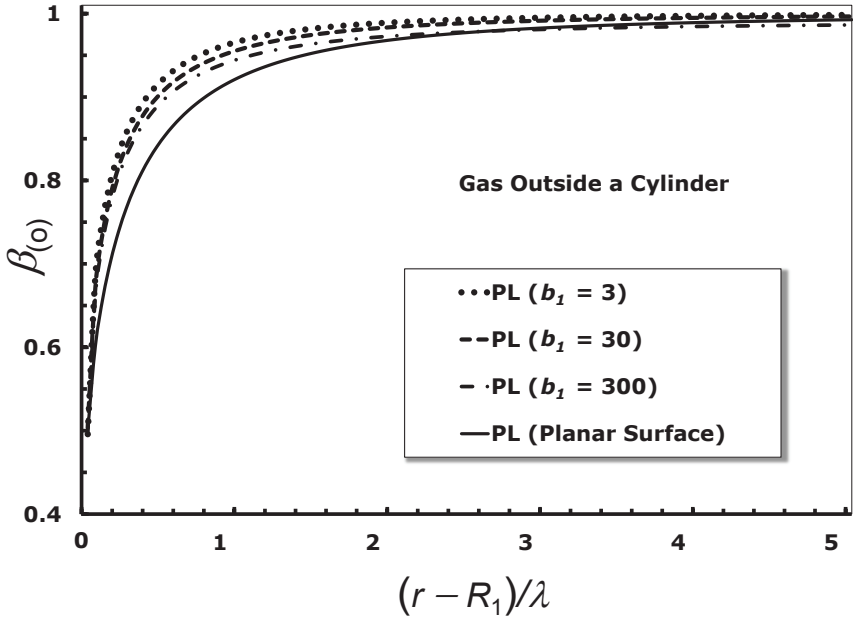

Figure 3.7: Variation of the effective mean free path of gas molecules outside a solid cylinder (surface with a convex curvature) as a function of non-dimensional wall-normal distance $[(r - R_1)/\lambda]$. Here, $r \geq R_1$, as the gas is outside the cylinder and, on the x-axis r is varied by fixing R_1 and λ, for a given value of b_1. The MFP profiles for various values of b_1 (R_1/λ) show the effect of the convex curvature and the comparison with the planar one-wall solution (Eq. 3.20).

where the subscript (o) denotes our considerations of gas molecules *outside* a cylindrical surface. For a given angle, Eq. (3.31) is dependent on r, R_1 and λ, and can be evaluated as a function of the non-dimensional wall-normal distance $[(r - R_1)/\lambda]$, using the parameter $b_1 = R_1/\lambda$. It should be noted that a is also dependent on the mean free path (see Eq. 3.12) and $r \geq R_1$, as the gas is placed outside the cylinder. Eq. (3.31) can be computed numerically using Simpson's rule; in the present study, we have used 16 subintervals.

The parameter b_1 denotes the inverse of the normalized curvature and as $b_1 \to \infty$, the solution of Eq. (3.31) should reduce to the planar case. To verify this limiting case, the normalized effective MFP solutions (i.e. $\beta_{(o)}$) based on Eq. (3.31), are plotted in Fig. 3.7 for various values of b_1 and are compared with the planar one-wall solution. For a value of $b_1 = 3$, the non-planar solution predicts a higher β value at the surface and also exhibits a sharper gradient compared to the planar one-wall case. Fig. 3.7 shows that, as the radius R_1 of the cylinder increases, our non-planar solution tends to the planar solution.

3.3.3 Gas inside a cylinder

Using a similar approach, it is possible to obtain the effective mean free path for gas molecules inside a hollow cylinder of radius R_2, i.e. for a surface with a concave curvature. As illustrated in Fig. 3.6b, r is a target molecule's radial distance from the centre of the cylinder and R^+ is the molecule's distance to the wall if the molecule has a traveling trajectory of θ^+.

To calculate the effective mean free path, the wall distance of the molecule has first to be calculated using the cosine law:

$$R_2^2 = r^2 + (R^+)^2 + 2rR^+\cos(\theta^+), \tag{3.32}$$

where the molecule's traveling trajectory θ^+ can vary from 0 to π. The molecular traveling distance to the wall, R^+, depends on r and θ^+ and can be expressed as:

$$R^+(r,\theta^+) = -r\cos(\theta^+) + \sqrt{(r\cos(\theta^+))^2 + R_2^2 - r^2}. \tag{3.33}$$

The solid angle subtended by the cylinder at a point lying inside the cylinder is 2π. Using half symmetry, it is sufficient to integrate θ^+ from 0 to π. Using our PL distribution to describe the molecular free paths (Eq. 3.17), the expression for the effective mean free path of a gas molecule inside a cylinder (i.e. interacting with a surface with concave curvature) is:

$$\lambda_{\text{eff(conc)}} = \lambda\left[1 - \frac{1}{\pi}\int_0^\pi \left(1 + \frac{R^+(r,\theta^+)}{a}\right)^{(1-n)} d\theta^+\right], \tag{3.34}$$

or the normalised expression:

$$\beta_{\text{(i)}} = \frac{\lambda_{\text{eff(conc)}}}{\lambda}, \tag{3.35}$$

where the subscript (i) denotes that the gas molecules are located *inside* the cylinder. Eq. (3.35) is dependent on r, R_2 and λ, and can be evaluated as a function of the non-dimensional wall-normal distance $[(R_2 - r)/\lambda]$, using the parameter $b_2 = R_2/\lambda$. Here $r \leq R_2$, as the gas is inside the cylinder.

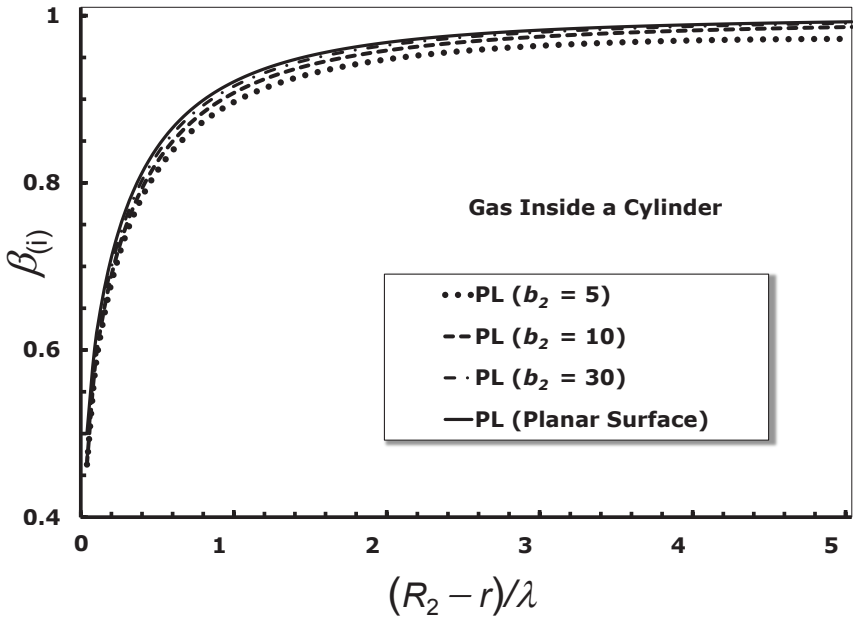

Figure 3.8: Variation of the effective mean free path of a gas molecule inside a cylinder (i.e. a bounding surface with concave curvature) as a function of non-dimensional wall-normal distance $[(R_2 - r)/\lambda]$. Here, $r \leq R_2$, as the gas is placed inside the cylinder and on the x-axis, r is varied by fixing R_2 and λ, for a given value of b_2. The MFP profiles for various values of b_2 (R_2/λ) are illustrated to show the effect of the concave curvature and their comparison with the planar one-wall solution (Eq. 3.20).

In a similar manner to the convex case, the effective MFP solution for a concave surface must also reduce to the planar one-wall case when the radius of the cylinder tends to infinity. Fig. 3.8 shows the variation of the normalized effective mean free path $\beta_{(\mathrm{i})}$, for various b_2 values and a comparison with the planar one-wall solution. For a value of $b_2 = 5$, the non-planar solution predicts a lower $\beta_{(\mathrm{i})}$ value at the surface and exhibits a shallower gradient compared to the planar case. For higher values of b_2, the non-planar concave solution approaches the planar case. However, at the surface, even for $b_2 = 30$, the non-planar solution predicts a lower value of $\beta_{(\mathrm{i})} \sim 0.4691$ compared to the corresponding planar wall value of 0.5. This is due to the concave nature of the surface, where a molecule will encounter more frequent collisions with the wall.

3.3.4 Gas confined between concentric cylinders

We now consider a gas between two concentric cylinders, with R_1 and R_2 being the radii of the inner and outer cylinders, respectively. Let us consider a molecule

situated at a distance r from the coincident centres of the two cylinders. The inner cylinder presents a surface with convex curvature (Fig. 3.6a) to the molecule and the outer cylinder presents a surface with a concave curvature (Fig. 3.6b). The probability of a molecule traveling towards the inner and outer cylinder directions can be evaluated as θ_u^-/π and $[1-(\theta_u^-/\pi)]$, respectively. Using Eqs. (3.29) and (3.34) and accounting for this weighting, the complete expression for the effective mean free path of a gas confined between two concentric cylinders is:

$$\lambda_{\text{eff}} = \lambda_{\text{eff(conv)}} \left(\frac{\theta_u^-}{\pi}\right) + \lambda_{\text{eff(conc)}} \left[1 - \left(\frac{\theta_u^-}{\pi}\right)\right], \tag{3.36}$$

where $\lambda_{\text{eff}} = \lambda\ \beta_{\text{NP}}$, and so

$$\beta_{\text{NP}} = \left(\frac{\theta_u^-}{\pi}\right)\left[1 - \frac{1}{\theta_u^-}\int_0^{\theta_u^-}\left(1+\frac{R^-(r,\theta^-)}{a}\right)^{(1-n)} d\theta^-\right] + \left[1-\left(\frac{\theta_u^-}{\pi}\right)\right]\left[1 - \frac{1}{\theta_u^+}\int_0^{\theta_u^+}\left(1+\frac{R^+(r,\theta^+)}{a}\right)^{(1-n)} d\theta^+\right], \tag{3.37}$$

with

$$\theta_u^+ = \pi - \theta_u^-. \tag{3.38}$$

Here, β_{NP} is the geometry-dependent MFP based on a power-law distribution function and is dependent on the Knudsen number, Kn, through the mean free path, λ (noting that $a = \lambda(n-2)$), and a geometry constraint, R_2/R_1. The Knudsen number is defined as:

$$Kn = \frac{\lambda}{R_2 - R_1}. \tag{3.39}$$

Fig. 3.9a shows the variation of β_{NP} between the inner and outer cylinders for various Knudsen numbers in the slip and early transition regimes, for $R_2/R_1 = 5/3$. The MFP profiles are sharper at the inner cylinder and shallower at the outer cylinder and they are also not symmetric about the midpoint of the gap between the cylinders. This finding is in contrast to the solution for the planar parallel walls

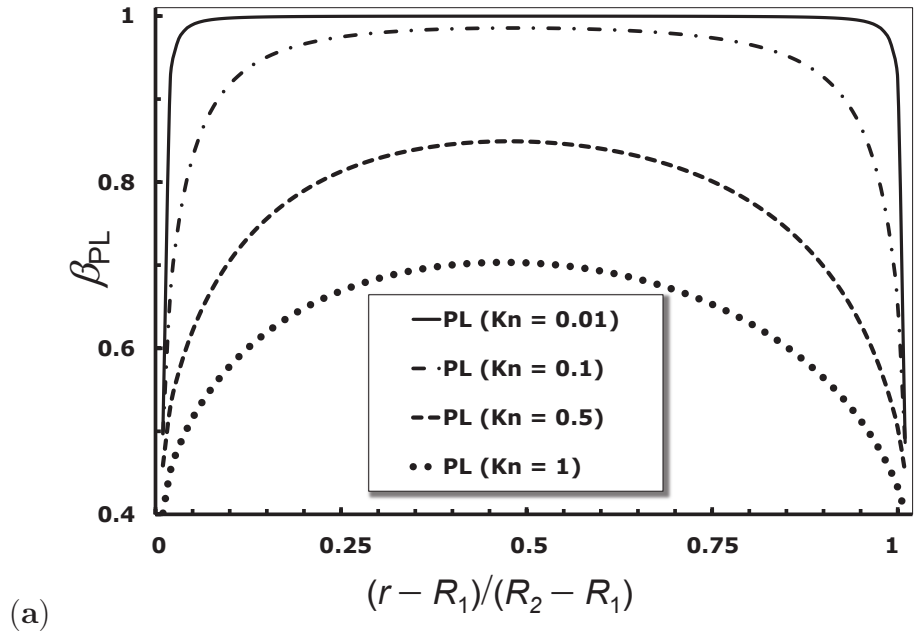

(a)

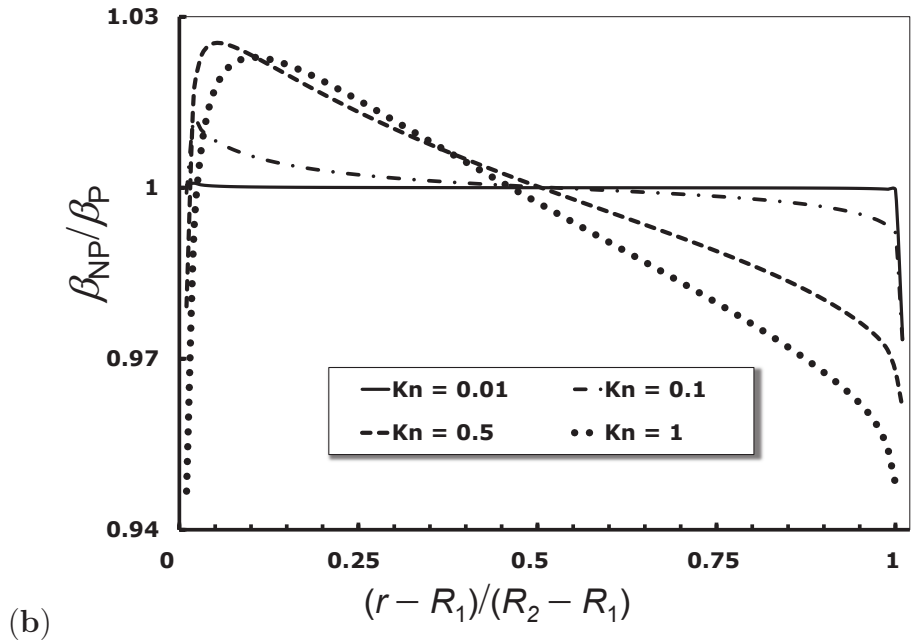

(b)

Figure 3.9: (**a**) Variation of β_{NP} as a function of normalized radial distance $(r-R_1)/R_2-R_1$ between the inner and outer cylinders for various Knudsen numbers in the slip and transition regimes, for the case of $R_2/R_1 = 5/3$. (**b**) Illustration of the curvature effects by evaluating the ratio of the normalized MFP values of gas confined between non-planar and planar surfaces. The non-planar solution is obtained from Eq. 3.37 and the planar-surface values are computed using Eq. (3.20). The subscripts NP and PL correspond to the non-planar and planar MFP solutions, respectively.

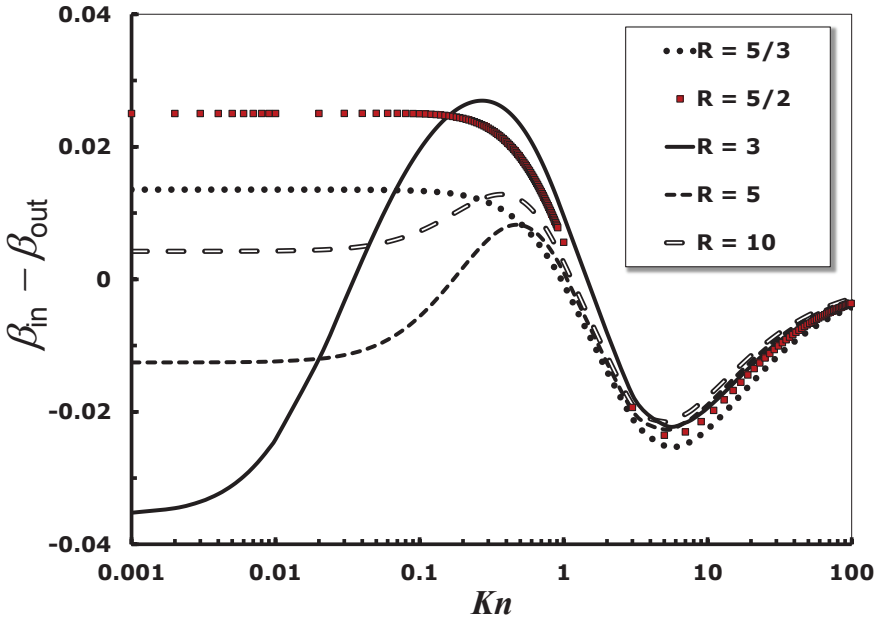

Figure 3.10: Variation of the difference in β_{NP} values at the inner and outer cylinders, as a function of Knudsen number for various geometric configurations of R ($= R_2/R_1$). The subscripts in and out correspond to values at the inner and outer cylinder surfaces, respectively.

case, where the MFP profile is symmetric about the midpoint of the gap between the walls. This anti-symmetric effect increases with Knudsen number. The values of β_{NP} are relatively high at the inner cylinder surface compared to the outer cylinder, due to the convex and concave curvature effects, respectively. The difference in the values of β_{NP} at the inner and outer cylinders is also dependent on the Knudsen number.

To demonstrate the curvature effects, Fig. 3.9b presents the ratio of the effective MFP between non-planar and planar solutions. The non-planar MFP (β_{NP}) values are obtained from Eq. (3.37) for $R_2/R_1 = 5/3$ and the MFP values for the case of planar parallel walls (β_{PL}) are evaluated using Eq. (3.20). For $Kn = 0.01$, the curvature effects are negligible, except in a thin layer close to the outer cylinder surface. As the Knudsen number increases, both the curvature and anti-symmetric effects become more pronounced, whereas the difference in the values of β at the inner and outer cylinders decreases. The ratio $\beta_{\mathrm{NP}}/\beta_{\mathrm{PL}}$ has its minimum at the outer cylinder for all Kn and the maximum is achieved at a position close to the surface of the inner-cylinder. However, this point moves away from the inner cylinder

with an increase in Kn, as the thickness of the Knudsen-layer increases.

Fig. 3.10 shows the difference in the values of β_{NP} at the inner and outer cylinders, as a function of Knudsen number for various geometric configurations of $R = R_2/R_1$. In the slip flow regime, the difference is a maximum for the case of $R = 5/3$ and with further increase in Kn, the difference decreases to a minimum value at the end of the transition regime ($Kn \approx 10$). Similar trends are noticed for $R = 2.5$ with slightly lower values in comparison to the $R = 5/3$ case. Increasing the ratio of the radii to $R_2/R_1 = 3$, the difference in the values of β_{NP} starts at a lower value in the slip regime and increases with Knudsen number, attaining a maximum value around $Kn \approx 0.3$. In the latter part of the transition regime, the profile follows the trends of the first two cases both qualitatively and quantitatively. Cases with larger ratios of the cylinder radii (i.e $R > 5$) qualitatively follow the $R = 3$ case, but predict slightly higher β differences in the slip regime. Fig. 3.10 illustrates that the effect of the convex and concave surfaces is more pronounced for the geometric configurations of $5/3 < R < 5$.

3.3.5 Spherical obstacle case

Using the identical approach as for the gas outside a cylinder case, the effective mean free path model can also be obtained for the case of molecules in the close vicinity of a sphere. Fig. 3.11 presents the situation of a gas molecule outside a solid cylinder of radius R, at a distance r from the center of the sphere. The only difference is in weighting of probabilities when compared to the cylindrical test case. In the present case, the probabilities are $\sin^2(\theta_u^-/2)$ and $\left[1 - \sin^2(\theta_u^-/2)\right]$, for a molecule traveling in the direction of the cylinder, as opposed to traveling towards the bulk, respectively. From this weighting, the general expression for the normalised effective mean free path of a gas outside a sphere:

$$\lambda_{\mathrm{eff(sp)}} = \lambda_{\mathrm{eff(conc)}} \sin^2\left(\frac{\theta_u^-}{2}\right) + \lambda\left(1 - \sin^2\left(\frac{\theta_u^-}{2}\right)\right), \tag{3.40}$$

here λ is the unconfined mean free path and $\lambda_{\mathrm{eff(sp)}} = \lambda\ \beta_{\mathrm{(sp)}}$, where

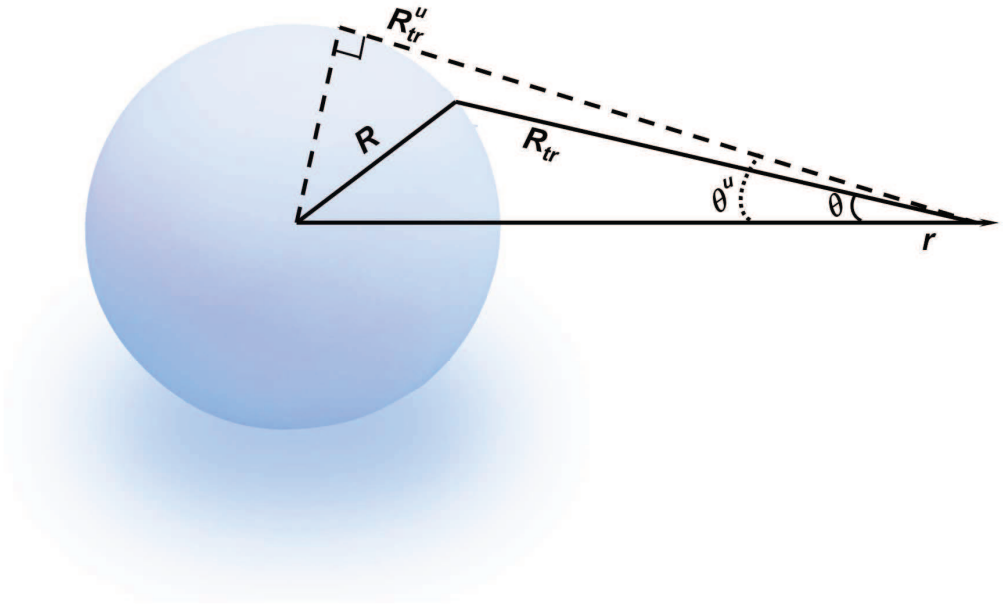

Figure 3.11: A gas test molecule outside a spherical obstacle and situated at a radial distance r from the centre of the sphere of radius R. R_{tr} is the travelling distance limit for a molecule moving towards the cylinder surface, for a given zenith angle θ. The largest travelling distance R_{tr}^{u} is achieved for the zenith angle direction θ^{u}, above which the molecule by-passes the cylinder surface and travels into the bulk.

$$\beta_{(\mathrm{sp})} = \left[\sin^2\left(\frac{\theta_u^-}{2}\right)\right]\left[1 - \frac{1}{\theta_u^-}\int_0^{\theta_u^-}\left(1 + \frac{R^-(r,\theta^-)}{a}\right)^{(1-n)}\right] + \left[1 - \sin^2\left(\frac{\theta_u^-}{2}\right)\right], \tag{3.41}$$

which is the normalized effective MFP based on the power-law distribution function of a gas molecule placed outside spherical obstacle.

Fig. 3.12 shows the variation of the normalised effective mean free path as a function of non-dimensional free path distance from the surface $[(r - R)/\lambda]$. Here, $r \geq R$, as the gas is outside the sphere and, on the x-axis r is varied by fixing R and λ, for a given value of Kn. The MFP profiles for various values of Kn (λ/R) show the effect of the convex curvature and for $Kn = 0.001$ the spherical solution effectively reduces to the planar one. Fig. 3.13 shows the variation of the normalised effective mean free path as a function of non-dimensional wall-normal distance $[(r - R)/R]$. The MFP profiles for various values of Kn illustrate the effect of the rarefaction in

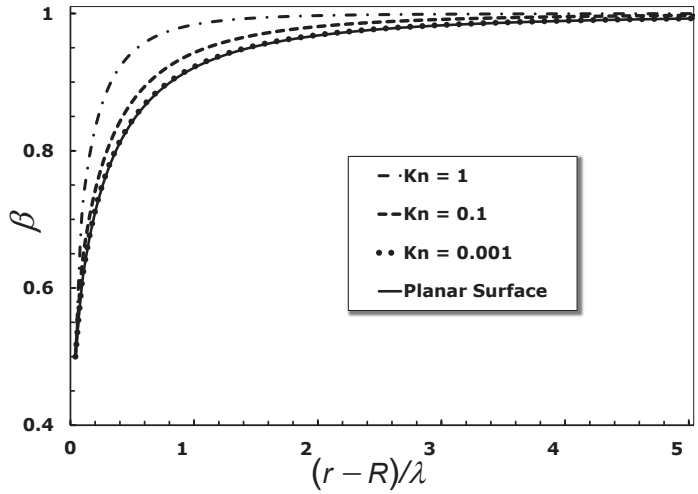

Figure 3.12: Variation of the normalised effective mean free path of gas molecules as a function of non-dimensional free path distance from the surface $[(r-R)/\lambda]$. Here, $r \geq R$, as the gas is outside the sphere and, on the x-axis r is varied by fixing R and λ, for a given value of Kn. The MFP profiles for various values of Kn (λ/R) show the effect of the convex curvature and the comparison with the planar one-wall solution.

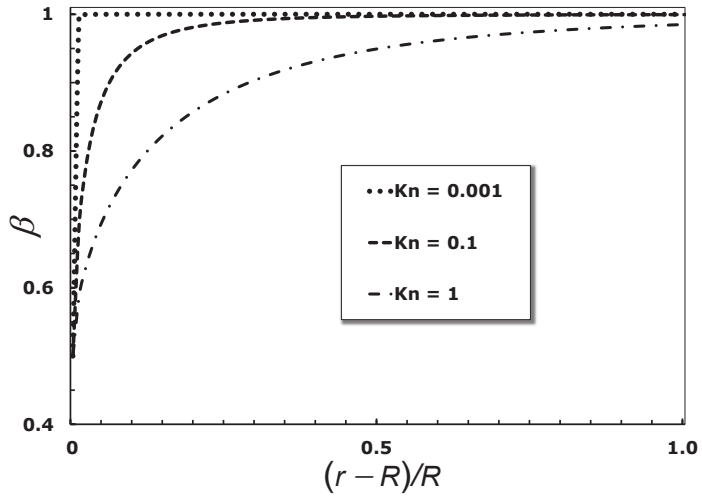

Figure 3.13: Variation of the normalised effective mean free path of gas molecules outside a spherical obstacle as a function of non-dimensional wall-normal distance $[(r-R)/R]$. Here, $r \geq R$, as the gas is outside the sphere and, on the x-axis r is varied by fixing R and λ, for a given value of Kn. The MFP profiles for various values of Kn (λ/R) illustrate the effect of the rarefaction in the near-wall region.

the Knudsen layers.

3.4 Discussion

In this chapter a new power-law (PL) probability distribution function to describe gas free paths has been hypothesised, and a geometry dependent effective mean free path (MFP) expression derived. This effective MFP is dependent on the free path probability distribution of a molecule traveling a certain distance without experiencing a collision. By integrating this probability distribution function, with respect to an unconfined space, from zero to infinity, the conventional unconfined value has been deduced. As this thesis focuses on modeling non-equilibrium gas flows in the Knudsen layers, i.e. near-wall regions, the conventional method has been extended by integrating the distribution function from zero to the distance of a confining wall instead. This upper limit is interpreted as a molecule will experience a collision by hitting the wall, which terminates its free path. By averaging the resultant function over all possible traveling directions, the effective MFP β as a function of wall normal distance has been obtained. This new method has been applied to both planar and non-planar wall confinements.

For planar cases, the effective MFP has been obtained for a parallel wall geometry, and a single-wall case deduced from this two-wall solution. For both the single planar wall case and parallel planar walls case at $Kn \sim 0$, at large wall distances the method fulfills the basic requirement of asymptotically approaching the unconfined MFP. In the near-wall region the requirement that the effective MFP should reach half the value of unconfined MFP is obtained. For parallel planar wall cases, in the transition regime ($0.1 < Kn < 10$), it is noticed that PL-based β profiles significantly differ from the classical exponential ones with the PL model exhibiting sharper gradients in the near-wall region. In the free molecular regime ($Kn > 10$), both effective MFP models are flat, which fulfills the requirement noted by Knudsen (1909).

Non-planar wall cases studied are the cylindrical obstacle case and the cylindrical cavity case, i.e. a gas interacting with concave and convex surfaces, respectively.

Curvature effects on the effective MFP have been investigated by varying the radii of the cylinders relative to the unconfined MFP value. Both the concave and convex β solutions reduce to the single planar wall solution when the radii of the cylinders tend to infinity. Using the effective MFP solutions of both the concave and convex cases, the β expression for a gas confined between concentric cylinders has also been obtained. Curvature effects depending on the rarefaction parameter have been discussed.

In the next chapter both the new PL and the classical exponential distribution functions for molecular free paths are compared with molecular dynamics (MD) numerical experiments. The β profiles of both these models are also validated against MD results in the transition flow regime.

Chapter 4

Molecular Dynamics Simulations

Reality must take precedence over public relations,
for nature cannot be fooled
- Richard P. Feynman

As discussed in the previous chapters, micro and nano-scale gas flows often display non-standard fluid behaviour. While bulk gas flow properties, such as the average mass flowrate along a micro channel, can be experimentally measured, interpretation of a single integral flow parameter in terms of the components making up the flow model is problematic. Any deviation of an integral quantity from its value calculated using conventional macroscopic fluid mechanics could be ascribed to multiple and competing causes, e.g. deficiencies in the bounding surface slip model, the effect of Knudsen layers, non-linear constitutive behaviour in the bulk, etc. *A posteriori* fitting of macroscopic theories to the experimental data with the aid of tuning parameters is unlikely to be physically realistic, or general enough, although it is widely practised (Karniadakis et al., 2005).

In this situation, and in order to shed light on the molecular phenomena that determine the macroscopic behaviour, simulating rarefied gases determinstically comes to the fore. Simulation methods such as Molecular Dynamics (MD) can allow us to assess fundamental molecular properties of the gas — the inter-molecular collision rate, the velocity distribution, the distribution of free paths between collisions — over a range of rarefied conditions, and in both unconfined spaces and confined

complex geometries (Rapaport, 2004). MD is the most appropriate method as it is deterministic, allowing for realistic molecular behaviour, i.e. molecular attractions, repulsions, movements and scatterings.

This chapter presents the results of numerical MD experiments on simple rarefied gases. We highlight the substantively different behaviour of the molecular free paths, collision rates, and mean free path profiles from their classical equilibrium counterparts. In particular, we show that the Lévy-type or power-law descriptions of chapter 3 better describe the rarefied gas behaviour. As the diffusive transport coefficients of gases can be interpreted in terms of the collisions of molecules, and of the free paths of the molecules between collisions (Kennard, 1938; Cercignani, 2000), MD results may yield new insight into the fluid mechanics of the rarefied case.

4.1 MD overview

Molecular dynamics is a computer simulation technique where the time evolution of a set of interacting molecules is followed. This is done by numerically solving the equations of motion (Newton's laws) of classical multibody systems. Given the positions, masses, and velocities of all particles in the system, and the forces acting on the particles, the motion of all molecules can be followed in time by calculating the (deterministic) particle trajectories. Matter is explicitly modelled by atoms or molecules, which interact together through "potentials". A potential between a pair of molecules can be conceptualised by an imaginary "spring" connected between the midpoints. As the two molecules approach each other, the spring becomes stiffer, and the molecules experience a pair-wise repulsive force. On the other hand when they move apart, the spring stretches so the molecules experience an attractive force.

To simulate gases, the open source software OpenFOAM (Open Field Operation and Manipulation) is used with the molecular dynamics toolbox mdFoam implemented by Macpherson *et al.* (2007; 2008) and Borg *et al.* (2008). The molecular dynamics method is often used to simulate liquids at the nano-scale because liquid molecules experience constant molecular interactions, which are considered to

be correctly taken into account using this method. The argument for simulating domains at the nano-scale is simply that at such a small scale the liquid is comprised of a manageable number of molecules. It is, however, possible to simulate larger domains for gases than for liquids. This is due to the fact that the density of gases is much lower than the density of liquids and so there are considerably larger separation distances between gas molecules than liquid molecules. Thereby fewer gas molecules than liquid molecules are modelled in the same volume domain. For rarefied gases MD can be used specially for estimating inter-molecular collisions, molecular free path distribution functions and gas mean free paths, because it is the only fully-deterministic approach available.

The theoretical unconfined mean free path (MFP) values are evaluated for a hard-sphere gas and Maxwellian gas. The mean free path for Maxwellian molecules is used for normalisation purposes in this thesis. In cases where the subscript of the mean free path is omitted it should be interpreted as being for a Maxwellian gas. The theoretical values of the mean free path of the two molecular representations are calculated for neon and argon gas at STP. The noble gases are considered because they are composed of monatomic molecules which only have translational motion, and therefore no molecular vibrational or rotational energies are present. This makes the noble gases easier to interpret theoretically and to model using molecular dynamics. Table 4.1 lists the gas parameters used for calculating the theoretical mean free paths at STP conditions. Here the specific gas constant has been calculated using $\Re = \Re_u/M$, where $\Re_u$ is the universal gas constant of 8.3145 [J/(mol K)]. The mean free path of the hard-sphere model is greater by a factor of $16/5\pi \sim 1.02$ then that of Maxwellian molecules (Kandlikar et al., 2005). The molecular masses of the gases neon and argon can be calculated by M/N_{Av}, where N_{Av} is Avogadro's constant equal to 6.0221367 $\times 10^{23}$ molecules per mol.

4.1.1 Intermolecular potentials

The choice of intermolecular potentials is key to the results obtained in any molecular dynamics simulation. The general potential energy equation between a set of

Table 4.1: Gas data of standard temperature and pressure for neon and argon gases (Nordling and Osterman, 1999).

Gas Property	Neon	Argon
dynamic viscosity, $\mu \times 10^6$ [kg/(m s)]	29.7	20.8
density, ρ [kg/m^3]	0.901	1.784
molecular mass, M [kg/mol]	20.18	39.95
specific gas constant, $\Re$ [J/kg K]	412.2	208.1
MFP of Maxwellian gas λ_{MM} (λ) $\times 10^7$ [m]	1.233	0.613
MFP of hard-sphere gas λ_{HS} (λ_k) $\times 10^7$ [m]	1.256	0.624

N interacting particles can be expressed by external fields, pair-interactions and higher-order interactions (multi-body potentials). In many atomistic simulations, it is sufficient to use only pair-wise interactions (two-body) to capture the essential physics. The most commonly-used potential to describe the Van der Waals interactions between non-bonded molecules is the Lennard-Jones (LJ) 12-6 potential:

$$U_{LJ}\left(r_{ij}\right) = 4\epsilon\left[\left(\frac{d}{r_{ij}}\right)^{12} - \left(\frac{d}{r_{ij}}\right)^{6}\right], \tag{4.1}$$

where $r_{ij} = \mid \overrightarrow{r}_{ij} \mid$ is the separation distance between two molecules (i, j), d is the molecular diameter and corresponds to the separation distance where the potential energy is zero, and ϵ is the intermolecular energy well-depth. The potential is repulsive at small molecular separations and is attractive at long separations; potential energy is zero for infinite separation lengths. While the strongly repulsive core arising from (in quantum mechanics) the nonbonded overlap between the electron clouds has a rather arbitrary form, and other powers and functional forms are sometimes used, the attractive tail actually represents the van der Waals interaction due to electron correlations. The interactions involve individual pairs of atoms: each pair is treated independently, with other atoms in the neighborhood having no effect on the force between them.

The d values or molecular diameters are presented in Table 4.2 for monatomic gases neon and argon (Allen and Tildesley, 1987). It is here chosen to set d equal to the hard-sphere diameter of a monatomic gas in order to compare the molecular dynamics measurements of rarefied gas properties to classical kinetic theory results.

Table 4.2: Lennard-Jones parameter data for neon and argon molecules. Prime notation indicates commonly used data for liquid molecules and these parameters are used here for scaling ϵ (Allen and Tildesley, 1987).

LJ Property	Neon	Argon
$d^{'}$ $\times 10^{10}$ [m]	2.720	3.405
$\epsilon^{'}$ $\times 10^{22}$ [J]	6.4891	17.2857
d $\times 10^{10}$ [m]	2.5836	3.6614
ϵ $\times 10^{22}$ [J]	7.1924	14.9496

The commonly used Lennard-Jones parameters for liquids, used for scaling, are denoted by a prime symbol. Since the molecular mass is independent of the choice of Lennard-Jones parameters, ϵ is obtained from the relation $\epsilon = d^{'2}\epsilon^{'}/d^2$ (Guarini et al., 2005), under the assumption that this law is appropriate to scale liquid to gas properties in the same way as between liquid properties. The sensitivity of ϵ on the mean free path is tested in this thesis for argon gas, where it is found that by reducing ϵ by one half resulted in an ϵ value of 7.4748 $\times 10^{-22}$ decreases the mean free path by about 0.29%, so the solution is considered to be essentially insensitive to this parameter.

The potential, $U_{LJ}\left(r_{ij}\right)$, of the Lennard-Jones model is shown in Fig. 4.1 for neon and argon gases. Here it is possible to distinguish the effect of the first and second terms in the Lennard-Jones potential. The former is repulsive short-ranged and the latter is attractive and long-ranged. It is noted that argon gas has the larger ϵ value with the deepest potential well, and it consequently also possess the stronger interaction force. It is also noted that d corresponds to the molecular separation distance where the molecular potential switches between positive and negative. Formally, in the Lennard-Jones potential all interactions between all nonbonded particles have to be calculated. However, as this potential vanishes at larger r it can be truncated at a cut-off separation distance r_c so as to improve the computational speed of the MD simulation. Each molecule does not need to interact with all N molecules in the system, but solely with those molecules that are located within a sphere of radius r_c. A cut off radius of $r_c = 3\ d$ is set in order to most closely resemble the actual Lennard-Jones potential.

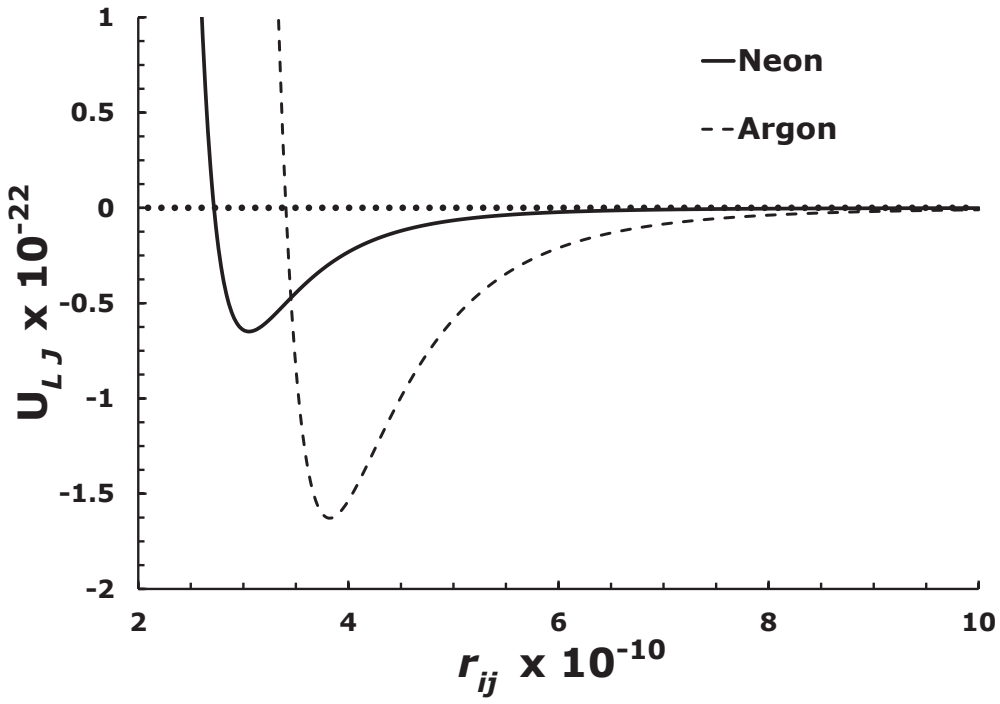

Figure 4.1: Potential energy between molecules i and j for neon and argon gases.

4.1.2 Boundary conditions

The first aim is to validate the MD measurement of the mean free path by recovering the theoretical value of the unconfined MFP in neon and argon gases (i.e. unaffected by any solid boundaries). In this attempt it is chosen to simulate a cube shaped geometry with periodic boundaries, shown schematically in Fig. 4.2. The introduction of periodic boundaries is equivalent to considering an infinite, space-filling array of identical copies of the simulation region. There are two consequences of this periodicity. The first is that an atom that leaves the simulation region through a particular bounding face immediately reenters the region through the opposite face. The second is that atoms lying within a distance r_c of a boundary interact with atoms in an adjacent copy of the system, or, equivalently, with atoms near the opposite boundary a wraparound effect. Another way of regarding periodic boundaries is to think of mapping the region (topologically, not spatially) onto the equivalent of a torus in four dimensions (a two-dimensional system is mapped onto a torus); then it is obvious that there are no physical boundaries. In this way it

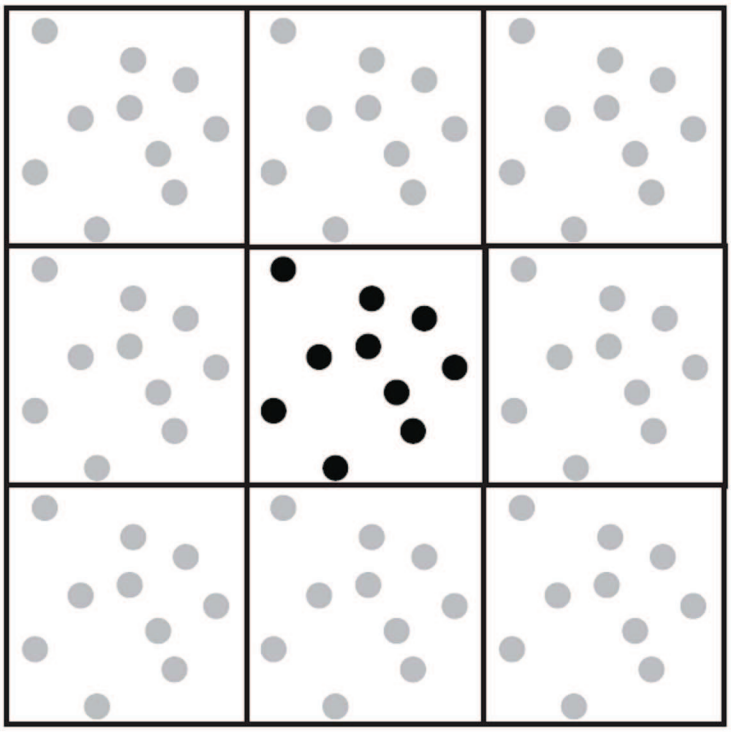

Figure 4.2: The meaning of periodic boundary conditions (the two-dimensional case is shown).

is possible to model systems that are effectively bounded but that are nevertheless spatially homogeneous insofar as boundaries are concerned.

The wraparound effect of the periodic boundaries must be taken into account in both the integration of the equations of motion and the interaction computations. After each integration step the coordinates must be examined, and if an atom is found to have moved outside the region its coordinates must be adjusted to bring it back inside. Even with periodic boundaries, finite-size effects are still present. As a minimal requirement, the size should exceed the range of any significant correlations. In the current chapter, the size of a chosen system in each dimension is at least 100 times larger than σ, so that correlation effects are minimal.

There is however a difficulty in simulating the solid boundary walls explicitly, consisting of molecules in an arranged structure. This is because the walls are about as dense as liquids and will therefore require a large number of molecules to be represented. Explicit walls therefore need to be very thin (just a few molecular layers) in order for the simulation not to be too computationally expensive. Due

Table 4.3: Reduced units for MD simulations. Reference values are taken to be the Lennard-Jones potential characteristics for Argon. A property q in SI units is converted into a reduced unit q^* using its reference property q_r, given in the last column of the table.

Fundamental quantities		
length	$l^* = l/\sigma_r$	$\sigma_r = 3.6614 \times 10^{-10}$ m
energy	$\epsilon^* = \epsilon/\epsilon_r$	$\epsilon_r = 14.9496 \times 10^{-22}$ J
mass	$m^* = m/m_r$	$m_r = 6.6904 \times 10^{-26}$ kg
Derived quantities		
time	$t^* = t/t_r$	$t_r = \sqrt{m_r\sigma_r^2/\epsilon_r} = 2.16059 \times 10^{-12}$ s
force	$f^* = f/f_r$	$f_r = \epsilon_r/\sigma_r = 4.87288 \times 10^{-12}$ N
acceleration	$a^* = a/a_r$	$a_r = \epsilon_r/m_r\sigma_r = 7.28340 \times 10^{13}$ m s^{-2}
velocity	$u^* = u/u_r$	$u_r = \sqrt{\epsilon_r/m_r} = 157.364$ m s^{-1}
mass density	$\rho^* = \rho/\rho_r$	$\rho_r = m_r\sigma_r^{-3} = 1702.22$ kg m^{-3}
temperature	$T^* = T/T_r$	$T_r = \epsilon_r/k_b = 120$ K
pressure	$p^* = p/p_r$	$p_r = \epsilon_r\sigma_r^{-3} = 42.153 \times 10^6$ N m^{-2}

to the expensive simulations of explicit walls it is quite common to simulate walls implicitly, in which cases they are replaced by a surface which reflects molecules specularly, diffusively or in a combination of the both. In this chapter we present MD results with implicit walls.

4.1.3 Reduced units

It is common practice to convert all MD quantities into reduced units, using only three fundamental normalisation parameters for length σ_r, mass m_r and energy ϵ_r. All other properties are variants of these parameters. Values for the normalisation parameters are typically chosen to correspond to the LJ characteristic values, σ, m and ϵ respectively, see Table 4.3. Choosing the reference length and energy to be the same as those in the intermolecular potential being used, and the reference mass to be that of the molecules being simulated, simplifies and speeds up the calculation of intermolecular forces because those variables may be eliminated from the force equation. This is intended to create a general framework for simulation of multicomponent fluids and mixed form potential functions, so the reduced units cannot be used to remove parameters from equations, merely to scale them.

4.1.4 Measurement of free paths

A collision occurs when the magnitude of the distance R between a molecule i and its nearest neighbour j, is smaller than the target collision distance r_{col}. At any time-step a molecule can be in any of four different phases of a collision:

- The molecule has just collided between this time-step and the previous one. Conditions: if ($R < r_{col}$, and $collisionStatus = false$), measure final set of properties and set $collisionStatus$ of molecule to $true$ and $time_{col}[id] = 0$, where $time_{col}$ stores the value of time spent by a molecule id during the inter-molecular collision with another molecule.
- The molecule is still undergoing collision. Conditions: if ($R < r_{col}$, and $collisionStatus = true$), $time_{col} = +\Delta t_m$, where Δt_m is the MD time step.
- The molecule has left the collision. Conditions: if ($R \geq r_{col}$, and $collisionStatus = true$), set $collisionStatus$ to $false$.
- The molecule is in free flight. Conditions: if ($R \geq r_{col}$, and $collisionStatus = false$), measure and append properties.

R and $collisionStatus$ are two properties defined in the molecule class: R is updated by the intermolecular force calculation part of the existing $mdFoam$ code, while $collisionStatus$ is updated by this measurement model.

The way velocities are calculated in the Leap-Frog algorithm, might lead to an error if one is to calculate the travelled distance of a molecule in the previous time-step from velocities. If measured at the end of the time-step (in which a second update of velocity takes place after the molecule tracking step), measurement of displacement from the velocity of a molecule should be properly given as:

$$\Delta r = \mid (v_i(t) - 0.5\Delta t_m a_i(t)) \mid \Delta t_m, \tag{4.2}$$

where $v_i(t)$ is the velocity of molecule i at the end of the time-step, $a_i(t)$ is its acceleration calculated in a sub-step of the time-step.

The current method records the molecular free paths in every time step, and its major advantage is that we can calculate the probability that molecules travel a distance without experiencing a collision, i.e. the free path distribution function

(Dongari et al., 2011a). The average of these free paths of all simulated molecules is the mean free path. Additionally, the collision handling algorithm allows the evaluation of multiple collisions, i.e. collision events which involve three or more molecules simultaneously, and also records the time spent during the collision process. This means the dilute gas assumption employed in deriving the Boltzmann equation can be explored (Dongari et al., 2011d). It should be noted that the present recording of the mean free path does not affect the actual way the molecular dynamics solver predicts the dynamics of the gas.

All simulations are carried out for a problem-time ranging between 5 ns to 1 μs, with an integration step of 5 fs (i.e. minimum of 1 million samples). An initial equilibration time of 1000 ps is performed before sampling begins. During the equilibration time the system is coupled to a Berendsen thermostat at a temperature, which is then removed for the latter part of the simulation. The sampling is performed in the microcanonical ensemble (NVE) of constant number of atoms, constant volume, and constant energy. The gas molecules are initially placed on a rectangular lattice, which contained at least 50000 gas molecules. Samples of the trajectory and measured values are stored every 100 ps. Simulations typically took 2 - 10 days depending on the non-equilibrium nature of the test case, using 16 or 32 cores on a parallel machine.

4.2 Simulation results

4.2.1 Unconfined mean free paths

In order to be able to compare the theoretical values of the mean free path with molecular dynamics the definition of a collision needs to be defined, i.e. the occurrence of inter-molecular collisions in the MD simulations. While the instance of a collision is unambiguous only if the molecular interaction is a step potential (i.e. for hard-sphere molecules), the time step required for simulations in that case would need to be vanishingly small in order to capture the collision instant reliably (Rapaport, 2004). For the continuous and more physically-realistic LJ potential that

we use, we instead declare a collision to have occurred if two molecules are closer together than a distance r_{col}. Molecules in the simulation start to exchange momentum as soon as they are within the MD cut-off distance r_c, and they start to repel each other when they are closer than d. Hence, the closeness parameter r_{col} must lie between $2.5d$ and d.

An appropriate value for r_{col} can be evaluated through MD simulations to obtain the mean free path for unconfined Neon gas — λ_{MM} or $\lambda = (\mu/\rho)(\pi/2\Re T)^{1/2}$, where μ is gas dynamic viscosity, ρ is gas density, $\Re$ is specific gas constant and T is temperature — at standard (i.e. non-rarefied) conditions. While computationally time-consuming at standard gas densities, this is also an effective way of validating the MD technique overall. At STP, λ is 1.233×10^{-7} m (Cercignani, 2000). Using $r_{col} = \sigma$, the MD simulation retrieves this mean free path value within 1%. As a sensitivity check, if we use $r_{col} = 1.2\sigma$, the MD simulation result is 29% less than the theoretical mean free path value. So the appropriate value for r_{col} is d, and all the simulations in this thesis have been carried out using this default value, unless explicitly specified otherwise.

To validate our MD method, we first use it to deduce the unconfined value of the mean free path (MFP) of Neon gas at standard conditions. We simulate a cubic spatial geometry with periodic boundary conditions, i.e. if a molecule leaves the domain, it is reintroduced on the opposite side of the domain, retaining the same velocity. The side-length of this simulation domain is chosen to be the MFP of Neon at STP conditions, and the domain is filled with 51505 molecules to achieve a gas density of 0.9011 kg/m^3.

Fig. 4.3a shows the recorded MFP as the simulation progresses in time. The MD measurements relax to an MFP value of 1.221×10^{-7} m, that differs from the theoretical value of MFP by only 0.96%. The simulations also recorded the number of binary inter-molecular collisions (by discounting a molecule as undergoing a binary collision if its counterpart molecule is already undergoing a collision, i.e. a molecule with $collisionStatus = false$ cannot collide with a molecule with $collisionStatus = true$); at standard density, binary collisions account for 96.92% of all collisions, the remainder being multiple-molecule collisions. If only binary collisions are allowed to

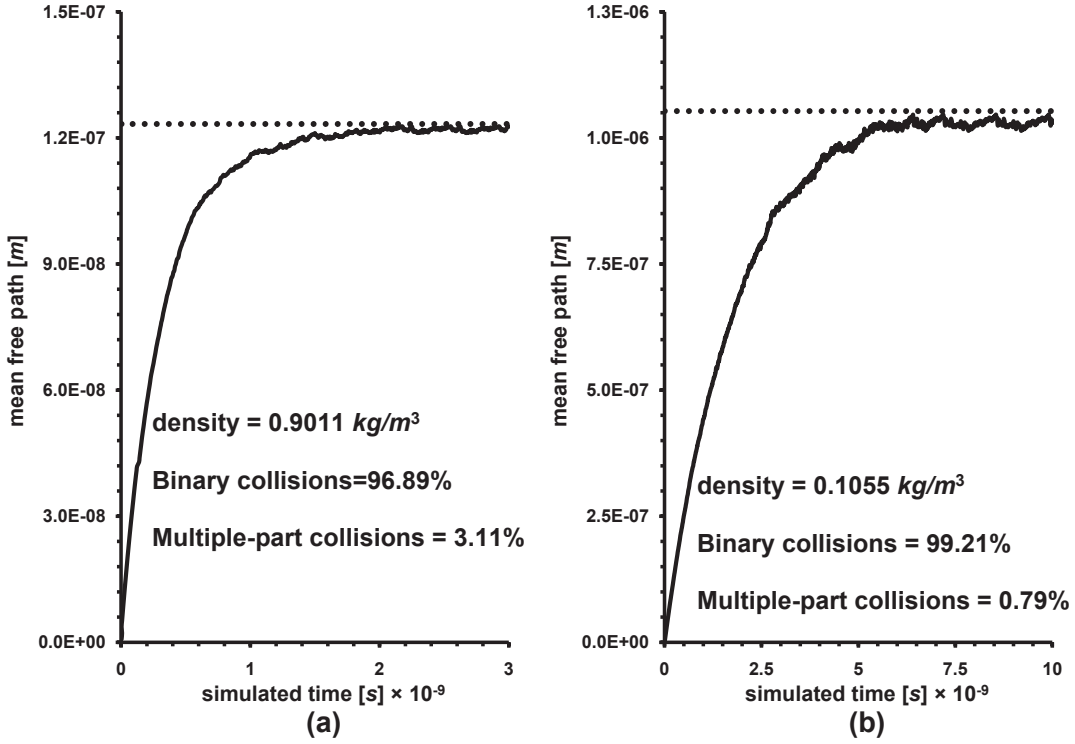

Figure 4.3: Relaxation to steady-state of the measured mean free path as the MD simulation progresses, for neon gas densities of (a) 0.9011 kg/m^3 and (b) 0.1055 kg/m^3. The theoretical values of the mean free path in each case are given by the straight dotted lines (Cercignani, 2000).

contribute to the MFP measurement we retrieve an MFP of 1.262×10^{-7} m, which is close to the hard-sphere value of 1.255×10^{-7} m given through (Kennard, 1938):

$$\lambda_k = \frac{m/N_{Av}}{\pi\rho\sigma^2\sqrt{2}}. \tag{4.3}$$

This indicates that the kinetic theory description of MFP is accurate if collisions are purely binary, as expected.

We then test a rarefied case: Neon gas of density 0.1055kg/m^3. The side-lengths of the simulation cubic domain were increased to $2.25\lambda_{Ne}$, and the domain is filled with 68687 molecules. In this rarefied case, a slightly larger number of molecules are simulated and the case run up to 10×10^{-9} s of problem time because, with a reduced frequency of inter-molecular collisions, the steady-state MFP is reached more slowly. Fig. 4.3b shows the MFP measurements from the simulations. As expected in this rarefied case, the equilibrium kinetic value of MFP given by Eq. (4.3) differs more

markedly from the deterministically-simulated MFP, in this case by about 2.31%. More than 99% of the inter-molecular collisions are binary, and fluctuations in the steady-state MFP value increase.

4.2.2 Free path distributions

Besides the value of the mean free path, the distribution of individual molecular free paths is also of interest (Kennard, 1938). The equilibrium expression for the free path distribution function in Eq. (3.5) is only valid if the molecular collision rate $\dot{\theta}_v$ is constant, or fluctuations in $\dot{\theta}_v$ are negligible. Fig. 4.4 shows the variation of collision rate per unit number density with MD simulation time, for neon gas densities of 0.9011 kg/m^3 and 0.1055 kg/m^3. At atmospheric density conditions in Fig. 4.4a, the mean and standard deviation of the collision rate are 4.1×10^{-11} and 9.49×10^{-12}, respectively, so the temporal fluctuations are low. For the rarefied case, Fig. 4.4(b), however, the fluctuations are significantly higher and the ratio of standard deviation to the mean of the collision rate is around 0.77. This indicates that the equilibrium assumption of a collision rate constant in time is not valid in rarefied conditions. Consequently, the probability distribution of free paths is not necessarily exponential in form in the rarefied case.

Our MD results allow us to test other forms of distribution function for the rarefied case, such as Lévy or power-law (PL) statistics (Fa and Lenzi, 2003; Montroll and Scher, 1973), described in Chapter 3. We therefore use our MD measurements to benchmark the PL distribution function of Eq. (3.17), and also to show the limitations of the classical exponential distribution function.

Figure 4.5 presents our MD results for the probability a molecule travels a normalised distance r/λ without experiencing a collision, at both atmospheric and rarefied conditions (where λ refers to the theoretical MFP at the corresponding densities). Three different normalised density test cases are simulated for $\rho^*(\rho/\rho_{atm}) = 1, 0.2$ and 0.1, where densities (ρ) are normalised with the atmospheric density value ($\rho_{atm} = 0.9011$ kg/m^3 for neon gas).

At atmospheric density ($\rho^* = 1$), both MD measurements and the PL distri-

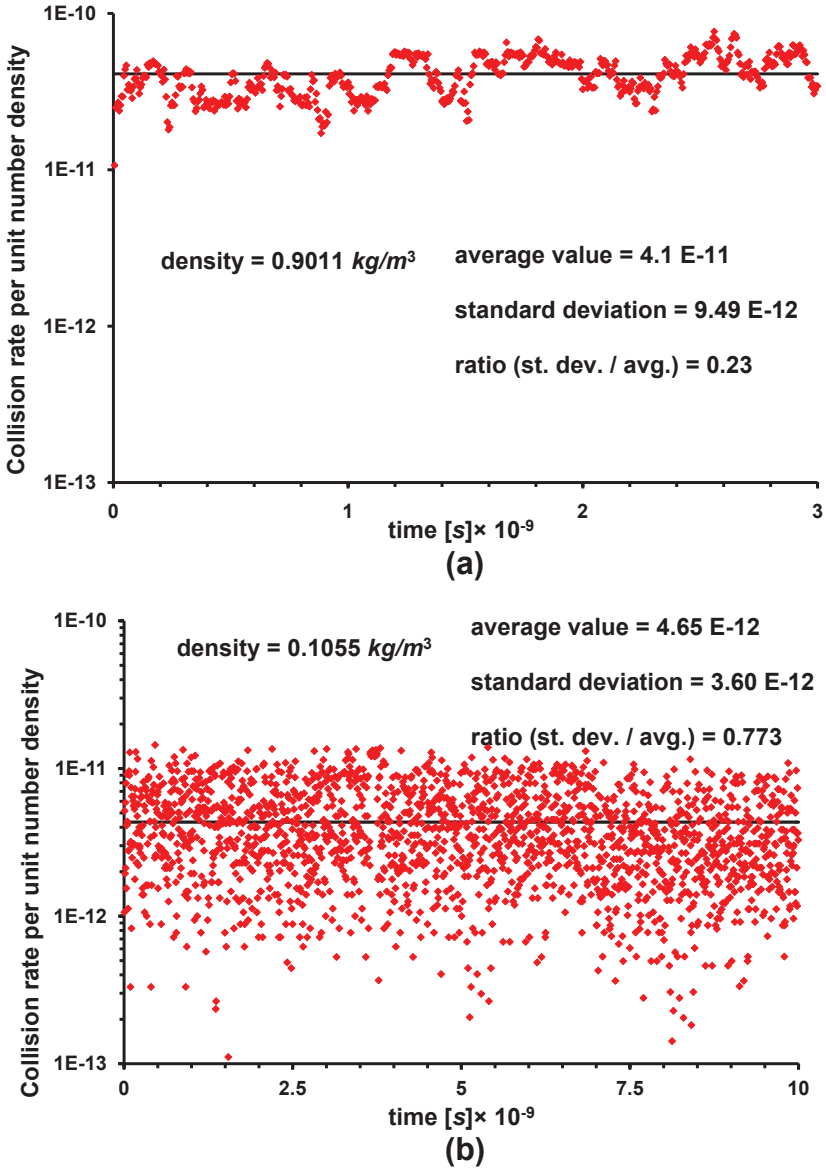

Figure 4.4: Collision rate per unit number density as a function of simulation time, for gas densities (a) 0.9011 kg/m^3 and (b) 0.1055 kg/m^3. The mean values of all samples are indicated by the straight lines.

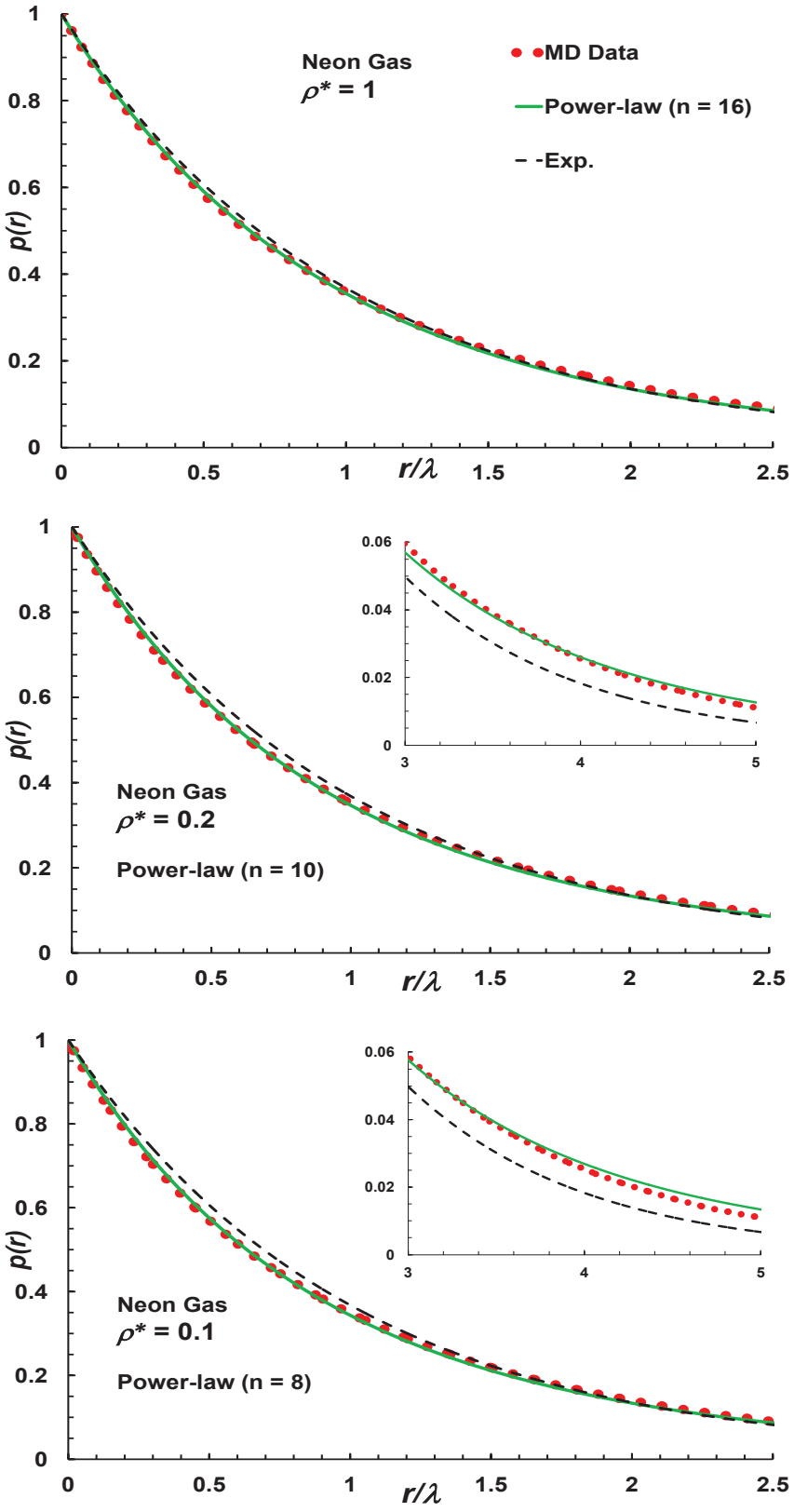

Figure 4.5: Probability molecules experience a collisionless travelling distance r/λ, in neon gas of normalised density values $\rho^* = 1, 0.2$ and 0.1. Molecular dynamics (MD) measurements are compared with the exponential and power-law distribution functions. Power-law exponent n values are 16, 10 and 8 for $\rho^* = 1, 0.2$ and 0.1, respectively.

bution agree well with the classical exponential distribution function. In this case $n = 16$ is used in the PL model to fit the MD data, and this larger value of n conveys that the system is quite close to equilibrium. As described in chapter 3, for a finite n value, the PL distribution function describes a system deviating from equilibrium. So n acts as a decisive parameter to define the extent of deviation from equilibrium. Minor deviations from the exponential distribution are noticed, and this is probably due to the consideration of multiple particle collisions. However, in low density cases ($\rho^* = 0.2$ and 0.1) the deviations between the MD measurements and the exponential distribution function are significant, with the discrepancies relatively higher at the longer free paths (see insets of this figure for $\rho^* = 0.2$ and 0.1). The PL model with exponent n values of 10 and 8 give good agreement with the MD data for $\rho^* = 0.2$ and 0.1, respectively.

MD simulations have been repeated with argon gas molecules and free path distribution function results are shown in Fig. 4.6 for normalised density test cases $\rho^* = 1$, 0.2 and 0.1, where the reference atmospheric density for argon is 1.784 kg/m^3. Similar findings are obtained, where the PL distribution function shown very good agreement with MD measurements with exponent values $n = 16$, 9 and 7 for $\rho^* = 1$, 0.2 and 0.1, respectively. For both neon and argon gas simulations, this decrease in n with increase in rarefaction illustrates that molecular transport in such systems are relatively more anomalous. Both the MD data and the power-law function predict a long tail to the distribution function, while classically there is a much faster decay of free paths. A faster decay indicates a system does not have many longer flights of molecules, and it follows the Brownian motion described by Einstein (1956). The MD data show longer Lévy-type free flights of molecules, and the long tail of the distribution function implies higher-order moments are diverging.

So far, all presented MD simulations have been carried out at temperature $T =$ 300 K. To check the sensitivity of temperature on molecular free paths or mean free path measurements, simulations at higher temperature are carried out. Figs. 4.7 and 4.8 presents free path distribution profiles at different temperatures for neon and argon gases, respectively. Two low density cases ($\rho^* = 0.2$ and 0.1) are simulated for each gas at $T = 300$ K and 600 K. Both low and high temperature test case

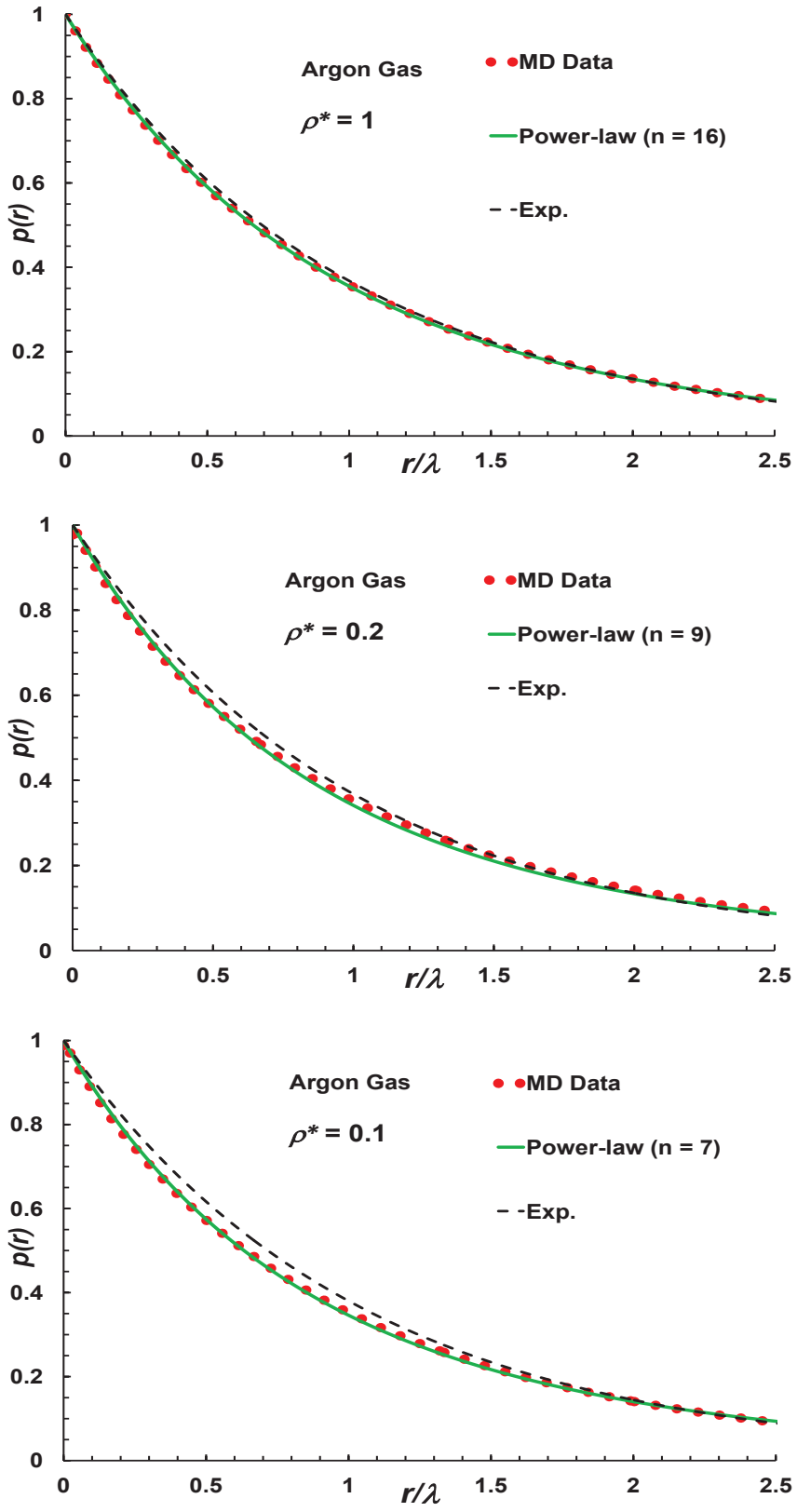

Figure 4.6: Probability molecules experience a collisionless travelling distance r/λ, in argon gas of normalised density values $\rho^* = 1, 0.2$ and 0.1. Molecular dynamics (MD) measurements are compared with the exponential and power-law distribution functions. Power-law exponent n values are 16, 10 and 8 for $\rho^* = 1, 0.2$ and 0.1, respectively.

results are found to be identical for different gases and at different densities. Both these figures convey that at a given density and for an unconfined gas, the free path distribution function is insensitive to temperature variation, i.e. the gas mean free path in unconfined spaces is only dependent on density. This MD finding is also consistent with the classical kinetic theory definition of mean free path, see Eq. (4.3). However, it is pertinent to note that this finding is limited to rarefied gases in unconfined spaces, where inter-molecular collisions are purely binary and the same needs to be verified for confined gases with moving and stationary boundaries. Such simulations are reported in Appendix B.

4.2.3 Confined mean free path profiles

The mean free path of the gas molecule ensemble approaches the theoretically predicted value only if the gas is unbounded (i.e. $r = 0 \rightarrow \infty$). If a solid bounding surface is included in the system, some molecules will hit the surface and their free flight paths will be terminated. The MFP of all the gas molecules in the system will therefore be reduced due to this boundary limiting effect. Stops (1970) derived such a geometry-dependent MFP but used an exponential free path distribution function, see Eq. (3.15), and we have derived a new effective MFP is using the PL distribution function, see Eq. (3.20) for planar surfaces.

We now make MD measurements of the MFP of neon gas molecules at 300 K when bounding planar surfaces are part of the system, and compare our simulation results with the theoretical geometry-dependent MFP models. All our simulations are of a six-sided cuboid domain, with two sides reflective bounding surfaces, and the other two pairs of sides periodic boundaries. This replicates a parallel plate configuration, with infinite width and length. The reflective surfaces are specular, i.e. the tangential velocity of molecules colliding with them is maintained, while the molecular normal velocity changes sign. Molecular reflections on the planar surfaces are recorded by setting $collisionStatus = true$ i.e. the molecular free path is terminated, as for gas inter-molecular collisions.

We investigate neon gases confined by both single and parallel planar surfaces:

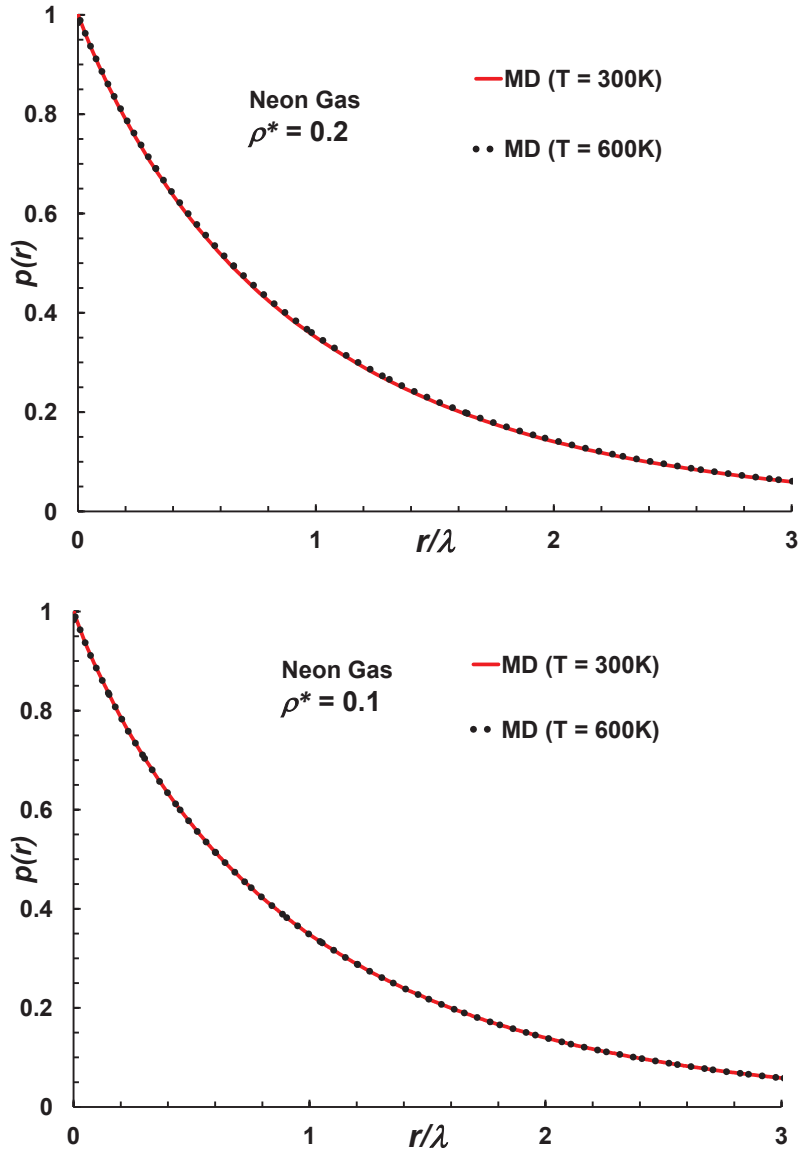

Figure 4.7: Comparison of free path distribution functions of neon gas for different temperatures $T = 300$ K and 600 K. Molecular dynamics (MD) simulations are carried out for normalised density values of $\rho^* = 0.2$ and 0.1

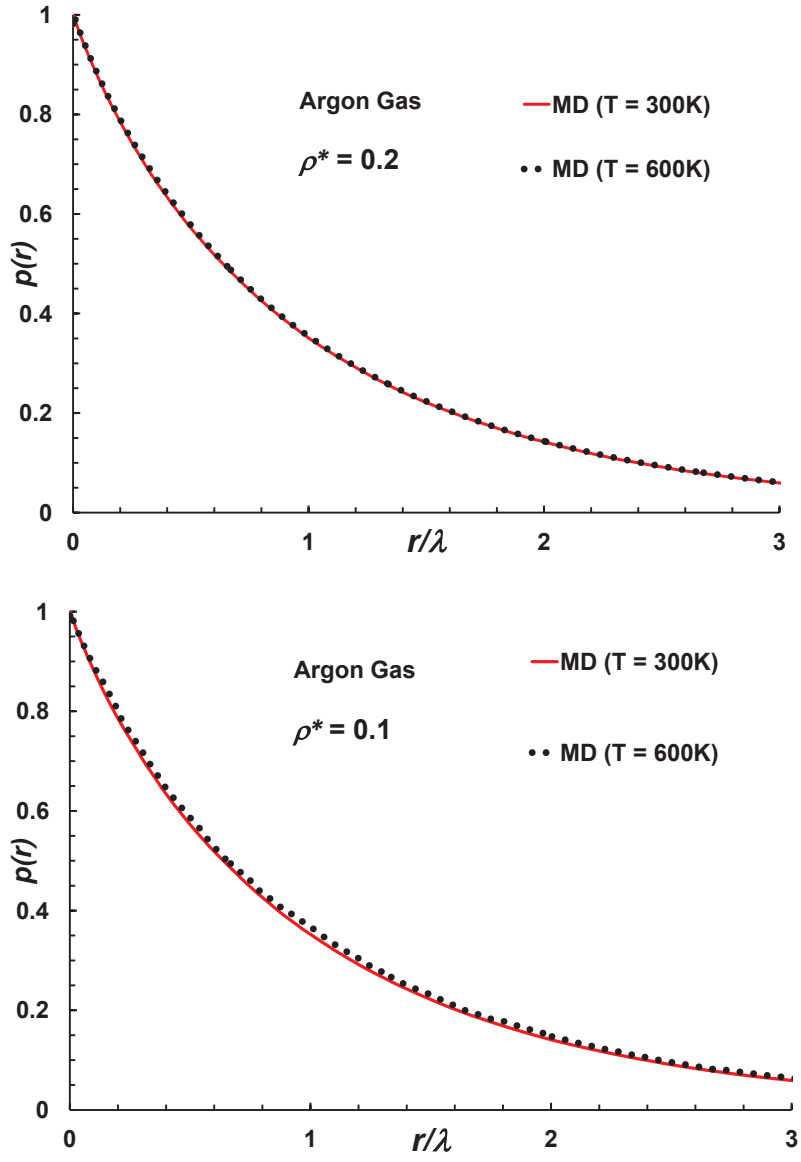

Figure 4.8: Comparison of free path distribution functions of argon gas for different temperatures $T = 300$ K and 600 K. Molecular dynamics (MD) simulations are carried out for normalised density values of $\rho^* = 0.2$ and 0.1.

a gas molecule's collision with a surface terminates that molecule's free path, so the local MFP should be shortened in the near-wall region. In the single-surface case, we use domain side lengths of λ in the directions of the periodic boundaries, and 2λ in the bounding surface directions. One of the reflective wall surfaces is then required to simulate the bulk of the gas, so all reflected molecules at this surface are set to have experienced a collisionless travel of one mean free path. The gas is represented by 102950 simulation particles, and the sampling of the local MFP, λ_{eff}, variation across the system is made over 10 nano seconds of problem time, taken after 3 nano seconds relaxation.

Fig. 4.9 shows the variation of the normalized local MFP for neon gas, $\beta = \lambda_{\text{eff}}/\lambda$, with normalized distance from the bounding surface y/λ. The MD data agrees with the PL model for the free path (with an exponent $n = 3$), although minor deviations are noticed in the bulk region. Both the MD measurements and the PL results have a sharp gradient close to the surface, while the conventional exponential model has shallower gradients and underpredicts the MFP values in the wall vicinity. It can be noticed that both the theoretical models achieve the same near-wall values and bulk values as the molecular dynamics simulation results.

For the parallel-surface case, a similar geometry is used and the Knudsen number is tuned by changing the gas density value. Results for the normalized local MFP between the two parallel surfaces are presented in Fig. 4.10. The total simulation time varied from 5 to 20 nano seconds, based on the degree of rarefaction. An exponent value $n = 3$ has been used in the PL effective MFP model predictions for all reported Knudsen numbers. At $Kn = 0.2$, the PL model is in fair agreement with the MD data in the near-wall region but deviates slightly in the bulk region. The exponential model underpredicts the MD data near-wall but shows fair agreement in the bulk. As the value of Kn increases the exponential model fails to predict the local MFP in the wall region, as well as in the bulk (so the exponential model results are not shown for comparison at $Kn = 2$). The MFP values predicted by the PL model compare very well to the MD data for both $Kn = 0.5$ and 1, although it slightly overpredicts for $Kn = 1$ in the bulk. By $Kn = 2$ the PL model shows significant deviations from the simulation data and overpredicts in the near-wall

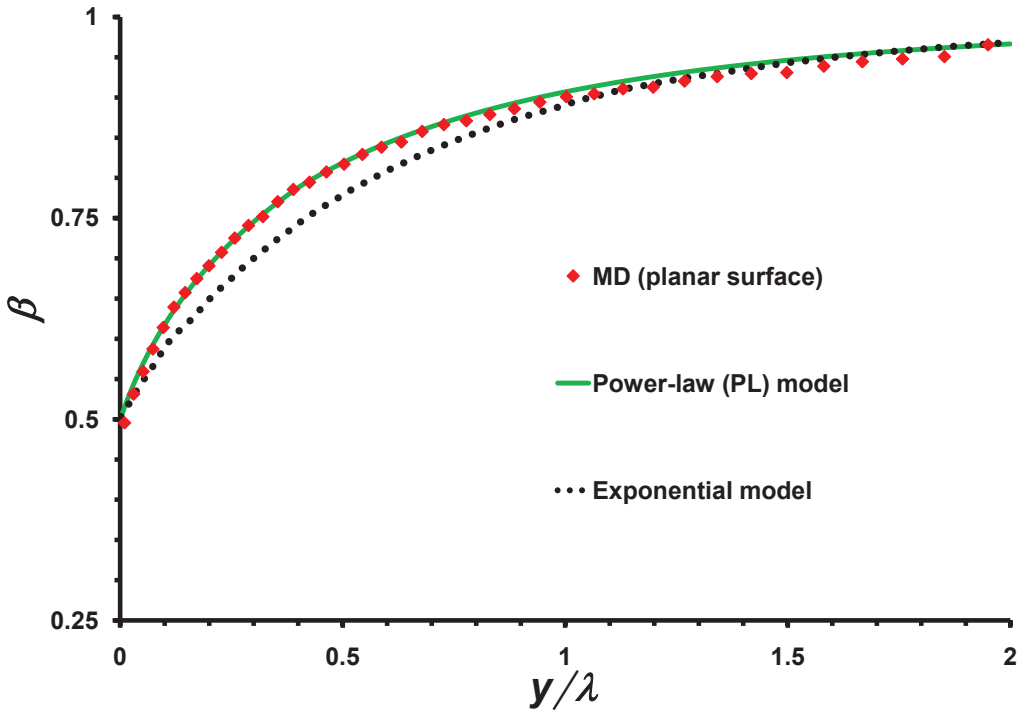

Figure 4.9: Variation of normalized mean free path β with normalized distance from the surface, for the planar single-surface case. Comparison of molecular simulation (MD) measurements for neon gas with the power-law (PL) and exponential MFP models.

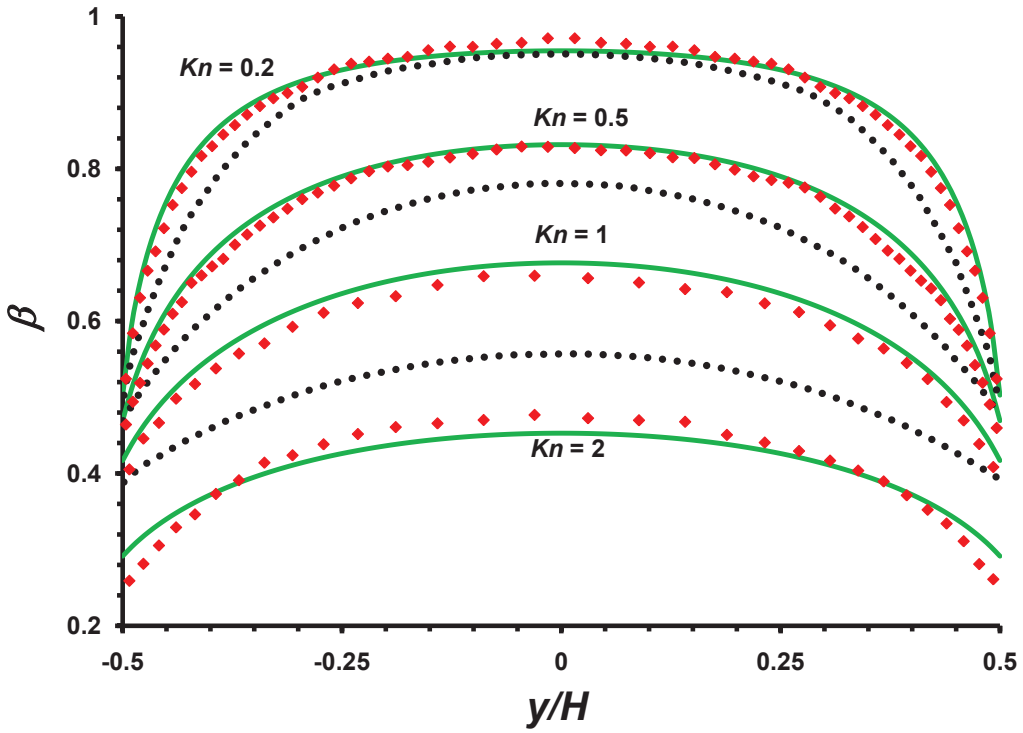

Figure 4.10: Variation of normalized mean free path, β, with normalized distance from a surface, for the planar parallel-surfaces case. Molecular dynamics simulation data of neon gas is compared with the power-law (PL) and exponential effective MFP models for Knudsen numbers ranging from the slip to the continuum-transition regimes. Symbols and lines are as in Fig. 4.9.

region, and underpredicts in the near-wall region. The MD data measurements and the PL model show relatively sharper gradients of effective MFP in the near-wall region, than the exponential model predictions.

Argon gas is also simulated at 300K in confined spaces and wall boundaries are modelled as smooth surfaces. 103790 molecules are filled in the domain for each test case and measurements are obtained for Kn = 0.27, 0.51, 1.01, 2.07, 3.08, 4.93, 7.62 and 10.90. The distance between parallel bounding planar wall surfaces is kept constant and the gas density is varied to attain these Knudsen numbers. To maintain the same number of molecules, the size of the domain is adjusted accordingly in its length and width directions. Collisionless free path distribution functions and geometry dependent MFP profiles in the whole transition regime are given in Figs. 4.11 and 4.12.

The PL model with different exponent values (n) is now fitted to the MD data

Table 4.4: Molecular Dynamics (MD) results for Argon gas at 300K, which is confined between two parallel walls. Power-law exponent (n) values, and the ratio of gas-wall to gas intermolecular collisions are listed for various Kn in the transition flow regime. n value is fine tuned such that the PL effective MFP model obtains the best possible agreement with MD measurements.

Case No.	Knudsen number (Kn)	Ratio of gas-wall to gas intermolecular collisions	Power-law exponent (n)
1	0.27	0.1555	4.3
2	0.51	0.2882	3.4
3	1.01	0.5718	3.0
4	2.07	1.2398	3.17
5	3.08	1.8350	3.4
6	4.93	2.9455	3.5
7	7.62	4.5215	3.5
8	10.90	6.3029	3.6

and the n value is fine tuned such that the PL effective MFP model obtains the best possible agreement with MD measurements. Table 4.4 lists the simulation cases in the transition flow regime, along with the ratio of gas-wall collisions to gas inter-molecular collisions. Optimum n values are reported at each Knudsen number, decreasing from 4.3 to 3.0 with increasing in Kn from 0.27 to 1.01. With further increase in Knudsen number to 10.90, the exponent rises to 3.6. The ratio of gas-wall collisions to gas inter-molecular collisions linearly increases with Kn.

Knudsen number and the PL exponent values are also included in each subplot of Figs 4.11 and 4.12. The left side plots show the free path distribution ($p(r)$) results, and the right side present effective MFP (β) profiles. The PL effective MFP model has much better agreement with the MD data at all Knudsen numbers, when compared to the exponential model results. The PL model exhibits excellent agreement with our numerical experiments up to Knudsen numbers around 5, by tuning the n value between 3 and 3.5. In the case of the probability distribution plots, the PL distribution function relatively underpredicts the MD free path measurements at shorter free paths and overpredicts at longer free paths. This is consistently noticed in the comparisons at all Knudsen numbers. However, the gas mean free path profiles show very good comparisons, as they are the average of all molecular free paths. The exponential distribution function underpredicts both MD data and the

PL model. The deviations are significant and they increase with Knudsen number.

4.3 Summary

A molecular dynamics simulation tool has been used to assess the fundamental gas properties: inter-molecular collision rates, molecular free path probability distribution, and mean free path values in unconfined and confined planar spaces. We simulated neon and argon gas molecules using the simple Lennard-Jones interaction potential function. Theoretical mean free path values are deduced for different values of gas density by simulating an unconfined gas domain in space with periodic boundary conditions. As the rarefaction increases, multiple particle collisions become negligible in comparison with binary collisions, and the dilute gas assumption is held to be valid under these conditions. These simplified assumptions employed in kinetic theory may, however, introduce noticeable errors at typical atmospheric conditions. It was shown that the values of the theoretical unconfined mean free paths were recovered for rarefied neon and argon gases, with the largest discrepancy of 2.36%.

Inter-molecular collision rate measurements show fewer fluctuations at standard density conditions, while the standard deviation is significantly higher for low-density cases, which illustrates the non-equilibrium nature of the rarefied gas. Correspondingly, molecular free path measurements have a long tail, and the classical exponential distribution function is only accurate under equilibrium conditions. The MD data follow a Lévy flights behaviour, and compare well with the PL distribution function of Chapter 3. The exponent value n in the PL distribution function is largest for dense systems, and it decreases with increasing in rarefaction. This conveys that the larger n values describe systems closer to equilibrium.

Molecular free paths are terminated when gas molecules hit a bounding wall surface, so wall-dependent MFP measurements have been carried out for planar single- and parallel-wall cases. MD data has been compared with the exponential and power-law based effective MFP solutions. The exponential solution underpredicts the measurements in the near-wall region for both single- and parallel-wall cases,

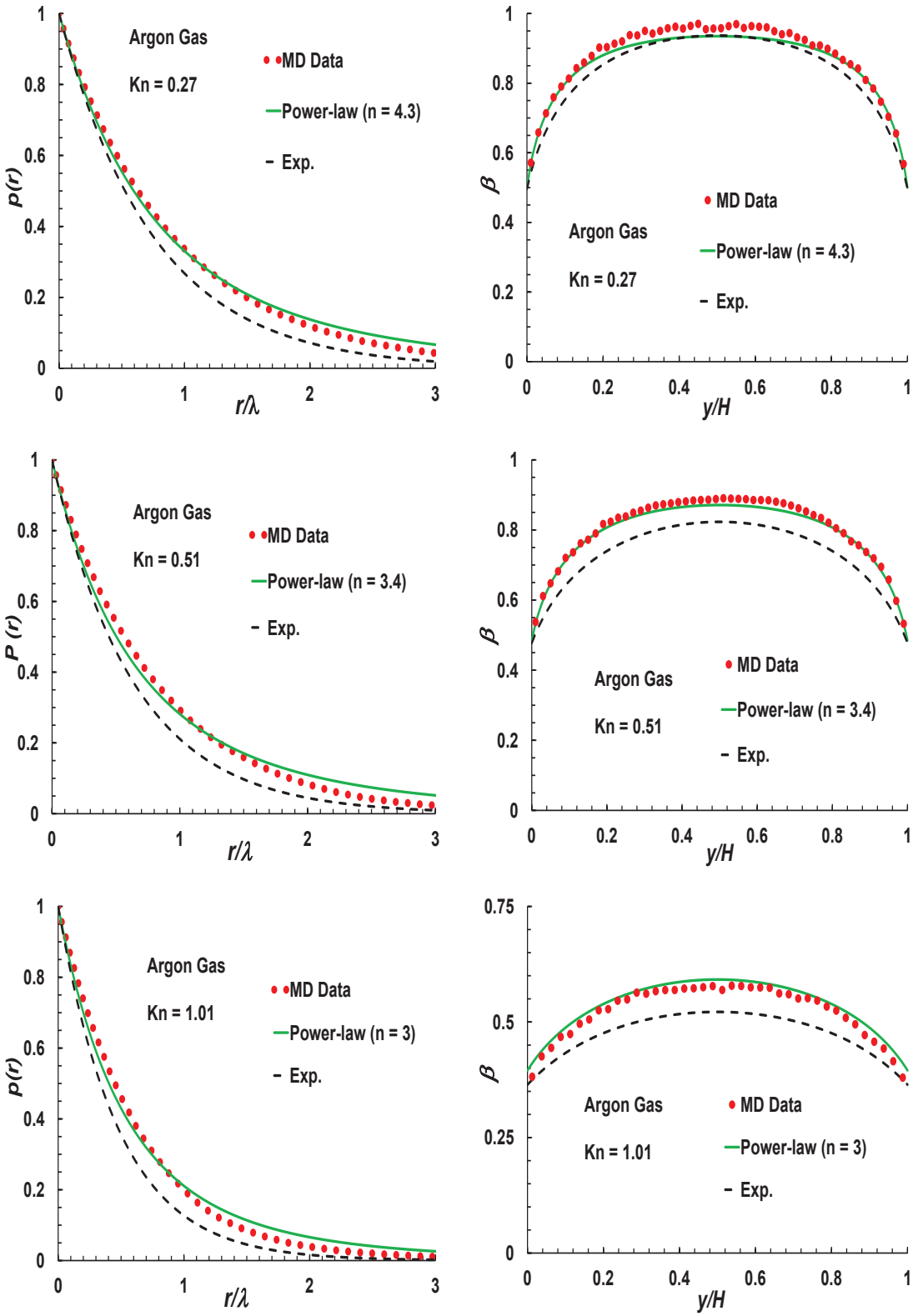

Figure 4.11: Molecular dynamics (MD) simulations results for argon free path probability distribution functions (left) and mean free path (MFP) profiles (right), for the early transition flow regime test cases $Kn = 0.27$, 0.51 and 1.01. Parallel walls are located at $y/H = 0$ and 1.

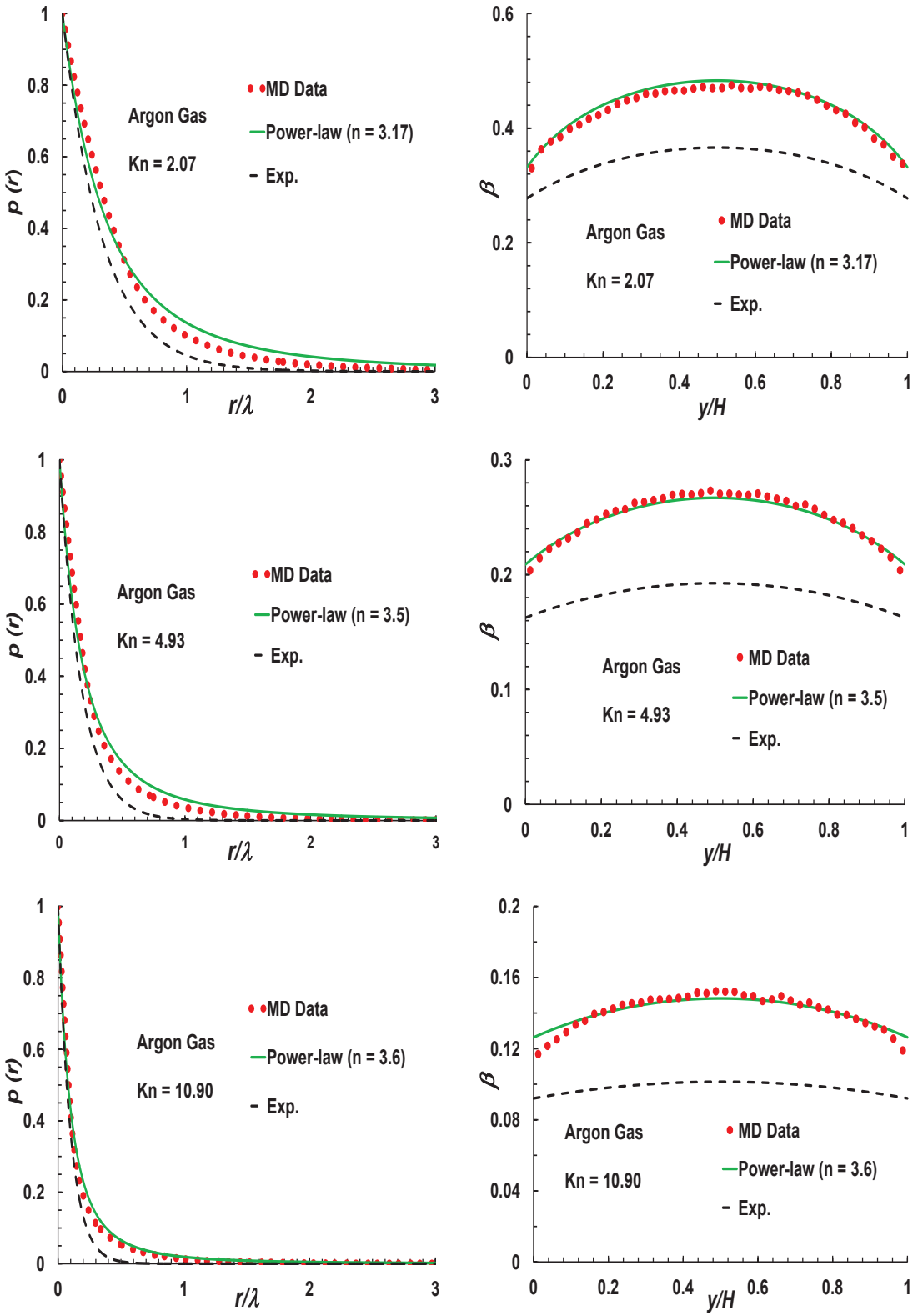

Figure 4.12: Molecular dynamics (MD) simulations results for argon free path probability distribution functions (left) and mean free path (MFP) profiles (right), for the late transition flow regime test cases $Kn = 2.07$, 4.93 and 10.90. Parallel walls are located at $y/H = 0$ and 1.

and shows shallower gradients close to the wall. Both the MD data and the power-law model predict sharper gradients in the near-wall region, with the power-law model having good agreement with the measurements up to $Kn \sim 2$. Deviations start to increase with further increase in Kn due to the overlap of Knudsen layers from both wall surfaces. The present MD results support the argument that anomalous behaviour of rarefied gases is better described with Lévy/power-law type of distribution functions, as compared to the classical exponential function.

Wall-scaling of the fluid constitutive relationships (Lockerby et al., 2004; Lockerby and Reese, 2008) has been shown to usefully extend the applicability of the Navier-Stokes-Fourier (N-S-F) equations into transition regime flows. However, these models are purely empirical, employing some tuning parameters, and may not offer deeper physical understanding of the complex dynamics of rarefied gases. We may appropriately derive modified constitutive relationships based on the Lévy/power-law types of free path distribution functions, as the gas transport properties are related to MFP through kinetic theory. MD data of MFP profiles will also be useful when applying boundary conditions, as velocity-slip and temperature-jump are dependent on a near-wall value of the MFP. Thus the results obtained in this chapter will aid in modelling micro gas flows using the Navier-Stokes-Fourier equations. In the next chapter isothermal and thermal, and planar and non-planar, test cases are presented using our power-law based effective MFP scaling methodology, with classical and higher-order slip and jump boundary conditions.

Chapter 5

Applications of the power-law model

When an idea exclusively occupies the mind,
it is transformed into an actual physical state
- Swami Vivekananda

In this chapter, applications of the power-law (PL) based wall mean free path (MFP) scaling methodology are investigated. As gas transport properties can be related to the mean free path through kinetic theory, the Navier-Stokes-Fourier (N-S-F) constitutive relations are then modified in order to better capture the flow behaviour in the Knudsen layers close to surfaces. The central idea is to incorporate the influence of the effective mean free path in the viscosity and thermal conductivity, and also the conventional velocity-slip and temperature-jump boundary conditions at the wall boundaries.

When constitutive relations and boundary conditions are scaled, the term "N-S-F solution" becomes inaccurate, as the N-S-F equations refer only to the continuity, momentum and energy equations linked by linear constitutive relationships. As the intention of constitutive scaling is not to alter a fluids properties, but merely to represent its behaviour when rarefied, the term *modified Navier-Stokes-Fourier equations* or the *power-law (PL) model* will continue to be used in this thesis for the sake of clarity when discussing constitutive scaling implemented in an N-S-F type

framework.

We validate our PL model against solutions of the Boltzmann equation, MD and DSMC simulation data, and published experimental data. We also compare the PL model results with other hydrodynamic models, such as the classical slip model, the R13 and R26 equations, and exponential wall MFP scaling models. Results for isothermal and thermal, and planar and non-planar test cases in rarefied gas flows are reported. The merits and limitations of the hypothesised PL model are outlined for both isothermal and thermal gas flows in planar and non-planar geometries.

5.1 Isothermal gas flows

5.1.1 Planar Poiseuille flow

Poiseuille flow is the name traditionally given to the flow of a viscous fluid in a channel or pipe driven by a constant pressure gradient (or acceleration), where pressure decreases in the direction of the flow. To test the merits of our PL-based effective MFP scaling, we first consider isothermal pressure-driven gas flow along a planar-wall channel with walls a distance H apart. In the present study, the coordinates are chosen such that the walls are parallel to the x-direction and y is the direction perpendicular to the plates. The walls are stationary and the temperatures of both the walls are equal to the temperature of the fluid. The channel height H is assumed to be much smaller than the channel width, so that the fluid essentially sees two infinite parallel plates separated by H, at coordinates $y = \pm H/2$. The flow is assumed to be fully hydrodynamically developed and two-dimensional, isothermal, laminar and steady, with a low Reynolds number (Re) so that inertial effects may be neglected.

With these assumptions, the governing equation is:

$$0 = -\frac{\partial P}{\partial x} - \frac{\partial \tau}{\partial y}, \tag{5.1}$$

where x is the streamwise coordinate, y the wall-normal coordinate, P the pressure and τ the stress, which is given as:

$$\tau = -\mu \left[\nabla \mathbf{U} + (\nabla \mathbf{U})^{tr}\right] + \left(\frac{2}{3}\mu - \kappa\right)(\nabla.\mathbf{U})I, \tag{5.2}$$

where μ is the fluid dynamic viscosity, κ the bulk viscosity, I the identity tensor and tr the transpose operator.

In Eq. (5.2) we can neglect volume dilation effects for rarefied gases (Bird et al., 1960). From the kinetic theory of gases, the fluid viscosity can be explained in terms of the collisions between gas molecules, and of the free paths which the molecules describe between collisions. The collision time, or equivalently the free flight path between two successive collisions of a gas molecule, is closely related to the momentum exchange. The unconfined MFP is therefore related to the shear viscosity (Cercignani, 1988):

$$\mu = \rho \frac{\lambda}{\sqrt{\pi/2\Re T}}, \tag{5.3}$$

where $\Re$ is the specific gas constant and T the gas temperature.

Equation (5.3) is assumed to be valid only for flows that are in quasi-equilibrium. As discussed in Chapters 3 and 4, within the KL the flight paths of gas molecules are affected by the presence of a solid wall. Using Eqs. (3.20) and (5.3) we can therefore posit a non-linear stress/strain-rate relation in the KL:

$$\tau = -\underbrace{\mu\beta_{\,\mathrm{PL}}}_{\mu_{\mathrm{eff(PL)}}} \frac{\partial U_x}{\partial y}, \tag{5.4}$$

where U_x is the fluid velocity in the axial direction and $\beta_{\,\mathrm{PL}}$ the PL based normalised effective mean free path (MFP).

Using Eq. (5.4) in Eq. (5.1) results in the following governing equation:

$$\mu \frac{\partial}{\partial y}\left(\beta_{\mathrm{PL}} \frac{\partial U_x}{\partial y}\right) = \frac{\partial P}{\partial x}. \tag{5.5}$$

This needs to be solved in conjunction with an appropriate slip boundary condition to capture the non-equilibrium phenomena in the slip and transition flow regimes.

The first-order slip boundary condition proposed by Maxwell (1879) fails to

predict the Knudsen-minimum in the mass flow rate (Dongari et al., 2007), and researchers have consequently proposed higher-order slip models for a wide-range of Knudsen numbers. A review of a number of these higher-order slip models can be found in Reese and Zhang (2009). Deissler (1964) derived a second-order slip boundary condition based on the concept of MFP for momentum and energy transfer, which can be expressed in its generalized form as:

$$U_{slip} = -C_1 \lambda \left(\frac{\partial U_x}{\partial y} \right)_w - C_2 \lambda^2 \left(\frac{\partial^2 U_x}{\partial y^2} \right)_w , \tag{5.6}$$

where U_{slip} is the slip velocity at the fluid-surface interface, and w indicates a quantity evaluated at the surface. While there is no general consensus on the slip coefficients C_1 and C_2, C_1 is set to ~ 1 by many authors and C_2 has a wide range from -0.5 to $5\pi/12$ (Reese and Zhang, 2009). Cercignani (1963) proposed C_2 to be 0.9756 from kinetic theory considerations, and Hadjiconstantinou (2003) corrected C_2 to 0.31.

It is important to note that Maxwell (1879) and Deissler (1964) derived first- and second-order slip boundary conditions assuming that the MFP is constant in the wall-adjacent gas layer. Guo et al. (2007) proposed the following heuristic slip boundary condition to take into account the KL correction:

$$U_{slip} = -C_1 \left(\lambda_{\text{eff}} \frac{\partial U_x}{\partial y} \right)_w - C_2 \left[\lambda_{\text{eff}} \frac{\partial}{\partial y} \left(\lambda_{\text{eff}} \frac{\partial U_x}{\partial y} \right) \right]_w . \tag{5.7}$$

This simply reduces to the conventional second-order slip boundary condition (5.6) if there is no KL, i.e. if $\lambda_{\text{eff}} = const.$ In the present analysis, we implement this second-order slip boundary condition, and use $\lambda_{\text{eff(PL)}}$ given by Eq. (3.20). Values of C_1 and C_2 are chosen as 1 and 0.31 respectively for the results reported below.

Solution procedure

We require results for the flow velocity profile across the channel, and some integral flow parameters, through solution of the governing Eq. (5.5) and slip boundary

condition (5.7), along with the ideal gas law

$$P = \rho \Re T, \tag{5.8}$$

and the Knudsen number

$$Kn = \frac{\lambda}{H}. \tag{5.9}$$

The wall-normal coordinate, y, is normalized by H, and the axial velocity, U_x, by the free-molecular velocity $U_0 = -2H(\partial P/\partial x)/(\rho\sqrt{2\Re T})$ (Ohwada et al., 1989). Using Eqs. (5.3) and (3.20), Eq. (5.5) in normalised form (indicated by $*$) is

$$\frac{\partial}{\partial y^*}\left(\beta_{\mathrm{PL}}\frac{\partial U^*}{\partial y^*}\right) = -\frac{\sqrt{\pi}}{2Kn}, \tag{5.10}$$

and Eq. (5.7) in normalised form is

$$\begin{aligned}(U^*)_{slip} = \; & - \; C_1 Kn \left(\beta_{\mathrm{PL}}\frac{\partial U^*}{\partial y^*}\right)_w \\ & - \; C_2 Kn^2 \left[\beta_{\mathrm{PL}}\frac{\partial}{\partial y^*}\left(\beta_{\mathrm{PL}}\frac{\partial U^*}{\partial y^*}\right)\right]_w .\end{aligned} \tag{5.11}$$

Equation (5.10) is numerically solved for the normalised axial velocity profiles U^* by applying the slip boundary condition (5.11) at the upper wall ($y^* = 0.5$) and a symmetry condition at the centre of the channel ($y^* = 0$).

The solution of the conventional N-S-F equations, with constant viscosity and first-order velocity slip, and using the unconfined MFP, is:

$$U^* = \frac{\sqrt{\pi}}{16Kn}\left[1 - 4(y^*)^2 + 4C_1 Kn\right], \tag{5.12}$$

while the NS solution with second-order velocity slip using the unconfined MFP, is:

$$U^* = \frac{\sqrt{\pi}}{16Kn}\left[1 - 4(y^*)^2 + 4C_1 Kn + 8C_2 Kn^2\right]. \tag{5.13}$$

The normalised mass flow rate G is in all cases

$$G = \frac{2\int_0^{H/2} \rho U_x dy}{\rho U_o H} = \int_0^{0.5} U^* dy^*. \tag{5.14}$$

Another integral parameter of interest to the engineering community is the skin friction coefficient, C_f

$$C_f = \frac{\tau_w}{(1/2)\rho(U_{xb})^2}, \tag{5.15}$$

in fully-developed flow. This is valid for all Knudsen numbers, and τ_w is the wall shear stress and U_{xb} the bulk velocity.

From Eq. (5.1), the pressure gradient must balance the wall shear stress leading to

$$\frac{2\tau_w}{H} = -\frac{dP}{dx}. \tag{5.16}$$

Combining Eqs. (5.15) and (5.16) leads to

$$C_f Re = \frac{-1}{2U_{xb}} \mu \frac{dP}{dx}, \tag{5.17}$$

with

$$Re = \frac{2\rho U_{xb} H}{\mu}, \tag{5.18}$$

where μ is given by Eq. (5.3). Eq. (5.10) with slip boundary condition (5.11) is used to obtain results for $C_f Re$ based on the N-S-F equations with $\lambda_{\text{eff(PL)}}$.

Using the conventional unconfined MFP in the N-S-F equation with a first-order boundary condition (by keeping $C_2 = 0$ in 5.6) gives

$$C_f Re = \frac{24}{(1 + 6C_1 Kn)}, \tag{5.19}$$

and with the second-order boundary condition (5.6) gives

$$C_f Re = \frac{24}{(1 + 6C_1 Kn + 12C_2 Kn^2)}. \tag{5.20}$$

Results

In what follows, the *PL model* is the modified governing equation (5.10), with the use of effective MFP (3.20) and the modified second-order slip boundary condition (5.11). The cross-sectional velocity profiles of pressure-driven Poiseuille flow over a range of Knudsen numbers are presented in Fig. 5.1. Our PL model is compared with the solution of the Boltzmann equation (Ohwada et al., 1989) and three hydrodynamic models: conventional first- (Eq. 5.12) and second-order (Eq. 5.13) slip models, and the R26 equations (Gu and Emerson, 2009). At $Kn = 0.113$, which is just beyond the slip-flow regime, the four hydrodynamic models predict similar values of slip velocity at the wall and all are close to the solution obtained from the Boltzmann equation. The conventional NS equations with both first- and second-order slip boundary conditions significantly underpredict the velocity in the bulk region. Our PL model and the R26 equations are in fair agreement with the Boltzmann solution, although the PL model very slightly underpredicts, and the R26 equations overpredict, the maximum velocity. At $Kn = 0.226$, the NS equations with slip boundary conditions overpredict the slip velocity and underpredict the maximum velocity at the centre. The second-order slip solution lies above the first-order slip results. Both our PL model and the R26 equations compare well with the solution obtained from the Boltzmann equation, however, the R26 equations show minor deviations in the wall-slip velocity.

At higher Kn, the flow enters the transition regime and Knudsen layers from each of the parallel walls start to overlap each other. Hence, the first-order slip model is solved only up to $Kn = 0.226$, and the second-order slip model up to $Kn = 1.128$. At $Kn = 0.451$ and $Kn = 0.677$, the PL model and R26 equations compare reasonably well with the Boltzmann solutions, although the R26 equations overpredict the slip velocity. At $Kn = 1.128$, deviations from the Boltzmann predictions are relatively less for our PL model than for the R26 equations.

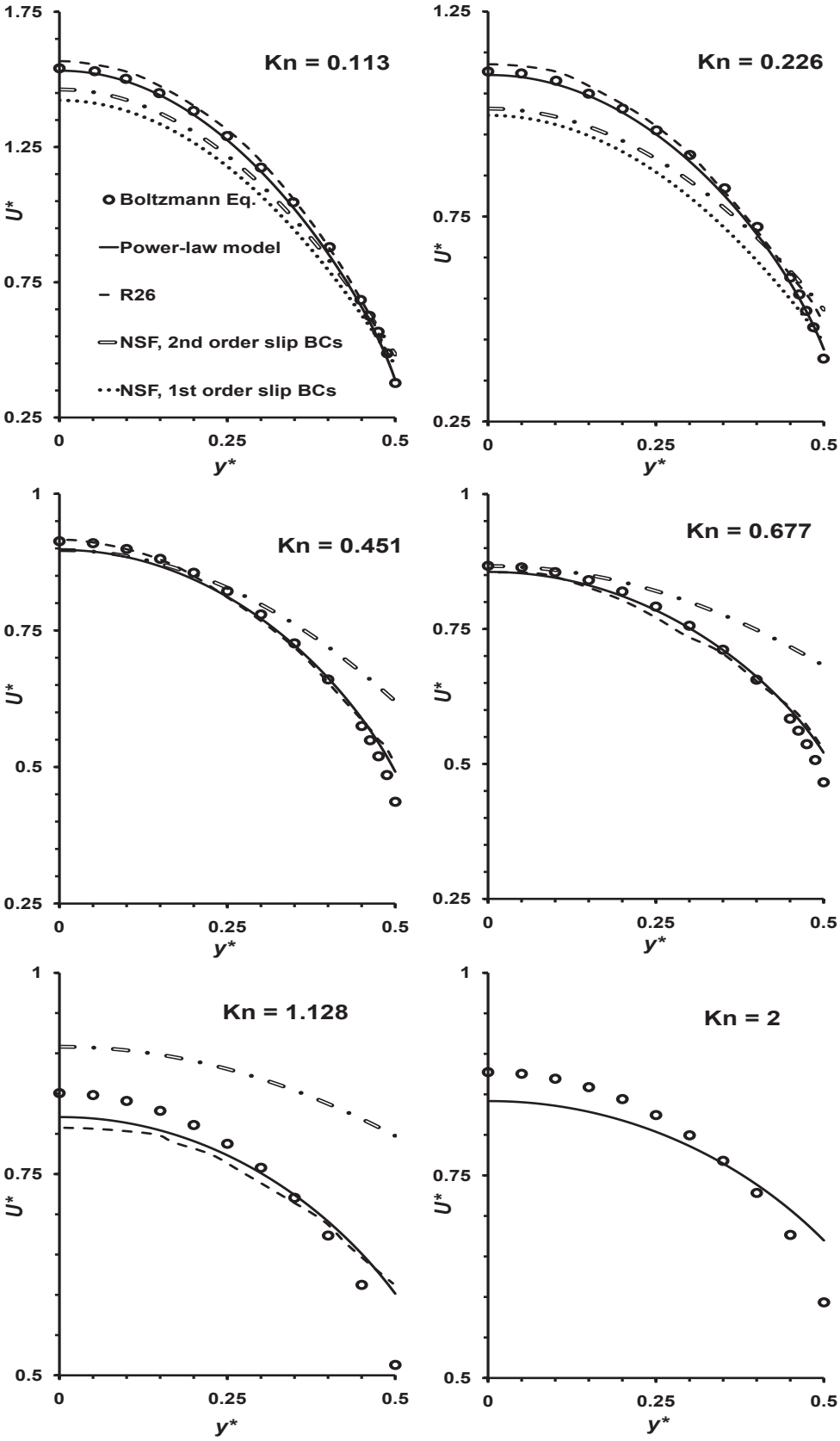

Figure 5.1: Normalised half cross-channel velocity profiles for various Knudsen numbers. Comparison of our power-law (PL) model results with the solution of the Boltzmann equation (Ohwada et al., 1989), R26 moment equations (Gu and Emerson, 2009), and conventional N-S-F equations with first- and second-order slip.

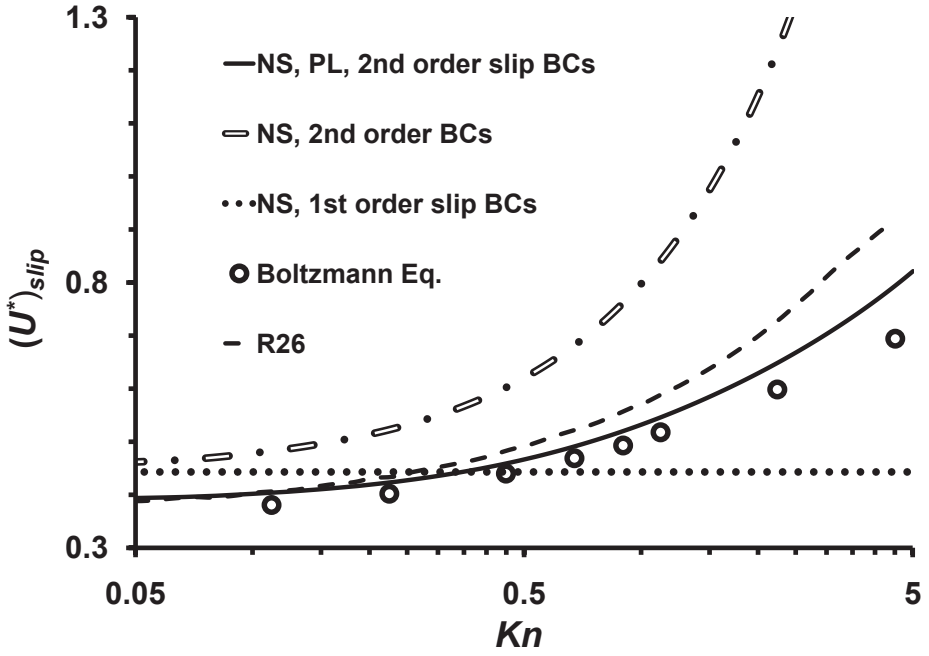

Figure 5.2: Variation of normalised slip velocity with Knudsen number, comparison of power-law (PL) model with the solution of the Boltzmann equation (Ohwada et al., 1989), R26 moment equations (Gu and Emerson, 2009), and the conventional N-S-F equations with first- and second-order slip.

Predictions of the normalised slip velocity $(U^*)_{slip}$ are presented as a function of Kn in Fig. 5.2, and compared to Boltzmann simulation data (Ohwada et al., 1989). First-order slip is a constant, and higher than the Boltzmann result for $Kn < 1$ and lower for $Kn > 1$. The second-order NS slip is too high, particularly at large Knudsen numbers. Our PL model and the R26 equations agree well with the Boltzmann solution up to $Kn \simeq 0.5$. Both models overpredict the wall-slip velocity for $Kn > 0.5$, though the deviations are relatively small with the PL model.

It is evident from Fig. 5.1 that in the transition regime, non-equilibrium effects are no longer limited to the wall-adjacent layer, but prevail in the bulk flow due to the overlap of Knudsen layers. Hence, simply using a higher-order slip model with modified slip coefficients may result in good wall slip-velocity results but will not improve the overall predictive capabilities of the N-S-F equations into the transition regime. The accurate prediction of integral flow parameters in micro/nano-conduits is important in engineering MEMS devices. To obtain the integral flow parameters correctly, it is essential that field variables such as MFP and cross-sectional velocities

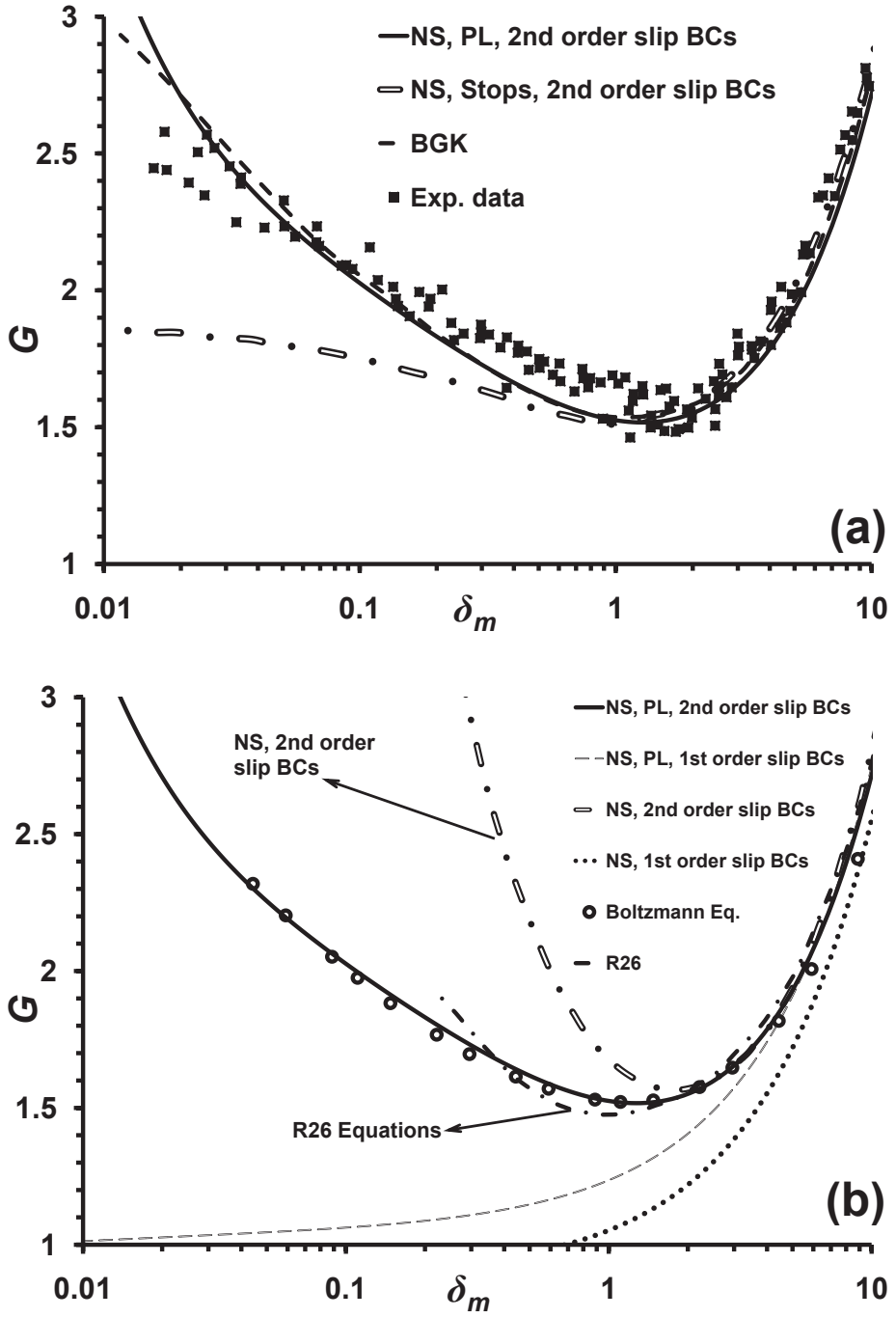

Figure 5.3: Normalised mass flow rate (G) variation with inverse Knudsen number (δ_m). Comparison of power-law (PL) model results with: (a) experimental data (Ewart et al., 2007) and BGK simulation results (Loyalka, 1975); (b) the solution of the Boltzmann equation (- -) (Ohwada et al., 1989), R26 moment equations (-·-) (Gu and Emerson, 2009) and the conventional N-S-F equations with first- and second-order slip.

are correct. However, it is important to note that the accurate prediction of integral flow parameters does not, in turn, guarantee that the local flow field is predicted accurately.

Figure 5.3 shows the variation of normalised flow rate G, with inverse Knudsen number, $\delta_m = \sqrt{\pi}/(2Kn)$. In Fig. 5.3a, our PL model results are compared with experimental data (Ewart et al., 2007), BGK simulation data (Loyalka, 1975) and the NS equations with Stops' MFP model and the second-order slip condition (5.11). In the slip flow regime, both the PL model and Stops' model agree reasonably well with the experimental data and the BGK simulation results. However, around $\delta_m \sim 1$, Stops' MFP based slip model starts to significantly underpredict the flow rate, whilst our PL model follows the BGK simulation data reasonably well until Kn reaches about 10.

Flow rate results of our PL model with $n = 3$ are shown in Fig. 5.3b to compare with the exact Boltzmann solution (Ohwada, 1989), DSMC data (Hadjiconstantinou, 2006), R26 results (Gu and Emerson, 2009), N-S-F equations with first- and second-order slip, and our PL model with first-order slip. Here the first-order slip for the PL model results are obtained simply by setting $C_2 = 0$. For $Kn > 0.1$, which is just beyond the slip flow regime, the NS equations with first-order slip underpredict the flow rate, although the other hydrodynamic models are in good agreement with the Boltzmann and DSMC data up to $Kn \sim 0.2$. The NS results with second-order slip are good up to $Kn \sim 0.5$, but significantly overpredict beyond that. The R26 equations show good agreement until $Kn \sim 2$. But our PL model with second-order slip follows the Boltzmann results up to $Kn \sim 10$. Both PL and N-S-F models with first-order slip fail to predict the Knudsen minimum. The other three hydrodynamic models show a Knudsen minimum; however, the NS equations with second-order slip predict the minimum at a value of Kn smaller than that predicted by the Boltzmann equation.

Figure 5.4 shows the variation of $C_f Re$ with Knudsen number, and our PL model is again compared with the exact solution of the Boltzmann equation (Ohwada et al., 1989), DSMC data (Hadjiconstantinou, 2006), and the N-S-F equations with first- and second-order slip. In the slip flow regime, the four hydrodynamic models are in good agreement with the Boltzmann equation, and also predict a constant value in the continuum regime. The NS equations with first-order slip overpredict the $C_f Re$ for $Kn > 0.1$, and the second-order slip underpredicts for $Kn > 0.5$,

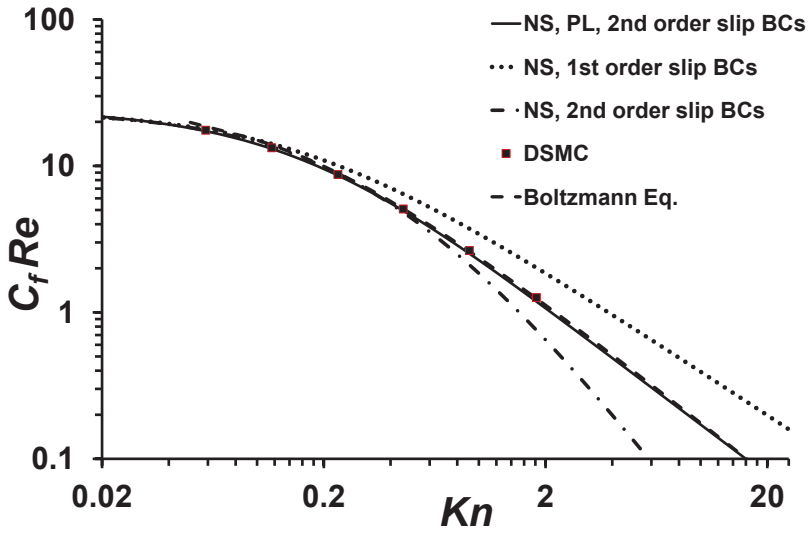

Figure 5.4: Variation of the product of friction factor (C_f) and Reynolds number (Re) with Knudsen number (Kn). Comparison of power-law (PL) model results with DSMC data (Hadjiconstantinou, 2006), the solution of the Boltzmann equation (Ohwada et al., 1989), and conventional N-S-F predictions with first- and second-order slip.

whilst the PL model is accurate up to $Kn \sim 10$ and shows only minor deviations with further increase in Knudsen number.

5.1.2 Planar Couette flow

To further test our PL based wall scaling approach for moving planar surfaces, here, we investigate rarefied Couette gas flows between parallel walls. Couette flow is driven by shear-forces arising in viscous fluids, for example, the relative motion of two parallel plates produces a velocity profile in a fluid between them. Shear-driven flows in other configurations, such as between concentric rotating cylinders, are also commonly referred to as Couette flows. Planar Couette flow, like Poiseuille flow, can be considered in simple 1D form, making the case ideal for validation analyses.

The distance between the two parallel plates is H, and they have been set at $y = \pm H/2$. The Knudsen number is given by $Kn = \lambda/H$. The upper and lower plates move with a constant velocity $U_w = \pm 50 ms^{-1}$, in opposite directions, and the external acceleration $a_x = a_y = 0$. Energy transfer considerations are not included

at this stage, but the plate temperatures are considered to be equal and constant to allow the properties of the gas flow to be determined.

Solution procedure

Using Eqs. (5.10) and (5.11), the governing equation and the first-order slip boundary condition in their normalised forms for this Couette flow can be given as:

$$\frac{\partial}{\partial y^*}\left(\beta_{\mathrm{PL}}\frac{\partial U^*}{\partial y^*}\right)=0, \tag{5.21}$$

and

$$(U^*)_{slip}=U_w-C_1Kn\left(\beta_{\mathrm{PL}}\frac{\partial U^*}{\partial y^*}\right)_w. \tag{5.22}$$

Equation (5.21) is numerically solved for the normalised axial velocity profiles U^* by applying the slip boundary condition (5.22) at the upper and lower walls (at $y^*=\pm 0.5$). Classical slip model results can also obtained using these two equations with $\beta_{\mathrm{PL}}=const.=1$. Second-order slip boundary condition has not been implemented, as the higher-order term reduces to zero due to Eq. (5.21)

We also carried out molecular dynamics (MD) simulations in order to assess the capability and limitations of the PL model, particularly in the transition regime. Lennard-Jones argon molecules are simulated, and initially the molecules are spatially distributed in the domain of interest with a random Gaussian velocity distribution corresponding to an initially prescribed gas temperature. They are then allowed to relax through collisions until reaching a steady state before we take measurements. To achieve smooth variation of fluid flow properties, molecular velocity samples are then taken in every time step (0.001 τ, where $\tau=\sqrt{md^2/\epsilon}$, with m being molar mass, d the diameter of the gas molecules, and ϵ being related to the interaction strength of the molecules) for a total run time of at least 30000 τ (in the extreme rarefied flow cases up to 100000 τ). We use 83500 molecules in each simulation, and assume diffuse gas molecule/wall interactions.

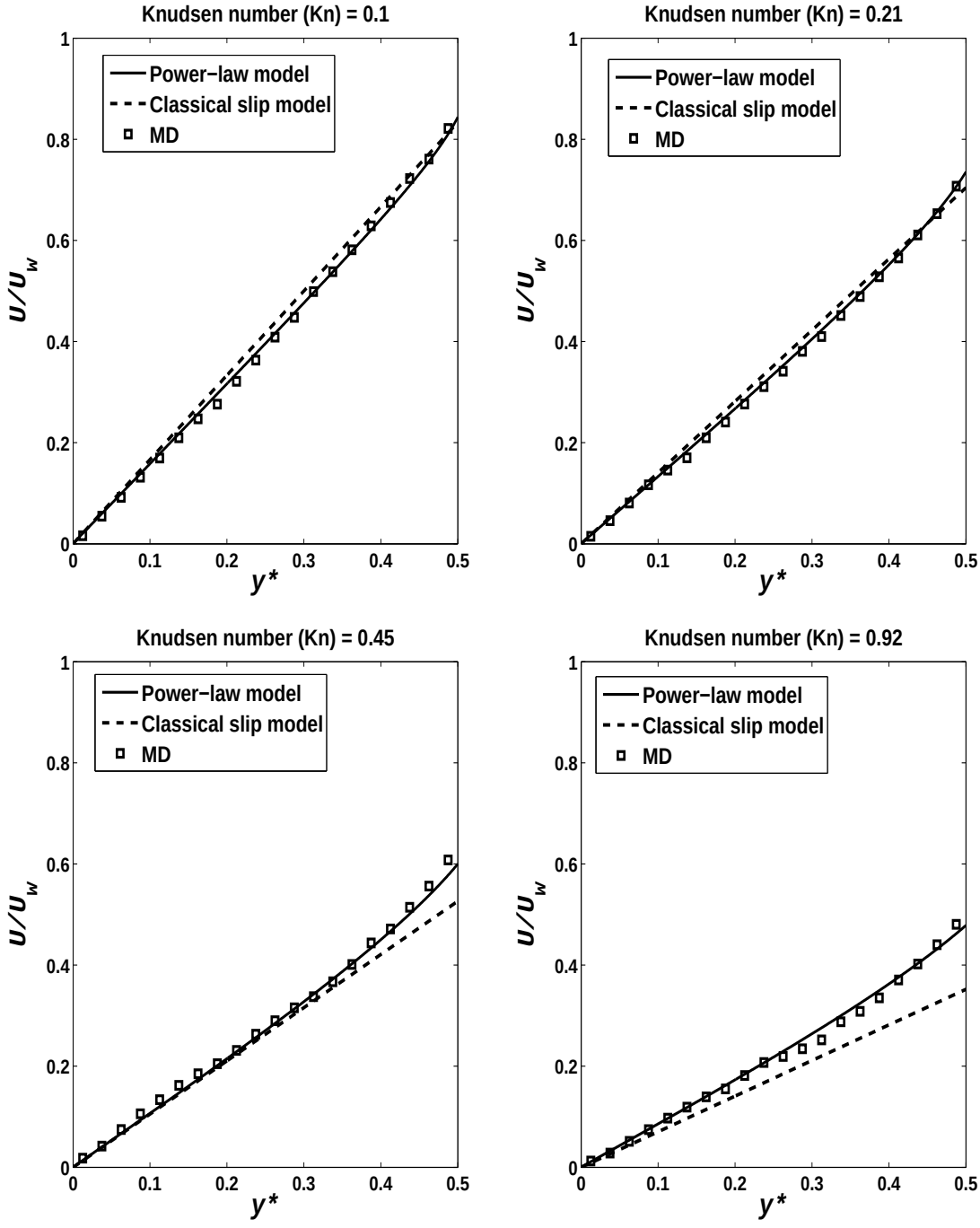

Figure 5.5: Normalised half channel velocity profiles for planar Couette flow at various Knudsen numbers. Validation of our power-law (PL) model against molecular simulation (MD) data and comparison with the classical slip model results.

Results

Fig. 5.5 shows the computed velocity profiles for planar Couette flow. Results are presented for Knudsen numbers $Kn = 0.1$, 0.21, 0.45 and 0.92, and the PL model is validated against our MD simulations, and also compared with the classical slip model results. The classical slip model results predict linear velocity profiles for all Kn cases and show significant deviations from the MD data for $Kn \geq 0.21$. The PL model results show good agreement with the MD data for all Kn cases and accurately predict the non-linear effects in near-wall regions.

In Fig. 5.6, we also compare our PL model results with results from the R13 and R26 equations (Gu and Emerson, 2009), in order to illustrate the predictive capabilities of our N-S-F based continuum equations relative to other extended hydrodynamic models. At the upper limit of the slip regime, $Kn = 0.1$, and early transition regime, $Kn = 0.25$, the velocity profile predicted by R13 equations is linear. In the core part of the flow (i.e. outside of the Knudsen layer), all three hydrodynamic models are in agreement with the DSMC data (Gu and Emerson, 2009). However, in the region close to the wall, the DSMC results indicate a Knudsen-layer velocity profile, i.e. non-linear variations. The R13 equations do not follow this behaviour, while the PL model and the R26 equations are in excellent agreement with the DSMC data. At $Kn = 0.5$ and above, i.e. well into the transition regime, the DSMC data clearly show the expected Knudsen-layer velocity profile with substantial velocity slip at the surface due to strong rarefaction effects. The R13 equations fail to capture this aspect of the velocity profile, and overpredict the amount of velocity slip. In contrast, the results from the PL model are in very good agreement with both the DSMC data and R26 equations, and the new model not only predicts the correct velocity slip but also, and more importantly, captures the power-law behaviour of the velocity profile in the Knudsen layer (Lilley and Sader, 2007), even up to $Kn = 1.0$.

Figs. 5.5 and 5.6 convey that a simple modification to the N-S-F constitutive relations through a geometry dependent mean free path model can significantly improve the predictive capabilities of the continuum equations. The PL model is

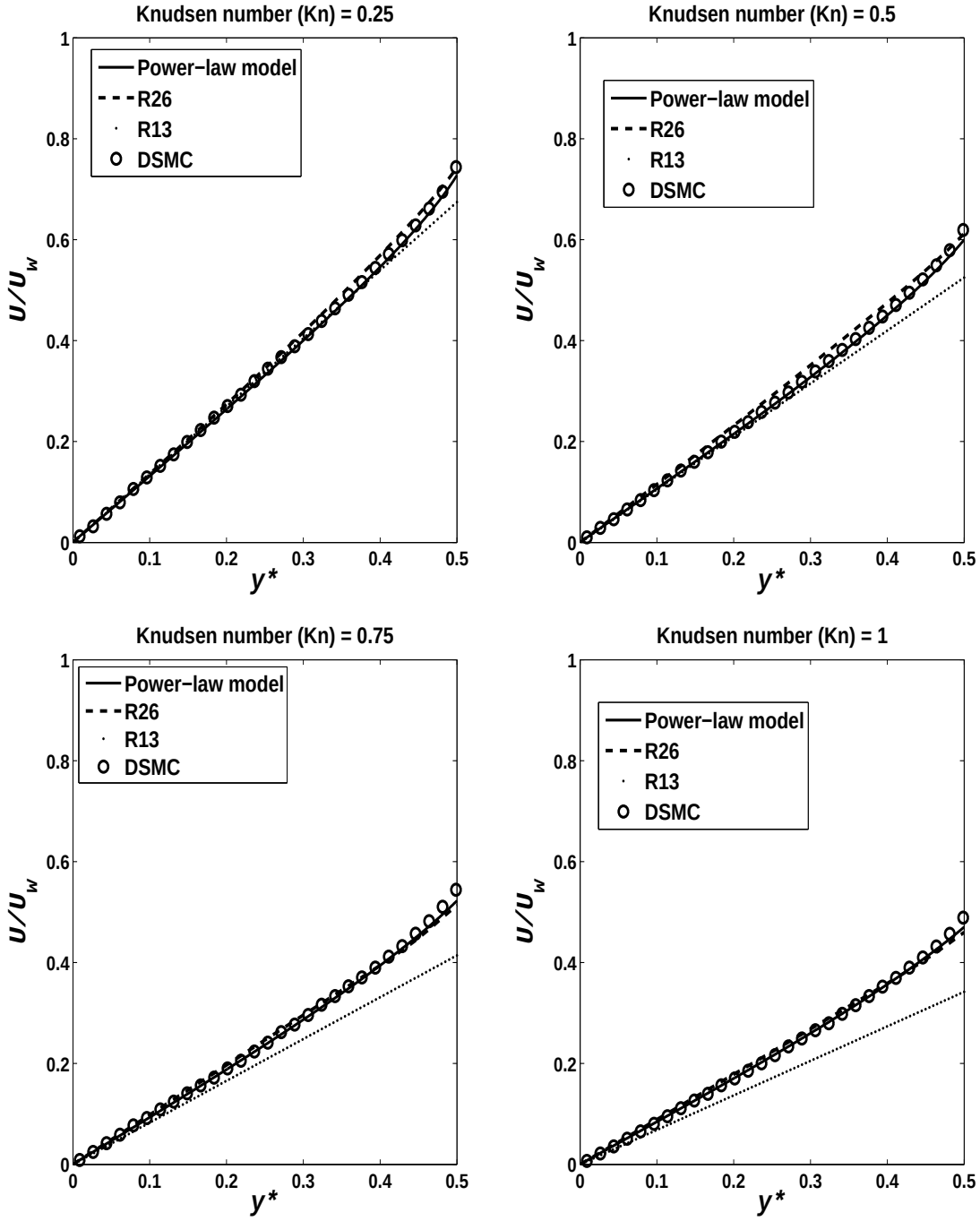

Figure 5.6: Normalised half channel velocity profiles for planar Couette flow at various Knudsen numbers. Comparison of our power-law (PL) model results with the DSMC data, and R26 and R13 moment equations (Gu and Emerson, 2009).

in good agreement with simulation data up to $Kn \sim 1$; the new approach is more accurate than the R13 equations and has predictive capabilities as good as the R26 equations.

5.1.3 Cylindrical Couette flow

A fundamental non-planar test case concerns the isothermal rarefied gas flow between two concentric rotating cylinders. This is a classical fluid dynamics problem that is treated for the no-slip case in many well-known textbooks (Schlichting, 1979). However, under certain conditions, the flow between the cylinders can exhibit highly non-intuitive behavior. For example, if the outer cylinder is stationary and the inner cylinder is rotating, it is possible for the velocity profile to become *inverted* i.e. the velocity will *increase* from the inner to the outer cylinder wall. This unusual phenomenon was first predicted by Einzel et al. (1995) for the case of liquid helium. Tibbs et al. (1997) extended the analysis to the case of a rarefied gas and, using DSMC, demonstrated that velocity inversion could occur provided the tangential momentum accommodation coefficient (TMAC) for the surfaces was small. This early work has led to a number of important curvature studies for rotating Couette flow (e.g. Aoki et al., 2003; Lockerby et al., 2005b; Barber et al., 2004; Yuhong et al., 2005; Myong et al., 2005) and oscillating Couette flow (Emerson et al., 2007). These confirmed the existence of velocity inversion for small values of the TMAC and also showed that the phenomenon could be related to a critical accommodation coefficient. Indeed, Yuhong et al. (2005) derived an analytical criterion for the critical accommodation coefficient and also showed that velocity inversion was solely dependent on the value of the TMAC of the stationary outer cylinder.

For this test case, we implement our PL-based effective MFP model for non-planar surfaces that incorporates the effects of curvature, which is derived in Chapter 3. Constitutive relations and velocity-slip boundary conditions are modified in accordance with the kinetic theory of gases. The modified governing equations are solved for low-speed gas flows, and semi-analytical solutions are derived for the velocity profiles, the critical accommodation coefficient for velocity inversion and the torque variations. Our PL model results are compared with an existing slip model (Yuhong et al., 2005), the linearized BGK solution (Aoki et al., 2003), and DSMC data (Tibbs et al., 1997; Stefanov et al., 2006). We show that our PL model captures important non-linear trends associated with the physics of cylindrical Cou-

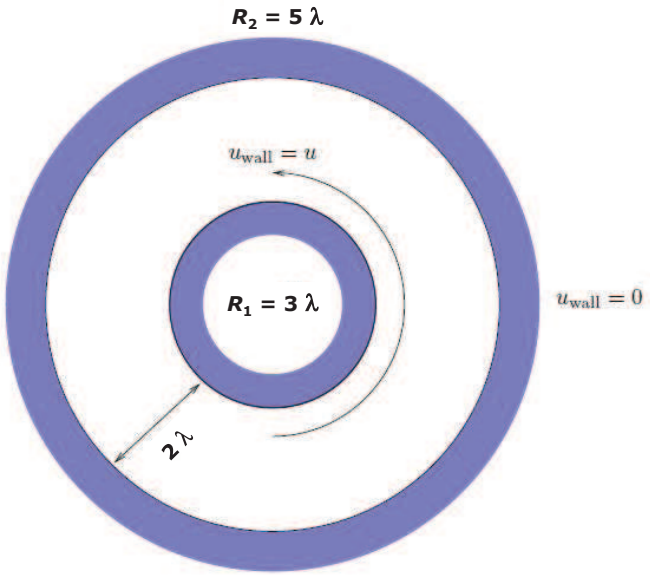

Figure 5.7: Schematic of Couette flow between concentric rotating cylinders.

ette gas flows in the transition regime.

Solution procedure

We consider a rarefied gas confined between two concentric rotating cylinders as shown in Fig. 5.7. The flow is assumed to be fully developed, two-dimensional, isothermal, laminar and steady, with a low Reynolds number (Re) so that inertial effects may be neglected.

With these assumptions, the governing flow equation in cylindrical coordinates is

$$\frac{1}{r^2}\frac{d}{dr}\left(r^2\tau_{r\phi}\right) = 0, \tag{5.23}$$

where r is the radial coordinate, ϕ is the tangential coordinate, and $\tau_{r\phi}$ is the tangential stress, which is defined as:

$$\tau_{r\phi} = \mu\left(\frac{du_\phi}{dr} - \frac{u_\phi}{r}\right), \tag{5.24}$$

where μ is the fluid dynamic viscosity and u_ϕ is the velocity of the fluid in the tangential direction.

Within the Knudsen layer, the flight paths of the gas molecules are affected by the presence of a solid wall. If the unconfined expression for the MFP, λ, is replaced by our geometry-dependent mean free path for non-planar cases, $\lambda_{\text{eff (NP)}}$, given by Eq. (3.37), we obtain a non-constant, geometry-dependent, effective viscosity, $\mu_{\text{eff (NP)}}$, that can then be used to deduce a non-linear stress/strain-rate relation:

$$\tau_{r\phi} = \underbrace{\mu\beta_{\text{NP}}}_{\mu_{\text{eff (NP)}}} \left(\frac{du_\phi}{dr} - \frac{u_\phi}{r}\right). \tag{5.25}$$

Substituting Eq. (5.25) into Eq. (5.23) results in the modified governing equation:

$$\frac{\mu}{r^2}\frac{d}{dr}\left[r^2\beta_{\text{NP}}\left(\frac{du_\phi}{dr} - \frac{u_\phi}{r}\right)\right] = 0. \tag{5.26}$$

This needs to be solved in conjunction with the following slip boundary conditions at the inner and outer cylinder surfaces (Yuhong et al., 2005), respectively:

$$u_\phi\,|_{r=R_1} = \omega_1 R_1 + \underbrace{\frac{2-\sigma_1}{\sigma_1}}_{\alpha_1}\lambda\left[\beta_{\text{NP}}\left(\frac{du_\phi}{dr} - \frac{u_\phi}{r}\right)\right]|_{r=R_1}, \tag{5.27}$$

$$u_\phi\,|_{r=R_2} = \omega_2 R_2 - \underbrace{\frac{2-\sigma_2}{\sigma_2}}_{\alpha_2}\lambda\left[\beta_{\text{NP}}\left(\frac{du_\phi}{dr} - \frac{u_\phi}{r}\right)\right]|_{r=R_2}, \tag{5.28}$$

where ω_1 and ω_2 are the angular velocities, and σ_1 and σ_2 are the tangential momentum accommodation coefficients (TMAC), of the inner and outer cylinders, respectively.

The solution for the velocity profile can then be obtained as:

$$u_\phi(r) = r\left[\omega_1 + \frac{\alpha_1\lambda C}{R_1^3} + G_1(r)C\right], \tag{5.29}$$

where

$$G_1(r) = \int_{R_1}^{r}\frac{dr}{r^3\beta_{\text{NP}}}, \tag{5.30}$$

$$C = \frac{\omega_2 - \omega_1}{\left[H_1 + \frac{\alpha_1 \lambda}{R_1^3} + \frac{\alpha_2 \lambda}{R_2^3}\right]}, \tag{5.31}$$

$$H_1 = \int_{R_1}^{R_2} \frac{dr}{r^3 \beta_{\mathrm{NP}}}. \tag{5.32}$$

When the effects of the Knudsen layer are neglected, i.e. the mean free path has no geometry dependence, then Eq. (5.29) simply reduces to the velocity profile based on the classical slip solution, as presented Yuhong et al. (2005).

Results

In the present study, we have carried out DSMC simulations to validate our PL model for rarefied gas flows in non-planar geometries.

The DSMC solver we use is *dsmcFoam*, an open source solver that is part of the C++ fluid dynamics toolbox, OpenFOAM. This solver has previously been rigorously validated for a variety of benchmark cases (Scanlon et al., 2010; Arlemark et al., 2012). 2D DSMC simulations of cylindrical Couette flows are carried out here, where argon gas is trapped between two concentric cylinders. The inner cylinder is rotating and the outer cylinder is stationary ($\omega_2 = 0$). Our simulations do not utilise quarter or half symmetry; a full circular domain is modelled.

For all of our DSMC simulations, the cell size is chosen such that the cells are much smaller than the unconfined mean free path and so that enough cells are placed throughout the domain to recover macroscopic properties with sufficient resolution. The time step is smaller than the mean collision time and also small enough that particles are likely to spend multiple time steps within a single computational cell. All simulations are initialised with at least 20 DSMC simulator particles per cell and 500,000 particles in the whole domain. Each case was solved in parallel on 4 cores of the 1100 core HPC facility at the University of Strathclyde. The run time for each case was around 60 hours to simulate 9 μs of problem time. Due to the low signal-to-noise ratio expected in these simulations, one million statistical samples are employed for each case. The variable hard sphere collision model (Bird, 1983) is used to perform collisions and all surface-particle interactions are dealt with

as a mixture of specular and Maxwellian diffuse interactions in order to simulate various TMAC values. The torque on the rotating cylinder is also calculated from the viscous drag force acting on the cylinder surface.

Numerical results are obtained for a variety of outer-to-inner cylinder radius ratios ($R_2/R_1 = 6/5$, $5/3$, 2, 3 and 5), Knudsen numbers ($Kn = 0.1$, 0.5 and 1.0) and TMAC values ($\sigma = 0.1$, 0.4, 0.7 and 1.0). The inner cylinder is rotating at a Mach number ($Ma = R_1\omega_1/\sqrt{RT}$) of 0.26. Normalised velocity profiles [$U^* = u_\phi/(\omega_1 R_1)$] are presented in Figs. (5.8 - 5.15).

For our initial set of results, the ratio of the radii of the inner and outer cylinders R_2/R_1, is chosen to be $5/3$, and the accommodation coefficients are assumed to be equal at the inner and outer surfaces ($\sigma_1 = \sigma_2 = \sigma$). Fig. 5.8a presents a comparison between our solution based on the PL effective MFP, i.e. Eq. (5.29), and the DSMC data. The PL model is in excellent agreement with the simulation data for the $Kn = 0.1$ case, and for all σ values. Fig. 5.8b presents the results based on the classical governing equation together with the conventional slip boundary conditions, i.e. without considering any Knudsen layer effects (see Yuhong et al., 2005), alongside the PL model results. The classical slip model results are in good agreement with the PL model results, with slight deviations in the near-wall regions. For $Kn = 0.1$, i.e. the end of the slip flow regime, no velocity inversion is predicted by the DSMC simulation or the theoretical models.

Comparisons for the $Kn = 0.5$ case are presented in Fig. 5.9. The PL model is in very good quantitative agreement with the DSMC results for the $\sigma = 1.0$ and 0.7 cases. The results show that the DSMC data and PL formulation follow the same basic trends, and predict an inverted velocity profile when the accommodation coefficient is 0.1. However, slight deviations are discernible at the surface of the outer cylinder for the $\sigma = 0.4$ and 0.1 cases. It is interesting to note that, for the specific case of the accommodation coefficients of the inner and outer cylinders having the same value, the family of velocity profiles all pass through a common point that is independent of the value of the accommodation coefficient. This intersection point in the PL profiles is fairly close to the point predicted by the DSMC data, whereas the classical slip solution predicts this point closer to the outer cylinder, as shown

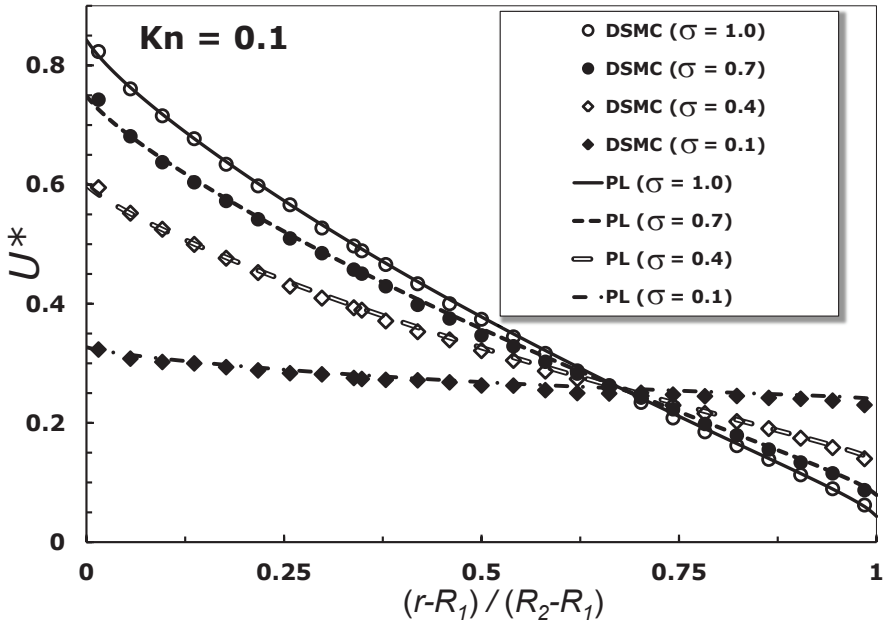

(a)

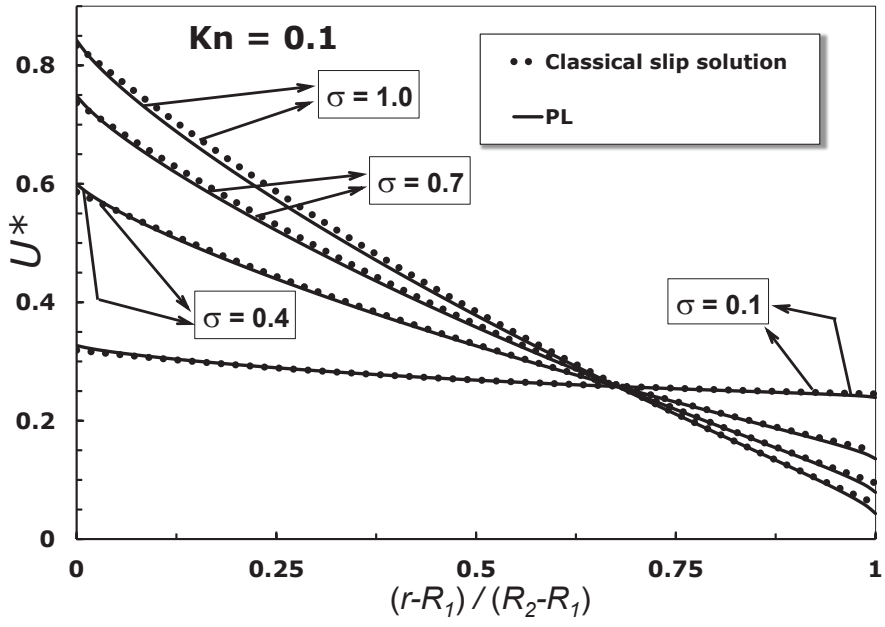

(b)

Figure 5.8: Variation of non-dimensional velocity $[U^* = u_\phi/(\omega_1 R_1)]$ as a function of radial distance for cylindrical Couette flow with $\sigma_1 = \sigma_2 = \sigma$. Comparison of PL model results against (**a**) DSMC data and (**b**) the classical slip solution (Yuhong et al., 2005). The results are presented for $Kn = 0.1$ and $R_2/R_1 = 5/3$.

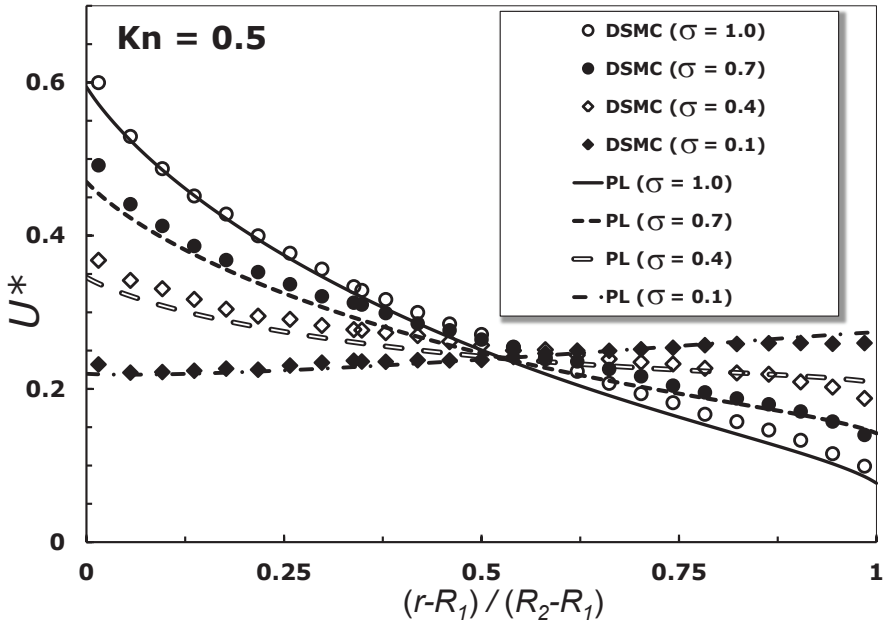

(a)

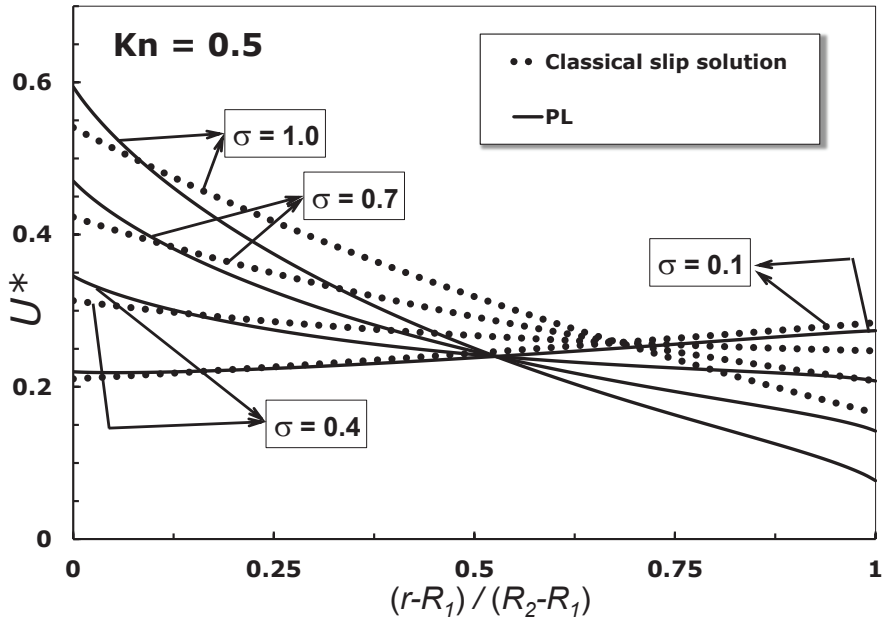

(b)

Figure 5.9: Variation of non-dimensional velocity $[U^* = u_\phi/(\omega_1 R_1)]$ as a function of radial distance for cylindrical Couette flow with $\sigma_1 = \sigma_2 = \sigma$. Comparison of PL model results against (**a**) DSMC data and (**b**) the classical slip solution (Yuhong et al., 2005). The results are presented for $Kn = 0.5$ and $R_2/R_1 = 5/3$.

in Fig. 5.9b. It is evident that the classical slip solution is unable to account for any variation in MFP and hence fails to capture non-linear effects associated with the Knudsen layers at the inner and outer cylinders. The classical slip model underpredicts the amount of slip at both the inner and outer cylinders, i.e. accounting for smaller slip effects. The discrepancies are greatest when $\sigma = 1.0$ and decrease as σ is reduced. At very low values of σ, the PL model and classical slip solutions are identical and yield the same solid body rotation solution as $\sigma \to 0$.

Fig. 5.10 shows velocity profiles for the $Kn = 1$ case, and deviations between the PL model and DSMC data are discernible in the near-wall regions at both inner and outer cylinders, for all σ values. The PL model underpredicts the velocity at the inner cylinder for all σ values, however at the outer cylinder, they are overpredicted for $\sigma = 0.1$, 0.4 and 0.7, and slightly underpredicted for $\sigma = 1$. The classical slip model comparisons with the PL model are quantitatively similar to the $Kn = 0.5$ case. The intersection point for the family of velocity profiles, for both the DSMC data and the PL model results, moves towards the inner cylinder from the outer cylinder, with increasing Kn. However, for the classical slip model, the intersection point is found to be approximately stationary (at around 0.7 on the x-axis) for all Kn cases.

Fig. 5.11 shows the case when the accommodation coefficient of the inner cylinder is maintained at unity ($\sigma_1 = 1.0$) whilst the accommodation coefficient of the outer cylinder (σ_2) is varied from 0.02 to 0.3. Normal (non-inverted), fully-inverted and partially-inverted velocity profiles are seen in both the PL model results and our DSMC data.

For the partially-inverted cases in Fig. 5.11, both the PL model and the DSMC data predict an initial decrease in velocity away from the inner cylinder, then an increase towards the outer cylinder, and then another decrease in a very thin layer close to the surface of the outer cylinder. This is in contrast to the predictions based on the classical slip solution (see Figure 5 in Yuhong et al., 2005) where the velocity profile has an initial decrease away from the inner cylinder and then just an increase towards the outer cylinder. Our PL model is able to predict the non-linear effects quite well, except very close to the surface of the outer cylinder, where the DSMC

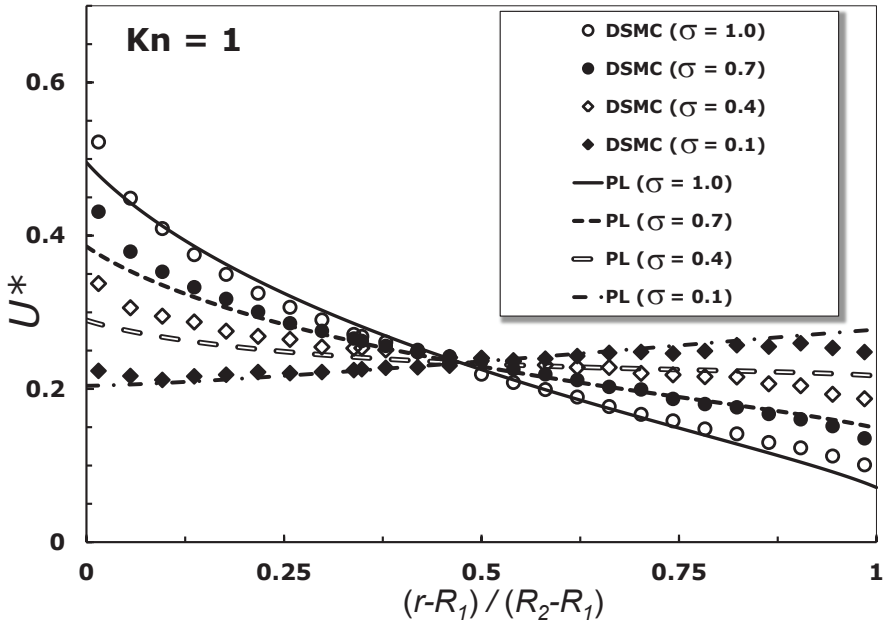

(a)

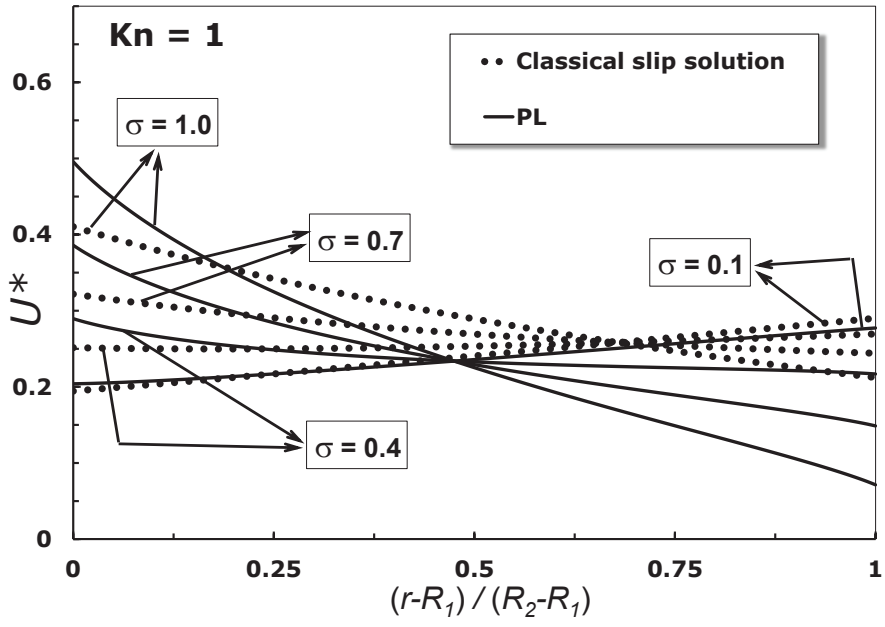

(b)

Figure 5.10: Variation of non-dimensional velocity $[U^* = u_\phi/(\omega_1 R_1)]$ as a function of radial distance for cylindrical Couette flow with $\sigma_1 = \sigma_2 = \sigma$. Comparison of PL model results against (**a**) DSMC data and (**b**) the classical slip solution (Yuhong et al., 2005). The results are presented for $Kn = 1$ and $R_2/R_1 = 5/3$.

data exhibit a sharp decrease in the velocity that is not captured by our model. Quantitative agreement with the DSMC data is good for $\sigma_2 > 0.2$ and $\sigma_2 < 0.1$. The PL model exhibits a conventional velocity profile until $\sigma_2 \sim 0.25$ and below that it shows a partially inverted profile up to $\sigma_2 \sim 0.10$, whereas the classical slip solution has the corresponding values 0.4 and 0.2 (see Figure 5 in Yuhong et al., 2005).

As mentioned earlier, the value of the power-law exponent has been fixed to $n = 3$ for all the reported results so far. Fig. (5.12) demonstrates the effect of the value of n on the structure of the velocity profile in the Knudsen layer, for $\sigma_1 = 1.0$ and (**a**) $\sigma_2 = 1.0$, (**b**) $\sigma_2 = 0.4$ and (**c**) $\sigma_2 = 0.15$. The velocity profiles are almost unaffected by the value of n at high values of the accommodation coefficients ($\sigma_2 = 1.0$) across the entire annular clearance. However, decreasing σ_2 to 0.4, the results are sensitive to the exponent value, but only in the Knudsen layer at the outer cylinder. For small accommodation coefficients ($\sigma_2 = 0.15$), the velocity profiles are shown clearly to depend on the value of n, and the sensitivity to this increases towards the outer cylinder.

Until now, all the comparisons between the PL model and DSMC data have been carried out for a fixed radius ratio value $R_2/R_1 = 5/3$. To check the sensitivity of curvature effects on the velocity profiles, we present results for $R_2/R_1 = 6/5$, 2, 3 and 5 cases, at $Kn = 0.1, 0.5$ and 1. The radius ratio is varied by fixing R_1 and increasing R_2, and Kn is maintained at a desired value by proportionally modifying the gas density.

Fig. 5.13 demonstrates the velocity profiles for $Kn = 0.1$ case, at different R_2/R_1 values. For each R_2/R_1 value, the PL model results are compared with DSMC data for $\sigma = 0.1$, 0.4, 0.7 and 1. For the lower R_2/R_1 values (i.e. 6/5 and 2), our theoretical model has excellent agreement with simulation data across the annular gap. However, with an increase in R_2/R_1, deviations are noticed in the near-wall region at the inner cylinder: the PL model slightly underpredicts velocities for R_2/R_1 = 3 and 5 cases, while at the outer cylinder, velocities are accurately predicted. The intersection point, where the family of velocity profiles pass through a common point, moves towards the outer cylinder with an increase in R_2/R_1. The amount of slip

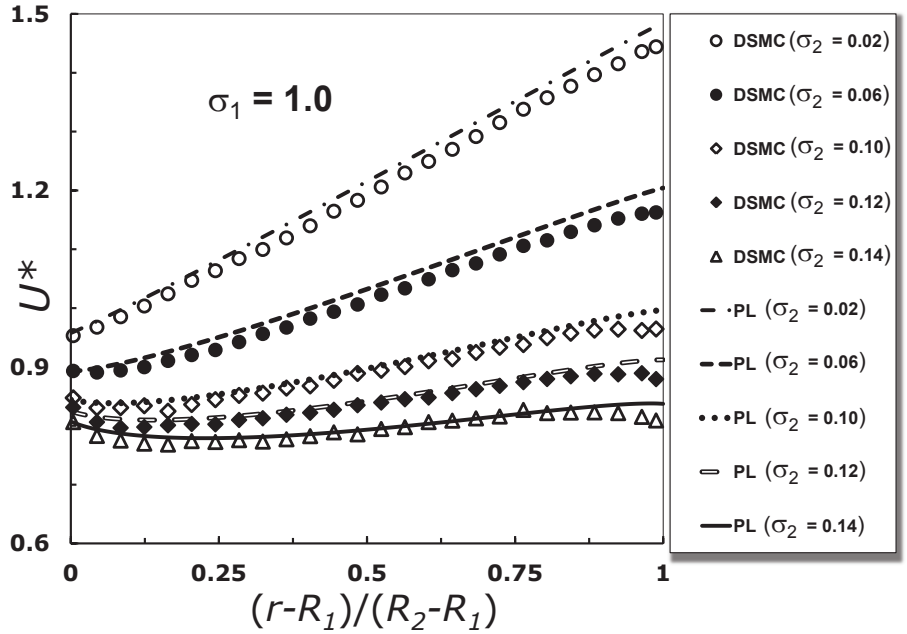

(a)

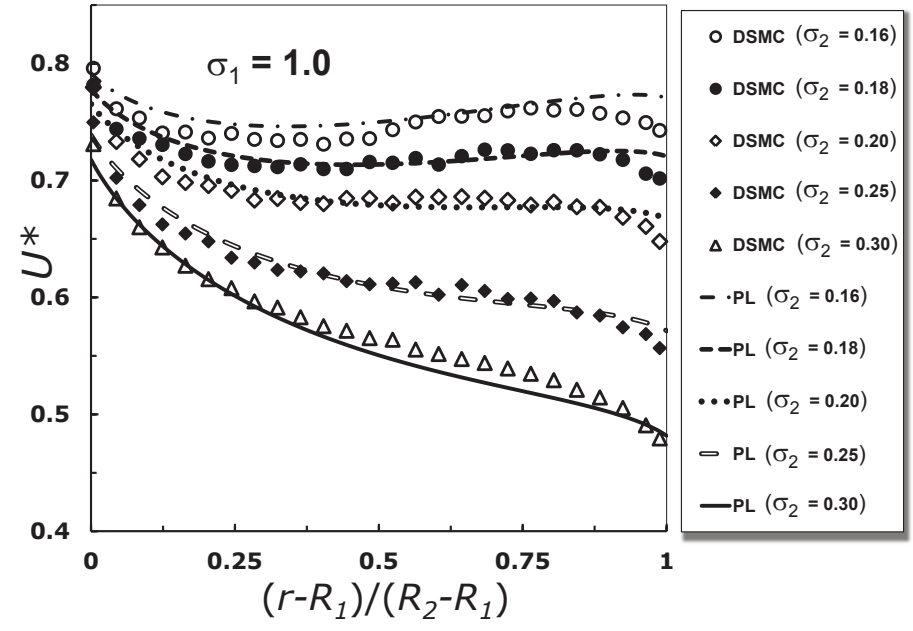

(b)

Figure 5.11: Variation of the non-dimensional cylindrical Couette flow velocity $[U^* = u_\phi/(\omega_1 R_1)]$ as a function of the radial distance for $\sigma_1 = 1.0$ and various values of σ_2, ranging from (**a**) 0.02 to 0.14 and (**b**) 0.16 to 0.30. Normal, fully-inverted and partially-inverted velocity profiles are seen in the PL model results and the DSMC data, for $Kn = 0.5$ and $R_2/R_1 = 5/3$.

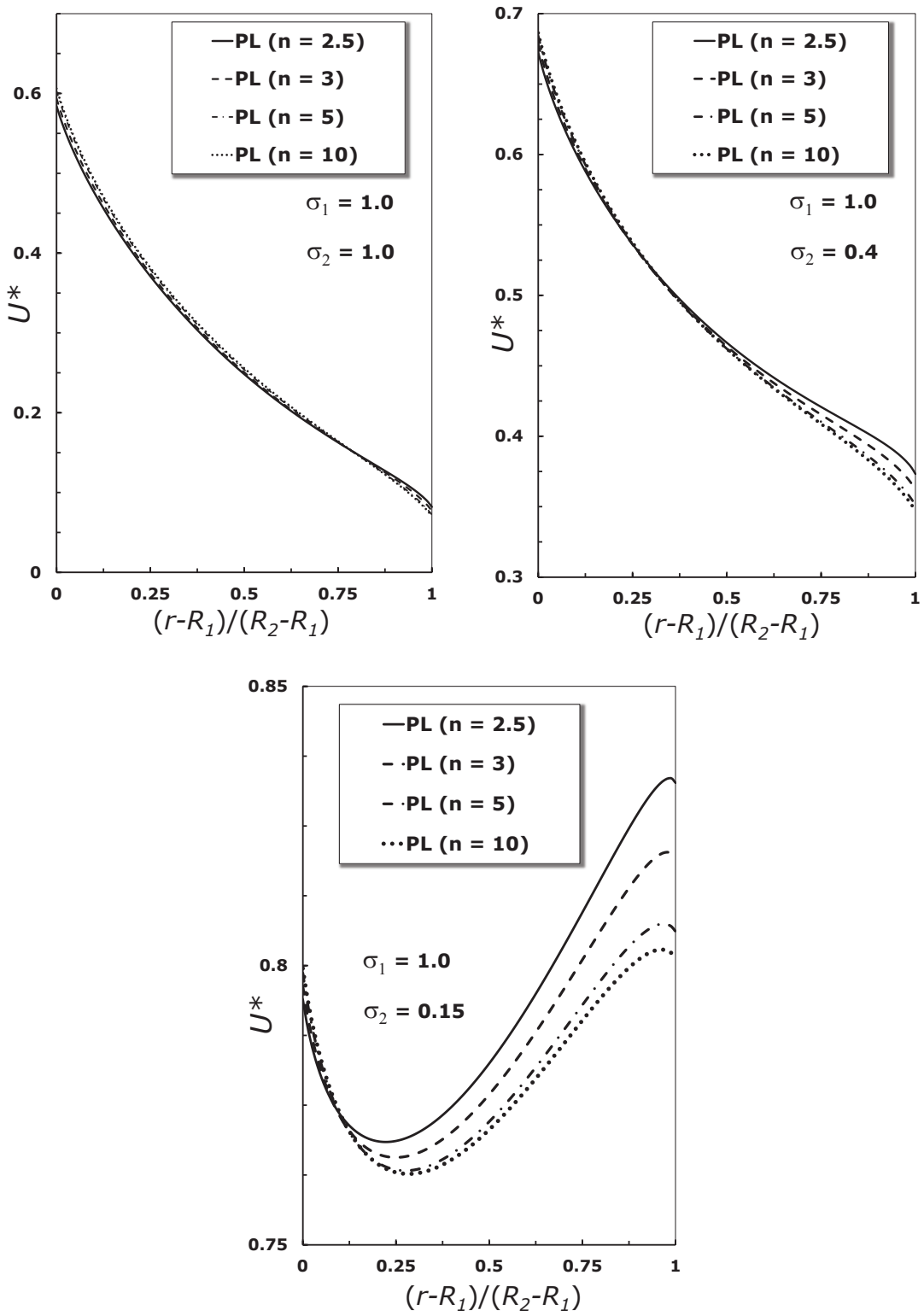

Figure 5.12: Effect of the power-law (PL) distribution function exponent, n, on the cylindrical Couette flow velocity profiles. Variation of the non-dimensional velocity $[U^* = u_\phi/(\omega_1 R_1)]$ with radial distance for $\sigma_1 = 1.0$ and (**a**) $\sigma_2 = 1.0$, (**b**) $\sigma_2 = 0.4$ and (**c**) $\sigma_2 = 0.15$, for $Kn = 0.5$ and $R_2/R_1 = 5/3$.

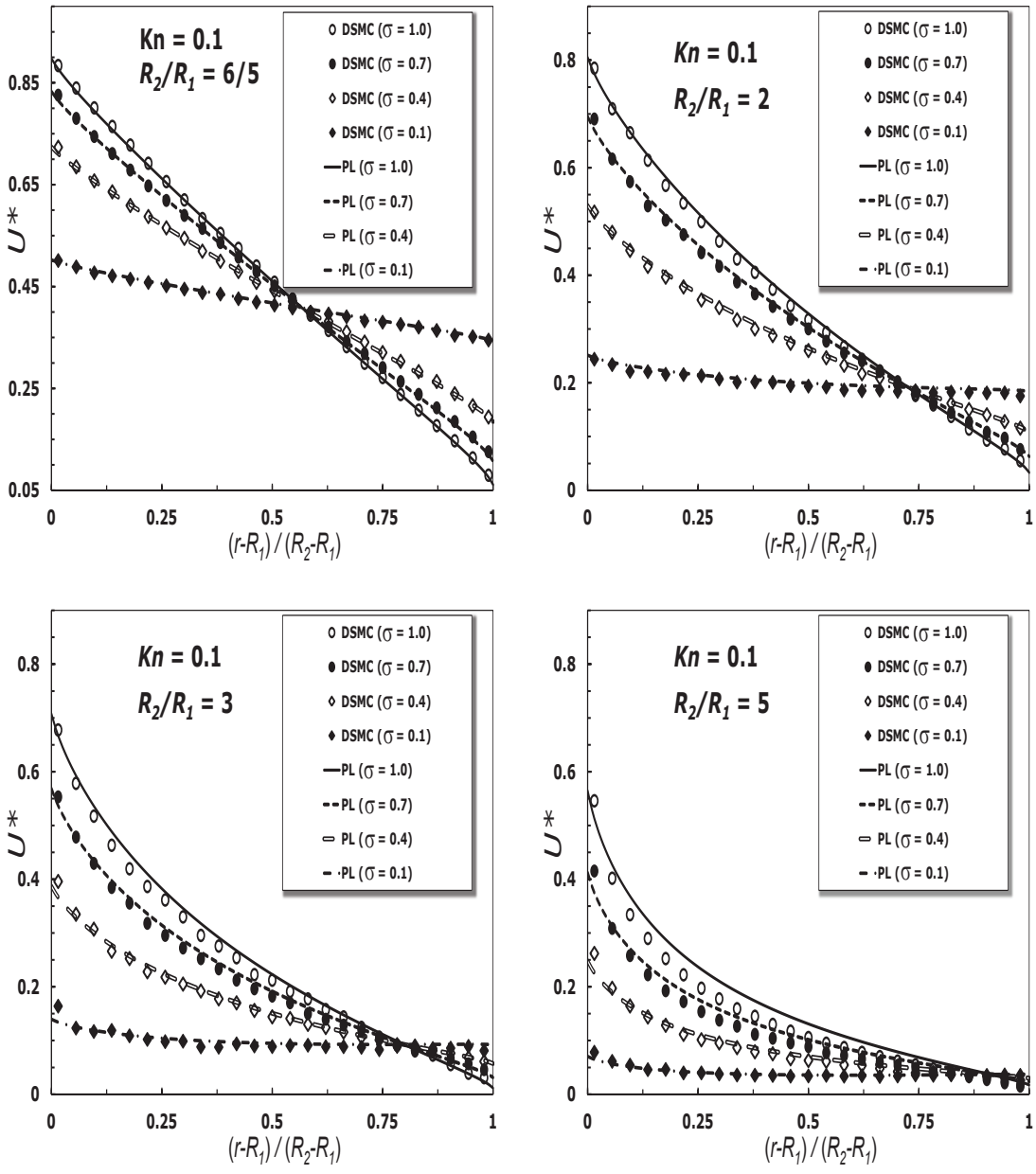

Figure 5.13: Variation of non-dimensional cylindrical Couette flow velocity $[U^* = u_\phi/(\omega_1 R_1)]$ as a function of normalised radial distance with $\sigma_1 = \sigma_2 = \sigma$. Comparison of PL model results against DSMC data. The results are presented for $Kn = 0.1$ and $R_2/R_1 = 6/5$ (top left), 2 (top right), 3 (bottom left) and 5 (bottom right).

increases at both inner and outer cylinders, with an increase in R_2/R_1. When the size of the inner cylinder is relatively reduced in comparison with the outer one, larger and smaller slip effects are noticed, at the inner and outer cylinders, respectively. This may be due to relatively fewer molecules collide with the inner cylinder, when compared to the outer one. On the other hand, for the $R_2/R_1 = 6/5$ case, no velocity inversion is observed when $\sigma = 0.1$, however, partially-inverted velocity profiles are predicted for higher values of R_2/R_1 cases. For partial inversions, the gradient of the velocity profile has to be zero at some position in the annular gap, and this point moves towards the inner cylinder from the outer one, with increase in R_2/R_1.

Similar comparisons are carried out for $Kn = 0.5$ and 1 cases, and are shown in Figs. 5.14 and 5.15. For the $R_2/R_1 = 6/5$ case, the PL model is in excellent agreement with the DSMC data at both $Kn = 0.5$ and 1. Deviations are noticed as R_2/R_1 increase, and these are quite significant for the $R_2/R_1 = 5$ case, especially near the inner cylinder. Similar to the $Kn = 0.1$ case, the amount of slip at the inner cylinder increases significantly with an increase in R_2/R_1. For the $Kn = 0.5$ and $\sigma = 1$ case, with an increase in R_2/R_1, velocities at the inner cylinder, predicted by DSMC, vary from approximately 0.73 to 0.4, whereas for the PL model from 0.72 to 0.25. For the $Kn = 1$ and $\sigma = 1$ case, they vary from 0.7 to 0.38, and from 0.68 to 0.2, for the DSMC and PL models, respectively. The position of the intersection point of the velocity profiles is relatively insensitive to a change in R_2/R_1 in the $Kn = 0.5$ and 1 cases, when compared with the $Kn = 0.1$ case. On the other hand, for $R_2/R_1 = 6/5$ complete velocity inversion is observed at $\sigma = 0.1$. Partially-inverted velocity profiles are predicted for higher values of R_2/R_1 at $\sigma = 0.1$. For $Kn = 0.5$ and 1, the position where the gradient of the velocity profile becomes zero moves away from the inner cylinder as R_2/R_1 increases. These findings are in contrast to the velocity profiles for the $Kn = 0.1$ case, see Fig. 5.13.

Critical accommodation coefficients

In this section, we identify limiting criteria for critical accommodation coefficients that produce (i) normal, (ii) fully-inverted, and (iii) partially-inverted velocity pro-

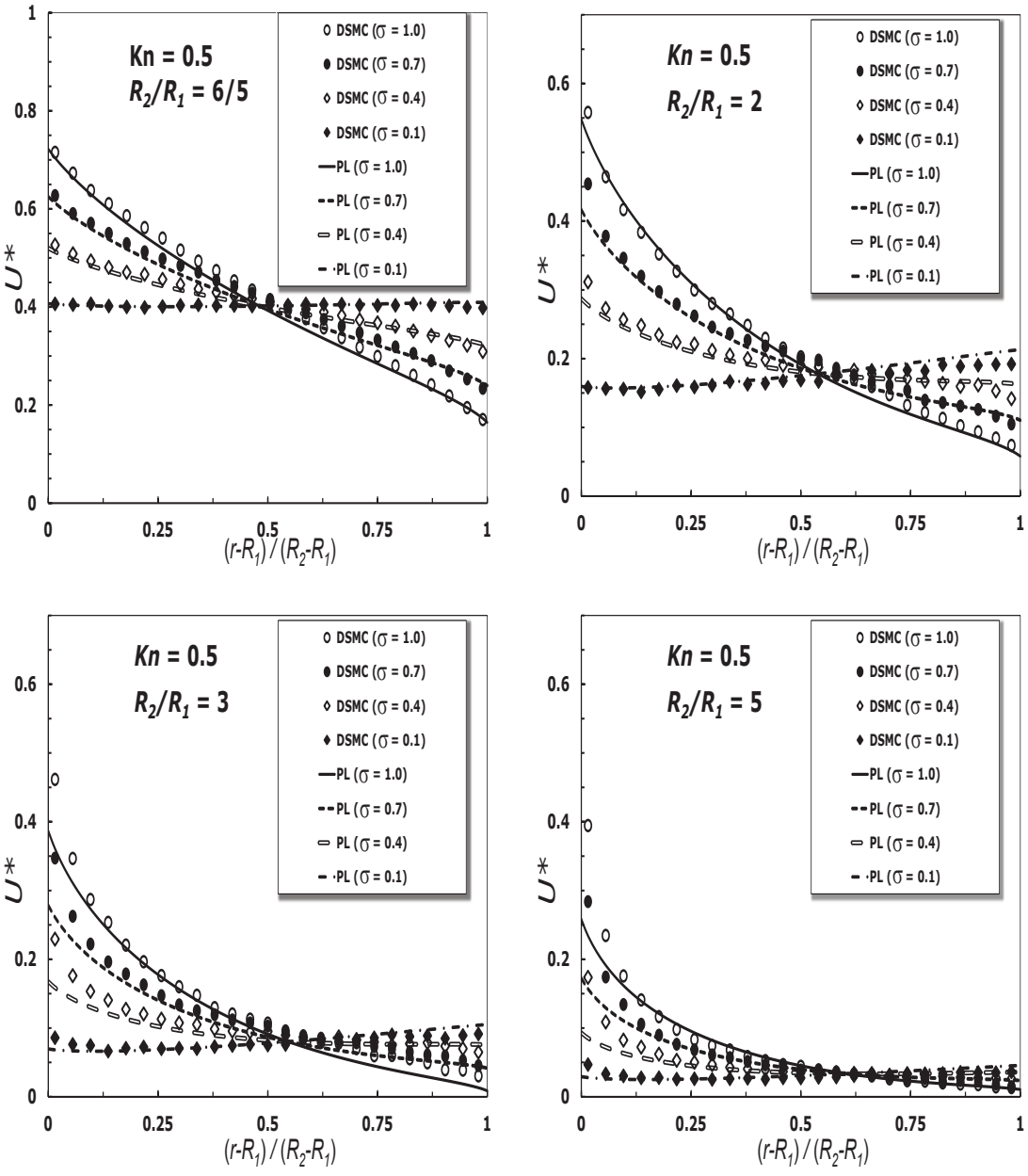

Figure 5.14: Variation of non-dimensional cylindrical Couette flow velocity $[U^* = u_\phi/(\omega_1 R_1)]$ as a function of normalised radial distance with $\sigma_1 = \sigma_2 = \sigma$. Comparison of PL model results against DSMC data. The results are presented for $Kn = 0.5$ and $R_2/R_1 = 6/5$ (top left), 2 (top right), 3 (bottom left) and 5 (bottom right).

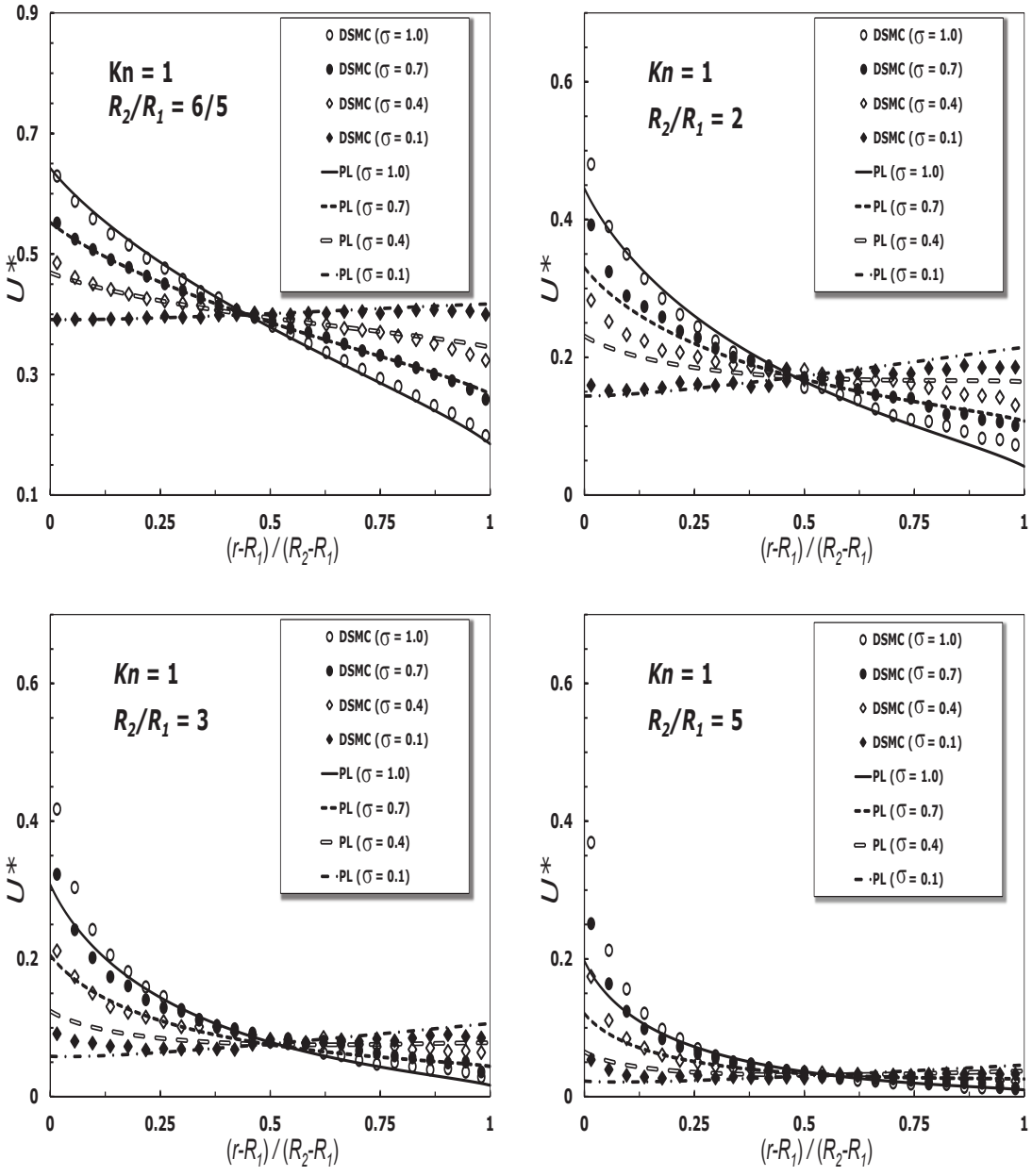

Figure 5.15: Variation of non-dimensional cylindrical Couette flow velocity $[U^* = u_\phi/(\omega_1 R_1)]$ as a function of normalised radial distance with $\sigma_1 = \sigma_2 = \sigma$. Comparison of PL model results against DSMC data. The results are presented for $Kn = 1$ and $R_2/R_1 = 6/5$ (top left), 2 (top right), 3 (bottom left) and 5 (bottom right).

files. A normal (non-inverted) velocity profile occurs when the tangential velocity decreases monotonically from the inner to the outer cylinder. In contrast, a fully-inverted case occurs when the velocity monotonically increases. Finally, a partially-inverted profile occurs when there is a decrease and increase at multiple locations between the inner and outer cylinders.

The velocity profile is given in Eq. (5.29); the gradient of this can be used as a criterion to judge whether the function is monotonically decreasing or increasing. After some simplifications, the velocity gradient for the case of a rotating inner cylinder and stationary outer cylinder can be expressed as:

$$\frac{du_\phi}{dr} = \omega_1 \left[1 - \frac{1}{H_1 + \frac{\alpha_1 \lambda}{R_1^3} + \frac{\alpha_2 \lambda}{R_2^3}} \left(\frac{\alpha_1 \lambda}{R_1^3} + G_1(r) + \frac{1}{r^2 \beta_{\mathrm{NP}}} \right) \right]. \tag{5.33}$$

If $du_\phi/dr > 0$, a fully inverted velocity profile exists, and this is only satisfied when:

$$\frac{\left(\frac{\alpha_1 \lambda}{R_1^3} + G_1(r) + \frac{1}{r^2 \beta_{\mathrm{NP}}} \right)}{H_1 + \frac{\alpha_1 \lambda}{R_1^3} + \frac{\alpha_2 \lambda}{R_2^3}} < 1, \tag{5.34}$$

which can only hold throughout the annular clearance ($R_1 \leq r \leq R_2$), when $[G(r) + 1/(r^2 \beta_{\mathrm{NP}})]$ is at its maximum value, which occurs at $r = R_1$. Using this condition, the criterion for the critical accommodation coefficient for a fully inverted velocity profile (i.e. positive velocity gradient) can be expressed as:

$$(\sigma_2)_{\mathrm{P}} = 2 \left[1 + \frac{R_2^3}{R_1^2 \beta_{\mathrm{NP}} \lambda} - \frac{R_2^3}{\lambda} H_1 \right]^{-1}. \tag{5.35}$$

Eq. (5.35) provides an upper bound, so for $\sigma_2 < (\sigma_2)_{\mathrm{P}}$ a fully inverted velocity will always occur, and this phenomenon is independent of the value of the accommodation coefficient at the inner cylinder. In the absence of any Knudsen layer in the flow, i.e. a constant mean free path between the inner and outer cylinders, Eq. (5.35) simply reduces to the classical slip solution presented in Eq. (17) of Yuhong et al. (2005).

From Eq. (5.33), if $du_\phi/dr < 0$ the velocity will be a decreasing function of r and no inverted velocity profile will be observed. This situation can only exist when:

$$\frac{\left(\frac{\alpha_1\lambda}{R_1^3} + G_1(r) + \frac{1}{r^2\beta_{\mathrm{NP}}}\right)}{H_1 + \frac{\alpha_1\lambda}{R_1^3} + \frac{\alpha_2\lambda}{R_2^3}} > 1, \tag{5.36}$$

which can only hold throughout the annular clearance ($R_1 \leq r \leq R_2$) when $G(r) + 1/(r^2\beta_{\mathrm{NP}})$ is at its minimum value, which occurs for $r = R_m$ ($R_1 < R_m < R_2$). The value of R_m can be obtained numerically for a given Kn and R_2/R_1 and then the critical accommodation coefficient for no velocity inversion (i.e. negative velocity gradient) follows as:

$$(\sigma_2)_{\mathrm{N}} = 2\left[1 + \frac{R_2^3}{R_m^2\beta_{\mathrm{NP}}(R_m)\lambda} - \frac{R_2^3}{\lambda}\left(G_1(R_m) - H_1\right)\right]^{-1}. \tag{5.37}$$

Eq. (5.37) provides a lower bound, so for $\sigma_2 > (\sigma_2)_{\mathrm{N}}$ no inverted velocity profile will occur and this phenomenon is also independent of the value of the accommodation coefficient at the inner cylinder, as in the case above. When there is no mean free path variation between the inner and outer cylinders, Eq. (5.37) reduces to the corresponding classical slip solution (see Eq. 19 of Yuhong et al., 2005).

Considering these two cases given by Eqs. (5.35) and (5.37), where the velocity is monotonically decreasing or increasing, it is evident that a *partially-inverted* velocity profile will occur when the accommodation coefficient at the outer cylinder lies within the range:

$$(\sigma_2)_{\mathrm{P}} < \sigma_2 < (\sigma_2)_{\mathrm{N}}. \tag{5.38}$$

This also does not depend on the accommodation coefficient of the inner cylinder.

Fig. 5.16a presents the variation of the critical accommodation coefficient $(\sigma_2)_{\mathrm{N}}$ as a function of Knudsen number for the case of no velocity inversion. Our PL model results are compared with DSMC data (Stefanov et al., 2006), the classical slip solution (Eq. 19 of Yuhong et al., 2005) and the linearized BGK model (Aoki et al., 2003), in the flow regime $0 < Kn < 1$. In the continuum regime ($Kn < 0.001$), all three theoretical models converge to similar values. In the slip flow regime ($0.001 < Kn < 0.1$), the PL model lies below the classical slip solution and the

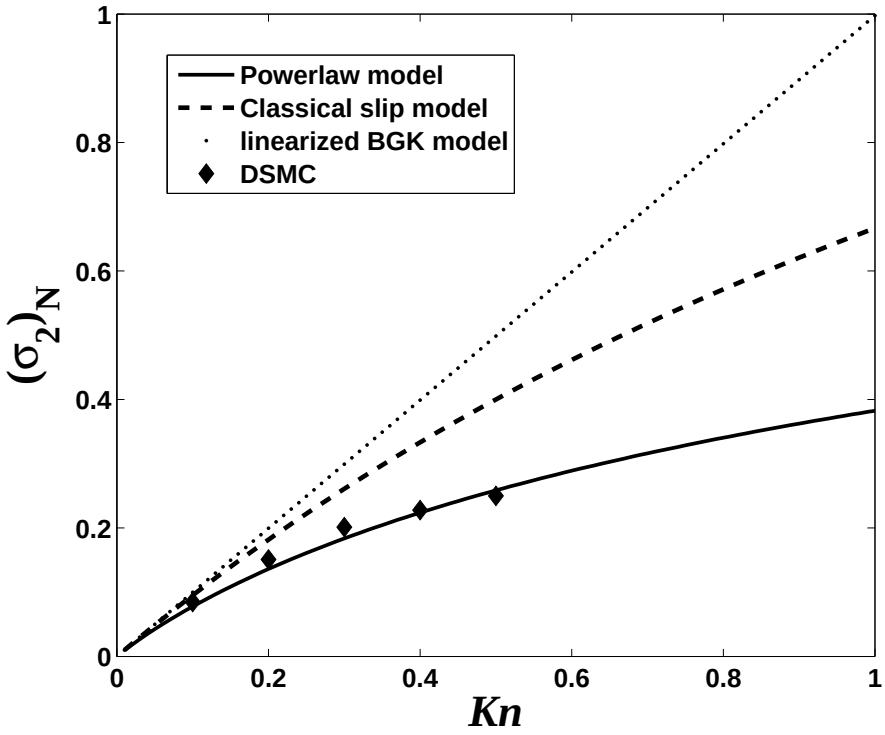

(a)

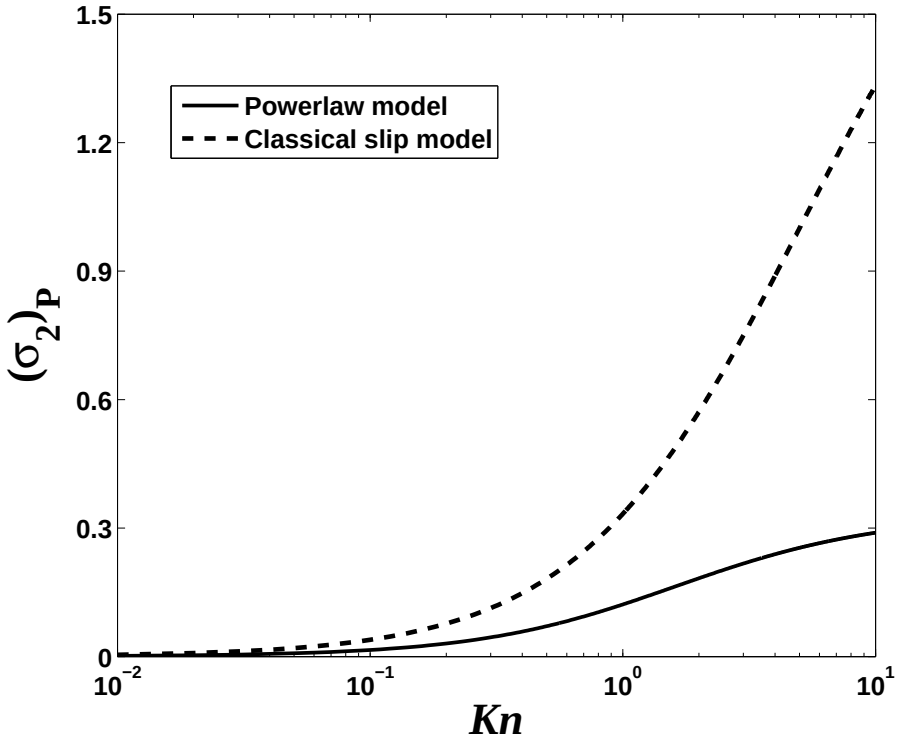

(b)

Figure 5.16: Variation of critical accommodation coefficient with Knudsen number predicted for the cylindrical Couette flow geometric configuration of $R_2/R_1 = 5/3$; (**a**) $(\sigma_2)_{\mathrm{N}}$ the lower bound for no velocity inversion, i.e. negative velocity gradient throughout the annular clearance ($R_1 < r < R_2$); (**b**) $(\sigma_2)_{\mathrm{P}}$ the upper bound for full velocity inversion, i.e. positive velocity gradient throughout the annular clearance.

BGK model. The PL model results show very good quantitative agreement with the DSMC data in the early transition regime ($0.1 < Kn < 0.5$), whereas the other two models show significant deviations. Although DSMC data are not available beyond $Kn > 0.5$, by extrapolating the trend up to $Kn = 0.5$, the PL model is likely to slightly overpredict $(\sigma_2)_{\mathrm{N}}$ in the latter part of the transition regime. In the free-molecular regime, the PL model asymptotically reaches a constant value (~ 0.7) and both the classical slip solution and the BGK model diverge (not shown in Fig. 5.16a).

Fig.5.16b shows the variation of the critical accommodation coefficient, $(\sigma_2)_{\mathrm{P}}$, as a function of Knudsen number for a fully inverted velocity profile. Our PL model is compared with the classical slip solution (see Eq. 17 of Yuhong et al., 2005) from the slip to the free-molecular regime ($0.001 < Kn < 10$), although the continuum assumptions are highly questionable for $Kn > 1$. The classical slip solution significantly overpredicts the PL model in the transition regime and beyond. For $Kn >> 1$, the slip solution indeed shows a diverging and unphysical behavior with $(\sigma_2)_{\mathrm{P}}$ values rising greater than unity. Conversely, our PL model reaches a constant value of the accommodation coefficient of ~ 0.3.

Torque

The accurate prediction of integral flow parameters in micro/nano-conduits is important in engineering MEMS devices. Here, we present the torque exerted on the rotating inner cylinder, which can be given as:

$$\Gamma_{\mathrm{PL}} = f A R_1, \tag{5.39}$$

with

$$f = \left[\mu_{\mathrm{eff}} \left(\frac{du}{dr} - \frac{u}{r} \right) \right] |_{r=R_1}, \tag{5.40}$$

$$A = 2\pi R_1 L, \tag{5.41}$$

where L is the axial length of the inner cylinder. When the no-slip boundary condition is applied and the Knudsen layer effects are negligible, the torque expression for

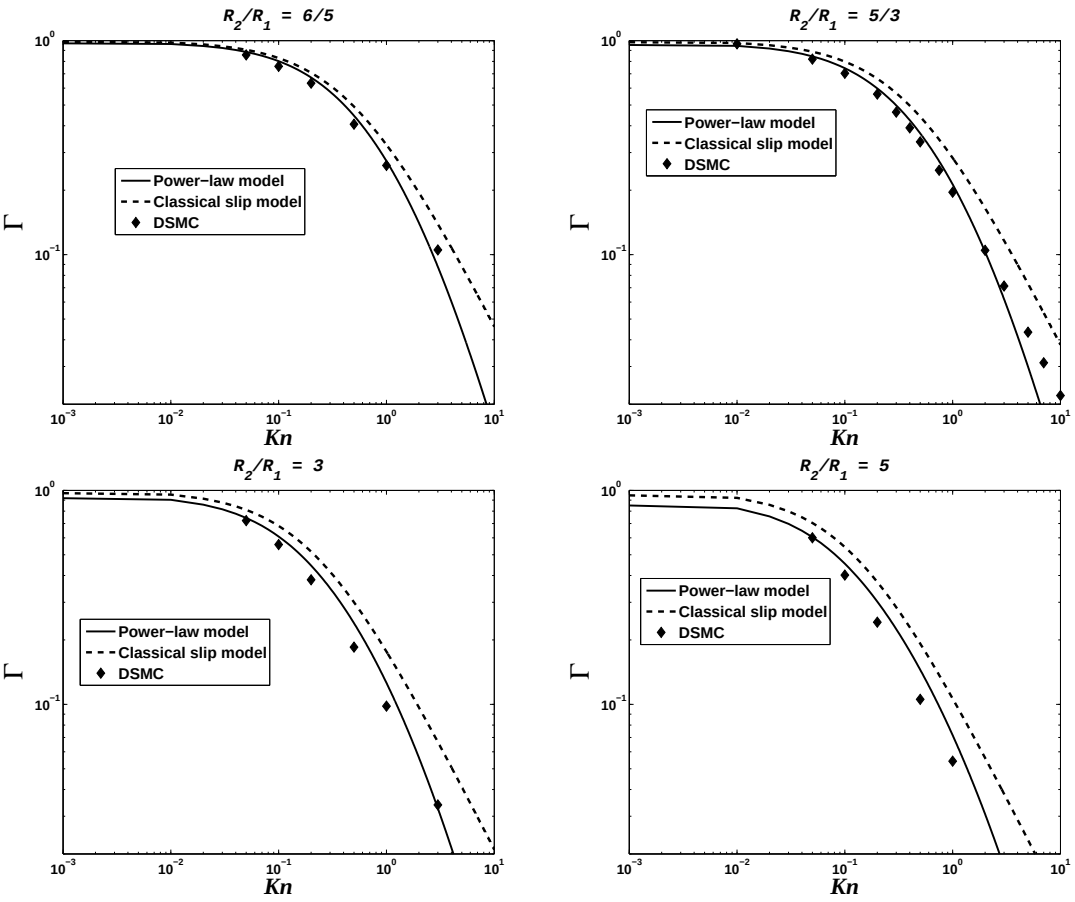

Figure 5.17: Variation of normalised torque Γ exerted on the rotating inner cylinder with Knudsen number (Kn). Our DSMC data is compared with both the slip and the PL models. The data is obtained for a specific case, where the accommodation coefficients of both the inner and outer cylinders are unity ($\sigma_1 = \sigma_2 = 1$) and $R_2/R_1 = 6/5$ (top left), 5/3 (top right), 3 (bottom left) and 5 (bottom right).

flows in the continuum regime can be expressed as (Agrawal and Prabhu, 2008b):

$$\Gamma_{\mathrm{C}} = \frac{4\pi\mu\omega L}{\left(\frac{1}{R_1^2} - \frac{1}{R_2^2}\right)}. \tag{5.42}$$

Figure 5.17 presents the variation of the normalised torque (Γ) exerted on the rotating inner cylinder with Knudsen number (Kn), and our DSMC data is compared with the slip and PL models. The data is obtained for a specific case, where the accommodation coefficients of both the inner and the outer cylinders are unity ($\sigma_1 = \sigma_2 = 1$), and for $R_2/R_1 = 6/5$, 5/3, 3 and 5. Torque values are normalised by the continuum-fluid values of the torque (Γ_{C}), see Equation (5.42). The PL model is in good agreement with the DSMC data up to $Kn \sim 2$ for $R_2/R_1 = 6/5$ and 5/3 (i.e. cases with lower curvature). The classical slip model, however, shows substantial deviations beyond $Kn \sim 0.2$. For cases with larger curvature ($R_2/R_1 =$ 3 and 5), the PL model also exhibits deviations from $Kn \sim 0.2$ onwards, although these are limited to 10-15% up to $Kn = 1$. The classical slip model predicts significant deviations even within the slip flow regime ($Kn \sim 0.05$), which conveys that non-equilibrium effects are more pronounced for larger curvature test cases.

5.1.4 Flow past a sphere

To further demonstrate the applicability of the proposed power-law model for more general non-planar cases, we now consider creeping flow past an unconfined stationary sphere, which has been widely studied both experimentally and theoretically (Basset, 1881; Millikan, 1923; Bailey et al., 2005). The present study describes an extension of Stokes analytical solution (Stokes, 1851) for creeping (low-speed) flow past a sphere which takes into account rarefaction (non-continuum) effects. In Stokes original analysis of creeping flow past a sphere, a continuum flow hypothesis was implemented and no-slip boundary conditions were utilised on the surface. However, when the size of the sphere approaches the mean free path of the gas molecules, Stokes continuum hypothesis breaks down and it is then important to account for rarefaction effects.

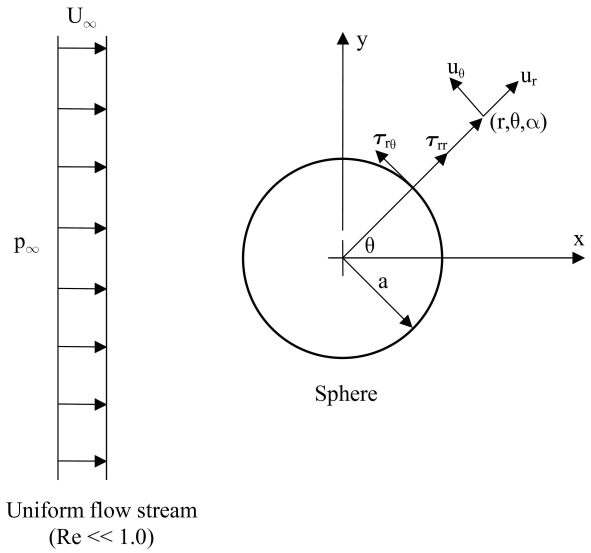

Figure 5.18: Schematic of low speed rarefied gas flow past a stationary solid sphere of radius R.

Solution procedure

Consider a stationary solid microsphere of radius R in an fluid of density ρ and free stream viscosity μ_∞, as shown in Fig. 5.18. The flow far from the sphere is of uniform speed U_∞. It is convenient to use spherical polar co-ordinates (r, θ, α) to analyse the problem, with the origin at the centre of the sphere and $\theta = 0$ aligned in the direction of U_∞. Since the flow field is axisymmetric, velocity and pressure are independent of α. In addition, as the approach flow is free from swirl, the entire flow domain will be free from swirl and consequently velocity has no component in the α-direction. It is therefore possible to analyse the problem as a planar two dimensional flow. We further assume that the fluid is incompressible and the flow obeys the Stokes equation with our geometry dependent viscosity, i.e., $\nabla.\mathbf{U} = 0$, $\nabla.\tau - \nabla p = 0$, with $\tau_{ij} = \mu_{\text{eff (sp)}} [\nabla_i u_j + \nabla_j u_i]$. We can express the effective viscosity as:

$$\mu_{\text{eff (sp)}} = \mu_\infty \beta_{\text{sp}}, \tag{5.43}$$

where β_{sp} is the geometry dependent MFP for spherical surface, which is given by Eq. (3.41).

Following the analysis of Mathews (1978), the flow velocity $\mathbf{U} = (u_r, u_\theta, u_\alpha)$ in the spherical coordinates (r, θ, α) and other flow properties can be related to a scalar variable $f(r)$ as

$$u_r = \sqrt{\frac{3}{2\pi}} \frac{f \cos\theta}{r}, \tag{5.44}$$

$$u_\theta = -\sqrt{\frac{3}{8\pi}} \left(\frac{df}{dr} + \frac{f}{r} \right) \sin\theta. \tag{5.45}$$

The drag force experienced by the sphere can be expressed as:

$$F = -\sqrt{\frac{2\pi}{3}} \left[\mu_{\text{eff (sp)}} \left(r^3 \frac{d^3 f}{dr^3} + r^2 \frac{d^2 f}{dr^2} - 6r \frac{df}{dr} + 6f \right) + \frac{d\mu_{\text{eff (sp)}}}{dr} \left(r^3 \frac{d^2 f}{dr^2} \right) \right], \tag{5.46}$$

where the scalar variable $f(r)$ can be solved from the ordinary differential equation:

$$\mu_{\text{eff (sp)}} \left(r \frac{d^4 f}{dr^4} + 4 \frac{d^3 f}{dr^3} - \frac{4}{r} \frac{d^2 f}{dr^2} \right) + \frac{d\mu_{\text{eff (sp)}}}{dr} \left(2r \frac{d^3 f}{dr^3} + 4 \frac{d^2 f}{dr^2} - \frac{6}{r} \frac{df}{dr} + \frac{6}{r^2} f \right) + \frac{d^2 \mu_{\text{eff (sp)}}}{dr^2} \left(r \frac{d^2 f}{dr^2} \right) = 0, \tag{5.47}$$

subject to boundary conditions for f, which can be derived from those for the velocity: at infinity, $u_r \to U_\infty \cos\theta$ and $u_\theta \to U_\infty \sin\theta$, where U_∞ is the free stream velocity; at the surface of the sphere ($r = R$), an impermeable condition is imposed for the radial velocity component i.e. ($u_r = 0$), and for the tangential velocity component u_θ, a velocity slip boundary condition need to be used.

The generalised first-order slip boundary condition at $r = R$ can be expressed as:

$$u_\theta = C_1 \frac{\lambda}{\mu} \tau_{r\theta}, \tag{5.48}$$

with

$$\tau_{r\theta} = -\mu \left(\frac{1}{r}\frac{\partial u_r}{\partial \theta} - \frac{1}{r}u_\theta + \frac{\partial u_\theta}{\partial r} \right), \tag{5.49}$$

which is the shear stress acting on the $r = constant$ plane in the θ-direction in spherical co-ordinates.

But on the surface of the sphere

$$\frac{\partial u_r}{\partial \theta} = 0. \tag{5.50}$$

Using the above equation and the effective MFP (see, Eq. 3.40) for spherical surface, the first-order slip boundary condition at $r = R$ is reduced to the following form:

$$u_\theta = -C_1 \lambda_{\text{eff(sp)}} \left(\frac{\partial u_\theta}{\partial r} - \frac{u_\theta}{r} \right). \tag{5.51}$$

As previously discussed, the boundary conditions can be modified to be locally second-order accurate in Kn. A higher-order boundary condition appears desirable because the solution is dominated by gas-surface interactions. Following Lockerby et al. (2004), the Burnett equations can be employed to derive higher-order boundary conditions for the N-S-F equations. The complete solution is lengthy, so only the linear higher-order terms are considered in the present analysis. With the incorporation of effective MFP, the higher-order slip boundary condition for spherical surfaces at $r = R$ can be written as

$$\begin{aligned} u_\theta = & -C_1 \lambda_{\text{eff(sp)}} \left(\frac{\partial u_\theta}{\partial r} - \frac{u_\theta}{r} \right) - C_2 \lambda^2_{\text{eff(sp)}} \left[\frac{\partial^2 u_\theta}{\partial r^2} + \frac{1}{r}\frac{\partial u_\theta}{\partial r} - \frac{u_\theta}{r^2} \right. \\ & \left. + \frac{1}{\lambda_{\text{eff(sp)}}} \frac{\partial \lambda_{\text{eff(sp)}}}{\partial r} \left(\frac{\partial u_\theta}{\partial r} - \frac{u_\theta}{r} \right) \right]. \end{aligned} \tag{5.52}$$

With these boundary conditions, Eq. (5.47) is solved using a standard boundary-value numerical solver. $C_1 = 1$ and $C_2 = 0.5$ values have been used (Guo et al., 2007).

Results

In Figs. 5.19 and 5.20, the velocity profiles for different inverse Knudsen number, $\delta = (\sqrt{\pi}/2)Kn^{-1}$ ($Kn = \lambda/R$), are shown. The PL model predictions are compared with the results of the Boltzmann equation (Lea and Loyalka, 1982), Stops wall scaling model (Guo et al., 2007), and the classical Navier-Stokes equations with the second-order boundary condition but with a constant MFP (the conventional second-order slip model for the sake of brevity). The PL model has very good agreement with the kinetic theory results up to $\delta \sim 1$ for u_θ, and up to $\delta \sim 0.1$ for u_r. Both the Stops' wall scaling and conventional slip models overpredict the wall-slip velocities for u_θ. Sharper velocity gradients are noticed in the PL model predictions for both u_θ and u_r, whereas profiles are shallower for the other two theoretical models.

In Fig. 5.21, the drag force normalized by the Stokes drag for continuum flows, $D^* = F/(6\mu R U_\infty)$, is presented as a function of Kn. The PL model results are compared with experimental data (Millikan, 1923), R13 equations (Torrilhon, 2010), Grad's 13 moment equations (Goldberg, 1954), and the conventional second-order slip model. All four hydrodynamic models show very good agreement with the experimental data up to $Kn \sim 0.1$. However, with a further increase in Kn, excepting the PL model, the other three theoretical models, start to deviate substantially from the experimental data. The classical slip model and Grad's 13 moment equations overpredict the experimental data, where as the R13 equations underpredicts the data. The PL model has excellent agreement with the data up to $Kn \sim 0.6$ and slight deviations are noticed with further increase in Kn.

5.2 Thermal gas flows

5.2.1 Thermal creep between two plates

To test the applicability of our PL-based effective MFP scaling for thermal gas flows, we consider thermal transpiration of a rarefied gas along a planar-wall channel, with walls a distance H apart. We consider the steady state situation, where two containers, filled with a single-component rarefied gas, are kept at the same

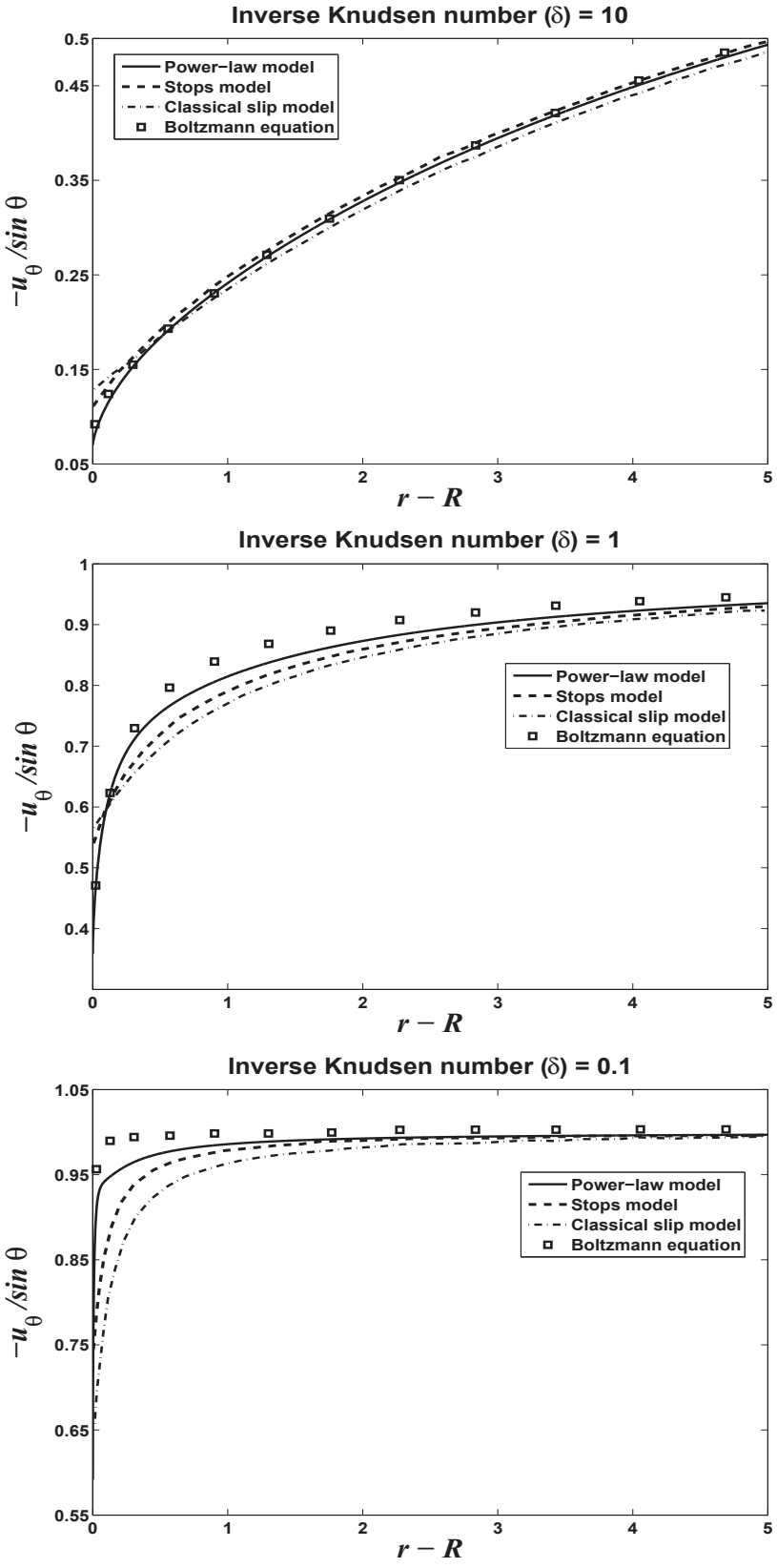

Figure 5.19: Flow past a sphere: normalised θ-component velocity profiles as a function of normalized radial distance for various inverse Knudsen numbers in the transition flow regime. Comparison of power-law model with the Boltzmann equation (Lea and Loyalka, 1982), Stops wall scaling model (Guo et al., 2007), and the conventional second-order slip model.

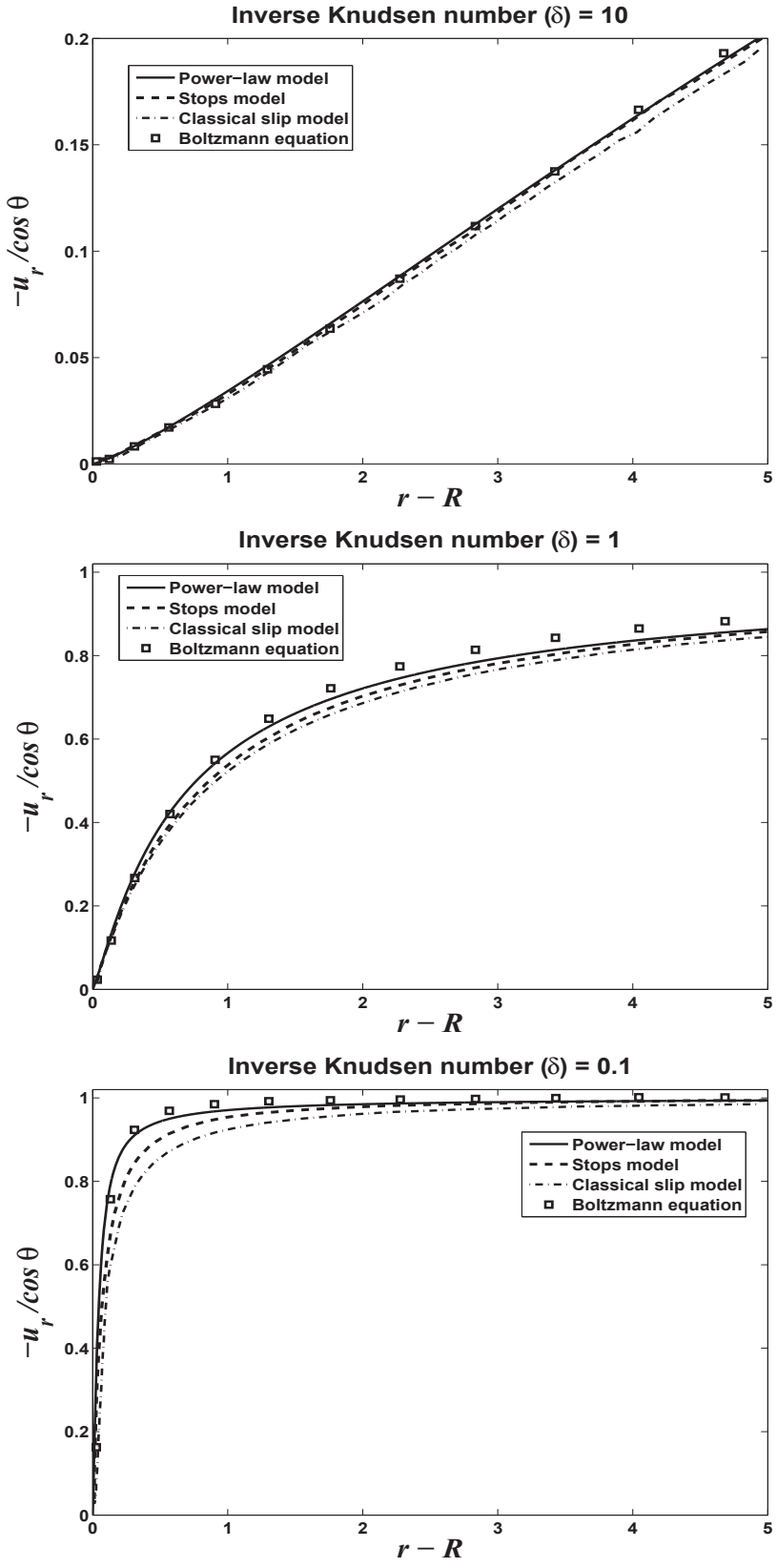

Figure 5.20: Flow past a sphere: normalised r-component velocity profiles as a function of normalized radial distance for various inverse Knudsen numbers in the transition flow regime. Comparison of power-law model with the Boltzmann equation (Lea and Loyalka, 1982), Stops wall scaling model (Guo et al., 2007) and, the conventional second-order slip model.

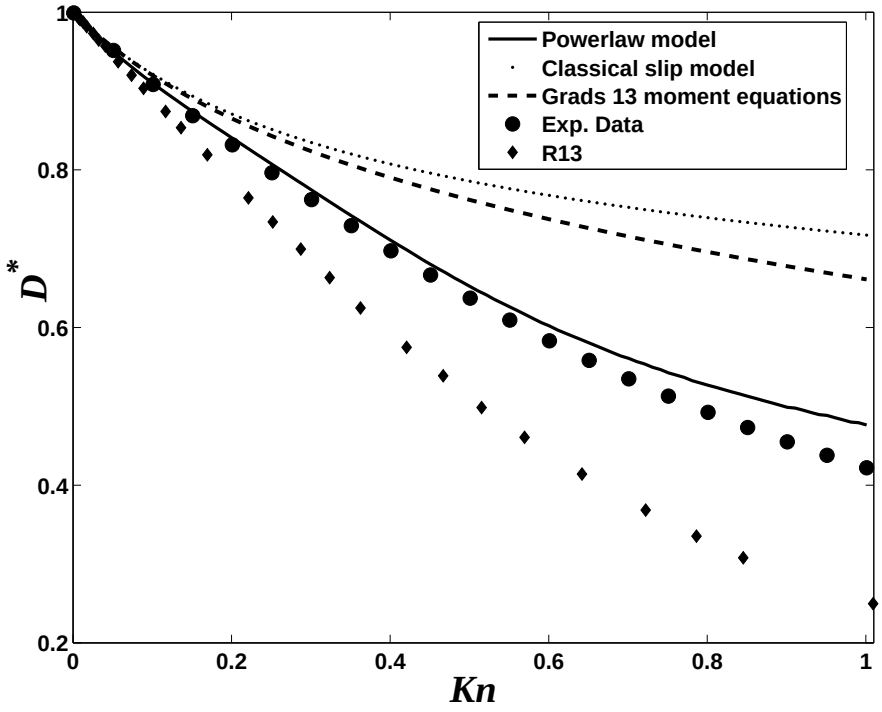

Figure 5.21: Flow past a sphere: variation of normalised drag force as a function of Kn. Power-law model results are compared to experimental data (Millikan, 1923), the conventional second-order slip model, R13 equations (Torrilhon, 2010), and Grad's 13 moment equations (Goldberg, 1954).

pressure, but at different uniform temperatures. Gravity effects are neglected, and two containers are connected by the planar-wall channel. According to the classical N-S-F equations, and using the no-slip boundary condition for the velocity, no fluid flow should occur in the channel. The only phenomenon that should take place is steady state axial heat conduction between the hot and cold ends of the channel, which results in a linear temperature variation along the length of the capillary, accompanied by a corresponding isobaric increase in the fluid's density. The pressure should be uniform throughout the channel, i.e. $P_1 = P_2$, due to the absence of fluid flow. On the contrary, Reynolds's experimental (Reynolds, 1880) and Maxwell's theoretical (Maxwell, 1879) studies on the viscous stresses in rarefied gases (arising from inequalities of temperature which exist along the channel) showed the phenomenon of thermal transpiration (creep), where the fluid starts creeping in the direction from cold toward hot. This thermal transpiration was originally named by Reynolds (1880), and later confirmed experimentally by many other researchers for different gases (Knudsen, 1910; Massen et al., 1967; Annis, 1972; Han et al., 2007).

Maxwell (1879) used non-continuum arguments based on the proposition that the presence of molecular-wall effects results in thermal slip (thermal creep) of the fluid's convection velocity at the wall in the streamwise direction. Although the this slip boundary condition was originally proposed for atomically smooth walls, Maxwell's non-continuum theory is widely accepted due to its qualitative agreement with experiment (Reynolds, 1880). Later, it is worth noting, many researchers have come up with alternative theoretical considerations to explain thermal transpiration, e.g. see Chapman and Cowling (1970) on the classical near-continuum first-order molecular theory, and Derjaguin and Yalamov (1967) combining kinetic theory with non-conventional irreversible thermodynamics. The physical explanation of thermal creep has been presented by Sone (2002).

Solution procedure

The flow is assumed to be fully hydrodynamically developed and two-dimensional, laminar and steady, i.e. zero net mass flow, with a low Reynolds number (Re) so that

inertial effects may be neglected. With these assumptions, the governing equations are:

$$0 = -\frac{\partial P}{\partial x} - \frac{\partial \tau}{\partial y}, \tag{5.53}$$

and

$$0 = -\frac{\partial q}{\partial x}, \tag{5.54}$$

where x and y are axial and wall normal coordinates, respectively, and q is the heat flux, which is given as:

$$q = -k\frac{\partial T}{\partial x}, \tag{5.55}$$

and k is the thermal conductivity, defined as:

$$k = \rho C_p \frac{\lambda_T}{\sqrt{\pi/2RT}}. \tag{5.56}$$

Using Eqs. (3.14 and 3.20), the non-dimensional effective MFP for a thermal case, $\beta_{\mathrm{PL(T)}}$, we therefore posit a non-linear constitutive relation for heat flux:

$$q = -k\beta_{\mathrm{PL(T)}}\frac{\partial T}{\partial x}. \tag{5.57}$$

Eqs. (5.53), (5.54) and (5.57) are solved in conjunction with the following slip boundary condition:

$$\begin{aligned} U_{slip} &= \underbrace{-C_1\lambda\left(\beta_{\mathrm{PL}}\frac{\partial U_x}{\partial y}\right)_w - C_2\lambda^2\left[\beta_{\mathrm{PL}}\frac{\partial}{\partial y}\left(\beta_{\mathrm{PL}}\frac{\partial U_x}{\partial y}\right)\right]_w}_{U_{Pslip}} \\ &+ \underbrace{\frac{3}{4}\frac{k\beta_{\mathrm{PL(T)}}}{C_v\rho T}\left(\frac{\partial T}{\partial x}\right)_w}_{U_{Tslip}}, \end{aligned} \tag{5.58}$$

where U_{Pslip} and U_{Tslip} are the isothermal and thermal creep components of the slip velocity. This boundary condition simply reduces to the conventional slip condition

if the Knudsen layer is ignored, i.e. if β_{PL} and $\beta_{\mathrm{PL(T)}}$ = const. = 1. The first- and second-order slip coefficients are fixed as $C_1 = 1$ and $C_2 = 0.31$.

The wall-normal coordinate, y, is normalised by H, i.e. $y^* = y/H$ and the axial velocity components, U_T the thermal creep velocity and U_P the Poiseuille velocity, by the free-molecular velocities $U_{T0} = \sqrt{2RT}(H/T)(\partial T/\partial x)$ and $U_{P0} = -2H(\partial P/\partial x)/(\rho\sqrt{2RT})$. Using Eqs. (5.3, 5.56, 3.20 and 5.5) we solve for the normalised velocity components (U_T^*, U_P^*), normalized flow rate components ($G_T = 2\int_0^{0.5} U_T^* dy^*$, $G_P = 2\int_0^{0.5} U_P^* dy^*$), and the thermo molecular pressure difference (TMPD) i.e. $(T/P)(dP/dx)/(dT/dx)$, assuming zero net mass flow rate at steady state. This parameter is of great interest in micro/nano machine engineering, as it describes the maximum pressure difference that a thermal creep pump can produce for a given temperature difference applied across the channel ends. Pumping devices without any mechanical parts are attractive, for example, in space, where natural heat and sink sources are available (Han et al., 2007).

Results

The thermal creep components of the cross-sectional velocity profiles over a range of Knudsen numbers are presented in Fig. 5.22. Our PL model for this thermal case is validated against the results of the Boltzmann equation (Ohawada et al., 1989) and compared with two other hydrodynamic models: a conventional slip solution, and the Arlemark et al. (2010) exponential wall scaling results. At $Kn = 0.2$, which is just beyond the slip-flow regime, our PL model predicts a wall-slip velocity close to the solution obtained from the Boltzmann equation, and displays minor deviations in the Knudsen layer. The exponential MFP model produces shallower gradients in the KL, compared to the PL model, and underpredicts the velocities in the bulk flow region. The conventional NS equations with second-order slip boundary conditions overpredicts in both the KL and bulk flow regions. At $Kn = 0.8$ and $Kn = 2.0$, which are in the transition regime, the exponential model overpredicts in both the Knudsen layer and the bulk flow. The PL model is in fair agreement in the region close to the wall, with minor deviations in the bulk. At even higher Kn, the non-

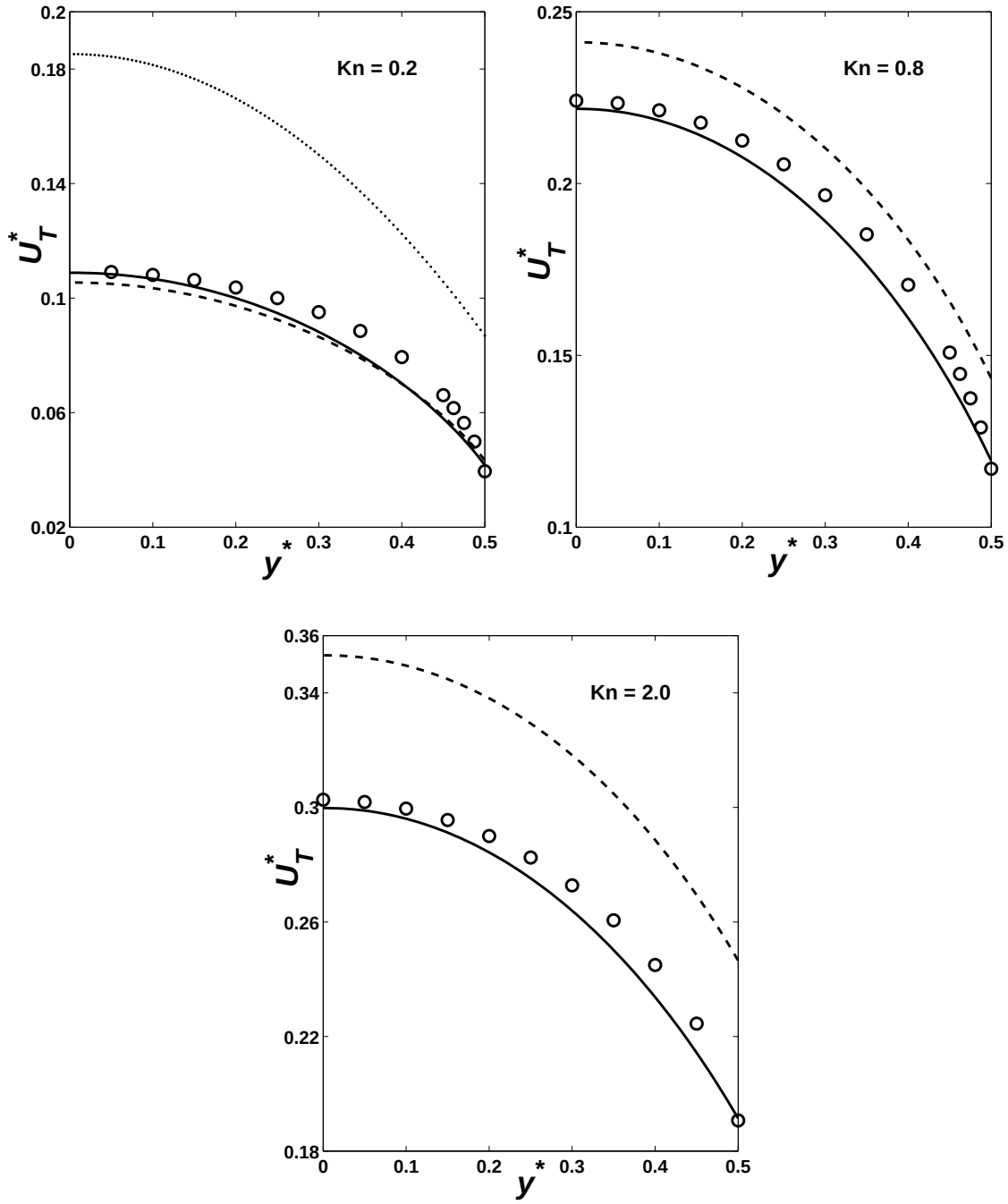

Figure 5.22: Normalised thermal creep component of half cross-channel velocity profiles for various Knudsen numbers. Comparison of our power-law (PL) model results (solid line) with the solution of the Boltzmann equation (symbols, Ohwada et al., 1989), exponential MFP model (dashed line, Arlemark et al., 2010), and the conventional second-order slip solution (dotted line).

equilibrium regions from each of the parallel walls start to overlap each other: the PL model underpredicts, and the exponential model overpredicts the results (Dongari et al., 2010b).

Fig. 5.23 shows the variations of the thermal creep and Poiseuille components of the normalized mass flow rates (G_T and G_P) with Knudsen number. Our PL model results are compared with hard sphere Boltzmann results (Sharipov, 2009), BGK simulation data (Loyalka, 1975), the NSF equations using the exponential wall scaling model, and the conventional second-order slip solution. The second-order slip solution is in fair agreement up to the slip flow regime, but diverges at higher Kn. The exponential wall scaling model predicts good results up to $Kn \sim 0.5$ in the case of the thermal creep component and up to $Kn \sim 2$ for the Poiseuille component, but overpredicts and underpredicts for higher Kn, respectively. The PL model however, is in fair agreement with the hard sphere data up to $Kn \sim 10$, with minor underpredictions for both G_T and G_P.

Figure (5.23) also shows the TMPD variation with Knudsen number. The conventional slip solution, the exponential and PL models show good agreement with the hard-sphere model up to $Kn \sim 0.05$, $Kn \sim 1$ and $Kn \sim 5$, respectively. The BGK simulation underpredicts throughout the Kn regime, which may be because of the limitations of the BGK model when applied to thermal flow cases.

It is commonly accepted that the flow close to the boundary will move from the cold to hot region, then return in the middle for a closed tube/channel. However, the current PL model results show that the flow patterns depend on Knudsen numbers, which is more non-intuitive than people originally think of. Fig. 5.24 shows the normalised slip velocity variation as a function of Knudsen number. The slip velocity is normalised by the free-molecular velocity $U_{P0} = -2H(\partial P/\partial x)/(\rho\sqrt{2RT})$. Surprisingly, with the increase of Knudsen number ($Kn > 0.1$), the flow can move along the tube surface from the hot to cold regions, while for $Kn < 0.1$ the creep at the boundary is taking place as expected, i.e. from cold to hot regions. Although this observation contradicts with the conventional theoretical prediction, qualitatively agrees with the recent findings of unified gas kinetic scheme and DSMC simulations (Xu, 2012).

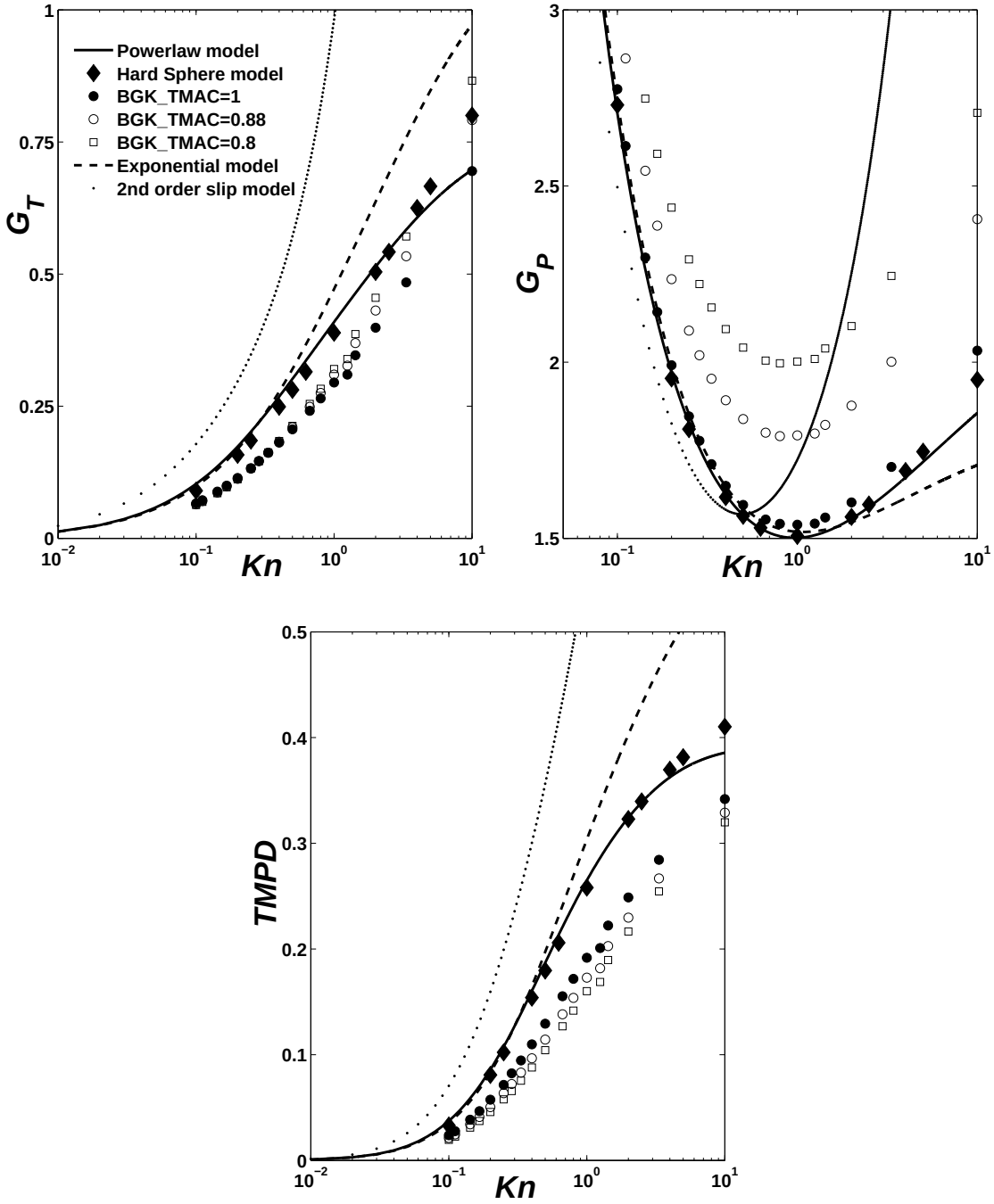

Figure 5.23: Variation of normalised thermal creep component (G_T) and Poiseuille component (G_P) of mass flow rates, and TMPD, with Knudsen number (Kn). Comparison of our power-law (PL) model results with: hard sphere Boltzmann equation (Sharipov, 2009), BGK simulation data (Loyalka, 1975), exponential MFP model (Arlemark et al., 2010), and the conventional second-order slip solution.

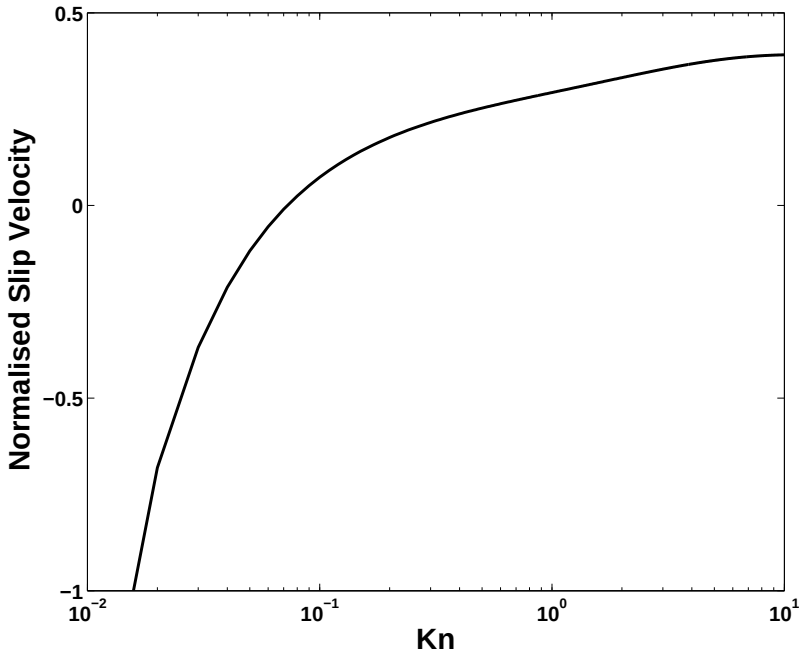

Figure 5.24: Variation of normalised slip velocity as a function of Knudsen number. The slip velocity is normalised by the free-molecular velocity $U_{P0} = -2H(\partial P/\partial x)/(\rho\sqrt{2RT})$. For $Kn > 0.1$ the flow can move along the tube surface from the hot to cold regions, while for $Kn < 0.1$ the creep at the boundary is taking place as expected, i.e. from cold to hot regions.

5.2.2 Fourier heat transfer between two plates

As a second test case for thermal flows, we consider Fourier heat transfer in a rarefied gas between two parallel plates. This fundamental problem in rarefied gas dynamics has attracted significant interest. The classical Fourier geometry is defined by a quiescent gas occupying the region between two infinite, parallel plates at unequal temperatures. The parallel plates are separated by a gap, H, and the coordinate system is defined such that its origin ($y = H/2$) corresponds to the centre of the gap between the two plates, and the y-axis is normal to the plates. Detailed descriptions of this test configuration are also presented in other works (for example, see Teagan and Springer, 1968). The temperature of the top plate, T_h, is assumed (without loss of generality) to be higher than that of the bottom plate, T_c. The mean temperature $(T_h + T_c)/2$ is used as a reference temperature T_0. Because of the imposed temperature difference, heat is conducted through the gas from the hot plate to the cold plate. The theoretical analyses assume that the gas is quiescent (no net mass flow). Radiation effects are assumed to be inconsequential in the present

analysis.

Solution procedure

For this flow configuration, the classical set of continuum equations reduces to the following: the continuity and momentum equations vanish, and we only need to solve the energy equation. The governing equation is:

$$0 = -\frac{\partial q}{\partial y}. \tag{5.59}$$

Using the non-dimensional effective MFP for a thermal case, $\beta_{\mathrm{PL(T)}}$, we posit a non-linear constitutive relation for the heat flux:

$$q = -k\beta_{\mathrm{PL(T)}}\frac{\partial T}{\partial y}. \tag{5.60}$$

Eqs. (5.59) and (5.60) are solved for temperature in conjunction with the following temperature jump boundary condition at both walls (Smoluchowski, 1898):

$$T_{jump} = T_w + \left(\frac{2-\alpha}{\alpha}\right)\left[\beta_{\mathrm{PL(T)}}\lambda\frac{\partial T}{\partial y}\right]_w, \tag{5.61}$$

where α is the thermal accommodation coefficient (TAC) and subscript w denotes the wall.

The wall-normal coordinate, y, is normalized by H, i.e. $y^* = y/H$ and the temperature T by the reference temperature T_0, i.e. $T^* = T/T_0$.

Results

Fig. 5.25 presents normalized temperature profiles between the plates for various Knudsen numbers in the slip and transition flow regimes. The PL model results are validated with the DSMC data (Gallis et al., 2002) and also compared with the classical temperature jump model (which has no MFP variation). The hot and cold plates are assumed to be fully diffuse ($\alpha = 1$) isothermally reflecting surfaces with temperatures $T_c = 263$ K and $T_h = 283$ K, respectively. It is expected that the classical jump model predicts linear temperature profiles, and it shows good

agreement with the DSMC data and the PL model up to $Kn = 0.158$. For higher Kn cases, the classical jump model significantly overpredicts the wall-jump effects. The PL model is able to accurately predict non-linear effects in the thermal Knudsen layer and shows good agreement with DSMC data up to $Kn = 1.58$. With further increase in Kn, the PL model also exhibits significant deviations from the simulation data, however, it has greatly improved the predictive capabilities of continuum equations in the transition flow regime.

To check the sensitivities of the thermal accommodation coefficient (α) and the temperature difference between the parallel plates, on the predictive capabilities of our wall-scaling approach, we compare our PL model with kinetic theory results for $\alpha = 0.826$, and T_h and T_c are 288 K and 368 K, respectively. Fig. 5.26 depicts the variations in the normalised temperature profiles as a function of the normalized distance from the wall, for Argon gas. Results from the Boltzmann equation (Ohwada, 1996), which is solved using the variational method (hard-sphere, Maxwell-type boundary condition) are shown in the figure for $Kn = 0.0658$, 0.1395, 0.9142, 0.2994 and 0.7582. The agreement between our model and the variational method is fair for all Knudsen numbers. The temperature profiles presented in Fig. 5.26 exhibit larger non-linear and wall-jump effects compared to the ones in Fig. 5.25. This may be due to the larger temperature difference between the parallel plates and smaller TAC value when compared to the former case.

Fig. 5.27 shows the variation of normalised heat flux as a function of inverse of Knudsen number for Argon and Nitrogen gases. The heat flux is normalised by the free molecular heat flux $Q_{FM} = -(\alpha/2 - \alpha)\rho\sqrt{(\Re T_0/2\pi)}(c_v + \Re/2)(T_h - T_c)$. As given by Teagan and Springer (1968), TAC values of 0.826 and 0.76 have been used to obtain the results for Argon and Nitrogen gases, respectively. Fig. 5.27 compares our PL model predictions with results from other existing theories as well as reported experiments. In the case of Argon gas, the agreement between the experimental data and the PL predictions is found to be good at higher Knudsen numbers. However, the results slightly deviate from the experimental and simulation data for lower Knudsen numbers. This discrepancy may be attributed to the fact that the accommodation coefficients of both plates were determined through Knudsen's for-

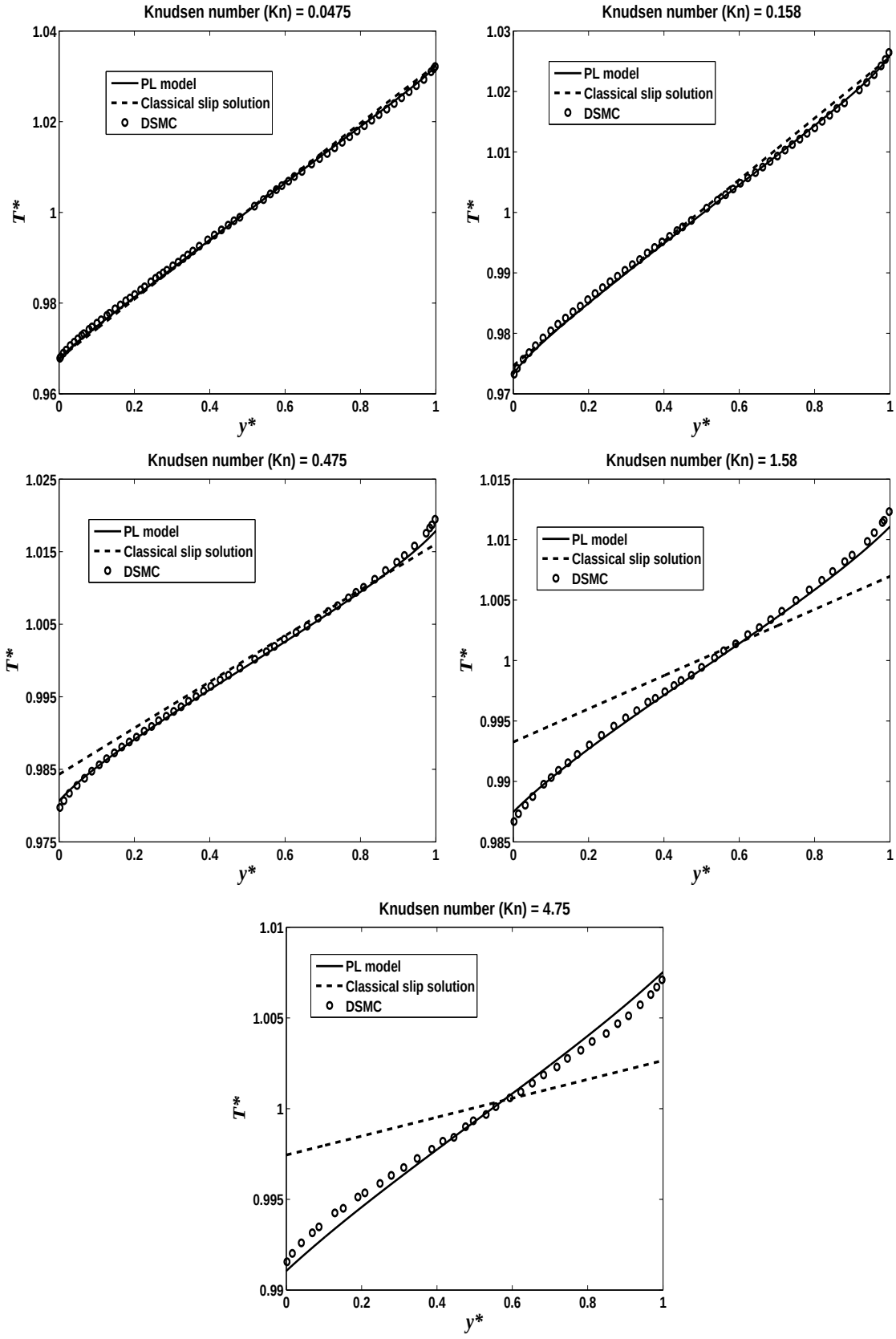

Figure 5.25: Nondimensional temperature profiles for rarefied Fourier flow of stationary Argon gas between two parallel plates. The hot and cold plates are at temperatures T_c = 263 K and T_h = 283 K, respectively. The power-law (PL) model results are validated against DSMC simulation data (Gallis et al., 2002) and also compared with the classical temperature jump model results in the slip and transition flow regimes.

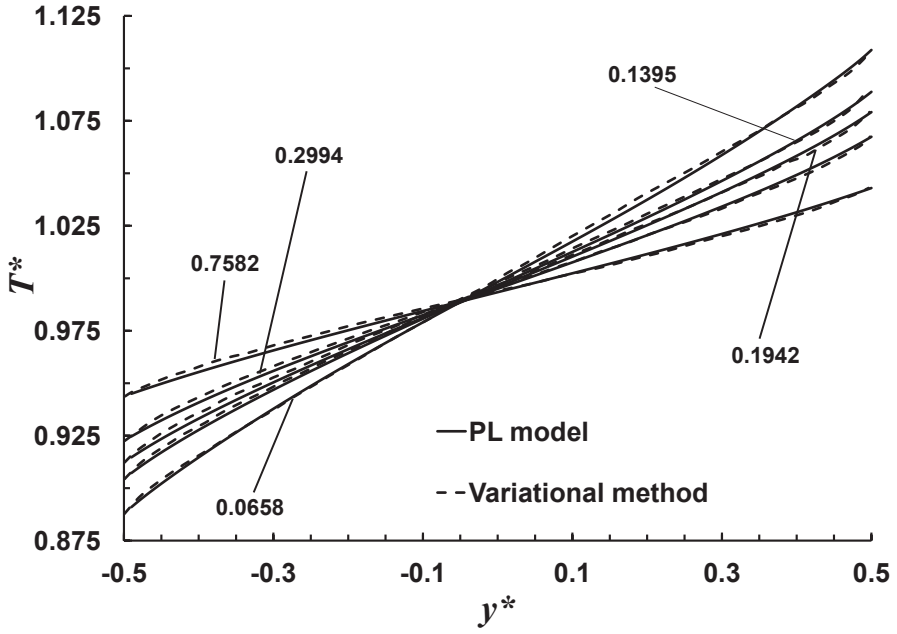

Figure 5.26: Nondimensional temperature profiles for rarefied Fourier flow of stationary Argon gas between two parallel plates with TAC value $\alpha = 0.826$. The hot and cold plates are at temperatures $T_c = 288$ K and $T_h = 368$ K, respectively. The power-law (PL) model is compared with the variational method results (Ohwada, 1996) in the slip and transition flow regimes.

mula from the heat flow measured under free-molecular conditions. Hence, these values may not remain the same for the whole range of Knudsen number and the agreement of the present theory can be improved by slightly decreasing the value of TAC. However, for a fixed value of accommodation coefficient, the average percentage deviation between the experimental results and the present solution is within 5.2%, over the entire Kn range. In the case of Nitrogen gas, the agreement between our model, and experimental and simulation data is fair.

5.3 Summary

Using our power-law geometry dependent MFP model, a simple constitutive scaling approach to model the Knudsen layer flow within a conventional continuum fluid dynamics framework has been described, in accordance with the kinetic theory of gases. The new methodology has been tested for the cases of isothermal and thermal rarefied gas flows in planar and non-planar geometries. The PL model is

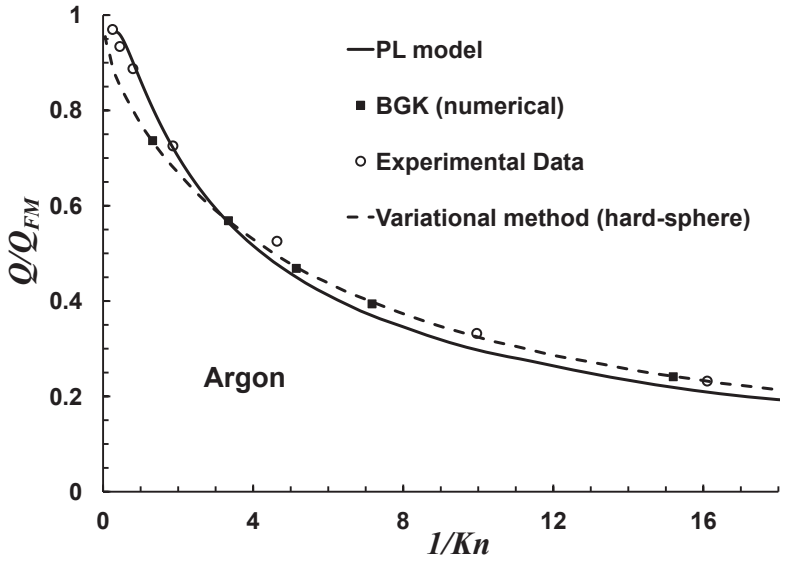

(a)

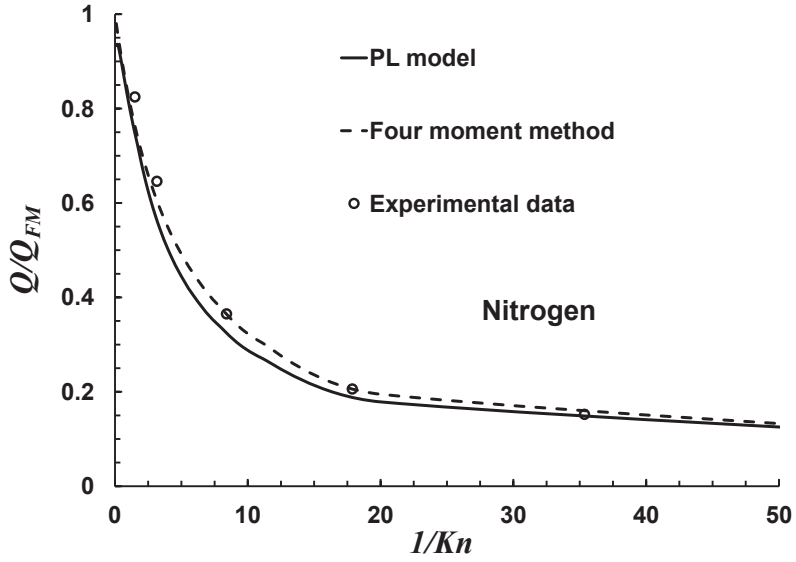

(b)

Figure 5.27: Variation of normalised heat flux in the Fourier heat flow case as a function of inverse Knudsen number for (**a**) Argon and (**b**) Nitrogen gas. Comparison of our model with the experimental data (Teagan and Springer, 1968) and simulation results. As given by Teagan and Springer (1968), TAC values of 0.826 and 0.76 have been used to obtain results for Argon and Nitrogen gases, respectively.

validated whenever possible against rigorous MD and DSMC simulation data for field properties, and experimental data for integral flow parameters.

In general, for planar geometries our new power-law model is more accurate than the conventional hydrodynamic model in capturing many non-equilibrium effects in the transition regime. Our results for both isothermal and thermal flows indicate that it provides a reasonable description of the nonlinear flow characteristics in the Knudsen layer up to $Kn \sim O(1)$. In predicting integral flow parameters, such as normalized flow rate, torque and the TMPD, the power-law model provides a significant improvement up to $Kn \sim 5$. The classical exponential probability distribution function MFP models provide accurate results in the Knudsen layer only up to $Kn \sim 0.2$, and integral flow parameter results only up to $Kn \sim 1$.

The N-S-F equations with higher-order slip boundary conditions can correctly capture the surface slip by tuning the slip coefficients, but they do not necessarily then provide accurate velocity profiles in both the Knudsen layer and the bulk flow regions. While the N-S-F equations with an exponential-based MFP can provide good velocity profiles in the Knudsen layer up to the early transition regime, with our new power-law model we can also adjust the velocity profile at a fixed Knudsen number by using the exponent n.

For cylindrical Couette flow test case, the PL model predictions are in very good agreement with DSMC data up to $Kn \sim 1$, with slight deviations in the near-wall region at the inner cylinder. The simulation data and the PL model also predict partially inverted velocity profiles for moderate σ values, whereas the slip model does not capture this phenomenon. However, the DSMC data at larger R_2/R_1 values also illuminates the limitations of the PL wall scaling model. With an increase in R_2/R_1, the PL model significantly underpredicts the velocity in the near-wall region of the inner cylinder, but does obtain fair comparison in the near-wall region of the outer cylinder. This shows that the non-equilibrium effects in the near-wall region are not merely dependent on Kn, but they are also influenced by curvature, since deviations between the DSMC data and PL model are more pronounced for larger R_2/R_1 values.

Although the predictive capabilities of the PL model are fair for torque com-

parisons up to the transition regime, the model fails to capture some of non-linear trends associated with the Knudsen layers at the inner cylinder for $R_2/R_1 = 3$ and 5. Hence, torque and velocity profile comparisons together also convey that mere prediction of integral flow parameters does not guarantee the complete accuracy of any theoretical model, and it is important to demonstrate that the field variables are also in agreement with other accurate simulation data.

Chapter 6

Conclusions

An error does not become truth by reason of multiplied propagation,
nor does truth become error because nobody sees it
- Mahatma Gandhi

6.1 Discussion and summary

In microsystems, the characteristic dimensions of a device can approach the mean free path of a gas flowing within it, causing the flow to become rarefied. As the flow becomes rarefied, the continuum and equilibrium assumptions of macroscale fluid dynamics begin to break down. The loss of local thermodynamic equilibrium implies that the microscopic behaviour of the gas can affect the distribution of macroscopic quantities such as velocity, temperature and pressure, resulting in large gradients in these fields. As such, the classical N-S-F equations with linear constitutive relations and the no-slip and jump boundary conditions, the traditional method of analysing fluid flow and heat transfer at the macroscale, are not suitable for gas microflows.

The Boltzmann equation and the kinetic theory of gases may be used to accurately determine the behaviour of rarefied gas flows, but are applicable in practice only to 1- and 2-dimensional problems (Cercignani, 2001). An equivalent to solving the Boltzmann equation is to use the numerical DSMC method, which averages macroscopic field variables from deterministic simulations of molecular interactions (Bird, 1994). Given sufficient computational resources, the DSMC method may be

used successfully to model flows in complex, practical geometry. The limiting factor on the application of DSMC is the requirement to reduce statistical scatter to produce accurate averaged quantities. For the low-speed flows common to microdevices, the low signal-to-noise ratio can make DSMC computationally intensive.

As many microscale devices are currently designed by trial and error, an efficient analytical tool for engineering design applications is required. One method of achieving this aim is to extend the N-S-F equations beyond the strict limits of their applicability into the slip- and transitional-Kn flow regimes. Two key aspects of gas rarefaction that cannot be captured using continuum methods are boundary discontinuities and the Knudsen layer. These surface phenomena are dominant in gas microflows, where the surface area-to-volume ratio is high.

A number of boundary conditions describing velocity-slip and temperature-jump phenomena are available for continuum analyses of rarefied flow. The robust phenomenological model proposed by Maxwell for velocity slip, and its equivalent proposed by Smoluchowski for temperature, are the most widely used of these boundary conditions (Maxwell, 1879; Smoluchowski, 1898). These boundary conditions are accurate in many applications if they are applied within the limits of their original derivations. For curved surfaces an extra term must be added to the slip boundary condition to describe wall-normal variation of velocity (Lockerby et al., 2004; Barber et al., 2004). When both slip and jump conditions are applied together, the assumptions implicit in the slip equation about the relative rate of exchange of energy and momentum must be taken into account (Maxwell, 1879).

The Knudsen layer is the near-wall region one to two mean free paths thick where local thermodynamic equilibrium is not maintained between a gas and its bounding surface. This region exists in gas flows at all scales, but is significant to the macroscopic behaviour of the flow only when the length scale of the mean free path approaches the length scale of the system. The Knudsen layer is characterised by strong departures from the linear constitutive relationships of the N-S-F equations for shear stress/strain-rate and heat flux/temperature-gradient. In rarefied flows the structure of the Knudsen layer can represent a significant proportion of a flow, and consequently affect its macroscopic behaviour (Lockerby et al., 2005b). Constitutive

scaling, which replaces viscosity and thermal conductivity with effective values, is an efficient method of incorporating non-linear Knudsen layer effects in continuum fluid dynamics simulations. Several constitutive scaling models have been proposed in the academic literature, the foremost of which are functions presented in (Lockerby et al., 2005a) and (Reese et al., 2007).

In this thesis an extension of the Navier-Stokes-Fourier equations is derived. This method is based on a description of how the travelling distance of molecules between collisions, the free path, is terminated by the gas molecules colliding with solid walls in addition to the inter-gas molecular collisions. The average of these distances is here considered to be a geometry-dependent mean free path (MFP) referred to as the effective MFP. It has been theoretically shown that the probability distribution of free paths, is only exponential under thermodynamic equilibrium conditions and when the gas is unbounded. It is pointed out that a finite moment of the probability distribution function implies an exponential character of the randomness. A distribution function with diverging higher-order moments (such as the standard deviation) is essential to anomalous transport. Hence, we hypothesise a power-law (PL) form with diverging higher-order moments, for the probability distribution function for non-equilibrium gas MFP, instead of the classical exponential form of distribution function.

For a gas in a near-wall region it is still assumed that the molecule is equally probable to travel in any direction and that this direction is independent of the speed that the molecule is travelling in. It is also assumed that molecules are equally probable to experience collisions in any part of their travelling trajectories towards solid boundaries as for molecules travelling in the direction of an unconfined gas. However, in case a molecule approaches a wall it will clearly experience a collision. This is accounted for in the probability function since the upper limit of the probability functions dependence on the travel distance is set to the wall distance. Based on the PL distribution function, effective MFP model is investigated in the close vicinity of geometries with one planar wall, two planar walls, cylindrical obstacle, hallow cylinder and a spherical obstacle.

A validation of the PL distribution function is performed using the method of

molecular dynamics for neon and argon gases. This method simulates the gas in a detailed manner by describing it as a discrete number of molecules interacting by Lennard-Jones repulsive short-range and attractive long-range forces. Since the molecules in this description do not experience collisions at instantaneous moments but instead interacts through continuous forces, the defined criterion of a collision has to be implemented. In the molecular dynamics simulations of this thesis a collision between molecules is considered to have occurred if they are closer to each other than their equivalent hard-sphere diameter. This criterion for molecular collisions is consistent with the theoretical description, which is essential for comparisons between these methods. The parameter used for determining the magnitude of the potential between the molecules is also chosen so that consideration is taken to the hard-sphere diameter so that the scattering of molecules occurs in a similar manner as for more commonly used Lennard-Jones parameters.

It is found that the molecular dynamics simulation reproduces the theoretical values of the mean free path for argon and neon within an approximate accuracy of 1%. Inter-molecular collision rate measurements show less fluctuations at standard density conditions and the standard deviation is significantly high for low density case, which illustrates the anomalous nature of the rarefied gas. Correspondingly, molecular free path measurements predict a long tail and the classical exponential distribution function is only accurate under equilibrium conditions, which describes the Brownian motion. On the other hand MD data also follow longer flights and compare well with the power-law distribution function. The free path measurements of individual molecules convey that conventional form of exponential distribution function is not valid under rarefied conditions and follow Lévy type of flights, *irrespective of the presence of the wall*.

MFP of the gas molecule ensemble reduces to the theoretical value of MFP, only if the gas is not bounded. If a solid bounding surface is included in the system, however, some molecules will hit the surface and their free flight paths will be terminated. The MFP of all the gas molecules in the system will therefore be smaller than λ, due to this boundary limiting effect. Wall-dependent MFP measurements are carried out for planar single- and parallel-walls cases. Total simulation time

varied from 5 to 20 nano seconds based on the degree of rarefaction. MD data is compared with the exponential and power-law based effective MFP profile solutions. Power-law exponent n value is considered to be 3 for both single- and parallel-wall comparisons.

At $Kn = 0.2$, which is just beyond the slip-flow regime, the PL model is in fair agreement with the MD data in the near-wall region but deviates slightly in the bulk region. The exponential model underpredict the MD data in the Knudsen layer and show fair agreement in the bulk flow. As the value of Kn increases, and the flow becomes increasingly transition-continuum, the classical model fail to predict the effective MFP in the wall region, as well as in the bulk. Effective MFP values predicted by the PL model compare very well to the MD data for both $Kn = 0.5$ and 1, although it overpredicts for $Kn = 1$ in the bulk. By $Kn = 2$, when both the Knudsen layers completely overlap each other, the PL model shows significant deviations from the simulation data and overpredicts in the near-wall region, although there is fair agreement in the bulk region. The exponential solution show shallower gradients close to the wall, while both the MD data and the power-law model exhibit sharper gradients. The present MD results support the argument that anomalous behaviour of rarefied gases is better described with Lévy/power-law type of distribution functions as compared to the classical exponential function.

The PL based effective mean free path is applied for solving the N-S-F equations. For this method the effective mean free path is shown to relate to the viscosity through a linear relationship which in turn yields a geometry-dependent viscosity. It is also argued that the effective mean free path should be involved in the velocity-slip boundary conditions instead of the conventional unconfined mean-free-path value.

In general, our new power-law MFP model is more accurate than the conventional model in capturing many non-equilibrium effects in the transition regime. Our results for both isothermal and thermal flows of planar cases indicate that it provides a reasonable description of the nonlinear flow characteristics in the Knudsen layer up to $Kn \sim 1$. The N-S-F equations with higher-order slip boundary conditions can correctly capture the surface slip by tuning the slip coefficients, but do not necessarily then provide accurate velocity profiles in both the Knudsen layer and

the bulk flow regions. While the N-S-F equations with an exponential-based MFP can provide good velocity profiles in the Knudsen layer up to the early transition regime, with the new power-law model we can also adjust the velocity profile at a fixed Knudsen number by using the exponent n. In predicting integral flow parameters, such as normalized flow rate and the TMPD, the power-law model provides a significant improvement up to $Kn \sim 5$. The classical exponential probability distribution function MFP models provide accurate results in the Knudsen layer only up to $Kn \sim 0.2$, and integral flow parameter results are reasonable up to $Kn \sim 1$.

The non-equilibrium flow physics of rarefied gases interacting with non-planar surfaces also has been described using detailed DSMC simulations for different Knudsen numbers and a variety of TMAC values and various geometric configurations. Obtained data is compared with the existing theoretical models and their limitations are outlined. Velocity profile comparisons for $Kn = 0.1$, 0.5 and 1, at $R_2/R_1 = 5/3$, demonstrate that the classical slip model is valid only up to the end of the slip flow regime and exhibits significant deviations in the transition regime. The PL wall scaling model predictions are in very good agreement up to $Kn \sim 1$, with slight deviations in the near-wall region at the inner cylinder. The simulation data and the PL model also predict partially inverted velocity profiles for moderate σ values, whereas the slip model does not capture this phenomenon.

The DSMC data at larger R_2/R_1 values also illuminates the limitations of the PL wall scaling model. With increase in the R_2/R_1 value, the PL model significantly underpredicts the velocity in the near-wall region of the inner cylinder, but does obtain fair comparison in the near-wall region of the outer one. This shows that the non-equilibrium effects in the near-wall region are not merely dependent on Kn, but that they are also influenced by curvature, since deviations between the DSMC data and PL model are more pronounced for larger R_2/R_1 values. Torque measurements at the inner cylinder are also compared with the theoretical models. The PL model predictions are excellent, while classical slip flow theory exhibits fair agreement. Hence, torque comparisons convey that the mere prediction of integral flow parameters does not necessarily guarantee the accuracy of any theoretical model, and that it is important to demonstrate that the field variables are also in agreement with

other simulation data.

In addition to momentum Knudsen layer, thermal Knudsen layer aspects are also investigated using the PL model. Thermal creep and Fourier heat transfer test cases have been studied in the transition flow regime, and the PL model results are compared with DSMC simulation data, the solution of the Boltzmann equation and other theoretical models. The PL model exhibits very good agreement up to $Kn \sim 1$ for velocity and temperature profiles, and up to Kn 5 for integral flow parameters such as heat transfer and TMPD. The PL model also capable of predicting the non-intuitive phenomenon of thermal creep flow reversal in the transition regime. With the increase of Knudsen number ($Kn > 0.1$), the flow can move along the tube surface from the hot to cold regions, while for $Kn < 0.1$ the creep at the boundary is taking place as expected, i.e. from cold to hot regions. Although this observation contradicts with the conventional theoretical prediction, qualitatively agrees with the recent findings of unified gas kinetic scheme and DSMC simulations (Xu, 2012).

Overall, in the cases studied, the predictive capabilities of the PL model are also found to be much better than those of the R13 equations, and the same as the R26 equations. The advantage of the power-law MFP constitutive scaling technique over solving the R26 equations is that it is based on simple physical arguments, and it can easily be implemented in conventional CFD codes in order to capture some of the important trends associated with the complex non-equilibrium physics of the Knudsen layer.

In the current thesis, all the investigated test cases were low-speed gas flows in which local flow gradients are relatively small. In such flow systems, the molecular velocity distribution can be described using either the equilibrium Maxwellian alone or with an additional first-order correction from the Chapman-Enskog expansion. However, gas micro flow systems still exhibit significant non-intuitive behaviour, and this is mainly due to the formation of Knudsen layers. This layer is formed solely due to gas surface interactions, i.e. it exists in bounded gas flows, irrespective of the wall movement and local flow gradients. The rigorous MD simulations in Chapter 4 also support this conjecture that the molecular free path distribution of rarefied gases in near-wall regions significantly deviate from the classical exponential

distribution function (Kennard, 1938). These simulations were performed for a gas that is at rest (i.e. the molecular velocity distribution is Maxwellian) and confined between non-moving specular wall boundaries (i.e. no local flow gradients).

Hence, N-S-F types of continuum models can appropriately describe *low-speed micro gas flows* up to $Kn \sim 1$, provided that the methodology incorporates an accurate Knudsen layer description through the employment of non-linear constitutive relations and appropriate slip/jump boundary conditions. Conversely, merely implementing higher-order terms in a continuum model may not always result in good predictions of transition regime gas flows, unless appropriate boundary conditions and non-linear constitutive forms are employed.

Modeling the non-equilibrium flow regions such as KL should ideally be performed using detailed kinetic theory. It is important to stress that we do not attempt to assess the accuracy of the present physical model underpinning the Boltzmann equation. However an appropriate extension to the N-S-F equations would be less time-consuming and less demanding of computational capacity and our motivation is to compare the predictive capabilities of competing continuum equation sets relative to a more computationally expensive molecular technique. Hence, the current work is significant from the numerical simulation of low-speed microscale gas flows point of view. This stems from the fact that simulation tools are better developed for N-S-F equations when compared to other higher order hydrodynamic models such as Burnett, R13 and R26 equations.

However, another mode of non-equilibrium can be caused due to the deviation of the molecular velocity distribution function from the classical Maxwellian one. This effect arises due to significant local flow gradients and is irrespective of the presence of confining wall boundaries. For example, high speed gas flows (e.g. 1-D shock waves), which are classified according to their Mach number (Ma). In such instances, modelling the non-linear constitutive relations/boundary conditions may not be sufficient and it is pertinent to use higher-order (i^{th}) equations, where $i \to \infty$ may approximately describe the Botlzmann equation. Hence, it is imperative to quantitatively measure the departure from local equilibrium and define the range of appropriateness of Navier-Stokes-Fourier equations.

Hence, in the appendix A, we discuss in detail about MD simulations of *high speed* rarefied gas flows to quantify the departure from local equilibrium based on both Knudsen and Mach numbers.

6.2 Future developments

There are two key areas of future work that are outlined below.

Since our power-law model is not derived to account for long-range molecular potentials or different molecular reflection characteristics, further investigation in this area could make the theoretical model more realistic. The MD simulations reported in this thesis only involve simple geometries with planar surfaces and isothermal gases with no external flow. It is important to validate the power-law model against MD data for complex geometries, and for non-isothermal/isothermal fluid flows. It would also be interesting to investigate how well the extended N-S-F equations would solve different flow cases with an effective mean free path description based on partly specular reflection and partly diffusive reflections. It is also pertinent to measure the effective mean free path profile for an explicit wall that is sufficiently thick for the effective mean free path profile not to change shape using marginally more or less molecules in the wall.

Another key aspect of future work is to develop full set of 3-D extended N-S-F equations with the incorporation of power-law wall scaling MFP, which could be implemented in a open source CFD solver such as OpenFOAM. This would be beneficial in the sense that flow cases for arbitrary geometrical configurations could then be modelled as opposed to simple planar, cylindrical and spherical test cases studied in the current thesis. For this model to be implemented the effective mean free path of every point of the gas domain needs to be determined, however the form of the domain is shaped. One method of doing this could be to use an already existing tool, which calculates the closest distance to the boundaries from any point of the gas domain. This function would then be modified to find various wall distances for various directions, being distributed with equal angular separation from the point of interest. The usage of wall distances from these trajectories is in consistency with

the point of view that molecules are equally probable to travel in any direction which is used in this thesis. The wall distances would then be inserted in the theoretically derived mean free path probability function for a single travelling direction, and then averaged with respect to all the effective mean free paths obtained from all directions. The main geometrical effect becomes apparent once these values are averaged yielding the mean free paths for equally probable travelling direction. The velocity slip and the temperature jump boundary conditions would also have to be implemented dependent on these effective mean free paths.

In addition to above major works, the current thesis may also motivate future work including:

(i) rigorous molecular dynamics simulations of rarefied gases confined in arbitrary geometries and subjected to a range of complex flow conditions, for establishing properly and generally the value of n for non-planar test cases;

(ii) whether Lévy free flights is an appropriate model for molecules of rarefied gases in non-planar geometries, or whether an alternative form of distribution function is necessary;

(iii) revisiting the classical slip and jump boundary conditions, that were originally derived assuming constant MFP in Knudsen layers, and using geometry-dependent effective MFP models instead.

(iv) using MD simulation results to define a new collision time, which not only include gas-surface interactions but also the effect of flow variable gradients.

(v) carrying out MD simulations and the PL model for studying thermal creep phenomenon in 2-D short channels to capture complex clockwise and anti-clockwise vortex rotations.

Bibliography

Agrawal, A., Djenidi, L. and Antonia, R.A. (2005) Simulation of gas flow in micro-channels with a sudden expansion or contraction. *Journal of Fluid Mechanics*, 530:135-144.

Agrawal, A. and Agrawal, A. (2006) Three-dimensional simulation of gas flow in different aspect ratio microducts. *Physics of Fluids*, 18(103604):1-11.

Agrawal, A. and Prabhu, S.V. (2008a) Survey on measurement of tangential momentum accommadation coefficient. *Journal of Vacuum Science and Technology A*, 26:634-645.

Agrawal, A. and Prabhu, S.V. (2008b) Deduction of slip coefficient in slip and transition regimes from existing cylindrical Couette flow data. *Experimental Thermal and Fluid Science*, 32:991-996.

Allen, M.P. and Tildesley, D.J. (1987) *Computer Simulation of Liquids*, Oxford University Press, Oxford, England.

Aoki, K., Yoshida, H., Nakanishi. T. and Garcia, A.L. (2003) Inverted velocity profile in the cylindrical Couette flow of a rarefied gas. *Physical Review E*, 68:016302.

Anderson, D.A., Tannehill, J.C. and Pletcher, R.H. (1984) *Computa-*

tional Fluid Mechanics and Heat Transfer. Mcgraw-Hill, Newyork.

Annis, B.K. (1972) Thermal creep in gases. *The Journal of Chemcal Physics*, 57(7):2898-2905.

Arkilic, E.B., Schmidt, M.A. and Breuer, K.S. (1997) Gaseous Slip Flow in Long Microchannels. *Journal of Micro Electro Mechanical Systems*, 6(2):167-178.

Arkilic, E.B., Breuer, K.S. and Schmidt, M.A. (2001) Mass flow and tangential momentum accomodation in silicon micromachined channels. *Journal of Fluid Mechanics*, 437:29-43.

Arlemark, E.J., Dadzie, S.K. and Reese, J.M. (2010) An Extension to the Navier-Stokes Equations to Incorporate Gas Molecular Collisions With Boundaries. *Journal of Heat Transfer*, 132:041006. Bahukudumbi, P., Park, J.H. and Beskok, A. (2003) A unified engineering model for steady and unsteady shear-driven gas microflows. *Microscale Thermophysical Engineering*, 7:291.

Baker, L.L. and Hadjiconstantinou, L.L. (2005) Variance reduction for Monte Carlo solutions of the Boltzmann equation. *Physics of Fluids*, 17:051703.

Barber, R.W., Sun, Y., Gu, X.J. and Emerson, D.R. (2004) Isothermal slip flow over curved surfaces. *Vacuum*, 76:73-81.

Barber, R.W. and Emerson, D.R. (2006) Challenges in modeling gas-phase flow in microchannels: from slip to transition. *Heat Transfer Engineering*, 27(4):3-12

Bassous, E., Taub, H.H. and Kuhn, L. (1977) Ink jet printing nozzle arrays etched in silicon. *Applied Physics Letters*, 31:135-137.

Benisti, D. and Escande, D.F. (1998) Nonstandard diffusion properties of the standard map, *Physical Review Letters*, 80:4781-4874.

Beskok, A. (2001) Validation of a new velocity-slip model for separated gas microflows. *Numerical Heat Transfer Part B: Fundamentals*, 40(6):451-471.

Beskok, A. and Karniadakis, G.E. (1999) A model for flows in channels, pipes, and ducts at micro and nano scales. *Microscale Thermophysical Engineering*, 3:43-77.

Bird, R.B., Stewart, W.E. and Lightfoot, E.N. (1960) *Transport phenomena*. John Wiley and Sons (WIE).

Bird, G.A. (1986) Definition of mean free path for real gases. *Physics of Fluids*, 26:3222-3223.

Bird, G.A. (1994) *Molecular gas dynamics and the direct simulation of gas flows*. Oxford University Press, New York.

Bhatnagar, P.L., Gross, E.P. and Krook, M. (1954) A model for collision processes in gases in small amplitude processes in charged and neutral one-component systems. *Physical Review*, 94(3):511-525.

Burnett, D. (1935) The distribution of molecular velocities and the mean motion in a non-unifrom gas. *Proceedings of the London Mathematical Society*, 40:382-435.

Cercignani, C. (1964) *Higher order slip according to the linearized Boltzmann equation*. Institute of Engineering Research Report AS-64-19, University of California, Berkeley.

Cercignani, C. (1988) *The Boltzmann equation and its applications*. Springer-Verlag, New York

Cercignani, C. (1990) *Mathematical Methods in Kinetic Theory*, Plenum Press, New York.

Cercignani, C. (2000) *Rarefied Gas Dynamics: From Basic Concepts to Actual Calculations*. Cambridge University Press.

Cercignani, C. and Lampis, M. (1971) Kinetic model for gas-surface interaction. *Transport Theory and Statistical Physics*, 1:101-114.

Cercignani, C., Lampis, M. and Lorenzani, S. (2004) Variational approach to gas flows in microchannels. *Physics of Fluids*, 16:3426-3436.

Cercignani, C., Frangi, A., Lorenzani, S. and Vigna, B. (2007) BEM Approaches and Simplified Kinetic Models for the Analysis of Damping in Deformable MEMS. *Engineering Analysis with Boundary Elements*, 31:451-457.

Chapman, S. and Cowling, T.G. (1970) *Mathematical theory of non-uniform gases*. 3rd edition, Cambridge University Press.

Colin, S. (2005) Rarefaction and compressibility effects on steady and transient gas flows in microchannels. *Microfluidics and Nanofluidics*, 1(3):268-279.

Colin, S., Lalonde, P. and Caen, R. (2004) Validation of a second-order slip flow model in rectangular microchannels. *Heat Transfer Engineering*, 25(3):23-30.

Deissler, R.G. (1964) An analysis of second-order slip flow and temperature jump boundary conditions for rarefied gases, *International Journal of Heat and Mass Transfer*, 7:681-694.

del-Castillo-Negrete, D., Carreras, B.A. and Lynch, V.E. (2005) Nondiffusive transport in plasma turbulence: a fractional diffusion approach, *Physical Review Letters*, 9:065003.

del-Castillo-Negrete, D. (2008) Nondiffusive transport modelling: statistical basis and applications, in *Turbulent Transport in Fusion Plasmas*, ed. S Benkadda, New York: American Institute of Physics.

Derjaguin, B.V. and Yalamov, Y.U. (1965) Theory of Thermophoresis of Large Aerosol Particles. *Journal of Colloidal Science*, 17:768-780.

Dongari, N., Agrawal, A. and Agrawal, A. (2007) Analytical solution of gaseous slip flow in long microchannels. *International Journal of Heat and Mass Transfer*, 50:3411-3421.

Dongari, N., Sharma, A. and Durst, F. (2009) Pressure-driven diffusive gas flows in micro-channels: from the Knudsen to the continuum regimes. *Microfluidics and Nanofluidics*, 6(5):679-692.

Dongari, N., Durst, F. and Chakraborty, S. (2010a) Predicting microscale gas flows and rarefaction effects through extended NavierStokesFourier equations from phoretic transport considerations. *Microfluidics and Nanofluidics*, 9(4):831-846.

Dongari, N., Zhang, Y.H. and Reese, J.M. (2010b) The importance of mean free path in determining gas micro flow behaviour. *ASME 2010 8th International Conference on Nanochannels, Microchannels, and Minichannels:*

Parts A and B, FEDSM-ICNMM2010-30743:481-490.

Dongari N, Zhang YH, Reese JM (2011a) Molecular free path distribution in rarefied gases. *Journal of Physics D: Applied Physics*, 44:125502.

Dongari N, Zhang YH, Reese JM (2011b) Modeling of Knudsen layer effects in micro/nanoscale gas flows. *Journal of Fluids Engineering*, 133(7):071101.

Dongari N, Zhang YH, Reese JM (2011c) Behaviour of microscale gas flows based on a power-law free path distribution function. *AIP Conference Proceedings*, 1333:724-729.

Dongari, N., Zhang, Y.H. and Reese, J. M. (2011d) Molecular dynamics simulation of dense gases, in *Proceedings on CDROM of 3rd GASMEMS Workshop (GASMEMS11)*, Bertinoiro, Italy, pp. GASMEMS2011-20:1-10.

Dongari, N. and Agrawal, A. (2012a) Modeling of NavierStokes equations for high Knudsen number gas flows, *International Journal of Heat and Mass Transfer*, 55:4352-4358.

Dongari, N., Barber, R.W., Emerson, D.R., Stefanov, S.K., Zhang, Y.H. and Reese, J.M. (2012b) The effect of Knudsen layers on rarefied cylindrical Couette gas flows, *Microfluidics and Nanofluidics*, DOI:10.1007/s10404-012-1019-2.

Dongari, N., Barber, R. W., Emerson, D. R., Zhang, Y. H., and Reese, J. M. (2012c) Velocity inversion in cylindrical Couette gas flows, in *Journal of Physics: Conference Series - Proceedings of 1st European Conference on Gas MicroFlows (GASMEMS2012)*, 362:012009.

Einstein, A. (1956) *Investigations on the Theory of Brownian Movement*,

Dover, New York.

Einzel, D., Panzer, P., Liu, M. (1990) Boundary condition for fluid flow: Curved or rough surfaces. *Physical Review Letters*, 64:2269

Emerson, R.D., Gu, X.J., Stefanov, S.K., Yuhong, S. and Barber, R.W. (2007) Nonplanar oscillatory shear flow: From the continuum to the free-molecular regime. *Physics of Fluids*, 19:107105

Epstein, A.H., Senturia, S.D., Al-Midani, O., Anathasuresh, G., Ayon, A., Breuer, K., Chen, K.S., Ehrich, F.F., Esteve, E. and Frechette, L. (1997) Micro-heat engines, gas turbines and rocket engines the MIT micro-engine project. *Proceedings of AIAA Fluid Dynamics Conference*, CO, USA, AIAA19971773.

Ewart, T., Perrier, P., Graur, I.A. and Melonas, J.B. (2007) Mass flow rate measurements in a microchannel, from hydrodynamic to near free molecular regimes. *Journal of Fluid Mechanics*, 584:337-356.

Fa, K.S. and Lenzi, E.K. (2003) Power law diffusion coefficient and anomalous diffusion: analysis of solutions and first passage time, *Physical Review E*, 67:061105.

Fichman, M. and Hetsroni, G. (2005) Viscosity and slip velocity in gas flow in microchannels, *Physics of Fluids*, 17:123102.

Frangi, A., Frezzotti, A. and Lorenzani, S. (2007) On the application of the BGK kinetic model to the analysis of gas-structure interactions in MEMS. *Computers and Structures*, 85:810-817.

Fieseler, P. (1998) A method for solar sailing in a low earth orbit. *Acta*

Astronautica, 43:531-541.

Gad-el-Hak, M. (1999) Fluid mechanics of microdevices the Freeman Scholar lecture. *Journal of Fluids Engineering*, 121(1):533.

Gaede, W. (1913) Die Aussere Reibung der Gase. *Annalen der Physik*, 41:289.

Guarini, E., Bafile, U., Barocchi, F., Demmel, F., Formisano, F., Sampoli, M. and Venturi, G. (2005) Collective excitations in liquid cd4: Neutron scattering and moleculardynamics simulations. *Europhysics Letters*, 72(6):969-975.

Gemci, T., Ponyavin, V., Chen, Y., Chen, H. and Collins, R. (2008) Computational model of airflow in upper 17 generations of human respiratory tract. *Journal of Biomechanics*, 41(9):2047-2054.

Goldberg, R. (1954) *The slow flow of a rarefied gas past a spherical obstacle*. Ph.D. Thesis, New York University.

Gu, X.J. and Emerson, D.R. (2009) A high-order moment approach for capturing non-equilibrium phenomena in the transition regime. *Journal of Fluid Mechanics*, 636:177-226.

Guest, P.G. (1961) The solid angle subtended by a cylinder. *Review of Scientific Instruments*, 32:164.

Guo, Z.L., Shi, B.C., Zheng, C.G. (2011) Velocity inversion of micro cylindrical Couette flow: A lattice Boltzmann study. *Computers and Mathematics with Applications*, 61:3519-3527.

Guo, Z.L., Shi, B.C., Zheng, C.G. (2007) An extended Navier-Stokes formulation for gas flows in the Knudsen layer near a wall. *Europhysics Letters*, 80:24001-24006.

Grad, H. (1949) Note on N-dimensional hermite polynomials. *Communications on Pure and Applied Mathematics*, 2:325-330.

Grolimund, D., Borkovec, M., Federer, P. and Sticher, H. (1995) Measurement of sorption isotherms with flow-through reactors. *Environmental Science Technology*, 29:2317-2321.

Hadjiconstantinou, N.G. and Simek, O. (2002) Constant-wall-temperature Nusselt number in micro and nano Channels. *Journal of Heat Transfe*r, 124:356-364.

Hadjiconstantinou, N.G. (2003) Comment on Cercignani's second-order slip coefficient. *Physics of Fluids*, 15(8):2352-2355.

Hadjiconstantinou, N.G. (2006) The limits of Navier-Stokes theory and kinetic extensions for describing small scale gaseous hydrodynamics. *Physics of Fluids*, 18:111301.

Han, Y.L., Muntz, E.P., Alexeenko, A. and Young, M. (2007) Experimental and computational studies of temperature gradient-driven molecular transport in gas flows through nano/microscale channels. *Nanoscale and Microscale Thermophysical Engineering*, 11(1):151-175.

Harley, J.C., Huang, Y., Bau, H.H. and Zemel, J.N (1995) Gas flow in micro-channels. *Journal of Fluid Mechanics*, 284:257-274.

Hornung, C.H., Hallmark, B., Hesketh, R.P. and Mackley, M.R. (2006)

The fluid flow and heat transfer performance of thermoplastic Microcapillary films. *Journal of Micromechanics and Microengineering*, 16:434-447.

Jackson, J. and Robert, D. (2006) Nonlinear auditory mechanism enhances female sounds for male mosquitoes. *Proceedings of the National Academy of Sciences of the United States of America*, 103:16734-16739.

Jang, J. and Wereley, S. (2004) Pressure distributions of gaseous slip flow in straight and uniform rectangular microchannels. *Microfluidics and Nanofluidic*s, 1:41-51.

Kandlikar, S., Garimella, S., Li, D., Colin, S. and King, M. (2005) *Heat Transfer and Fluid Flow in Minichannels and Microchannels*. Elsevier.

Karniadakis, G.E., Beskok, A. and Aluru, N. (2005) *Microflows - Fundamentals and Simulations*. Springer-Verlag, New York.

Kennard, E.H. (1938) *Kinetic theory of gases with an introduction to statistical mechanics*. McGraw-Hill, New York.

Kim, S. (2009) Slip velocity and velocity inversion in a cylindrical Couette flow. *Physical Review E*, 79:036312.

Kogan, M.N. (1969) *Rarefied Gas Dynamics*. Plenum Press.

Knudsen, M. (1909) Die Gesetze der Molekularstrmung und der inneren Reibungsstrmung der Gase durch Rhren. *Annalen der Physik*, 28:75-130.

Knudsen, M. (1910) Thermischer Molekulardruck der Gase in Rhren. *Annalen der Physi*k, 33:1435-1448.

Landau, L.D. and Lifshitz, E.M. (1958) *Fluid Mechanics*, Pergamon, Oxford.

Lea, K.C. and Loyalka, S.K. (1982) Motion of a sphere in a rarefied gas. *Physics of Fluids*, 25:1550.

Lilley, C.R., Sader, J.E. (2007) Velocity gradient singulary and structure of the velocity profile in the Knudsen layer according to the Boltzmann equation. *Physical Review E*, 76:026315.

Lockerby, D.A., Reese, J.M., Emerson, D.R. and Barber, R.W. (2004) Velocity boundary condition at solid walls in rarefied gas calculations. *Physical Review E*, 70:017303.

Lockerby, D.A., Reese, J.M. and Gallis, M.A. (2005a) Capturing the Knudsen layer in continuum-fluid models of non-equilibrium gas flows, *AAIA Journal*, 43:1391-1393.

Lockerby, D.A., Reese, J.M. and Gallis, M.A. (2005b) The usefulness of higher-order constitutive relations for describing the Knudsen layer. *Physics of Fluids*, 19:100609.

Lockerby, D.A. and Reese, J.M. (2008) On the modelling of isothermal gas flows at the microscale. *Journal of Fluid Mechanics*, 604:235-261.

Loyalka, S. K. (1975) Kinetic theory of thermal transpiration and mechanocaloric effect. II, *The Journal of Chemical Physics*, 63(9):4054-4060.

Macpherson, G., Borg, M. and Reese, J.M. (2007) Generation of initial molecular dynamics configurations in arbitrary geometries and in parallel.

Molecular Simulation, 33(15):1199-1212.

Macpherson G. and Reese, J.M. (2008) Molecular dynamics in arbitrary geometries: parallel evaluation of pair forces. *Molecular Simulation*, 34(1):97-115.

Macpherson, G., Nordin, N. and Weller, H. (2009) Particle tracking in unstructured, arbitrary polyhedral meshes for use in cfd and molecular dynamics. *Communications in Numerical Methods in Engineering*, 25(3):263-273.

Mahulikar, S., Herwig, H. and Hausner, O. (2007) Study of gas microconvection for synthesis of rarefaction and nonrarefaction effects. *Journal of Microelectro Mechanical Systems*, 16(6):1543-1556.

Maurer, J., Tabeling, P., Joseph, P. and Willaime, H. (2003) Second-order slip laws in micro-channels for helium and nitrogen. *Physics of Fluids*, 15(9):2613-2621.

Maxwell, J.C. (1867) On the dynamical theory of gases. *Philosophical Transactions of the Royal Society of London*, 157:49-88.

Maxwell, J.C. (1879) On stresses in rarefied gases arising from inequalities of temperature. *Philosophical Transactions of the Royal Society of London*, 170:231-256.

Mehregany, M., Nagarkar, P., Senturia, S. and Lang, J.H. (1990) Operation of microfabricated harmonic and ordinary side drive motor. In: *IEEE micro electro mechanical system workshop*, pp. 344-352.

Meng, J.P., Dongari, N., Reese, J.M. and Zhang, Y.H. (2012) A kinetic switching criterion for hybrid modelling of multiscale gas flows, in *Journal of*

Physics: Conference Series - Proceedings of 1st European Conference on Gas MicroFlows (GASMEMS2012), 362:012006.

Montroll, E.W. and Scher, H. (1973) Random walks on lattices. IV. Continuous-time walks and influence of absorbing boundaries. *Journal of Statistical Physics*, 9(2):101-135 .

Moss, J.N., Gupta, R.N. and Price, J.M. (1995) *DSMC simulations of OREX entry conditions*. NASA Technical Note 111621, NASA.

Moss, J.N., Gupta, R.N. and Price, J.M. (2006) DSMC simulations of Apollo capsule aerodynamics for hypersonic rarefied conditions. *Proceedings of 9th AIAA ASME Joint Thermophysics and Heat Transfer Conference*, San Francisco, CA, USA, AIAA Paper 2006-3577.

Myong, R.S., Reese, J.M., Barber, R.W. and Emerson, D.R. (2005) Velocity slip in microscale cylindrical Couette flow: The Langmuir model. *Physics of Fluids*, 17:087105.

Nordling, C. and Osterman, J. (1999) *Physics Handbook for Science and Engineering*. Studentlitteratur, 6th edition.

Langmuir, I. (1933) Surface chemistry. *Chemical Review*, 13(2):147-191.

O'Hare, L., Scanlon, T.J., Emerson, D.R. and Reese, J.M. (2008) Evaluating constitutive scaling models for application to compressible microflows. *International Journal of Heat and Mass Transfer*, 51:1281-1292.

Ohwada, T., Sone, Y. and Aoki, K. (1989) Numerical analysis of the Poiseuille and thermal transpiration flows between two parallel plates on the basis of the Boltzmann equation for hard sphere molecules. *Physics of Fluids*

A, 1(12):2042-2049.

Pfahler, J., Harley, J., Bau, H. and Zemel, J. N. (1991) Gas and liquid flow in small channels. *Micromechanical Sensors, Actuators and Systems*, 32:49-60.

Rapaport, D.C. (2004) *The Art of Molecular Dynamics Simulation*. Cambridge University Press, 2nd edition.

Reese, J. M. (1993) *On the structure of shockwaves in monotomic rarefied gases*. PhD thesis, Oxford University, UK.

Reese, J. M., Gallis, M. and Lockerby, D.A. (2003) New directions in fluid dynamics: nonequilibrium aerodynamic and microsystem flows. *Royal Society of London Philosophical Transactions Series A*, 361:2967-2988.

Reese, J.M., Zheng, Y. and Lockerby, D.A. (2007) Computing the near-wall region in gas micro- and nanofluidics: critical Knudsen layer phenomena. *Journal of Computational and Theoretical Nanoscience*, 4(4):807-813.

Reese, J.M. and Zhang, Y.H. (2009) Simulating fluid flows in micro and nano devices: the challenge of non-equilibrium behaviour, *Journal of Computational and Theoretical Nanoscience*, 14:2061-2074.

Reynolds, O. (1880) On certain dimensional properties of matter in the gaseous state. Part I. Experimental researches on thermal transpiration of gases through porous plates and on the laws of transpiration and impulsion, including an experimental proof that gas is not a continuous plenum. Part II. On an extension of the dynamical theory of gas, which includes the stresses, tangential and normal, caused by a varying condition of gas, and affords an explanation of the phenomena of transpiration and impulsion. *Philosophical*

Transactions of the Royal Society of London B, (170):727-845.

Saha, M. N. and Srivastava, B. N. (1958) *A Treatise on Heat*, Indian Press, Allahabad.

Schaaf, S.A. and Chambre, P.L. (1961) *Flow of Rarefied Gases*. Princeton University Press.

Scharfe, M.E. (1970) Transient photoconductivity in vitreous as2se3. *Physical Review B*, 2(12):5025.

Schlichting, H. (1979) *Boundary-layer theory*. 7th ed. McGraw-Hill, New York.

Sharipov, F. (1999) Rarefied gas flow through a long rectangular channel. *Journal of Vacuum Science and Technology* A, 17(5):3062-3066.

Sharipov, F. (2003) Application of the Cercignani-Lampis scattering kernel to calculations of rarefied gas flows. II. Slip and jump coefficients. *European Journal of Mechanics B/Fluid*s, 22:133-143.

Sharipov, F. and Bertoldo, G. (2009) Poiseuille flow and thermal creep based on the Boltzmann equation with the Lennard-Jones potential over a wide range of the Knudsen number. *Physics of Fluids*, 21:067101.

Shlesinger, M.F. (1974) Asymptotic solutions of continuous-time random walks. *Journal of Statistical Physics*, 10:421-434.

Shlesinger, M.F., Klafter, K. and Zumofen, G. (1999) Above, below and beyond Brownian motion. *American Journal of Physics*, 67:1253-1259.

Von Smoluchowski, M. (1898) ber wrmeleitung in verdunnten gasen. *Annalen der Physik und Chemie*, 64:101-130.

Sone, Y. (2002) *Kinetic theory and fluid dynamics*. Birkhauser, Boston.

Squires, T.M. and Quake, S.R. (2005) Microfluidics: Fluid physics at nanolitre scale. *Reviews of Modern Physics*, 77:977-1026.

Sreekanth, A.K. (1969) Slip flow through long circular tubes, in: L. Trilling, H.Y. Wachman (Eds.). *Proceedings of the sixth international symposium on Rarefied Gas Dynamics*, Academic Press, pp. 667-680.

Steckelmacher, W. (1986) Knudsen flow 75 years on: the current state of the art for flow of rarefied gases in tubes and systems. *Reports on Progress in Physics*, 49(10):1083-1107.

Stefanov, S.K., Gospodinov, P. and Cercignani, C. (1998) Monte Carlo simulation and Navier-Stokes finite difference calculation of unsteady-state rarefied gas flows. *Physics of Fluids*, 10:289.

Stefanov, S.K., Barber, R.W., Emerson, D.R. and Reese, J.M. (2006) The critical accommodation coefficient for velocity inversion in rarefied cylindrical Couette flow in the slip and near free-molecular regimes. *Proceedings of 25th International Symposium on Rarefied Gas Dynamics*, St. Petersburg, Russia, edited by M. S. Ivanov and A. K. Rebrov (Publishing House of the Siberian Branch of the Russian Academy of Sciences, Novosibirsk, Russia), pp. 1146-1151.

Stokes, G.G. (1851) On the effect of the internal friction of fluids on the motion of pendulums, *Cambridge Philosophical Society*, 9:8-106.

Stops, D.W. (1970) The mean free path of gas molecules in the transition regime. *Journal of Physics D: Applied Physics*, 3:685-696.

Struchtrup, H. (2005) *Macroscopic Transport Equations for Rarefied Gas Flows*, Springer, Heidelberg.

Sun, J. and Li, Z. (2009) Molecular dynamics simulations of energy accommodation coefficients for gas flows in nano-channels. *Molecular Simulation*, 35(3):228-233.

Tai, Y.C., Fan, L.S. and Muller, R.S. (1989) IC-processed micro-motors: design, technology, and testing. In: *IEEE micro electro mechanical system workshop*, vol 16, pp. 20-22.

Thomson, J.J. (1901) *Proceedings of Cambridge Philosophical Society*, 11:120.

Tibbs, K.W., Baras, F., Garcia, A.L. (1997) Anomalous flow profile due to the curvature effect on slip length. *Physical Review E*, 56:2282.

Tison, S.A. (1993) Experimental data and theoretical modeling of gas flows through metal capillary leaks. *Vacuum* 44:1171-1175.

Trimmer, W. (1997) Micromechanics and MEMS, Classic and seminar papers to 1990, *IEEE Order Number PC4390*, ISBN 0-7803-1085-3.

Trilling, L. (1975) The Knudsen boundary layer in low density gas flow past a crystal. *SIAM Journal on Applied Mathematics*, 28(4):757-777.

Turner, S., Lam, L., Faghri, M. and Gregory, O. (2004) Experimental investigation of gas flow in microchannels. *Journal of Heat Transfer*,

126(5):753-763.

Veijola, T., Kuisma, H., Lahdenpura, J. and Ryhanen, T. (1995) Equivalent-circuit model of the squeezed gas film in a silicon accelerometer. *Sensors and Actuators A*, 48:239-248.

Wagner, W. (1992) A convergence proof for Birds direct simulation Monte Carlo method for the Boltzmann equation. *Journal of Statistical Physics*, 66:1011-1044.

Weisberg, A., Bau, H.H. and Zeimel, J.N. (1992) Analysis of micro-channels for integrated cooling. *International Journal of Heat and Mass Transfer*, 35(10):2465-2474.

Xu, K. (2012) Unified treatment of rarefied and continuum fluid flows. *Encyclopedia of Aerospace Engineering*, DOI: 10.1002/9780470686652.eae601.

Xue, H. Ji, H. M. and Shu, C. (2001) Analysis of micro-couette flow using the burnett equations. *International Journal of Heat and Mass Transfer*, 44(21):4139-4146.

Yuhong, S., Chan, W.K. and Ningyu, L. (2002) A slip model with molecular dynamics. *Journal of Micromechanics and Microengineering*, 12(3):316-322.

Yuhong, S. and Chan, W.K. (2004) Analytical modeling of rarefied Poiseuille flow in microchannels. *Journal of Vacuum Science and Technology A: Vacuum Surfaces and Films*, 22(2):383-394.

Yuhong, S., Barber, R.W. and Emerson, D.R. (2005) Inverted velocity profiles in rarefied cylindrical Couette gas flow and the impact of the accommodation coefficient. *Physics Fluids*, 17:047102

Zhang, Y.H., Gu, X.J., Barber, R.W. and Emerson, D.R. (2006) Capturing Knudsen layer phenomena using a lattice Boltzmann model. *Physical Review E*, 74:046704.

Zheng, Y., Reese, J.M., Scanlon, T. J. and Lockerby, D. A. (2006) Scaled Navier-Stokes-Fourier equations for rarefied gas flow and heat transfer phenomena in micro- and nanosystems. *Proceedings of ASME ICNMM2006*, Limerick, Ireland, ICNMM200696066.

Appendix A

Microscopic evaluation of non-equilibrium

The Navier-Stokes-Fourier (N-S-F) equations are the most widely-used model for fluid dynamics. Their impact is far-ranging, e.g. weather forecasting, modern transport system design including aeroplanes, cars, and ships, and energy generation from wind turbines. The fundamental assumptions for the N-S-F model are that the fluid is a continuous medium, and the flow is close to thermodynamic equilibrium. Some of the above mentioned flows may involve large variations of fluid properties. The large variation in properties results in some regions where the flow can be described as a continuum, modeled with the N-S-F equations, and solved numerically by computational fluid dynamics (CFD) approaches. The wide variation in flow properties may also lead to some regions where the flow is rarefied and the N-S-F equations are no longer applicable. Such non-equilibrium regions can accurately be modelled by kinetic theory or particle methods.

However, these methods cannot be fully used for large systems, as it demands huge amounts of computational capacity in regions where the flow is dense and in the continuum regime. With the well-known fact that the N-S-F equations will fail for rarefied flows, it is necessary to have an approach that is physically accurate and numerically efficient. One way to achieve this objective is to combine the particle and CFD methods. The primary issue associated with the combination of the two

numerical methods is to determine when to switch between the methods. As the continuum equations are not valid under rarefied conditions, it is very important to use an accurate breakdown parameter as the criterion for switching between methods.

The current chapter presents a study of the breakdown of the N-S-F equations in flow regimes encompassing a wide range of rarefaction and compressibility conditions. Investigations are performed by carrying out rigorous molecular dynamics simulations. The objective of the study is to accurately predict conditions under which the N-S-F equations may be expected to invalid. New breakdown parameters are proposed, which can predict the failure of the continuum approach and also the absolute deviation from local thermodynamic equilibrium, for planar Couette flow.

A.1 Classical schemes to quantify non-equilibrium

Various types of breakdown criteria have been used to assess when the N-S-F equations are appropriate. The most basic and well-known parameter to classify non-equilibrium gas flows is based on the global Knudsen number (the ratio of the molecular mean free path λ to the system characteristic length L) (Chapman, 1953). This criteria is appropriate only for low-speed gas flows and high-speed gas flows show strong dependence on the Mach number. Another type is the local Knudsen number, $\lambda/\phi|d\phi/dx|$, where ϕ denotes a macroscopic flow quantity (typically density, temperature or pressure). The other type is the product of Mach and global Knudsen numbers, or its equivalent. The former criterion indicates that the Knudsen number has to be small for the N-S-F model to be valid. The latter criterion requires the product of Ma and Kn to be small. However, the latter is not appropriate for the low Mach number flows typically found in micro/nano-devices, as the evidence is that the N-S-F equations fail for a small $KnMa$ but moderate Kn (Hadjiconstantinou, 2006).

The inconsistency in the above mentioned types of criteria raises a fundamental question: is there a better way to assess the level of thermodynamic non-equilibrium in the local flow field and the appropriateness of the N-S-F equations? As the N-

S-F equations are the cornerstone of modern CFD, their validity range as a model should be clearly defined. Here, we address this fundamental issue, aiming to accurately assess the level of non-equilibrium of the local flow field, and so redefine the applicability regime of the N-S-F equations.

A.2 New schemes based on molecular velocity distribution

For a gas, the N-S-F equations can be regarded as a first order approximate solution to the Boltzmann equation, in terms of the Knudsen number Kn. The Boltzmann equation assumes both binary collisions between gas molecules and molecular chaos, so a single particle velocity distribution function can be employed. The Chapman-Enskog (C-E) approach to the Boltzmann equation assumes

$$f = f^{(0)} + f^{(1)} + f^{(2)} + \cdots + f^{(\alpha)} + \cdots , \tag{A.1}$$

where the distribution functions $f^{(\alpha)}$ can be asymptotically obtained from the Boltzmann equation.

The Maxwell-Boltzmann equilibrium distribution,

$$f^{eq} = \frac{\rho}{(2\pi RT)^{3/2}} \exp\left[-\frac{\varsigma^2}{2RT}\right], \tag{A.2}$$

is the zeroth-order solution $f^{(0)}$, and leads to the Euler fluid equations. Here, ρ denotes the gas density, T the temperature, R the gas constant, and ς the peculiar velocity of molecules, which is $\xi - u$ where ξ represents the molecular velocity and u is the macroscopic fluid velocity. In Eq.(A.1), $f^{(1)}$ provides a non-equilibrium correction of the order of Kn. To recover the N-S-F equations,

$$f^{(1)} = f^{eq}\left[\left(\frac{\sigma_{ij}\varsigma_{<i}\varsigma_{j>}}{2pRT}\right) + \frac{2q_i\varsigma_i}{5pRT}\left(\frac{\varsigma^2}{2RT} - \frac{5}{2}\right)\right], \tag{A.3}$$

where, p is the gas pressure, and the shear stress σ_{ij} and the heat flux q_i are related

to the following first-order gradients of velocity and temperature,

$$\sigma_{ij} = -2\mu \frac{\partial u_{<i}}{\partial x_{j>}}, \quad q_i = -\kappa \frac{\partial T}{\partial x_i}, \tag{A.4}$$

where μ and κ denote the viscosity and thermal conductivity. We can continue the series to obtain α-order corrections to the distribution function in terms of the Knudsen number. The C-E expansion produces a series of continuum equations that are assumed to converge to the Boltzmann equation with increasing order. Practically, this assumption of convergence implies a limit to the degree of departure from the equilibrium state that may be successfully predicted using the C-E expansion. The Chapman-Enskog technique indicates that the Euler equations are appropriate for thermodynamically equilibrium flows with $Kn = 0$, while the Navier-Stokes equations are valid for linear departures from equilibrium where the Knudsen number is close to zero.

To zeroth-order in Kn, the C-E series produces the Euler equations, which are inviscid constitutive relations, and valid for gas flows far from bounding surfaces when Kn is below approximately 10^{-2}. To first-order in Kn, the series results in the viscous N-S-F equations. The higher the order of the terms in the series, in theory, the greater the departure from the equilibrium distribution that may be modelled. At the second-order in Kn, the Burnett equations are produced, which are similar to the N-S-F equations, but include more complex constitutive expressions for stress and heat flux.

In high altitude applications, such as spacecraft re-entry into planetary atmospheres, or vacuum applications, low-pressure chemical processes, and micro/nano devices, the flows can be highly non-equilibrium and the N-S-F and other higher order equations fail to provide an adequate description. However, the Knudsen number alone may not be sufficient to describe the level of non-equilibrium in the flow field, and to assess whether the N-S-F equations are applicable or not. Both simulation data and theoretical analysis indicate that the level of non-equilibrium is also strongly influenced by the Mach number.

Instead of using Knudsen and Mach numbers defined by macroscopic flow proper-

ties, the fundamental direct evidence for the level of thermodynamic non-equilibrium in the local flowfield resides in the distribution function itself. The distribution function may be considered in two parts: the equilibrium and the non-equilibrium components, i.e.

$$f = f^{eq} + f^{neq}. \tag{A.5}$$

In order to consider the validity of the N-S-F equations, the non-equilibrium part f^{neq} may be further divided into two components, i.e.

$$f^{neq} = f^{(1)} + f^{(H)}, \tag{A.6}$$

where $f^{(1)}$ is the first order non-equilibrium correction (at the N-S-F level) which is given by Eq. (A.3), and $f^{(H)}$ is the higher-order non-equilibrium correction beyond the N-S-F level. So, the distribution function can be split into three components:

$$f = f^{eq} + f^{(1)} + f^{(H)}. \tag{A.7}$$

If the non-equilibrium part f^{neq} is negligible in comparison to f^{eq}, then the flow is in equilibrium, and the Euler equations can be recovered from the Boltzmann equation. Only when $f^{(1)} \gg f^{(H)}$ are the N-S-F equations recovered from the Boltzmann equation. Using the distribution function directly we can thereby assess when the N-S-F equations are valid, which is not only physically sound but also practical as many computational methods provide information on the distribution function during simulations, e.g. direct solution of the Boltzmann equation (Sone, 2002), the lattice Boltzmann method (Meng et al., 2011), the direct simulation Monte Carlo method (Bird, 1978), and molecular dynamics (Dongari et al., 2011a; Dongari et al., 2012b).

To evaluate how far the flowfield is away from equilibrium, we introduce a parameter C_0 to describe the departure from local equilibrium:

$$C_0 = \sqrt{\frac{\int (f^{neq})^2 d\xi}{\int (f^{eq})^2 d\xi}} = \sqrt{\frac{\int (f - f^{eq})^2 d\xi}{\int (f^{eq})^2 d\xi}} = \frac{\sqrt{8}\pi^{3/4}(RT)^{3/4}}{\rho} \sqrt{\int (f - f^{eq})^2 d\xi}, \tag{A.8}$$

which is a relative error of f to the Maxwellian f^{eq}. Similarly, a parameter C_1 can be introduced to describe how far the flowfield is away from the Navier-Stokes-Fourier regime:

$$C_1 = \sqrt{\frac{\int (f^{(H)})^2 d\xi}{\int (f^{(1)})^2 d\xi}} = \sqrt{\frac{\int (f - f^{eq} - f^{(1)})^2 d\xi}{\int (f^{(1)})^2 d\xi}}. \tag{A.9}$$

Here, C_1 is a direct indicator of the relative error introduced by using a N-S-F model on the flowfield. Together, C_0 and C_1 provide both an accurate assessment of the level of non-equilibrium in the local flowfield, and an indication of the appropriateness of using the N-S-F equations.

A.2.1 MD measurements

In the following section, we show quantitatively why the commonly used Knudsen and Mach numbers fail as local flowfield indicators, and how they are related to C_0 and C_1. We use nonlinear shear-driven Couette flows as examples, where the two plates are moving with a speed of U_w in opposite directions with their temperatures set to T_0. To obtain accurate gas molecular velocity distribution functions, we perform molecular dynamics (MD) simulations using the OpenFOAM code that includes the MD routines implemented in Chapter 4. Monatomic Lennard-Jones argon molecules are simulated, and initially the molecules are spatially distributed in the domain of interest with a random Gaussian velocity distribution corresponding to an initially prescribed gas temperature. They are then allowed to relax through collisions until reaching a steady state before we take measurements. To achieve a smooth velocity distribution function, molecular velocity samples are then taken in every time step (0.001 τ, where $\tau = \sqrt{md^2/\epsilon}$, with m being molar mass, d, the

diameter of gas molecules, and ϵ being related to the interaction strength of the molecules) for a total run time of at least 30000 τ (in the extreme rarefied and high speed flow case below, up to 100000 τ). We use 83500 molecules in each simulation, and assume diffuse gas molecule/wall interactions.

A.2.2 Quantification of non-equilibrium

The profiles of C_0 and C_1 for various Couette flow cases are presented in Figs. (A.1)-(A.4). The first two figures represent the slip flow regime and the later ones describe flows in the transition regime. It is clearly shown that the level of non-equilibrium depends on both the Knudsen number and the Mach number ($Ma = U_w/\sqrt{RT_0}$). C_0, the indicator of departure from equilibrium, is small at $Kn = 0.01$ especially in the bulk region (Y=0). However, when the Mach number increases, C_0 becomes larger and the increment is more pronounced in the near-wall region compared to the bulk region. The C_0 profiles are quite sharp in the wall-region and significantly flatter in the bulk region. This is due to the Knudsen layer effects are being limited to the near-wall region and at $Kn = 0.01$, this layer thickness is very thin. For the $Kn = 0.1$ case, the C_0 profiles are qualitatively similar to $Kn = 0.01$ and predicting relatively higher values in the near-wall region.

C_0 variations in the transition flow regime, i.e. $Kn = 0.5$ and 1 cases, are illustrated in Figs. (A.3) and (A.4). The trends are significantly shallower in the both the wall and bulk regions, when compared to the ones in the slip flow regime cases. With increase in Kn, C_0 values increase in the wall region and the increment is much more pronounced in the bulk region. This is due to, at higher Kn, the effect of Knudsen layer not being limited to the near-wall region, but also reaching into the bulk flow region as well. At $Ma = 10$, the bulk and wall C_0 values vary from 0.04 to 0.5, 0.075 to 0.75. 0.69 to 1.2, and 1.1 to 1.37, for $Kn = 0.01$, 0.1, 0.5 and 1, respectively. At higher Mach and lower Knudsen numbers ($Ma = 5$ and $Kn = 0.01$), the values of C_0 are similar to those in a flow with a much higher Knudsen number (see $Kn = 0.5$ and $Ma = 0.2$ in Fig. A.3), showing that the extent of departure from equilibrium can be similar for two flows with very different

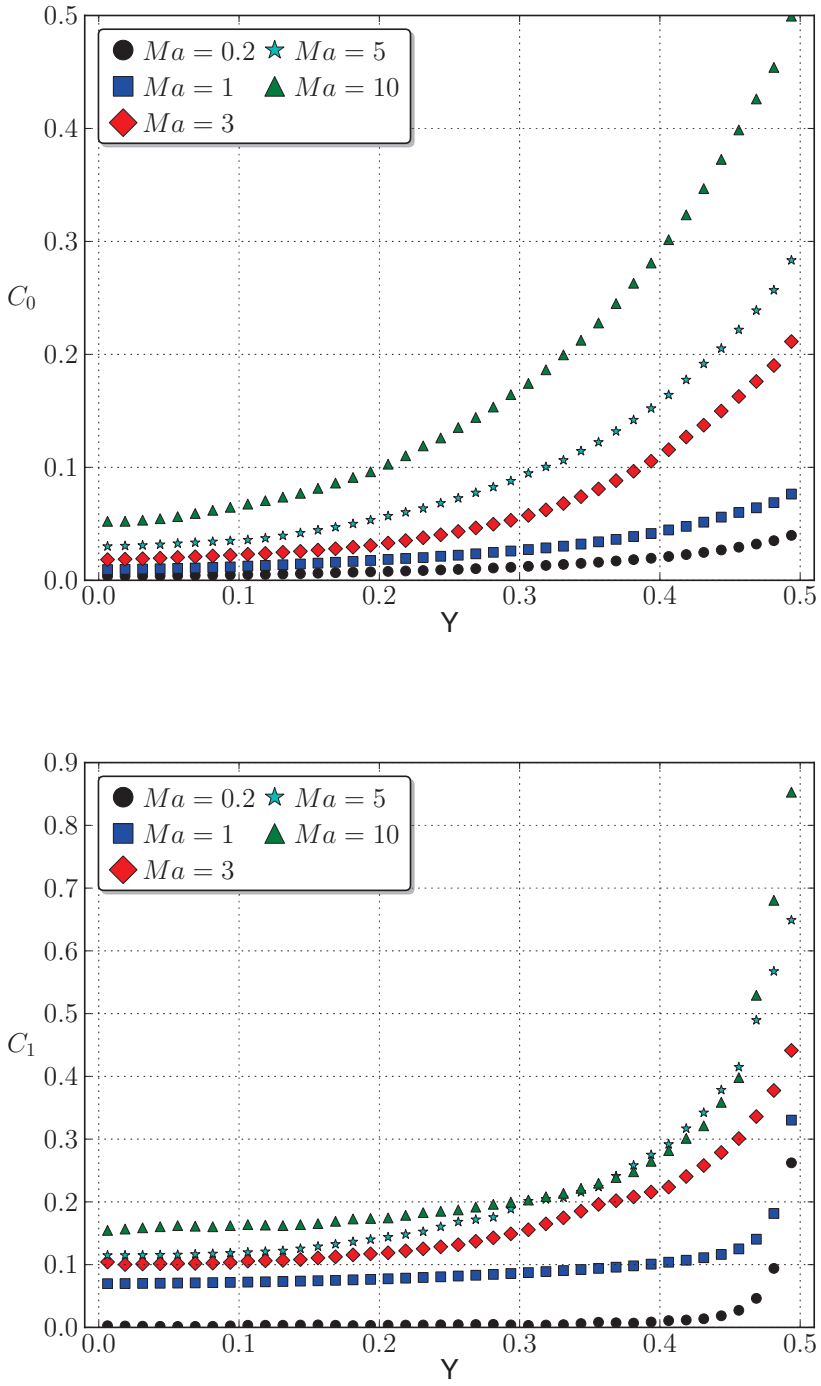

Figure A.1: Half-channel profiles of C_0 and C_1 at $Kn = 0.01$, for various Ma. The top ($Y = 0.5$) and bottom ($Y = -0.5$) plates are moving with speeds U_w in opposite directions.

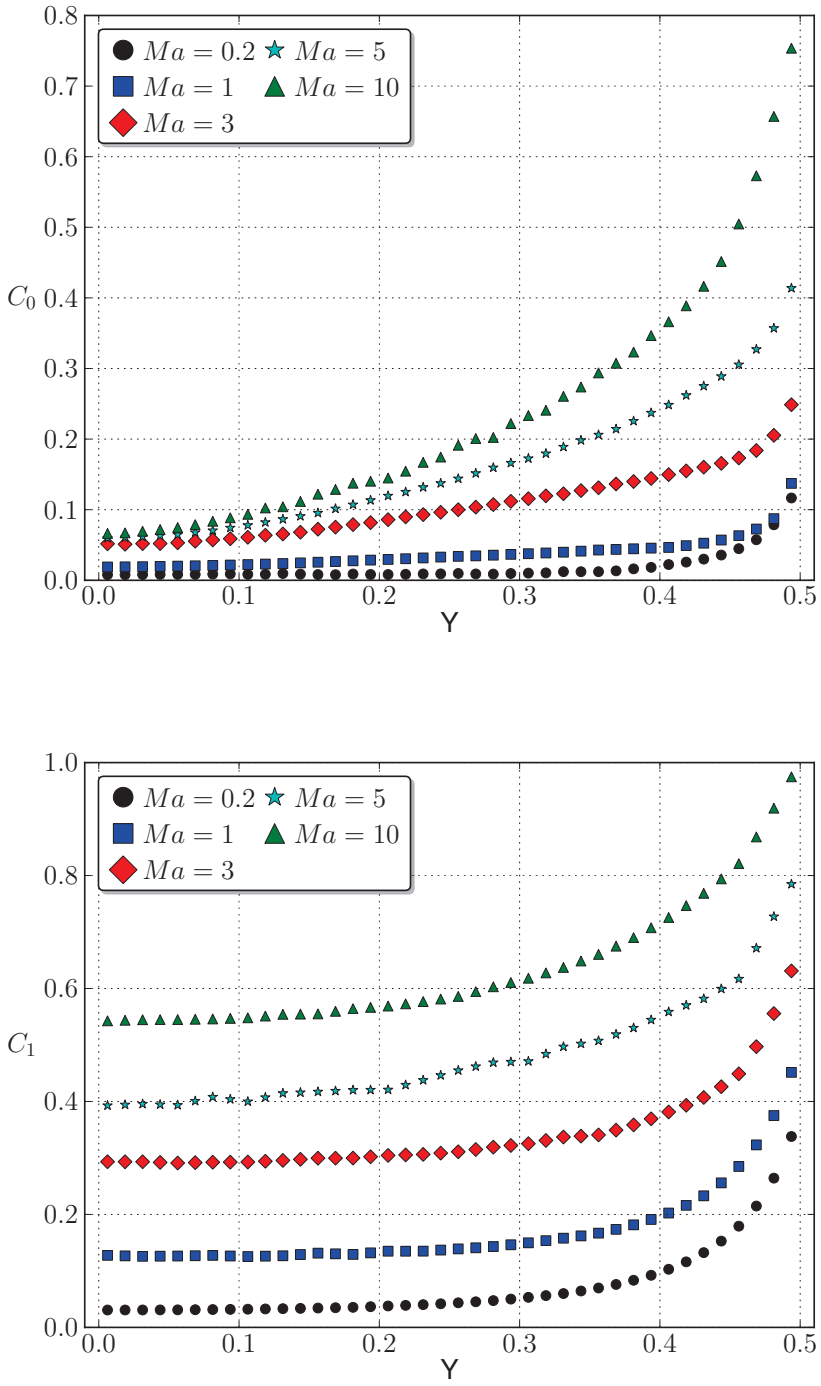

Figure A.2: Half-channel profiles of C_0 and C_1 at $Kn = 0.1$, for various Ma. The top ($Y = 0.5$) and bottom ($Y = -0.5$) plates are moving with speeds U_w in opposite directions.

Knudsen numbers. The Knudsen number alone does not determine the level of thermodynamic non-equilibrium.

For a Knudsen number of 0.01, the N-S-F equations are usually regarded as valid. However, the value of C_1, which inversely indicates the appropriateness of using the N-S-F equations, can increase with the Mach number, see Fig. A.1. When the Mach number is 1.0 and above, a significant proportion of the non-equilibrium flow information cannot be captured by the N-S-F equations, even in this simple flow configuration. When $Ma = 0.2$, in the bulk region ($Y = 0$), the N-S-F equations hold because $C_1 \ll 1$. However, in the wall region, the N-S-F equations are less accurate. The reason for this is the presence of the Knudsen layer in the near-wall region, where the linear constitutive relations for stress and heat conduction that are assumed in the N-S-F equations becomes inappropriate. When Ma increases to 1.0, higher-order fluid models may be required, even in the bulk, to accurately capture non-equilibrium information at conventional Knudsen numbers as low as 0.01. The C_1 profiles exhibit sharp gradients in the adjacent thin layer close to the wall and they became significantly shallower in the bulk region.

For flows with Kn around 0.1, which is in the end of the slip flow regime, it is generally assumed that the N-S-F equations will still be useful in the bulk flow region. Indeed, Fig. A.2 shows that less than 10% error will be introduced to the non-equilibrium distribution function if the N-S-F equations are used for a flow with $Ma = 0.2$. However, C_1 is larger than 0.1 in the bulk region when Ma is above 0.2, so substantial non-equilibrium flow information would not be captured by a N-S-F analysis in these cases. The C_1 profiles are relatively shallower in the near-wall region, when compared with the $Kn = 0.01$ case and also predict significantly higher values in the bulk region. At $Ma = 10$, the bulk and wall values approximately vary from 0.15 to 0.85 and 0.55 to 0.97, for $Kn = 0.01$ and 0.1 cases, respectively. This finding firmly conveys that the extent of deviation from the N-S-F equations is not simply linearly proportional to the Knudsen number, even in the slip flow regime.

Fig. A.3 also shows that non-equilibrium information cannot be properly captured, even for Mach numbers as low as 0.2, when the Knudsen number becomes large (e.g. 0.5). At Ma = 0.2, 1 and 3, C_1 values decrease from the wall region

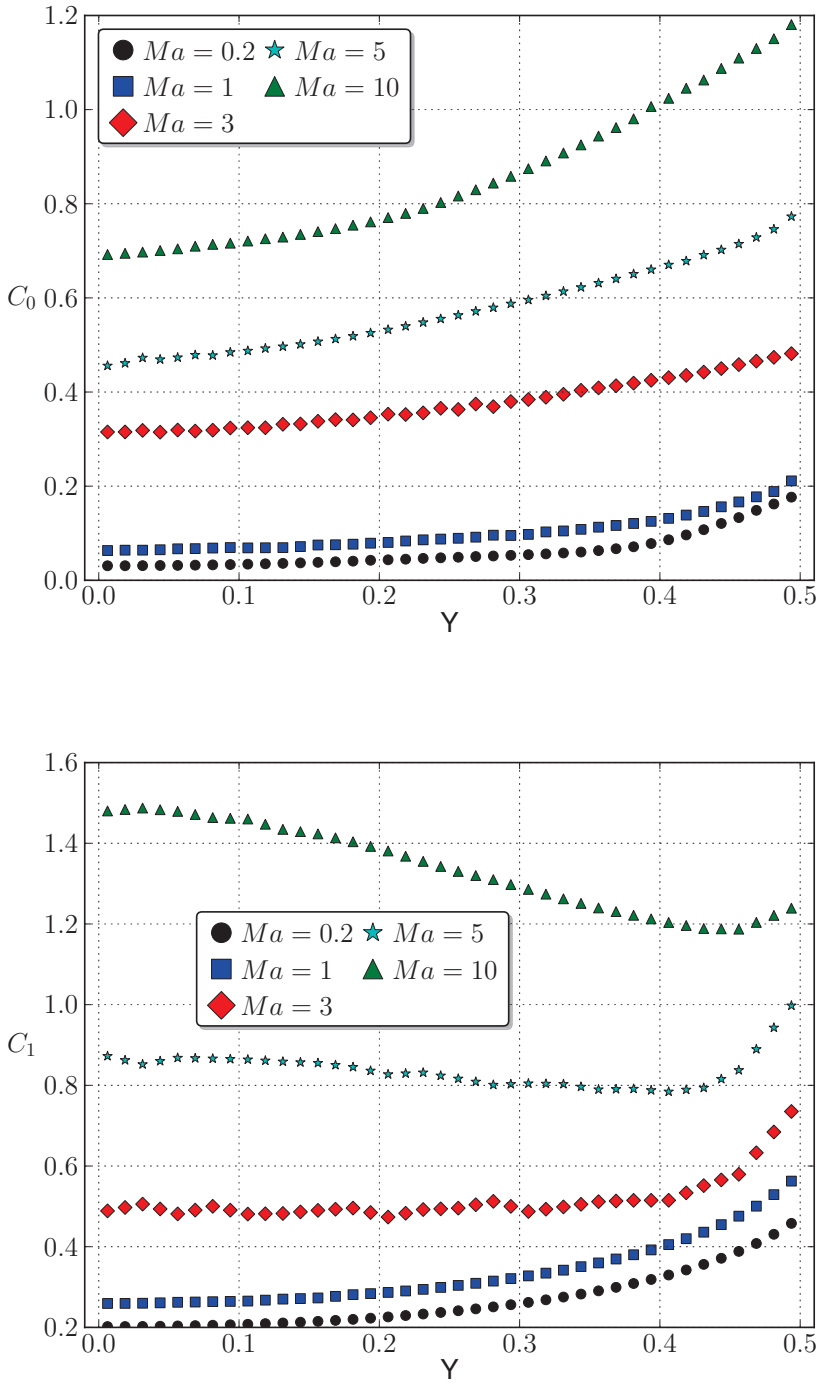

Figure A.3: Half-channel profiles of C_0 and C_1 at $Kn = 0.5$, for various Ma. The top ($Y = 0.5$) and bottom ($Y = -0.5$) plates are moving with speeds U_w in opposite directions.

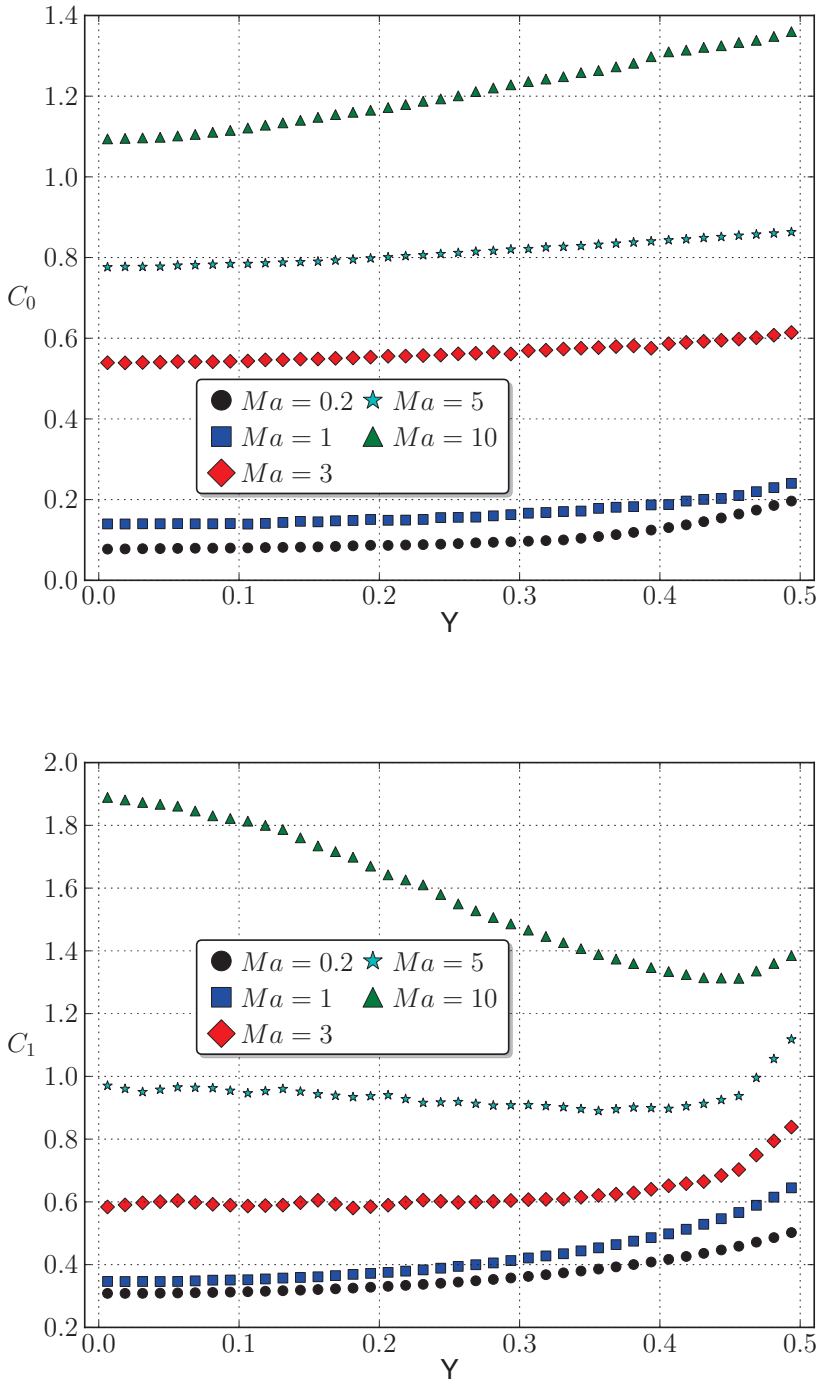

Figure A.4: Half-channel profiles of C_0 and C_1 at $Kn = 1$, for various Ma. The top ($Y = 0.5$) and bottom ($Y = -0.5$) plates are moving with speeds U_w in opposite directions.

to the bulk, as expected due to the presence of Knudsen layer effect in the near-wall region. However, at higher Mach numbers, the C_1 profiles exhibit contrasting behaviours. When the flow reaches the end of the supersonic regime ($Ma = 5$), the C_1 value decreases in the wall region and later increases into the bulk region, with the bulk value being still less than the wall value. At hypersonic conditions ($Ma = 10$), the C_1 value decreases from 1.45 in the bulk region to 1.24 in the wall region. Figs. A.1-A.4 together show that neither the Knudsen number nor the simple product of Mach and Knudsen numbers can appropriately assess the level of thermodynamic non-equilibrium in flowfields. However, we can discover the appropriate dependencies of C_0 on Kn and Ma in certain flows. The numerical data shown in Figs. A.5 and A.6 suggest a complicated general dependency of C_0 and C_1 on the Knudsen and Mach numbers.

When the Knudsen number is small, $f^{neq} \backsim f^{(1)}$ as a first order approximation, hence,

$$\begin{aligned} C_0 &\sim \sqrt{\frac{\int (f^{(1)})^2 d\xi}{\int (f^{eq})^2 d\xi}} \\ &= \sqrt{\frac{\int (f^{eq})^2 \left[\frac{\mu}{pRT}\frac{du_{<i}}{dx_{j>}}\varsigma_{<i}\varsigma_{j>} + \frac{2\kappa}{5pRT}\frac{dT}{dx_i}\varsigma_i\left(\frac{\varsigma_j\varsigma_j}{2RT} - \frac{5}{2}\right)\right]^2 d\xi}{\int (f^{eq})^2 d\xi}}. \end{aligned} \tag{A.10}$$

For Couette flows, this can be simplified to

$$C_0 \sim \sqrt{\frac{\int (f^{eq})^2 \left[\frac{\mu}{pRT}\frac{du_x}{dy}\varsigma_x\varsigma_y + \frac{2\kappa}{5pRT}\frac{dT}{dy}\varsigma_y\left(\frac{\varsigma_x^2+\varsigma_y^2+\varsigma_z^2}{2RT} - \frac{5}{2}\right)\right]^2 d\xi}{\int (f^{eq})^2 d\xi}}. \tag{A.11}$$

In the N-S-F model, the velocity gradient turns out as $2U_w/L$ over the whole flowfield. The temperature gradient can vary with position, but is zero at the centerline and $\sim 2U_w^2\mu/\kappa L$ at the wall. So we estimate C_0 at the centerline from Eq. (A.11) to be

$$C_0 \sim \frac{U_w\mu}{Lp} = \frac{\mu\sqrt{RT_0}}{pL}Ma \backsim KnMa, \tag{A.12}$$

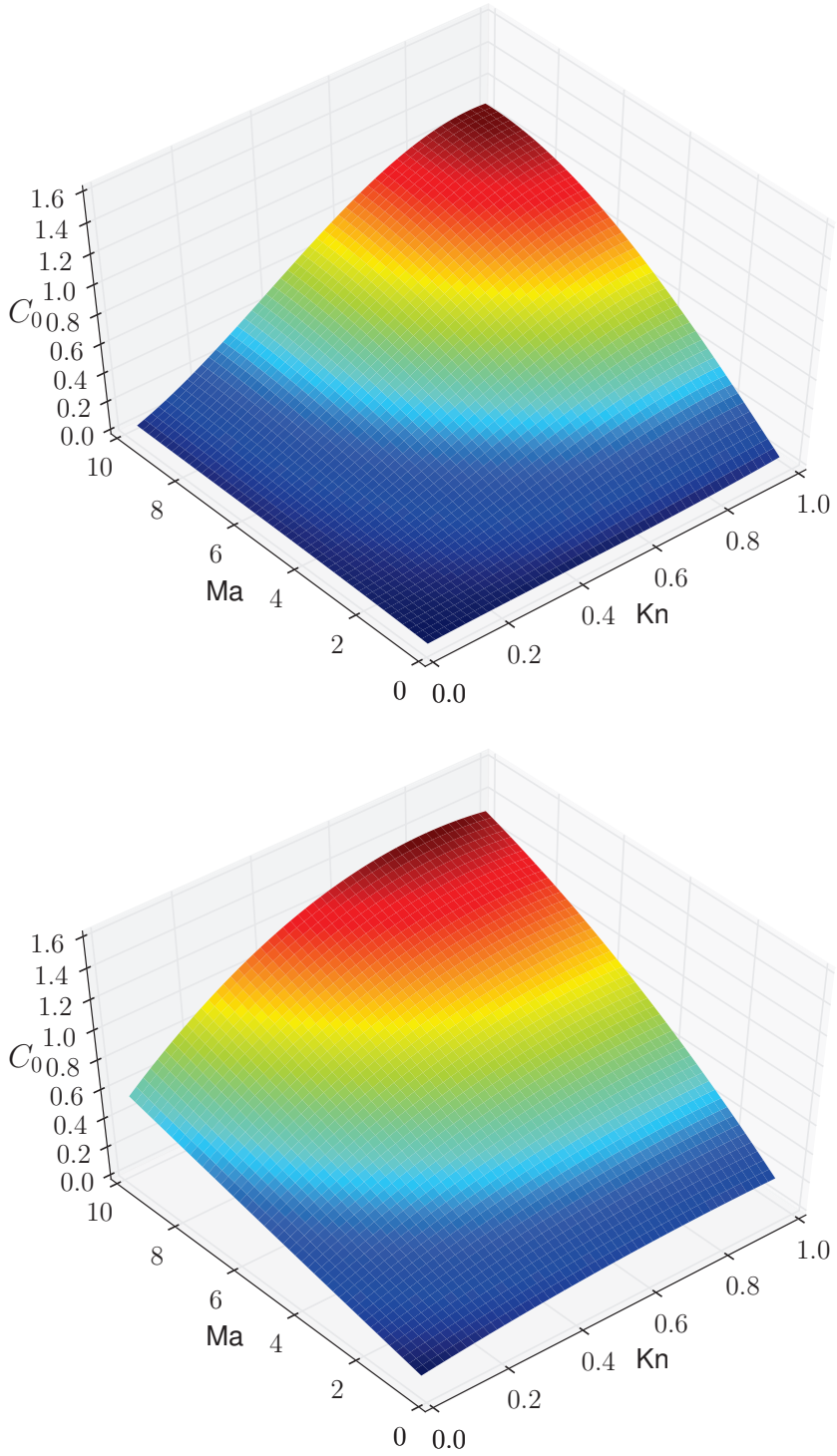

Figure A.5: Dependence of C_0 on Kn and Ma in the bulk (top) and at the wall (bottom).

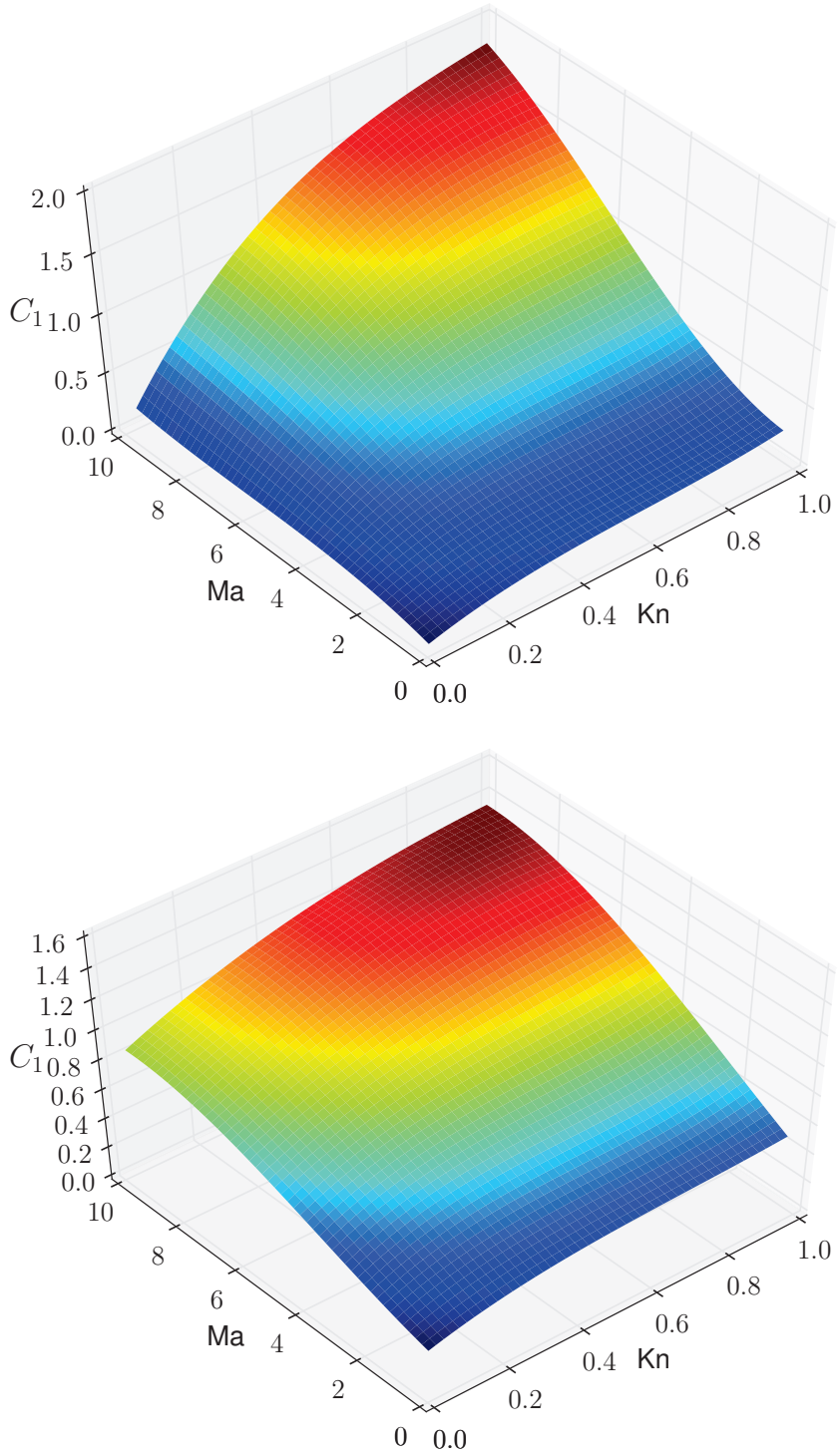

Figure A.6: Dependence of C_1 on Kn and Ma in the bulk (left) and at the wall (right).

and at the wall as

$$\begin{aligned} C_0 &\sim \sqrt{\frac{7U_w^4\mu^2}{10L^2p^2RT} + \frac{U_w^2\mu^2}{L^2p^2}} \\ &\sim \sqrt{\frac{\mu^2RT_0}{p^2L^2}\frac{T_0}{T}Ma^4 + \left(\frac{\mu\sqrt{RT_0}}{pL}Ma\right)^2} \\ &\sim KnMa\sqrt{1+Ma^2}. \end{aligned} \tag{A.13}$$

Therefore, the level of non-equilibrium increases with both the Knudsen and the Mach numbers. Note that this estimation is only appropriate when the Knudsen number is not too large. For large Kn, we must need to analyse the relation numerically. For C_1, it is difficult to provide a solution even for small Knudsen numbers, as no generally agreed Burnett-order solution for $f^{(2)}$ is available.

Figures (A.7)-(A.10) provide variations of bulk and wall, C_0 and C_1 values, with various parametric functions of Knudsen and Mach numbers. As given by Eq. (6.12), bulk C_0 values vary linearly as a function of $\sqrt{Kn^2(Ma^2)}$ until 0.1 (on $x-axis$), i.e. for small Kn and Ma. At large Knudsen and Mach numbers, the data is scattered for all compared parametric functions, see Fig. (A.7). Wall C_0 values do not show linear dependence with any of the compared parametric functions, even at low Kn and Ma, see Fig. (A.8). However, the parametric function $\sqrt{Kn^2(Ma^2+Ma^4)}$ show better fitting among all. Both the bulk and wall C_1 values are presented in Figs. (A.9) and (A.10), respectively. Both of them approximately show better fitting with the parametric function $\sqrt{Kn^2(1+Ma^2+Ma^4)}$. These parametric studies reveal that C_0, i.e. absolute deviation from the local equilibrium, may tend to be small when $Ma \to 0$ or $Kn \to 0$. However, C_1 may tend to be negligible only when both Ma and Kn are small ($\ll 1$). This finding is also consistent with the applicability of Navier-Stokes-Fourier equations, which are not applicable for high Kn low-speed micro-scale gas flows.

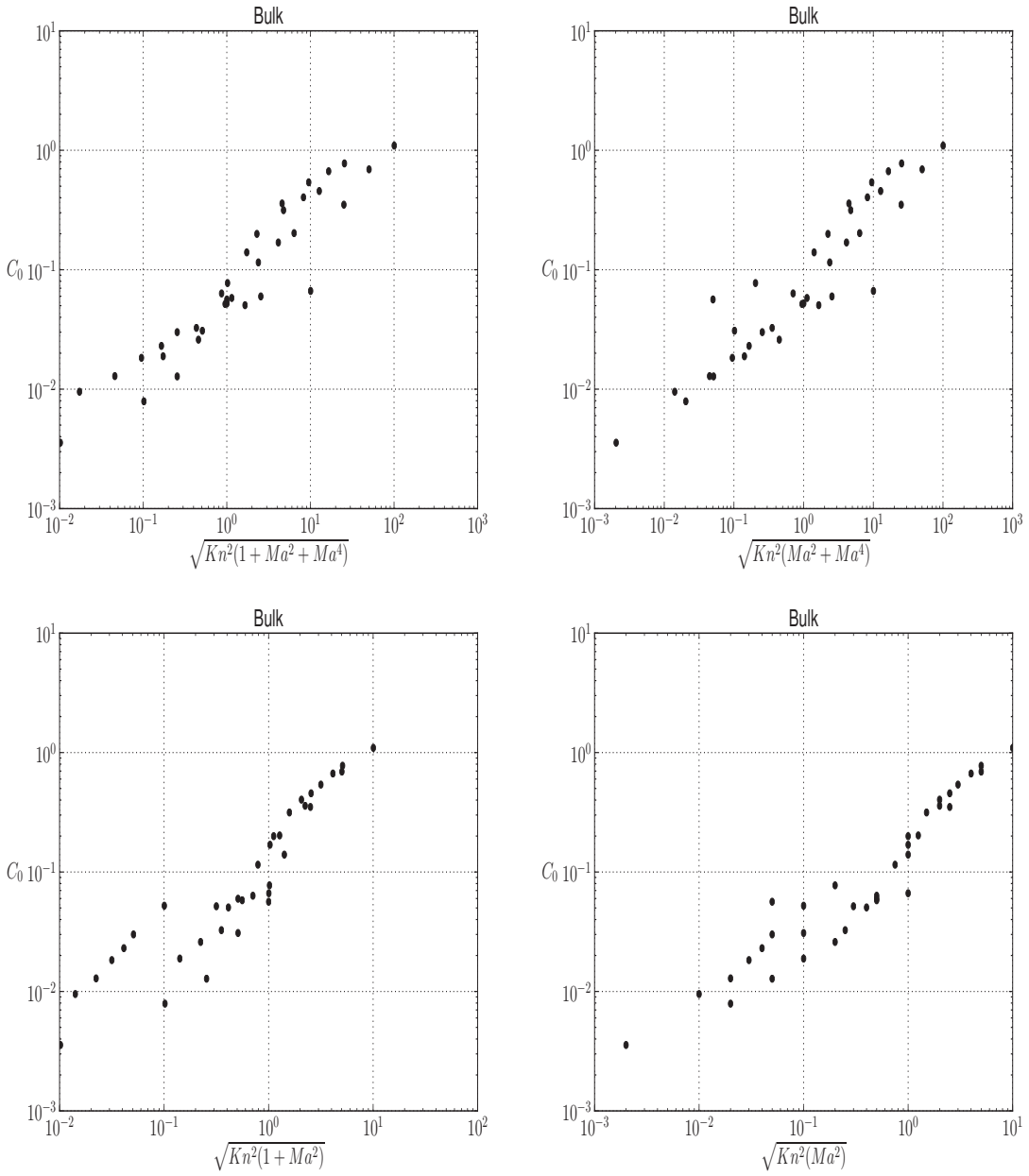

Figure A.7: Bulk C_0 variations with various parametric functions of Knudsen and Mach numbers.

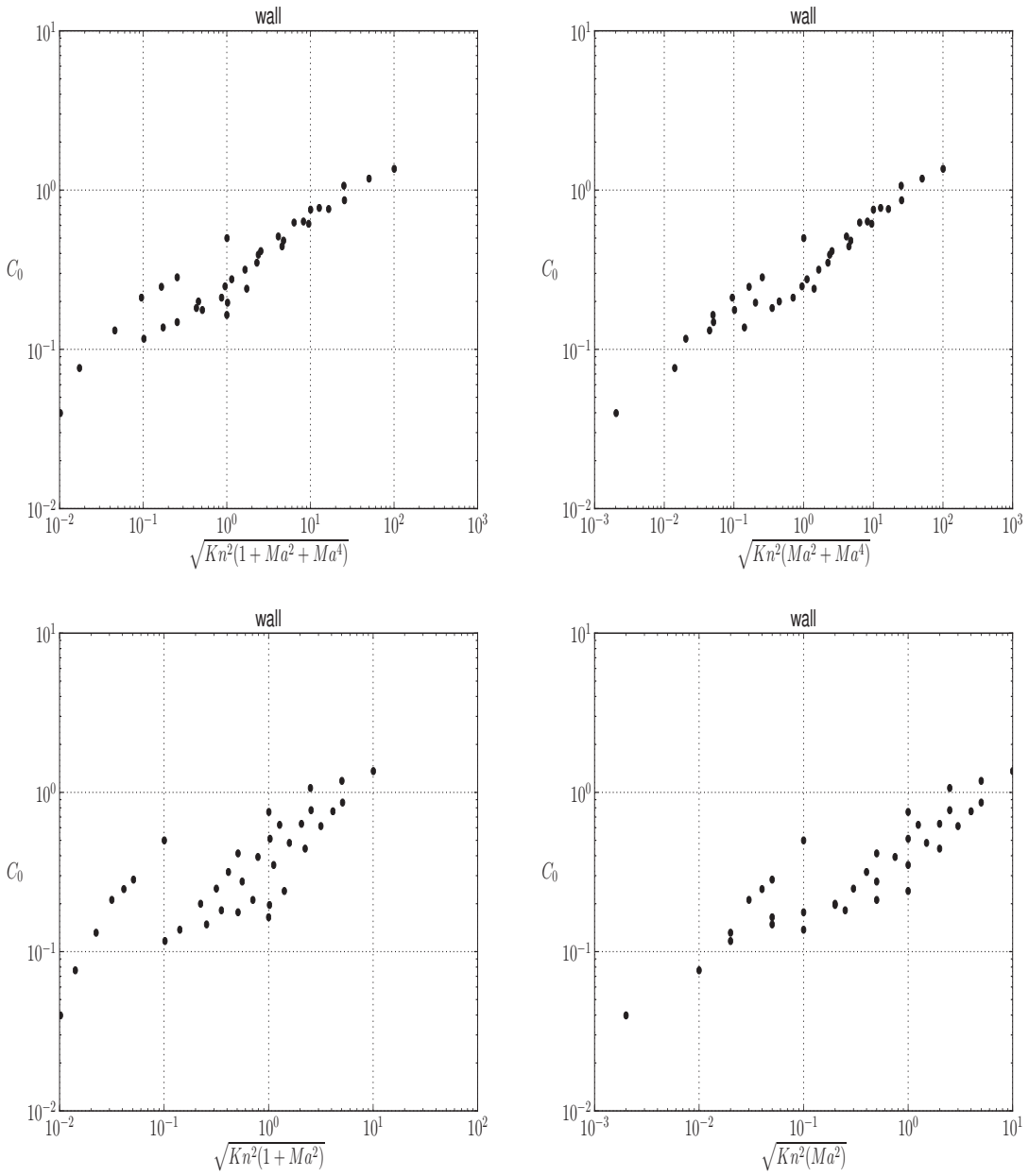

Figure A.8: Wall C_0 variations with various parametric functions of Knudsen and Mach numbers.

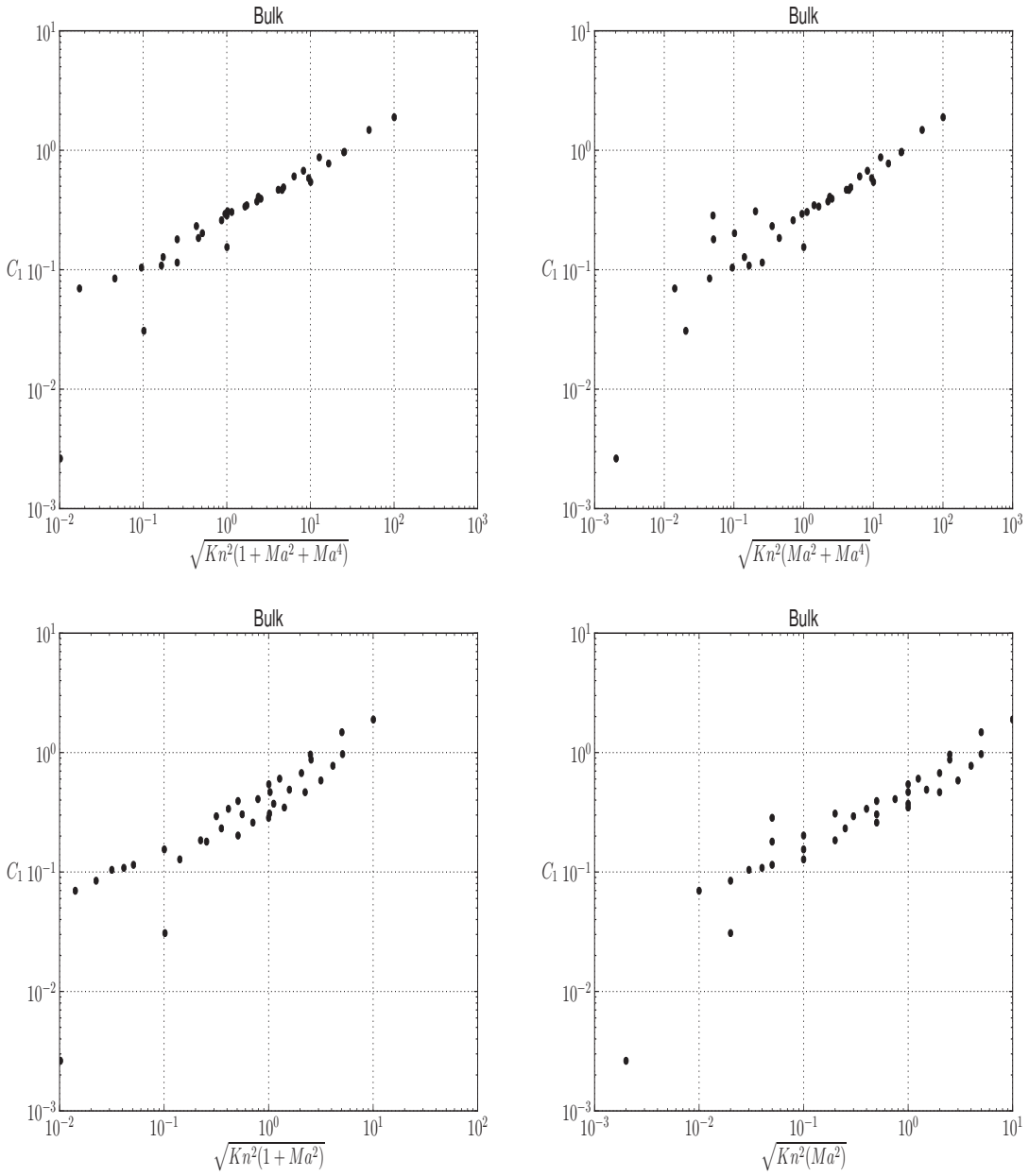

Figure A.9: Bulk C_1 variations with various parametric functions of Knudsen and Mach numbers.

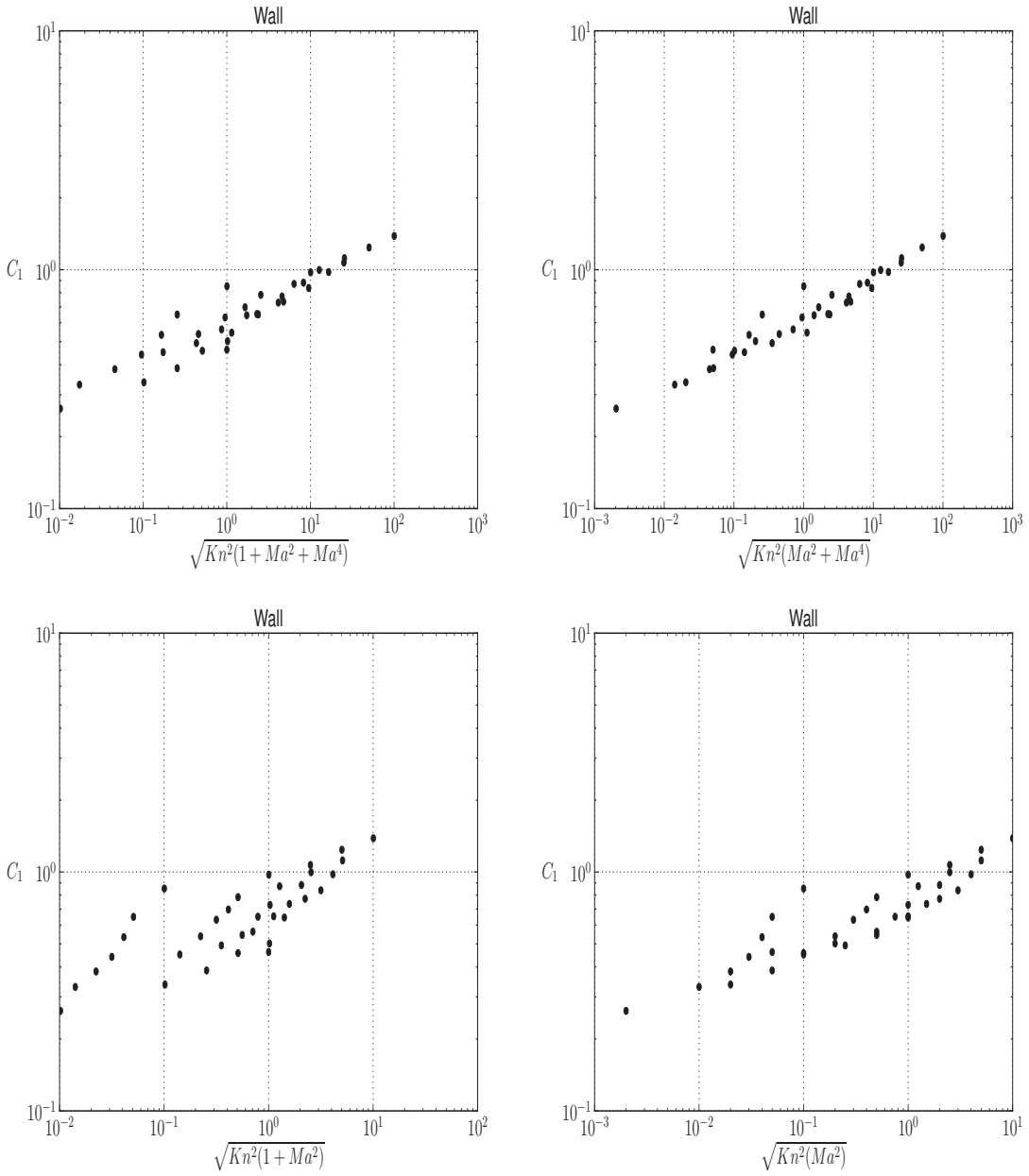

Figure A.10: Wall C_1 variations with various parametric functions of Knudsen and Mach numbers.

Appendix B

Mean free path profiles in high speed gas flows

The gas mean free path (MFP) is central to most models of transport phenomena in gases (Kennard, 1938; Cercignani, 1990), so we measure MFP values in our MD simulations. The ensemble value of MFP approaches the theoretically predicted value (λ_{th}) only if the gas is unbounded. It is known that if a solid bounding surface is included in the system, some molecules will hit the surface and their free flight paths will be terminated. The MFP of all the gas molecules in the system will therefore be reduced due to this boundary limiting effect (Stops, 1970). This is related to the formation of a Knudsen layer (KL) (Cercignani, 1990). Figs. (B.1) and (B.2) show the variation of the normalised local MFP $\beta = \lambda_{MD}/\lambda_{th}$ at different rarefaction and flow speed conditions.

MFP profiles for $Kn = 0.1$ and 0.25 and for $Ma = 0.2$, 1, 3, 5 and 10 are illustrated in Fig. (B.1). For the $Kn = 0.1$ case, i.e. at the end of the slip regime, sharper gradients are noted in the near-wall region. With further increase in Ma, gradients become shallower and MFP values decrease throughout the cross-section, although they are more pronounced in the bulk region. For an unbounded gas, it is well known that the MFP value is constant for a given density value and it does not show any dependency on temperature (Kennard, 1938). However, for bounded surfaces, an increase in wall velocities leads to a rise in gas temperature, which

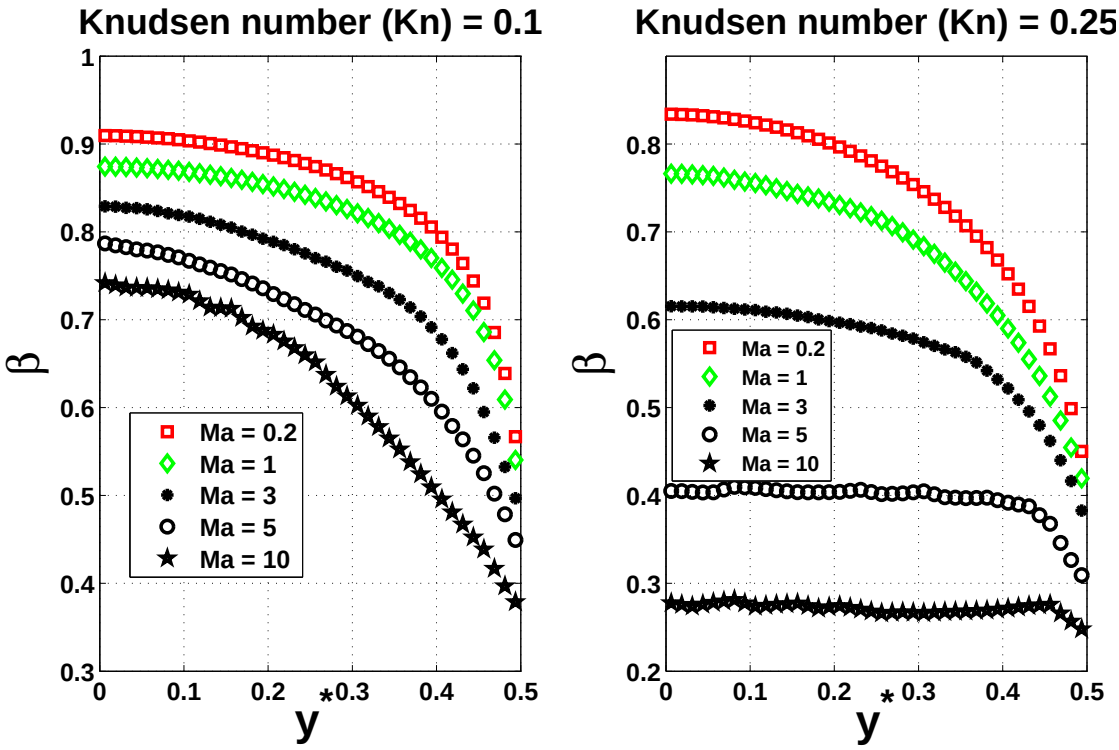

Figure B.1: Variations of normalised mean free path (MFP) profiles with the normalized cross-channel distance. Results are presented for various Ma and at $Kn = 0.1$ and 0.25. The solid channel walls are located at $y^* = \pm 0.5$.

results in more frequent collisions of gas molecules with the solid walls. This leads to a reduction in MFP values for an increase in Ma. For the $Kn = 0.25$ case, which is in the early transition regime, the MFP profiles are shallower relative to the $Kn = 0.1$ case, and the reduction in bulk MFP values is more significant. For the $Kn = 0.1$ case, with an increase in Ma the bulk and wall normalised MFP values varied from 0.92 to 0.74 and 0.57 to 0.38, respectively, while at $Kn = 0.25$, the bulk and wall normalised MFP values varied from 0.84 to 0.28 and 0.45 to 0.24, respectively.

MFP variations at higher Kn values are presented in Fig. (B.2). The profiles for $Ma = 0.2$, 1 and 3 show similar trends: MFP values increase with normalised distance away from the bounding surface ($y^* = 0.5$) and reach maximum values in the bulk region ($y^* = 0$). These trends are consistent with theoretical predictions in Chapters 3 and 4, and the reduction in MFP is more pronounced in the near-wall region due to frequent collisions with the solid surface.

Profiles for $Ma = 5$ and 10 appear to be paradoxical, as the MFP values in the

bulk are found to be lower than in the near-wall region. Viscous heating effects increase with increasing Kn, which results in significantly larger temperatures in the bulk region compared to the wall region. Consequently, gas molecules in the bulk have larger thermal speeds compared to the ones close to the wall, so they then have a greater probability of colliding with the walls, which results in the significant reduction of MFP in the bulk region.

The Knudsen layer, a non-equilibrium region, exists for bounded gas flows, irrespective of the wall movement. Its thickness is approximately the order of a mean free path. So at higher Knudsen numbers ($Kn > 0.5$), the layers from parallel walls overlap in the bulk region. When moving boundaries are introduced, an additional mode of non-equilibrium effects are introduced. MD results in Chapter 4 have shown that the molecular free path distribution of a rarefied gas confined between parallel plates significantly deviates from the classical exponential distribution function (Kennard, 1938). They performed simulations for a gas that is at rest (i.e. the molecular velocity distribution is Maxiwellian) and confined between non-moving specular wall boundaries. So, the Knudsen layer is formed solely may due to the gas surface interactions and molecular free paths more frequently terminated in this layer, i.e. deviation of the free path distribution from the classical one. While the other mode of non-equilibrium effect is caused due to the deviation of the molecular velocity distribution function from the classical Maxwellian one. Our MD results convey that flow properties in the near-wall non-equilibrium region do not just depend on Kn, they are also significantly affected by Ma.

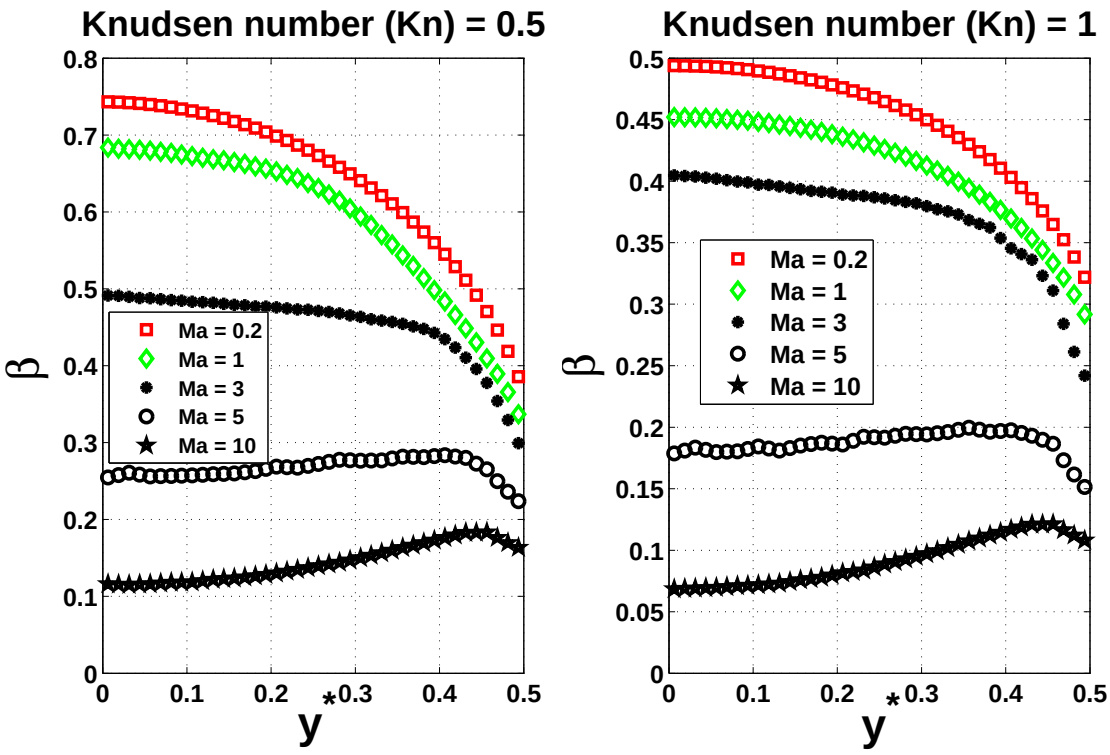

Figure B.2: Variations of normalised mean free path (MFP) profiles with the normalized cross-channel distance. Results are presented for various Ma and at $Kn = 0.5$ and 1. The solid channel walls are located at $y^* = \pm 0.5$.